

HOMOGENEOUS CATALYTIC OXIDATION OF AMMONIA
UNDER MILD CONDITIONS

By

Faezeh Habib Zadeh

A DISSERTATION

Submitted to
Michigan State University
in partial fulfillment of the requirements
for the degree of

Chemistry-Doctor of Philosophy

2019

ABSTRACT

HOMOGENEOUS CATALYTIC OXIDATION OF AMMONIA UNDER MILD CONDITIONS

By

Faezeh Habib Zadeh

Electrochemical ammonia splitting as a route for extracting hydrogen from ammonia, is plagued by relatively high oxidation overpotentials. Such requirements for an extra energy input are often caused by the sluggish kinetics associated to the multi-electron, multi-proton nature of the oxidation of ammonia to dinitrogen (N_2). A molecular catalyst added homogeneously to the solutions of ammonia, is a novel approach to assist the kinetics of the oxidation process and consequently lower the required overpotentials. In this dissertation, ruthenium (II) polypyridyl ammine complexes are employed as homogeneous catalysts for electro-oxidation of ammonia in tetrahydrofuran (THF) at room temperature and ambient pressure. Oxidation of ammonia was conducted in the presence of the catalyst at a constant applied anodic potential and evolution of N_2 and H_2 gases as the products of the electrolysis was confirmed by gas chromatography. The possibility of a heterogenous mechanism for the catalysis was dismissed after control rinse tests and microscopic examination of the working electrode showed that no active ruthenium depositions were formed on the electrode surface.

Authentic samples of ruthenium (III) polypyridyl ammine and ruthenium (II) polypyridyl hydrazine complexes were synthesized and characterized, and their role in the catalytic cycle were investigated. Isotopic N-labeling experiments, revealed that both the coordinated ammine and the free ammonia in the solution participate in the N_2 formation, enlightened the path for generation of a hydrazine intermediate. The hydrazine complex was observed in low temperature 1H NMR experiments, in which the Ru(III) ammine complex was treated with NH_3 . Interestingly, reactions

between the Ru(III) ammine complex and ammonia resulted in regeneration of the Ru(II) ammine complex. Same observations was made when a non-coordinating base was used instead of ammonia, suggesting that in the presence of a proton acceptor a redox disproportionation would afford the Ru(II) ammine from Ru(III) ammine.

Our further electrochemical, spectrophotocatalytic and mass spectroscopy results that are discussed in this dissertation, enabled us to construct a proposed catalytic cycle for oxidation of ammonia in THF using the ruthenium (II) ammine catalyst. In this dissertation the first example of a molecular transition metal is introduced that can catalyze ammonia electro-oxidation, opening up the gate for further developments and progresses in the field of electrochemical ammonia oxidation.

ACKNOWLEDGEMENTS

Firstly, I would like to express my sincere gratitude to my advisor Prof. Thomas Hamann for the continuous support of my Ph.D. study and related research, for his patience, motivation, and immense knowledge. His guidance helped me in all the time of research and writing of this thesis.

Besides my advisor, I would like to thank the rest of my thesis committee: Prof. Arron Odom, Prof. Mitch Smith, and Prof. Dana Spence, for their insightful comments and encouragement. My special gratitude goes out to Prof. Smith and Dr. S. Miller for their invaluable contribution in my project, and also for our very helpful discussions which incited me to widen my research from various perspectives.

I would like to specially mention my friends Mrs. Parisa Shadabipour, Miss. Yujue Wang, Mrs. Mersedeh Sanipey and Miss. Nona Ehyaei and my former and present colleagues in Hamann lab. It was fantastic to have the opportunity to work with you and sharing the laboratory with you during last five years. You made graduate school fun!

I am also thankful to Michigan State University and the U.S. Department of Energy for helping me and providing the funding for the work, and Michigan State University's department of Chemistry faculty and staff for having their doors open and being supportive and helpful.

TABLE OF CONTENTS

LIST OF TABLES.....	viii
LIST OF FIGURES	ix
LIST OF SCHEMES	xv
KEY TO ABBREVIATIONS.....	xvi
CHAPTER 1: INTRODUCTION	1
1.1. The Essence of Carbon Neutrality	2
1.2. Carbon-Neutral Fuels	4
1.3. Energy-Related Applications of Ammonia	6
1.3.1. Using NH ₃ in Internal Combustion Engines.....	6
1.3.2. Ammonia-Fueled Solid Oxide Fuel Cells (SOFC).....	6
1.3.3. Ammonia as a Hydrogen Carrier.....	6
1.4. Ammonia Splitting	9
1.4.1. Thermal Cracking of Gaseous NH ₃	9
1.4.2. Ammonolysis of Alkali Metal Hydrides	10
1.4.3. Electrolysis of Ammonia.....	10
1.5. Transition Metal Complexes as Catalysts for Ammonia Oxidation	13
1.6. This work.....	17
APPENDIX.....	19
REFERENCES	22
CHAPTER 2: EXPERIMENTAL DETAILS	27
2.1. General Materials and Methods	28
2.2. Preparation of Dry Liquid Ammonia	29
2.3. Preparation of Saturated ¹⁵ NH ₃ Solutions in Tetrahydrofuran (THF).....	30
2.4. Electrochemistry.....	31
2.4.1. Cyclic Voltammetry (CV)	31
2.4.2. Determination of the Onset Potential	33
2.4.3. Hydrodynamic Voltammetry	33
2.4.4. Controlled Potential Electrolysis (CPE).....	34
2.5. Gas Chromatography (GC)	36
2.5.1. GC Calibration.....	37
2.6. GC-MS Experiment.....	38
2.7. X-Ray Spectroscopy.....	39
REFERENCES	40
CHAPTER 3: CATALYTIC ACTIVITY OF [Ru(TRPY)(DMABPY)NH ₃] ²⁺ IN THF.....	42
3.1. Synthesis of [Ru(trpy)(bpy)NH ₃](PF ₆) ₂ (1a).....	43
3.1.1. Synthesis of (2,2':6',2''-terpyridyl) trichloro ruthenium (III), [Ru(trpy)Cl ₃].....	43

3.1.2. (2,2':6',2''-terpyridyl) (2,2'-bipyridyl) chloro ruthenium (II) chloride, [Ru(trpy)(bpy)Cl]Cl.	43
3.1.3. (2,2':6',2''-Terpyridyl)(2,2'-bipyridyl)ruthenium(II) ammine dihexafluoro phosphate, [Ru(trpy)(bpy)NH ₃](PF ₆) ₂ , (1a).	44
3.2. Catalytic Activity of 1a in THF	44
3.3. Synthesis of [Ru(trpy)(dmabpy)NH ₃](PF ₆) ₂ (2a).....	49
3.3.1. (2,2':6',2''-Terpyridyl)(4,4'-bis(N,N-dimethylamino)-2,2'-bipyridyl)chloro ruthenium(II) chloride, [Ru(trpy)(bdmabpy)Cl]Cl.....	49
3.3.2. (2,2':6',2''-Terpyridyl)(4,4'-bis(N,N-dimethylamino)-2,2'-bipyridyl)ruthenium(II) ammine dihexafluoro phosphate, [Ru(trpy)(dmabpy)NH ₃](PF ₆) ₂ , (2a).	50
3.4. Catalytic Activity of 2a in THF	51
3.4.1. Assessment of the Catalytic Current by Cyclic Voltammetry	51
3.4.2. Quantification of the Products of the Electrolysis Using Gas Chromatography	53
3.5. Homogeneous vs. Heterogeneous Catalysis.....	56
3.6. Isotopic Labeling Experiments.....	59
3.6.1. Synthesis of [Ru(trpy)(dmabpy) ¹⁵ NH ₃](PF ₆) ₂ (¹⁵ N- 2a)	60
3.6.2. Electrolysis of ¹⁵ NH ₃ using 2a and ¹⁵ N- 2a	60
3.7. Conclusions	61
APPENDIX.....	63
REFERENCE.....	83
CHAPTER 4: THE RU(III) INTERMEDIATE	85
4.1. Synthesis of [Ru(trpy)(dmabpy)NH ₃](PF ₆) ₃ , (2b).....	86
4.1.1. Electrochemical Synthesis.....	86
4.1.2. Chemical Synthesis	87
4.2. Characterization of 2b	88
4.2.1. Proton NMR	88
4.2.2. Elemental Analysis	88
4.2.3. Magnetic Susceptibility	89
4.2.4. Electrochemistry.....	91
4.3. Deprotonation of [Ru(trpy)(dmabpy)NH ₃] ⁺³	93
4.4. Regeneration of 2a from 2b	98
4.5. Reaction of [Ru(trpy)(dmabpy)NH ₃] ⁺³ With Bases	101
4.5.1. Electrochemistry.....	101
4.5.2. ¹ H NMR Studies	104
4.5.3. UV-Vis Spectrophotometric Titrations	106
4.6. Rotating Ring Disk Electrode (RRDE) Experiments.....	111
4.6.1. Titration with DBU: Scanning E _D , Constant E _R	113
4.6.2. Titration with DBU: Scanning E _R , Constant E _D	118
4.7. Conclusions	122
APPENDIX.....	123
REFERENCES	142
CHAPTER 5: THE [RU(TRPY)(DMABPY)N ₂ H ₄] ²⁺ INTERMEDIATE	144
5.1. Synthesis of an Authentic Sample of [Ru(trpy)(bpy)N ₂ H ₄] ²⁺ Complex (2e).....	146
5.2. Ligand Displacement in 2e / THF / NH ₃	147

5.3. Cyclic Voltammetry Studies	148
5.4. Variable Temperature (VT) ¹ H NMR Experiments ⁶	155
5.5. Spectrophotocatalytic Studies	159
5.6. Conclusions	162
APPENDIX.....	163
REFERENCES	166

CHAPTER 6: PRELIMINARY ELECTROCHEMICAL STUDIES OF OTHER RUTHENIUM POLYPYRIDYL AMINE CATALYSTS..... 169

6.1. [Ru(Me ₃ trpy)(dmabpy)NH ₃](PF ₆) ₂ , (3a).....	170
6.1.1. Synthesis.....	170
6.1.1.1. (4',4,4''-trimethyl-2,2':6',2''-terpyridine)(4,4'-bis(N,N-dimethylamino)-2,2'-bipyridyl) chloro ruthenium(II) chloride, [Ru(Me ₃ trpy)(dmabpy)Cl]Cl.....	170
6.1.1.2. (4',4,4''-trimethyl-2,2':6',2''-terpyridine) (4,4'-bis(N,N-dimethylamino)-2,2'-bipyridyl) ruthenium (II) ammine dihexafluorophosphate, [Ru(Me ₃ trpy)(bdmabpy)NH ₃](PF ₆) ₂ , (3a).	171
6.1.2. Ammonia Oxidation Using 3a as the Catalyst	171
6.2. [Ru(^t Bu ₃ trpy)(dmabpy)NH ₃](PF ₆) ₂ , (4a).....	174
6.2.1. Synthesis.....	174
6.2.1.1. (4',4,4''-tri-tert-butyl-2,2':6',2''-terpyridine)(4,4'-bis(N,N-dimethylamino)-2,2'-bipyridyl) chloro ruthenium (II) chloride, [Ru(^t Bu ₃ trpy)(dmabpy)Cl]Cl.....	174
6.2.1.2. (4',4,4''-tri-tert-butyl-2,2':6',2''-terpyridine)(4,4'-bis(N,N-dimethylamino)-2,2'-bipyridyl) ruthenium(II) ammine dihexafluorophosphate, (4a).	174
6.2.2. Ammonia Oxidation Using 4a as the Catalyst	175
6.3. [Ru(dmaptrpy)(dmabpy)NH ₃](PF ₆) ₂ , (5a).	178
6.3.1. Synthesis.....	178
6.3.1.1. (4-N,N-dimethylaminophenyl)-2,2',6',2''-terpyridine, dmaptrpy.	178
6.3.1.2. ((4-N,N-dimethylaminophenyl)-2,2',6',2''-terpyridine)(4,4'-bis(N,N-dimethylamino)-2,2'-bipyridyl) chloro ruthenium (II) chloride, [Ru(dmaptrpy)(dmabpy)Cl]Cl.....	179
6.3.1.3. ((4-N,N-dimethylaminophenyl)-2,2',6',2''-terpyridine)(4,4'-bis(N,N-dimethylamino)-2,2'-bipyridyl) ruthenium(II) ammine dihexafluorophosphate, (5a).....	179
6.3.2. Ammonia Oxidation Using 5a as the Catalyst	180
6.4. Conclusions	182
APPENDIX.....	184
REFERENCES	190

CHAPTER 7: CONCLUDING REMARKS AND FUTURE DIRECTIONS 192

LIST OF TABLES

Table 2.1 Comparison of energy densities between hydrogen and ammonia as fuels. Gasoline is also shown as the reference.....	5
Table 2.1 Experimental data used for GC signal calibration for moles of injected N ₂ and H ₂ . Red and blue colored numbers are used to construct the corresponding calibration lines in Fig. 2.5.2.	37

LIST OF FIGURES

Figure 1.1.1 Relative amounts (in percent) of U.S. greenhouse gas emissions in 2016, shows the large contribution of CO ₂ . Figure reproduced from ref. [2].	2
Figure 1.1.2 The U.S. energy consumption in 2017 from various sources shows the significance reliance on the fossil fuels. Figure reproduced from ref. [2].	3
Figure 1.3.1 The ideal carbon-neutral energy cycle of ammonia as a hydron carrier.	8
Figure 1.4.1 An ammonia cracker by Sam Gas Projects Pvt. Ltd. (India) which is maintained at 850 °C using an electric furnace. The purity of the produced hydrogen is 99.5% (0.5% nitrogen contamination). Visit: https://www.psa-nitrogen.com .	10
Figure 1.6.1 Ruthenium catalysts 1a-5a used in this study.	18
Figure 2.2.1 The apparatus used for the storage of dry liquid ammonia under ambient pressure.	30
Figure 2.4.1 Diagram of the three-electrode electrochemical cell used for CV experiments. The side arms are inert gas inlet and outlets. CE: Counter Electrode, WE: Working Electrode and RE: Reference Electrode.	31
Figure 2.4.2 CVs (three cycles) of ferrocene in THF and NM using the Ag/AgNO ₃ reference electrode. Top: 3.0×10 ⁻³ M ferrocene in THF, and Bottom: 1.6×10 ⁻³ M ferrocene in NM. CVs were obtained at 0.1 V s ⁻¹ scan rate. E _{p,a} and E _{p,c} stand for anodic and cathodic peak potentials, respectively. The E _{1/2} is defined as the midpoint between E _{p,a} and E _{p,c} and is calculated as their arithmetic average.	32
Figure 2.4.3 Determination of the onset potential for oxidation of ammonia at the surface of the glassy carbon electrode in THF. The potential of the cross-point between the baseline and the oxidation current is considered as the onset potential.	33
Figure 2.4.4 Diagram of the three-electrode electrochemical cell used in RDE and RRDE experiments. The side arms are inert gas inlet and outlets. CE: Counter Electrode, WE: Working Electrode and RE: Reference Electrode.	34
Figure 2.4.5 The cell used in some controlled potential electrolysis experiments. An empty cell is presented here for better visibility. The counter electrode is Pt mesh, and working is glassy carbon plate. The inset shows the position of the sampling port.	35
Figure 2.5.1 Full TCD Chromatograms obtained for two headspace injections. Injection A (black): Headspace of a cell containing THF and the catalyst. Injection B (red): Headspace of the cell after 2 h of electrolysis in the presence of NH ₃ and the catalyst. At point 1, a GC column valve switches to isolate N ₂ , H ₂ , and residual O ₂ in the molsieve column, while heavier volatiles, THF, and NH ₃ , elute through the PLOT/U column to the detector during time window 2. At time point 3, the column isolation valve resets and diatomic gases elute through the molsieve column to the thermal conductivity detector as seen in time window 4.	36

Figure 2.5.2 Gas Chromatography calibration lines obtained for N ₂ (top, blue) and H ₂ (bottom, red) based on data in Table 2.1.	38
Figure 3.2.1 Top: Scan rate dependence of the current in 2.13×10^{-3} M [Ru(trpy)(bpy)NH ₃](PF ₆) ₂ (1a) in THF shown for seven scan rates. Bottom: Plots of anodic and cathodic peak currents obtained from CVs on the top <i>versus</i> square root of the scan rate. From the slope of the anodic branch a diffusion coefficient of $D_{ox} = 4.06 \times 10^{-6}$ cm ² s ⁻¹ is calculated for 1a	46
Figure 3.2.2 Cyclic voltammograms for a solution containing ferrocene in THF with (red) and without (blue) NH ₃ (0.34M). The onset of the direct ammonia oxidation was measured as +0.25 V vs. ferrocene. In solutions that do not contain ferrocene, the oxidation of ammonia appears at the same potential using an Ag/AgNO ₃ reference electrode that is separately calibrated with Fc ⁺⁰ in THF.	47
Figure 3.2.3 Top: Cyclic voltammograms for THF solutions of 2.13×10^{-3} M catalyst 1a (blue), 0.34 M NH ₃ added to the solution of 2.13×10^{-3} M catalyst 1a (red) and direct NH ₃ oxidation in THF in the absence of 1a (dotted green). Scan rate 0.1 V s ⁻¹ . Bottom: Normalized catalytic (i/\sqrt{v}) currents when NH ₃ (0.34 M) is added to a solution of 2.13×10^{-3} M 1a obtained for mentioned scan rates. The magnitude and the onset of the normalized currents are being improved as the scan rate is decreasing.	48
Figure 3.4.1 Cyclic voltammograms for THF solutions of 2.5×10^{-3} M 2a (black), 2.5×10^{-3} M 2a and 0.34 M NH ₃ (red), uncatalyzed NH ₃ oxidation in THF, 0.34 M (green) and the electrolyte background (gray). Scan rate 0.1 Vs ⁻¹ . This figure shows that upon the presence of the catalyst 2a , a catalytic current is appeared at lower overpotentials relative to direct oxidation of ammonia in THF.	52
Figure 3.4.2 Dependence of catalytic current on the concentration of ammonia when [2a] = 2.5×10^{-3} M, [NH ₃] = (a) 0 M, (b) 0.008 M, (c) 0.04 M, (d) 0.07 M, (e) 0.17 M and (f) 0.34 M. Inset: Peak currents (at 0.90 V for catalytic currents) <i>versus</i> concentration of ammonia. The first data point (gray) is the anodic peak current for the catalyst in the absence of ammonia and is shown for comparison. Scan rate 100 mV s ⁻¹	53
Figure 3.4.3 Current passing during three steps of controlled potential electrolysis (each 3600 s) while the solution was being stirred under argon. [2a] = 2.7×10^{-3} M, [NH ₃] = 0.34 M, 0.1 M [NH ₄](PF ₆) in dry THF. Numbers show the amount of charge (q, in coulombs) passed in each step, calculated based on the integration of the area under each curve ($q = i \times t$).	54
Figure 3.4.4 Gas chromatograms obtained after injection of 100 μ L of the electrolysis headspace before applying potential and after 60, 120 and 180 min of electrolysis. The peaks associated with N ₂ and H ₂ are growing in after each step. The residual O ₂ in the headspace sample is attributed to the leaks. For full chromatogram See Appendix, Figure A3.4.4.1.	55
Figure 3.5.1 XPS spectra of the glassy carbon electrode after the BE. Top: full spectrum. The source of silicon and oxygen is electrode contamination with silicon grease during the removal of the electrode from the electrolysis cell. The grease was heavily applied around the joints to prevent leaks. Bottom: the scan around 285 eV where the characteristic peak for ruthenium is expected to appear if depositions have had taken place.	57

Figure 3.5.2 Rinse test results. Left: The CV recorded for a solution of $\text{NH}_3(\text{sat'd})/\text{THF}$ in which the rinsed glassy electrode was immersed. Scan rate 0.1 Vs^{-1} . Right: Current vs. times for three electrolysis steps of electrolysis. The inset is the gas chromatogram of the cell headspace injected to GC before the electrolysis and after the third hour of electrolysis. No H_2 is generated and the $\text{N}_2:\text{O}_2$ ratio matches with leaks from the air.....	58
Figure 3.5.3 EDS analysis of the selected area (red circle in the inset) on the glassy carbon electrode at the end of a failed electrolysis experiment. The insets are the SEM images of the electrode with two different magnifications. These results show that a ruthenium containing material has deposited on the surface, possibly acting as an active catalytic surface.	59
Figure 4.1.1 The diagram of the three-electrode electrolysis cell used for chemical oxidation of 2a to 2b	87
Figure 4.2.1 The ^1H NMR resonance shift observed for the standard ferrocene after addition of paramagnetic 2b	90
Figure 4.2.2 Top: CV of $4.5 \times 10^{-3} \text{ M}$ 2b (green) compared to the CV of $4.12 \times 10^{-3} \text{ M}$ 2a (orange) in NM. Both complexes appear at the same $E_{1/2}$, Bottom: Extended potential window CVs of $2.10 \times 10^{-3} \text{ M}$ 2b in NM shown for three scan rates. Here a second oxidation process is seen at 0.95 V vs. $\text{Fc}^{+/0}$ (labeled as II).	92
Figure 4.3.1 Total ion spectrum obtained for a solution containing $1.16 \times 10^{-7} \text{ M}$ 2b and $1.072 \times 10^{-7} \text{ M}$ DBU in NM.	96
Figure 4.3.2 Assignments to four selected m/z values III, V, VI, and VII. The spectra in red are the experimentally obtained spectra and the inset shows the simulated spectra.....	97
Figure 4.4.1 The structure of the mentioned Ru(IV)oxo species.	101
Figure 4.5.1 CVs of a solution of $5.36 \times 10^{-3} \text{ M}$ 2b in NM before (green) and after (orange) addition of $1.34 \times 10^{-2} \text{ M}$ DBU. Scan rate 0.1 Vs^{-1} . After the reaction with the base, the solution contains 2a and three new redox active species labeled as I, II and III.	102
Figure 4.5.2 CVs of a solution containing $4.30 \times 10^{-3} \text{ M}$ $[\text{Ru}(\text{trpy})(\text{dmabpy})\text{NH}_3]^{+3}$, 2b , in NM before (green) and after (red) addition of NH_3 (saturated, 0.93 M , determined by NMR measurements). The black curve shows the non-catalytic oxidation of NH_3 in NM.....	103
Figure 4.5.3 Vs of $4.30 \times 10^{-3} \text{ M}$ $[\text{Ru}(\text{trpy})(\text{dmabpy})\text{NH}_3]^{+3}$ in NM without NH_3 (green), and after addition of NH_3 ($4.60 \times 10^{-3} \text{ M}$, 1.06 equiv.) (brown).CV obtained for $2.80 \times 10^{-3} \text{ M}$ $[\text{Ru}(\text{trpy})(\text{dmabpy})\text{N}_2\text{H}_4](\text{PF}_6)_2$ in NM in the absence of NH_3	104
Figure 4.5.4 ^1H NMR spectra (rt, 500 MHz , nitromethane- d_3) of 2b (bottom, green), 2b + excess DBU (middle, brown) and 2a (top, red).Comparison between the spectrum obtained after addition of NH_3 to 2b and the spectrum of 2a in NM, shows that 2a is the main product of the reaction at room temperatures. The resonances at δ 1.65, 2.05, 2.97, 3.51 and 3.46 ppm are related to the added DBU.....	105

Figure 4.5.5 ^1H NMR spectra (rt, 500 MHz, nitromethane- d_3) of **2b** + excess NH_3 (bottom, black), **2e** (middle, blue) and **2a** (top, red). By comparing the spectra, the major product of the reaction between **2b** and NH_3 in NM is **2a**. 106

Figure 4.5.6 Top: Changes in the electronic absorption spectra of a green “starting solution” of 7.65×10^{-5} M **2b** with the addition of DBU to the orange “final solution”. Bottom: Increase in the absorbance at 490 nm due to generation of **2a** happens simultaneously with the decrease in absorbance at 730 nm due to consumption of **2b**. 108

Figure 4.5.7 Comparing the electronic absorption spectra obtained at the end of the titration, *i.e.* 1.4 equiv. DBU added (orange) with the constructed spectrum for 0.5 equiv. **2a** in NM (red) and constructed spectrum for 0.5 equiv. **2a** + DBU in NM (black). 110

Figure 4.6.1 The schematic structure of an RRDE electrode is illustrated on the left. On the right, the redox events at the disk and ring are displayed for a redox active species with a generic CV response as shown on the top. 112

Figure 4.6.2 Top: CVs obtained for a solution containing 5.57×10^{-4} M **2a** in THF collected at the ring and the disk show that the $E_{1/2}$ of the complex does not change with the material of the electrode. Bottom: The currents associated with the disk (i_D) and ring (i_R), when the potential of the disk is being scanned linearly and the ring is set at a constant reductive potential of 0.00 V vs. NHE. Three rotation speeds are shown: 200 rpm (red), 500 rpm (green) and 1000 rpm (blue). $N = 24\%$ (rotation speed independent), consistent with the value reported by the manufacturer. 115

Figure 4.6.3 Top: CVs obtained after addition of DBU to the solution containing 5.57×10^{-4} M **2a** in THF collected at the disk. Bottom: The currents associated with the disk and ring for the experiment with $[\text{DBU}] = 1.10 \times 10^{-5}$ M. Three rotation speeds are shown: 200 rpm (red), 500 rpm (green) and 1000 rpm (blue). $N < 24\%$ (rotation speed independent). 117

Figure 4.6.4 RRDE LSVs for 5.57×10^{-4} M **2a** in THF with the disk being held at a potential more positive than the $E_{1/2}$ of **2a**. Constant oxidative disk currents are labeled as i_D . The product of the disk oxidation is being collected and reduced at the ring when E_{ring} is lower than $E_{1/2}$ of **2a**. Three rotation speeds are shown: 200 rpm (red), 500 rpm (green) and 1000 rpm (blue). $N = 24\%$ (rotation speed independent). 119

Figure 4.6.5 RRDE LSVs for the experiment with 5.57×10^{-4} M **2a** and $[\text{DBU}] = 1.10 \times 10^{-5}$ M in THF. Three rotation speeds are shown: 200 rpm (red), 500 rpm (green) and 1000 rpm (blue). The potential of the disk is held at the constant value of 1.0 V vs. NHE, while the potential of the ring was scanned linearly at a rate of 10 mVs^{-1} 120

Figure 4.6.6 CVs taken at the disk without DBU (red) and after two additions of DBU. Top: raw data, Bottom: after the reversible processes (second peaks) were superimposed. 121

Figure 5.2.1 ^1H NMR reference spectrum (600 MHz, $\text{THF-}d_8$, 25°C) of complex **2e** with (top) and without (bottom) excess NH_3 . The starred peak is solvent residual. The displacement of the bound hydrazine with free ammonia was not observed. 148

Figure 5.3.1 CVs of 1.85×10^{-3} M **2e** in DCM. Top: the initial two cycles, Bottom: Three successive scans taken around 1 min after the CV in the top. Peak III appears after a couple scans

are taken in a freshly made solution, but it goes away with successive cycling of the potential. CVs taken after the one shown in the bottom, behave the same way. 149

Figure 5.3.2 CVs of 1.85×10^{-3} M **2e** in DCM in the absent (black. Three successive cycles) and presence of ammonia (red). The red curve is very similar to the catalytic oxidation of ammonia in the presence of **2a**. 150

Figure 5.3.3 CVs of 1.22×10^{-3} M **2e** in THF. Top: three successive cycles in a freshly made solution. Bottom: Changes in the CVs with scan rate (three cycles are shown for each scan rate). 151

Figure 5.3.4 CVs of 2.50×10^{-3} M **2e** in THF in the absence (black) and presence (red) of NH_3 . A shoulder that is evident at around -0.35 is marked with an arrow. 152

Figure 5.3.5 Cyclic voltammograms of a mixture solution of 1.05×10^{-3} M **2a** and 1.05×10^{-3} M **2e** in THF. Bottom: CVs of a mixture solution of **2a** and 1 equiv. NH_3 in THF. 153

Figure 5.3.6 Electro-oxidation of 4.0×10^{-2} M N_2H_4 in THF at the glassy carbon electrode. 155

Figure 5.4.1 ^1H NMR spectrum (500 MHz, $\text{THF}-d_8$, 25 °C) of the reaction solution of **2b** and excess NH_3 (top). ^1H NMR spectra (500 MHz, $\text{THF}-d_8$, 25 °C) of complex **2a** (middle) and **2e** obtained under same conditions, shown for comparison. 156

Figure 5.4.2 ^1H NMR spectra (500 MHz, CD_2Cl_2 , -75 °C) of complex **2a** with ~ 4000 equiv. NH_3 (top), complex **2e** with ~4000 equiv. NH_3 (middle), and the reaction mixture that results when ~ 4000 equiv. of NH_3 is added to **2b** at -85 °C. 157

Figure 5.4.3 Change in the ^1H NMR (500 MHz, CD_2Cl_2) spectral features as the temperature of the solution containing **2b** and excess NH_3 is increasing. As the temperature is being increased, the resonances related to the hydrazine complex vanish and the NMR spectrum at room temperature only contains **2a**. 158

Figure 5.5.1 Changes in the absorption spectrum of a solution of 9.70×10^{-5} M **2b** with the addition of NH_3 . The green curve is the spectrum of the starting solution and the final orange spectrum is when the titration was ended (the point where the addition of NH_3 did not change the spectra). All absorption spectra are corrected for dilution. 160

Figure 5.5.2 Comparison between the absorption spectra recorded at the end of titration (orange), the constructed spectra for 0.5 equiv. **2a** (black) and 0.5 equiv. **2e** (blue) and the arithmetic summation of the spectra of 0.5 equiv. **2a** (black) and 0.5 equiv. **2e** (blue) shown in dashed red. 161

Figure 6.1.1 Top: CVs of **3a** in the absence of NH_3 (sat'd) in THF. Scan rates: 0.05, 0.1, 0.25 and 0.5 Vs^{-1} . Bottom: The catalytic current (black) in a solution 2.7 mM **3a** in THF. Dotted green line is the non-catalytic NH_3 oxidation. Scan rate is 0.1 Vs^{-1} and the onset of the catalytic current is - 0.1 V versus $\text{Fc}^{+/0}$ 172

Figure 6.1.2 Top: Catalytic currents obtained in solutions of 2.7 mM **3a** and NH_3 (sat'd) in THF and their dependence on the scan rate. Bottom: the catalytic currents normalized for scan rate. 173

- Figure 6.2.1** CVs of **4a** in the absence (top) and presence (bottom) of NH_3 (sat'd) in THF. Scan rates for the CVs on the top: 0.05, 0.1, 0.25, 0.5 and 0.8 Vs^{-1} . On the bottom, the scan rate is 0.1 Vs^{-1} and the onset of the catalytic current is -0.15 V versus $\text{Fc}^{+/0}$ 176
- Figure 6.2.2** Top: Catalytic currents obtained in solutions of 2.51 mM **4a** and NH_3 (sat'd) in THF and their dependence on the scan rate. Bottom: the catalytic currents normalized for scan rate. 177
- Figure 6.3.1** The CVs obtained in solutions: $4.05 \times 10^{-3} \text{ M}$ **5a** in NM (red), 4.05 mM **5a** in the presence of NH_3 in NM (black) and a solution of NH_3 (sat'd)/NM. 180
- Figure 6.3.2** Top: The CVs of the catalytic ammonia oxidation in NM in the presence of $4.05 \times 10^{-3} \text{ M}$ **5a**, with different scan rates. Bottom: The normalized currents shown for the same set of data. The magnitudes of the normalized currents remain relatively constant at different scan rates.. 181
- Figure 6.3.3** Top: CVs for $1.68 \times 10^{-3} \text{ M}$ **3a** in NM in the absence (red) and presence (black) of NH_3 . Scan rate 0.1 Vs^{-1} . Bottom: CVs of the catalytic ammonia oxidation in NM in the presence of $1.68 \times 10^{-3} \text{ M}$ **3a**, with different scan rates (left). The normalized currents shown for the same set of data (right). 182

LIST OF SCHEMES

- Scheme 2.1** Two possible mechanisms for coupling of terminal nitrides: (top) coupling of two nitridyl radicals, (bottom) nucleophilic nitride addition to an electrophilic terminal nitride. 13
- Scheme 2.2** Formation of high valence Ru(IV) and Ru(V)oxo species in catalytic water oxidation. Only the coordinating N centers in the polypyridyl ligands are shown for simplicity. 14
- Scheme 2.3** Catalytic water oxidation where O-O bond formation happens via nucleophilic attack of water to a Ru(V) oxo intermediate as proposed by Concepcion et al. ref [53]. 15
- Scheme 5.1** The hydrazine pathway to formation of the N-N bond. The nucleophilic attack of the free NH_3 to an imido nitrogen leads into formation of a hydrazine intermediate. The polypyridyl ligands are omitted. 145
- Scheme 6.1** Synthesis of the dmaptrpy ligand. 178
- Scheme 7.1** The proposed catalytic cycle. The formation of the complexes highlighted in red has not yet been directly confirmed. 195

KET TO ABBREVIATIONS

A	Amperes, Surface Area (cm ²), Absorption
ATR	Attenuated Total Reflectance
b	Pathlength of light, 1 cm
BE	Bulk Electrolysis
bpy	2,2'-bipyridine
BTU	British Thermal Unit
Bu	Butyl
C	Coulomb, Concentration (M), Temperature (celsius)
CE	Counter Electrode
CPE	Controlled Potential Electrolysis
CV	Cyclic Voltammetry
D	Diffusion Coefficient (cm ² s ⁻¹)
DBU	1,8-diazabicyclo [5.4.0] undec-7-ene
DCM	Dichloromethane
DI-MS	Direct Infusion Mass Spectrometry
DMSO	Dimethyl sulfoxide
dmabpy	4,4'-bis(N,N-dimethylamino)-2,2'-bipyridine
dmaptrpy	(4-N,N-dimethylaminophenyl)-2,2',6',2''-terpyridine
e ⁻	Electron
E [°]	Formal Potential
E _{1/2}	Half-Wave Potential

E_p	Peak Potential
EDS	Energy-dispersive X-ray Spectroscopy
ε	Molar Absorptivity ($M^{-1} \text{ cm}^{-1}$)
ESI ⁺	Electrospray Ionization – Positive Mode
F	Faraday Number
$\text{Fc}^{+/0}$	Ferrocenium/Ferrocene
FE	Faradaic Efficiencies
FT	Fourier Transform
^1H NMR	Proton Magnetic Nuclear Resonance
HRMS	High Resolution Mass Spectrometry
i_p	Peak Current
K_{eq}	Equilibrium Constant
LMCT	Ligand-to-Metal Charge Transfer
Me_3trpy	4',4,4''-trimethyl-2,2':6',2''-terpyridine
MHz	Mega Hertz
MLCT	Metal-to-Ligand Charge Transfer
MS	Mass Spectrometry
NHE	Normal Hydrogen Electrode
nm	Nanometer
NM	Nitromethane
Ox	Oxidized Form
PCET	Proton Coupled Electron Transfer
ppm	Part Per Million

QTOF	Quadrupole Time-of-Flight
rad	Radian
RE	Reference Electrode
Red	Reduced Form
RDE	Rotating Disk Electrode
RRDE	Rotating Ring Disk Electrode
rpm	Revolution Per Minute
Sat'd	Saturated
SHE	Standard Hydrogen Electrode
SOFC	Solid Oxide Fuel Cell
^t Bu	<i>Tert</i>-Butyl
^t Bu ₃ trpy	4',4,4''-tri-<i>tert</i>-butyl-2,2':6',2''-terpyridine
TCD	Thermal Conductivity Detector
THF	Tetrahydrofuran
TOF	Turnover Frequency (s⁻¹)
TON	Turnover Number
trpy	2,2':6',2''-terpyridine
UV	Ultraviolet
V	Volts
Vis	Visible
vs.	Versus
VT	Variable Temperature
WE	Working Electrode

XPS

X-ray Photoelectron Spectroscopy

CHAPTER 1: INTRODUCTION

1.1. The Essence of Carbon Neutrality

Greenhouse gases including carbon dioxide (CO_2), methane (CH_4), nitrous oxide (N_2O) and fluorinated gases trap heat in Earth's atmosphere, which results in an overall rise in the Earth's temperature and consequently causes harmful impacts on the ecosystem.¹ The first three gases are mainly introduced to the atmosphere through the burning of fossil fuels (coal, natural gas, and oil) and agricultural activities. This is inevitable, as the burning of these fuels is the predominate way to fulfill that growing demand of our thriving population and industrial activities. The global emission of greenhouse gases has a fast-increasing trend, with just the fossil fuel-related CO_2 emissions, reached the all-time high in 2018 and is projected to hit a record 37.1 billion metric tons by the end of this year.² Collectively, CO_2 , CH_4 , and N_2O compose the majority of the greenhouse emissions in the U.S. alone (Figure 1.1.1).³ This alarming release of greenhouse gasses has put the planet and its inhabitants in a critical situation and has urged us to look for alternative energy resources to replace the dependency on fossil fuel. Nevertheless, moving from nonrenewable to sustainable and clean energy sources is still a huge challenge.

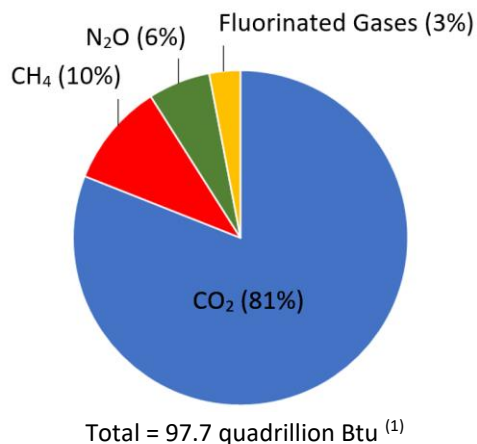


Figure 1.1.1 Relative amounts (in percent) of U.S. greenhouse gas emissions in 2016, shows the large contribution of CO_2 .¹ Figure reproduced from ref. [2].

¹ British Thermal Unit

The dependence of the industrial sector on efficient, cheap and easily accessible energy sources has restrained the demands in the renewable energy market. In 2017, around 80% of the U.S. energy sources were based on fossil fuels (Figure 1.1.2), releasing 5.14 billion metric tons of CO₂ as a byproduct.⁴

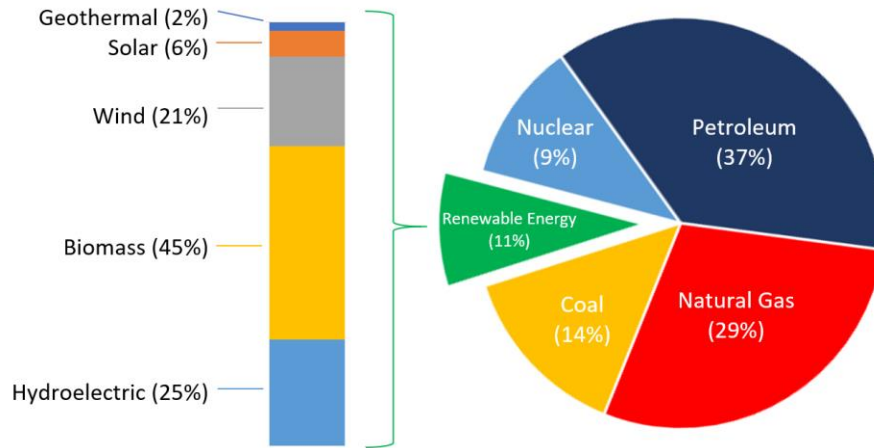


Figure 1.1.2 The U.S. energy consumption in 2017 from various sources shows the significance reliance on the fossil fuels. Figure reproduced from ref. [2].

The energy information agency projects that the global energy consumption will rise by 28% between 2015 and 2040, resulting in atmospheric energy-related CO₂ concentrations to increase by a rate of 0.6% per year.⁵ However, global energy-related CO₂ emissions increased higher than expectations by 1.7% in 2018 to reach a historic high of 33.1 Gt CO₂. It was the highest rate of growth since 2013, and 70% higher than the average increase since 2010.⁶ To stop or slow down this growth, extensive efforts and investments has to be made to replace fossil fuels with renewable sources of energy. Strategies regarding integrating renewable energy sources in energy systems, including developing technologies to harvest and store renewable energy are already being pursued. However, issues regarding the cost and storage are not easy to be solved. With operating costs considered, onshore wind plants and large-scale photovoltaic plants are 4.6 and 14.1 times as expensive as gas plant, respectively.⁷ Not only, the financial costs of building the 100%

renewable energy world are enormous, but the land area needed to accommodate the equipment required to harvest such diffuse sources of energy supply is just as daunting.

Despite these concerns, the potential of wind and solar energy sources to expand their applicability is substantial, especially if efficient ways for their storage and transportation are existent. Nature stores sunlight in the chemical bonds of the products of photosynthesis: sugar, which is further used as a fuel to run the metabolism in plants. Mimicking nature's photosynthesis to use photons of sunlight and atmospheric CO₂ to afford "useful chemicals" has been the goal of tremendous amount of research. However, another not fully developed approach is to store sunlight in the chemical bonds of a carbon-free compound with a feasible storage and transportation technology.

1.2. Carbon-Neutral Fuels

Hydrogen (H₂) and ammonia (NH₃) are two, known carbon-free energy carriers that have been used and applied commercially. While hydrogen is not abundant in its molecular pure form, it is the most abundant element in its atomic form and is estimated to make up to $\frac{3}{4}$ of the universe's mass.⁸ H₂ that can be sustainably produced from electrolysis of water. It is combusted with oxygen to reproduce water in zero-emission fuel cells with high efficiencies.⁹ Due to its small molecular mass, H₂ has the highest gravimetric energy density (140.4 MJ kg⁻¹) of any fuel. This value is three times of the gravimetric energy density of gasoline (48.6 MJ kg⁻¹).¹⁰ However, even when stored as compressed gas (700 bar, 15 °C), its volumetric energy density is as low as 5.3 MJ L⁻¹, significantly lower than the value for gasoline (31.1 MJ L⁻¹).¹¹ The safety issues regarding transportation of such pressurized H₂ tanks demand different safety considerations for onboard applications in hydrogen driven vehicles compared to electric or internal combustion cars. Such challenges are less prominent for NH₃. Being a polar molecule with the capability of hydrogen

bonding, NH_3 liquification takes place at much lower pressures (10 bar at 20 °C) compared to H_2 , resulting in relatively lower storage costs.¹² This also results in volumetric energy density of ammonia being almost three times higher than H_2 , as well. In terms of driving range, a fuel tank containing 16 gal of ammonia provides a driving range of 470 miles, while the same volume of liquid hydrogen provides a driving range of 259 miles.¹³ Table 1 summarizes the energy-related properties of H_2 and NH_3 , compared with gasoline as conventional fuel.

Another attractive feature of NH_3 as a fuel and hydrogen carrier is its availability and accessibility. Ammonia is the second largest produced chemical in the world *via* the Haber-Bosch process, a revolutionary industrial method¹⁴ developed in the first decade of the 20th century that currently is responsible for the production of more than 200 million metric tons of ammonia per annum.¹⁵ Additionally, the required infrastructure already exists for ammonia transportation and storage in large quantities. For example, a very large well-established transportation system based on pipelines, trains, trucks and barges exists in the Midwest and retail ammonia outlets exist in practically every state.¹⁶ However, extension of the distribution network to more urban and industrial areas across the U.S. is still required.

Table 1.1 Comparison of energy densities between hydrogen and ammonia as fuels. Gasoline is also shown as the reference.

Energy Carrier	H (%wt)	Volumetric Energy Density (MJ l ⁻¹)	Gravimetric Energy Density (MJ kg ⁻¹)
$\text{H}_2(l)$, -253 °C, 1 bar	100	5.3	140.4
$\text{NH}_3(l)$, 25 °C, 10 bar	17.6	13.6 ¹⁷	22.5 ⁶
Gasoline (l), 25 °C, 1 bar	15.7	31.1	48.6

1.3. Energy-Related Applications of Ammonia

1.3.1. Using NH_3 in Internal Combustion Engines

Ammonia can be directly burned in an internal combustion engine with minor modifications, emitting nitrogen and water vapor in the exhaust gas. Unburned ammonia and nitrogen oxides in the engine's exhaust can be removed by a selective catalyst reduction system. The “minor modifications” generally include incorporation of an “ignition promoters”, *i.e.*, a secondary fuel such as gasoline to overcome the low flammability of NH_3 and slow propagation of the flame. In 2007, an NH_3 Car departed Detroit and arrived in San Francisco a few days later, recording the longest trip made by an ammonia driven vehicle. In an NH_3 Car, a mixture of gasoline/ammonia was used to spark the ignition, but as the engine started the fuel was predominantly ammonia.¹⁸

1.3.2. Ammonia-Fueled Solid Oxide Fuel Cells (SOFC)

Ammonia SOFC are characterized by their high operational temperatures (500-700 °C) and are based on diffusion of gaseous NH_3 and air to an anode and cathode chamber, respectively.¹⁹ However, in addition to the need of high operational temperatures, employment of SOFC for onboard applications is limited by the low stability of the catalysts, brittleness of the ceramic parts in the SOFC, cathode poisoning arising from other components of the cathodic air feed and the possibility of formation of undesirable NO_x byproducts.^{20–22}

1.3.3. Ammonia as a Hydrogen Carrier

A more interesting approach to a nitrogen fuel economy would be to take advantage of the relatively practical storage and distribution of ammonia and to use it as a medium to store hydrogen which consequently allows storage of large amounts of energy.²³ Extraction of H_2 from NH_3 and

feeding the pure generated H_2 to an onboard hydrogen fuel cell is gaining attention. Recently Australian scientists at CSIRO ⁽¹⁾ were able to power vehicles with ammonia-derived hydrogen. This achievement hit the news highlights in August 2018 as being a “game changer” in the field of zero emission transportation.

Although Haber-Bosch process is affording large-scale production of ammonia, it is highly carbon-intensive. Not only the H_2 feed for this process is derived from natural gas (methane), also the energy production for the elevated temperatures and high pressures required for the chemical reaction is based on fossil fuels. Ammonia manufacturing is not only a very energy consuming process (2% of global energy consumption), is it also responsible for 1% of the global CO_2 emissions.²⁴

When the challenges in decarbonization of NH_3 synthesis are overcome, the energy cycle provided by ammonia would be totally carbon neutral. In that regards, various strategies are currently being investigated to produce “green” ammonia²⁵ through reduction of atmospheric N_2 coupled with splitting of H_2O as the source of protons using renewable energy sources such as wind²⁶, solar^{27–29} and electrical energy^{8,30}. Once produced, ammonia is easily liquefied, stored and transported to the consumer, where the energy stored in N-H bonds has to be extracted. After splitting NH_3 into its elemental components, N_2 and H_2 , the latter can be further fed to a hydrogen fuel cell where it combusts with O_2 , leaving clean H_2O vapor as the exhaust gas. Coupling photoelectrochemical water splitting with (photo)electrochemical N_2 reduction in the NH_3 synthesis plant would close the energy cycle as shown in Figure 1.3.1.

¹ The Commonwealth Scientific and Industrial Research Organization, www.csiro.au

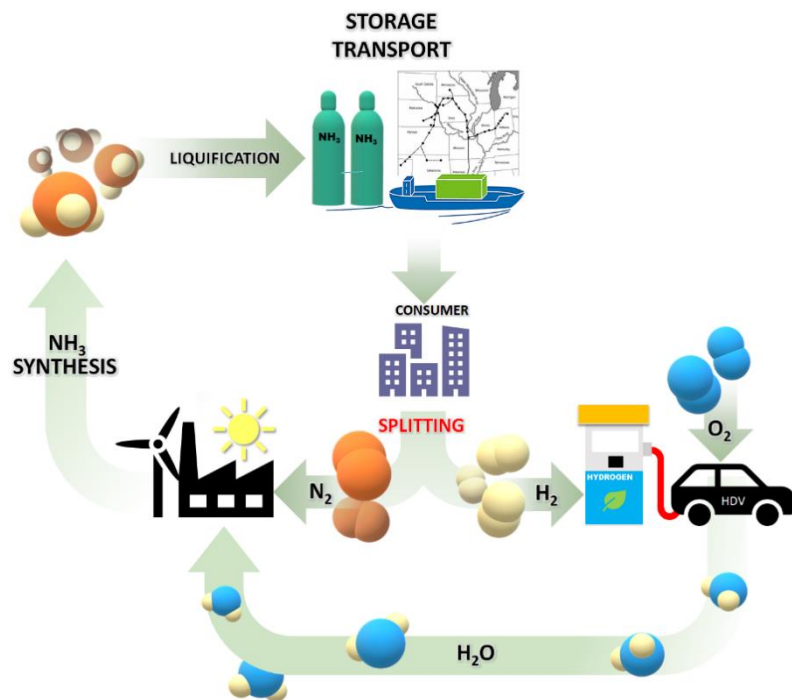


Figure 1.3.1 The ideal carbon-neutral energy cycle of ammonia as a hydron carrier.

1.4. Ammonia Splitting

While a hypothetical carbon neutral cycle of ammonia as a fuel or hydrogen carrier is not far from reality, the challenge remains the rapid and efficient conversion of ammonia into nitrogen and hydrogen. This is known as “Ammonia Splitting.” There are three common approaches to extract hydrogen from ammonia: Thermal cracking, ammonolysis of metal hydrides and electrolysis of ammonia.

1.4.1. Thermal Cracking of Gaseous NH₃

Decomposition of NH₃(g) over a heterogeneous catalyst such as Ni at elevated temperatures³¹ is the reverse reaction of the Haber-Bosch synthesis of ammonia:



This reaction is the primary choice for the production of H₂ that is used in alkaline hydrogen fuel cells, since the NH₃ remainings in the product gas mixture is problematic in the case of acidic prototypes, and the generated H₂ has to go through extra post-production purification processes.^{32,33} Despite being mildly endothermic, catalytic decomposition of NH₃ requires temperatures as high as 600°C since the catalyst is more active at elevated temperatures. In addition to product impurity and high temperature operational conditions, problems associated with the scale of equipment (Figure 1.4.1) limit the application of thermal cracking to mainly industrial purposes rather than onboard hydrogen production. The challenge of sufficiently scaling down the reforming unit while yet maintaining the capability to decompose ammonia at a rate in accordance with the consumption, has to be advised.¹³



Figure 1.4.1 An ammonia cracker by Sam Gas Projects Ptv. Ltd. (India) which is maintained at 850 °C using an electric furnace. The purity of the produced hydrogen is 99.5% (0.5% nitrogen contamination). Visit: <https://www.psa-nitrogen.com>

1.4.2. Ammonolysis of Alkali Metal Hydrides

The reaction between NH_3 and alkali metal hydrides, MH ($\text{M} = \text{Li}, \text{Na}, \text{and K}$), is an exothermic reaction that releases hydrogen at room temperature along with formation of alkali metal amides (MNH_2) as byproducts:³⁴

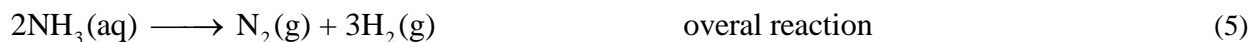


The regeneration of the metal hydride is performed at high temperatures (300 °C) and under a flow of H_2 over the metal amide product. During this process, decomposition of the MNH_2 to inactive products such as M_3N and MNH via ammonia desorption deactivates the material. Also, the repetitive recycling of the material results in brittleness.³⁵ Thus, such systems fall short on fast, reversible generation of H_2 especially for onboard applications.³⁶

1.4.3. Electrolysis of Ammonia

Electrochemical splitting of ammonia in solution phase is a very attractive approach to extract high purity hydrogen for mobile applications. Most advances are related to electrolysis of aqueous

alkaline solutions of ammonia, where at the anode ammonia undergoes oxidation to produce N_2 and protons, while H_2 is evolved at the cathode:



The thermodynamic potential for the oxidation reactions is -0.77 V versus standard hydrogen electrode (SHE). The reduction of water in basic conditions requires an energy input of -0.83 V versus SHE. Thus the driving potential for the overall reaction is +0.06 V, comparably less than the 1.23 V required for the analogous water splitting reaction.³⁷ The electrolysis is done at room temperature, and ambient pressure and the thermodynamic energy input is achievable by renewable sources such as electricity or solar.³⁷ Feasible coupling of ammonia electrolysis with hydrogen fuel cells is also another advantage which makes this method an excellent choice for on-demand hydrogen production.

Though the electrolysis of ammonia appears to be very promising, there are some important issues associated with it. One is the highly corrosive nature of alkaline solutions of ammonia which abates the applications of this procedure. Also, while the thermodynamic potential of the overall reaction is small, large overpotentials are required to run the half reactions. This is more significant for the anodic oxidation of ammonia since the kinetics of the 6 electron/6 proton reaction of NH_3 oxidation are sluggish and large anodic overpotentials are required to initiate the oxidation. The selection of a suitable anode material is also a challenge since it has to simultaneously meet two essential criteria: providing a catalytic interface to reduce the kinetic overpotential and to be resistive to poisoning effects caused by strongly adhered NH_x species.³⁸ Competitive formation of oxygen-containing products such as nitrate with N_2 is also an undesired process that lowers the faradaic

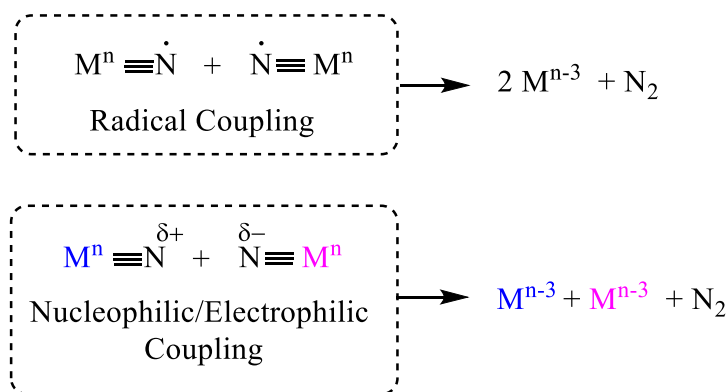
efficiencies. Electrolysis of pure NH_3 in its liquid state is an alternative approach taken to eliminate the interference of water in the electrolysis process. Several recent reports highlight the promising aspects of $\text{NH}_3(l)$ splitting. The thermodynamic potential of the overall splitting of $\text{NH}_3(l)$ is 0.1 V, only slightly higher than the value for aqueous electrolysis.³⁹ The problem with the high anodic overpotentials could be lessened by choosing a suitable anode material. For example, Dong *et al.* were able to reduce the $\text{NH}_3(l)$ electrolysis voltage from 1.2 V to 0.47 V by switching from a Pt anode to a more active Rh-Pt-Ir alloy electrode.⁴⁰ However, the deactivation of the electrode at high current densities, which are mainly due to developments of a passivating layer of strongly adhered species on to the surface of the electrode, was still problematic.⁴¹

Since the performance of most heterogeneous active surfaces seem to diminish due to poisoning, going towards homogenous catalysis has to be considered. A homogenous catalyst is a molecular substance added to the solution of ammonia to facilitate the kinetics of the reaction. In this scenario, the surface of the electrode is not actively involved in bond breaking and forming and only serves as a platform for delivery, or removal of electrons; thus, the poisoning effects have eliminated. Homogeneous systems also provide a molecular-level probe to understand the mechanism of the oxidation of NH_3 to N_2 . The general methodology is based on activation of N-H bonds in an NH_3 ligand that is coordinated to a transition metal center. The energetics of the metal complex can be tuned by the right choice of spectator ligands, which consequently enables easier access to high oxidation states for the metal. As a result, lower onset potentials for oxidation of ammonia can be possibly achieved. However, a true molecular transition metal catalyst for the electro-oxidation of ammonia to N_2 has not been reported. The first challenge is to achieve an actual catalytic turnover. A goal for which three hydrogens must be abstracted from the coordinated NH_3 and a triple bond has to form between two nitrogen molecules followed by the

evolution of the final N₂ atoms. Most previous reports of molecular transition metal complexes capable of ammonia activation, did not exhibit a full catalytic turnover.^{42–44} More details and examples are discussed in the next section.

1.5. Transition Metal Complexes as Catalysts for Ammonia Oxidation

Chemical or electrochemical oxidization of NH₃ to terminal nitrides, bridged μ -N₂ or N₂ have been reported using metal complexes of Mn,⁴³ Mo,⁴⁵ Ir,⁴⁶ Ru,⁴⁷ and Os.⁴⁸ The formation of the terminally bound or bridged N₂ in the final stage is usually the consequence of coupling of two terminal nitride nitrogens via one of two coupling mechanisms: coupling of the terminal nitridyl radicals, and nucleophilic-electrophilic coupling of the terminal nitrides (Scheme 1.1).⁴³

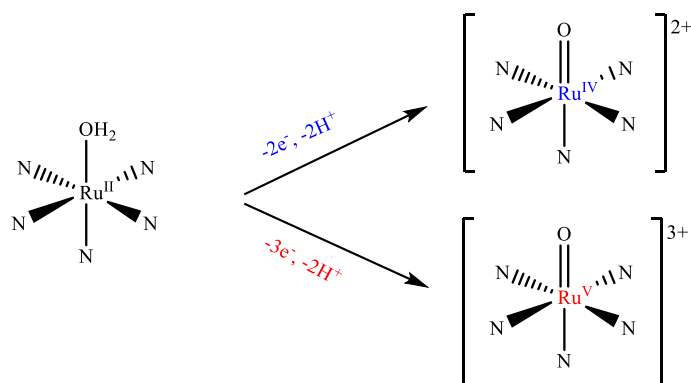


Scheme 1.1 Two possible mechanisms for coupling of terminal nitrides: (top) coupling of two nitridyl radicals, (bottom) nucleophilic nitride addition to an electrophilic terminal nitride.

While significant progress has been made towards N-H bond activation and NH₃ oxidation to various products, a fully closed catalytic cycle was not reported. However, mono- or binuclear transition metal complexes based on metals such as Ru and Os are very well studied for their catalytic role in chemical or electrochemical oxidation of water to O₂.^{49–52} Most molecular

ruthenium water oxidation catalysts use polypyridyl spectator ligands that were selected with careful attention given to their rigidity as well as the positioning of substituent groups having different steric and electronic effects. Polypyridines chelate with Ru through multidentate sites preventing ligand displacement by water under acidic or alkaline conditions. Additionally, the polypyridine ligands are generally believed to be redox inactive when the Ru(II) metal centers are exposed to oxidizing conditions, allowing for the assumption that all electron transfer processes of the complexes are metal-based.

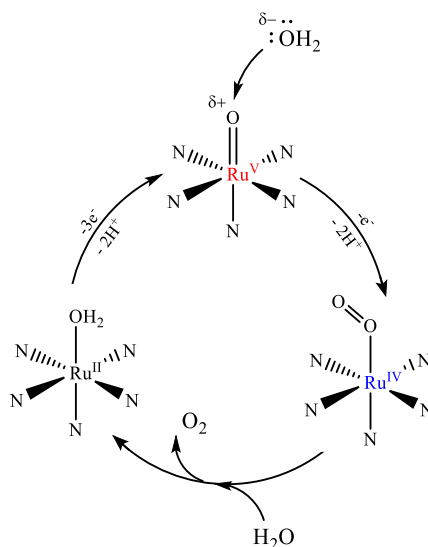
Starting Ru(II) aqua catalysts, when treated with an chemical oxidant, undergo a series of proton and electron losses to achieve high valance Ru(IV or V)oxo species (Scheme 1.2) that are considered to be the key intermediates in the catalytic cycle.



Scheme 1.2 Formation of high valence Ru(IV) and Ru(V)oxo species in catalytic water oxidation. Only the coordinating N centers in the polypyridyl ligands are shown for simplicity.

For example, Concepcion *et al.* suggested that changes in the UV-Vis absorption spectrum of an acidic solution of $[\text{Ru}(\text{trpy})(\text{bpm})(\text{OH}_2)]^{2+}$ (See Appendix A1.2 for terminology) after addition of 3 equiv. of Ce(IV) as the chemical oxidizing agent, was due to the formation of a transient Ru(V) oxo species, which further reacts with water to give a putative, not isolated $[\text{Ru}^{\text{III}}(\text{trpy})(\text{bpm})\text{OOH}]^{2+}$ intermediate. Under catalytic conditions (*i.e.*, excess oxidant added) a

tentative $[\text{Ru}^{\text{IV}}(\text{trpy})(\text{bpm})\text{O}_2]^{2+}$ species is formed from further oxidation of $[\text{Ru}^{\text{III}}(\text{trpy})(\text{bpm})\text{OOH}]^{2+}$. O_2 evolution is envisioned upon replacement of the coordinated dioxygen with water. The regeneration of the initial $[\text{Ru}^{\text{II}}(\text{trpy})(\text{bpm})\text{OH}_2]^{2+}$ catalyst enables a closed catalytic cycle with 7.5 turnovers (Scheme 1.3).⁵³

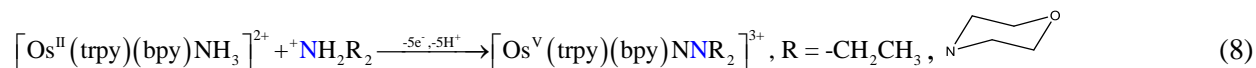


Scheme 1.3 Catalytic water oxidation where O-O bond formation happens via nucleophilic attack of water to a Ru(V) oxo intermediate as proposed by Concepcion et al. ref [53].

High valent ruthenium intermediates are hard to be isolated due to being very unstable and short-lived under catalytic conditions. Distinguishing between the two pathways of O-O formation (nucleophilic attack of water to $\text{Ru}=\text{O}$ or the coupling between two $\text{Ru}=\text{O}$ radicals which is more observed for bi- or multi-nuclear catalysts) is usually accomplished by isotopic labeling experiments using either the labeled catalyst, $\text{Ru}=\text{}^{18}\text{O}$ or labeled substrate $^{18}\text{OH}_2$.^{54,55} Also, the radical coupling mechanism would present a second order kinetics in concentration of catalyst compared to the substrate attacking mechanism.⁵⁶

We focused our attention to the $[\text{Ru}^{\text{II}}(\text{trpy})(\text{bpy})\text{OH}_2]^{2+}$ (See Appendix A1.2 for terminology) catalyst that were intensively studied mostly by Meyer and his coworkers.⁵¹ Berlinguette *et al.*

found that modification of the bpy ligands at the 4 and 4' positions by substituting electron-donating methoxy groups enhanced the catalytic efficiency of the catalyst compared to the parent $[\text{Ru}^{\text{II}}(\text{trpy})(\text{bpy})\text{OH}_2]^{2+}$ reflected by increased turnover frequencies (TOF). The rich catalytic chemistry of $[\text{Ru}^{\text{II}}(\text{trpy})(\text{bpy})\text{X}]^{2+}$ complexes (X is the reactive neutral ligand) towards activation of small molecules was not only limited to ruthenium and/or O-O formation. Meyer and coworkers were simultaneously studying equivalent $[\text{Os}^{\text{II}}(\text{trpy})(\text{bpy})\text{OH}_2]^{2+}$ complexes in the 1980s and expanded their work to analogous amine complexes a decade after. Interestingly, they observed that when electrooxidation of $[\text{Os}^{\text{II}}(\text{trpy})(\text{bpy})\text{NH}_3]^{2+}$ at pH 7 had proceeded in the presence of excess concentrations of a secondary amine, an osmium hydrazido product was formed that was further isolated from the electrolysis solution and characterized:⁵⁷



They proposed the nucleophilic attack of the secondary amine on a transient Os(IV) imido species to be the N-N bond-forming step. When the electro-oxidation was performed in the presence of primary amines or ammonia, an N₂ complex $[\text{Os}^{\text{II}}(\text{trpy})(\text{bpy})\text{N}_2]^{2+}$ was yielded.⁵⁸ Meyer and Thompson in 1981 reported that exhaustive oxidation of $[\text{Ru}^{\text{II}}(\text{trpy})(\text{bpy})\text{NH}_3]^{2+}$ in aqueous solutions (pH 6.8) yielded the formation of a N-O bond in a $[\text{Ru}^{\text{II}}(\text{trpy})(\text{bpy})\text{NO}_2]^+$ product, identified based on spectrophotometric and cyclic voltammetry experiments.⁵⁹

Inspired by the chemistry observed for N-N bond formation in osmium polypyridyl amine complexes, we hypothesized that similar molecular species would be able to act as catalysts for electro-oxidation of NH₃ in dry organic solvents where the interference of H₂O as an attacking nucleophile is prevented.

1.6. This work

The objective of this study is to evaluate ruthenium-based polypyridyl amine complexes as molecular electrocatalysts for oxidation of NH_3 . In that regard, several Ru amine complexes (Figure 1.6.1, **1a** to **5a**) were synthesized and characterized, and their catalytic activity was examined using electrochemical methods. Amongst the prepared catalysts, compound $[\text{Ru}^{\text{II}}(\text{trpy})(\text{bpy})\text{NH}_3]^{2+}$ (**2a**) was selected for further mechanistic studies for this project. Gaseous products of the headspace were quantified by gas chromatography and a variety of spectroscopic techniques were employed to provide insights on the mechanistic details. The synthesis and experimental setups are fully explained in Chapter 2. In Chapter 3, the catalytic activity of $[\text{Ru}^{\text{II}}(\text{trpy})(\text{bpy})\text{NH}_3]^{2+}$ (**2a**) and some insights into the chemistry of catalytic oxidation of ammonia are discussed. Chapter 4 is devoted to one of the isolated intermediates and its reactivity towards additional bases. Chapter 5 and 6 include the primary results on other prepared catalysts and their catalytic activity for NH_3 oxidation.

Assignment	Chemical Structure	Chemical formula
(1a)		$[\text{Ru}(\text{trpy})(\text{bpy})\text{NH}_3]^{2+}$
(2a)		$[\text{Ru}(\text{trpy})(\text{dmabpy})\text{NH}_3]^{2+}$
(3a)		$[\text{Ru}(\text{Me}_3\text{trpy})(\text{dmabpy})\text{NH}_3]^{2+}$
(4a)		$[\text{Ru}(\text{tBu}_3\text{trpy})(\text{dmabpy})\text{NH}_3]^{2+}$
(5a)		$[\text{Ru}(\text{dmaptrpy})(\text{dmabpy})\text{NH}_3]^{2+}$

Figure 1.6.1 Ruthenium catalysts **1a-5a** used in this study.

APPENDIX

A1.1.Terminology

A1.1.1. TON (Turnover Number)

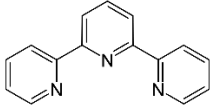
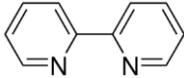
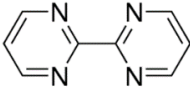
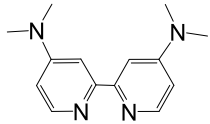
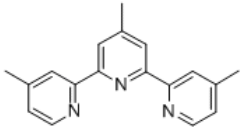
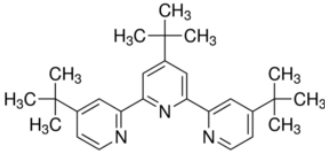
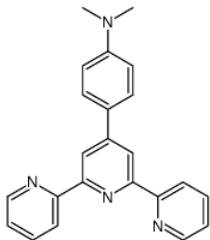
The number of moles of substrate that a mole of catalyst can convert before becoming inactivated and is the amount of substrate converted per the amount of catalyst used.

A1.1.2. TOF (Turnover Frequency), (time)⁻¹

The total number of moles transformed into the product by one mole of the active site per unit of time.

A1.2. Ligands

Table A1.1.2 Ligands mentioned or used in this study.

Abbreviation	Full name	Structure
trpy	2,2':6',2''-terpyridine	
bpy	2,2'-bipyridine	
bmp	2,2'-bipyrimidine	
dmabpy	4,4'-dimethylamoni-2,2'-dipyridine	
Me ₃ trpy	4',4,4''-trimethyl-2,2':6',2''-terpyridine	
^t Bu ₃ trpy	4',4,4''-tri- <i>tert</i> -butyl-2,2':6',2''-terpyridine	
dmaptrpy	(4-N,N-dimethylaminophenyl)-2,2',6',2''-terpyridine	

REFERENCES

REFERENCES

- (1) Greenhouse Gases Effect on Global Warming. <https://svs.gsfc.nasa.gov/20114>.
- (2) Jackson, R. B.; Le Quéré, C.; Andrew, R. M.; Canadell, J. G.; Korsbakken, J. I.; Liu, Z.; Peters, G. P.; Zheng, B. *Environ. Res. Lett.* **2018**, *13* (12), 120401.
- (3) U.S. Environmental Protection Agency (2018). Inventory of U.S. Greenhouse Gas Emissions and Sinks: 1990-2016 https://www.epa.gov/sites/production/files/styles/large/public/2018-04/total_type.png.
- (4) U.S. Energy Information Administration. U.S. Energy Facts Explained https://www.eia.gov/energyexplained/?page=us_energy_home.
- (5) U.S. Energy Information Administration. *International Energy Outlook 2017*; 2017.
- (6) International Energy Agency. *Global Energy & CO₂ Status Report*; 2018.
- (7) Lyman, R. *Friends of Science*. **2016**.
https://friendsofscience.org/assets/documents/Renewable-energy-cannot-replace-FF_Lyman.pdf
- (8) Los Alamos National Lab. PERIODIC TABLE OF ELEMENTS: LANL. <https://periodic.lanl.gov/index.shtml>
- (9) Staffell, I.; Scamman, D.; Abad, V.; Balcombe, P.; Dodds, P. E.; Ekins, P.; Ward, K. R. *Energy Environ. Sci.* **2019**, *12*, 463–491.
- (10) Siddharth, K.; Chan, Y.; Wang, L.; Shao, M. *Curr. Opin. Electrochem.* **2018**, No. 5.
- (11) Gupta, R. B. *Hydrogen fuel: production, transport and storage*, 1st ed.; CRC Press, 2008.
- (12) Brown, T. The new generation of fuel cells: fast, furious, and flexible. <https://www.ammoniaenergy.org/the-new-generation-of-fuel-cells-fast-furious-and-flexible/>.
- (13) Zamfirescu, C.; Dincer, I. *Fuel Process. Technol.* **2009**, *90* (5), 729–737.
- (14) Erisman, J. W.; Sutton, M. A.; Galloway, J.; Klimont, Z.; Winiwarter, W. *Nat. Geosci.* **2008**, *1* (10), 636–639.
- (15) Giddey, S.; Badwal, S. P. S.; Kulkarni, A. *Int. J. Hydrogen Energy* **2013**, *38* (34), 14576–14594.

- (16) Bartels, J. R., "A feasibility study of implementing an Ammonia Economy" (2008). Graduate Theses and Dissertations. 11132. <https://lib.dr.iastate.edu/etd/11132>.
- (17) Cheddie, D. In *Hydrogen Energy - Challenges and Perspectives*; Minic, D., Ed.; IntechOpen, 2012; pp 333–362.
- (18) The NH₃ Car Project, www.NH3CAR.com.
- (19) Okanishi, T.; Okura, K.; Srifa, A.; Muroyama, H.; Matsui, T.; Kishimoto, M.; Saito, M.; Iwai, H.; Yoshida, H.; Saito, M.; Koide, T.; Iwai, H.; Suzuki, S.; Takahashi, Y.; Horiuchi, T.; Yamasaki, H.; Matsumoto, S.; Yumoto, S.; Kubo, H.; Kawahara, J.; Okabe, A.; Kikkawa, Y.; Isomura, T.; Eguchi, K. *Fuel Cells* **2017**, 1–8.
- (20) Simons, E. L.; Cairns, E. J.; Surd, D. J. *J. Electrochem. Soc.* **1969**, 116 (5), 556.
- (21) Cinti, G.; Discepoli, G.; Sisani, E.; Desideri, U. *Int. J. Hydrogen Energy* **2016**, 41 (31), 13583–13590.
- (22) Lan, R.; Tao, S. *Electrochem. Solid-State Lett.* **2010**, 13 (8), B83.
- (23) Schüth, F. *Chemie Ing. Tech.* **2011**, 83 (11), 1984–1993.
- (24) Service, R. F. *Science* (80). **2018**. DOI 10.1126/science.aau7489.
- (25) Cherkasov, N.; Ibbadon, A. O.; Fitzpatrick, P. *Chem. Eng. Process. Process Intensif.* **2015**, 90, 24–33.
- (26) Malmali, M.; Reese, M.; McCormick, A. V.; Cussler, E. L. *ACS Sustain. Chem. Eng.* **2018**, 6 (1), 827–834.
- (27) Shiraishi, Y.; Shiota, S.; Kofuji, Y.; Hashimoto, M.; Chishiro, K.; Hirakawa, H.; Tanaka, S.; Ichikawa, S.; Hirai, T. *ACS Appl. Energy Mater.* **2018**, 1, 4169–4177.
- (28) Wang, L.; Xia, M.; Wang, H.; Huang, K.; Qian, C.; Maravelias, C. T.; Ozin, G. A. *Joule* **2018**, 1–20.
- (29) Bi, Y.; Wang, Y.; Dong, X.; Zheng, N.; Ma, H.; Zhang, X. *RSC Adv.* **2018**, 8 (39), 21871–21878.
- (30) Shipman, M. A.; Symes, M. D. *Catal. Today* **2016**, 1–12.
- (31) Bell, T. E.; Torrente-Murciano, L. *Top. Catal.* **2016**, 1–20.
- (32) Chellappa, A. S.; Fischer, C. M.; Thomson, W. J. *Appl. Catal. A Gen.* **2002**, 227 (1–2), 231–240.

- (33) Choudhary, T. V.; Sivadinarayana, C.; Goodman, D. W. *Catal. Letters* **2001**, 72 (3), 197–201.
- (34) Yamamoto, H.; Miyaoka, H.; Hino, S.; Nakanishi, H.; Ichikawa, T.; Kojima, Y. *Int. J. Hydrogen Energy* **2009**, 34 (24), 9760–9764.
- (35) Yamaguchi, S.; Miyaoka, H.; Ichikawa, T.; Kojima, Y. *Int. J. Hydrogen Energy* **2017**, 42 (8), 5213–5219.
- (36) Vegge, T.; Klerke, A.; Christensen, H.; Nørskov, K.; Vegge, T. *J. Mater. Chem.* **2008**, 18 (20), 2304–2310.
- (37) Vitse, F.; Cooper, M.; Botte, G. G. *J. Power Sources* **2005**, 142 (1–2), 18–26.
- (38) Bunce, N. J.; Bejan, D. *Electrochim. Acta* **2011**, 56 (24), 8085–8093.
- (39) Little, D. J.; Smith, III, M. R.; Hamann, T. W. *Energy Environ. Sci.* **2015**, 8, 2775–2781.
- (40) Dong, B. X.; Tian, H.; Wu, Y. C.; Bu, F. Y.; Liu, W. L.; Teng, Y. L.; Diao, G. W. *Int. J. Hydrogen Energy* **2016**, 41 (33), 14507–14518.
- (41) Ye, J.; Lin, J.; Zhou, Z.; Hong, Y.; Sheng, T.; Rauf, M. *J. Electroanal. Chem.* **2018**, 819 (November 2017), 495–501.
- (42) Margulieux, G. W.; Bezdek, J.; Turner, Z. R.; Chirik, P. J. *J. Am. Chem. Soc.* **2017**, 139, 6110–6113.
- (43) Keener, M.; Peterson, M.; Hernández Sánchez, R.; Oswald, V. F.; Wu, G.; Ménard, G. *Chem. Eur. J.* **2017**, 23, 11479–11484.
- (44) Chang, Y.; Nakajima, Y.; Tanaka, H.; Yoshizawa, K.; Ozawa, F. *J. Am. Chem. Soc.* **2013**, 135, 11791–11794.
- (45) Bhattacharya, P.; Heiden, Z. M.; Wiedner, E. S.; Raugei, S.; Piro, N. A.; Kassel, W. S.; Bullock, R. M.; Mock, M. T. *J. Am. Chem. Soc.* **2017**, 139 (8), 2916–2919.
- (46) Scheibel, M. G.; Abbenseth, J.; Kinauer, M.; Heinemann, F. W.; Würtele, C.; De Bruin, B.; Schneider, S. *Inorg. Chem.* **2015**, 54 (19), 9290–9302.
- (47) Ishitani, O.; Ando, E.; Meyer, T. J. *Inorg. Chem.* **2003**, 42 (5), 1707–1710.
- (48) Demadis, K. D.; Meyer, T. J.; White, P. S. *Inorg. Chem.* **1998**, 37, 838–839.
- (49) Tseng, H.-W.; Zong, R.; Muckerman, J. T.; Thummel, R. *Chem. Sci.* **2016**, 47 (24), 11763–11773.

- (50) Wada, T.; Nishimura, S.; Mochizuki, T.; Ando, T.; Miyazato, Y. *Catalysts* **2017**, 7 (2), 56.
- (51) Takeuchi, K.; Thompson, M.; Pipes, D. W.; Meyer, T. J. *Inorg. Chem.* **1984**, 23 (13), 1845–1851.
- (52) Gilbert, J. A.; Eggleston, D. S.; Murphy, W. R.; Geselowitz, D. A.; Gersten, S. W.; Hodgson, D. J.; Meyer, T. J. *J. Am. Chem. Soc.* **1985**, 107, 3855–3864.
- (53) Concepcion, J. J.; Jurss, J. W.; Templeton, J. L.; Meyer, T. J. *J. Am. Chem. Soc.* **2008**, 130 (49), 16462–16463.
- (54) Bozoglian, F.; Romain, S.; Ertem, M. Z.; Todorova, T. K.; Sens, C.; Mola, J.; Benet-buchholz, J.; Fontrodona, X.; Cramer, C. J.; Gagliardi, L.; Llobet, A. *J. Am. Chem. Soc.* **2009**, 131, 15176–15187.
- (55) Romain, S.; Bozoglian, F.; Sala, X.; Llobet, A. *J. Am. Chem. Soc.* **2009**, 131, 2768–2769.
- (56) Shaffer, D. W.; Xie, Y.; Concepcion, J. J. *Chem. Soc. Rev.* **2017**, 46, 6170–6193.
- (57) Coia, G. M.; White, P. S.; Meyer, T. J.; Wink, D. A.; Keefer, L. K.; Davis, W. M. *J. Am. Chem. Soc.* **1994**, 116 (4), 3649–3650.
- (58) Coia, G. M.; Devenney, M.; White, P. S.; Meyer, T. J.; Wink, D. a. *Inorg. Chem.* **1997**, 36 (11), 2341–2351.
- (59) Meyer, T. J.; Thompson, M. S. *J. Am. Chem. Soc.* **1981**, 103, 5579–5581.

CHAPTER 2: EXPERIMENTAL DETAILS

In this work, a variety of electrochemical and spectrochemical techniques were employed. This chapter focuses on the experimental procedures followed for those experiments. Preparation of some chemicals are also explained here.

2.1. General Materials and Methods

Concentrated ammonium hydroxide, hydrazine monohydrate, and solvents used in the synthesis of ruthenium complexes were reagent grade and used as received without further purification. Deuterated solvents and solvents used in electrochemistry were rigorously dried according to standard procedures prior to use.¹ Ruthenium trichloride hydrate, $\text{RuCl}_3 \cdot x\text{H}_2\text{O}$, was purchased from Sigma-Aldrich (USA) or Spectrum Chemical. 2,2':6',2''-Terpyridine (trpy), 97% was purchased from Alfa Aesar (USA) and recrystallized from hexane prior to use as follows:

5 g 2,2':6',2''-terpyridine (%97) was dissolved in 150 mL boiling hexane. The solution was filtered hot through a filter paper. Afterward, the volume was reduced to one-third by rotovaping. The flask content was heated to 80 °C to dissolve the solids that were formed during the solvent evaporation step. After all the solids were dissolved, the flask was left under a slow flow of nitrogen at room temperature to cool down overnight. Pale yellow crystals formed. The flask was attached to the vacuum line of a Schlenk line to evaporate the residual hexane and then was vacuum-dried for 48 h to complete dryness.

Tetrabutylammonium hexafluorophosphate $[\text{Bu}_4\text{N}](\text{PF}_6)$ 97% was purchased from Alfa Aesar (USA) and was recrystallized from ethanol following a similar procedure used for trpy. Ammonium hexafluorophosphate 99.5% $[\text{NH}_4](\text{PF}_6)$ was obtained from Alfa Aesar and was used without further recrystallization but was dried in a vacuum oven set at 50 °C for 48h and then stored in the glovebox. $^{15}\text{NH}_4\text{PF}_6$ was made by exchanging the chloride ion in $^{15}\text{NH}_4\text{Cl}$ (99% atom ^{15}N , Cambridge Isotope Laboratories, Inc., USA) with hexafluorophosphate by mixing $^{15}\text{NH}_4\text{Cl}$

and AgPF₆ (Sigma Aldrich, USA) 1:1 in deionized water. The AgCl precipitate was filtered twice using a Celite column. The product was collected as a solid after water was evaporated and then dried under vacuum overnight.

4,4'-bis(dimethylamino)-2,2'-bipyridine (dmabpy) and 2,2'-bipyridine (bpy) were purchased from Hetcat (Switzerland) and Sigma-Aldrich (USA), respectively and used without further purification. Nuclear magnetic resonance (NMR) spectra were recorded on a Varian Innova 600 MHz spectrometer equipped with a triple resonance indirect probe or a Varian 500 MHz DD2 spectrometer equipped with a Pulsed Field Gradient (PFG) Probe. Variable temperature NMR experiments were performed on a Varian Unity Plus 500 MHz spectrometer equipped with a NALORAC 5 mm PFG probe. CHN analyses were performed by Midwest Micro Lab (IN, USA). High-resolution mass spectra (HRMS) were obtained at the Michigan State University Mass Spectrometry Core using quadrupole time-of-flight instruments (QTOF). IR spectra was collected using a Jasco FT/IR 6600 spectrophotometer equipped with ATR PRO ONE Single-reflection ATR Accessory.

2.2. Preparation of Dry Liquid Ammonia

Ammonia gas (Airgas, USA) was condensed over metallic sodium in a previously dried one-neck round bottom flask equipped with two gas inlet arms, immersed in a methanol bath under an inert atmosphere of N₂ or Ar at ambient pressure (**Error! Reference source not found.**). The temperature of the methanol bath was set to -55 °C using a temperature control chiller equipped with a metal thermometer probe. The dry ammonia gas was then cannula transferred into another receptacle which could be either the electrochemistry cell or a secondary storage flask, depending on the experiment purpose. The quenching of the nonreacted sodium residuals in the leftover NH₃

was pursued by dropwise addition of isopropyl alcohol, followed by acetone and finally water until the final solution was cloudy white. This solution was then diluted with 1 L of water and was disposed in to an aqueous waste container.

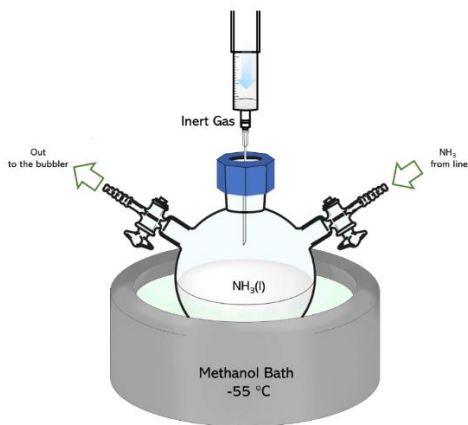


Figure 2.2.1 The apparatus used for the storage of dry liquid ammonia under ambient pressure.

2.3. Preparation of Saturated $^{15}\text{NH}_3$ Solutions in Tetrahydrofuran (THF)

^{15}N -labeled ammonia gas (98% atom ^{15}N) was purchased from Sigma Aldrich in 1 L quantities contained in a lecture-sized cylinder and used as received. A high-vacuum Schlenk line was used to transfer measured volumes of ammonia gas into heavy walled reaction vessels and gas-tight, Teflon-valved, medium pressure, high vacuum NMR tubes. Labeled ammonia in THF was prepared as a supersaturated solution by vacuum transfer of excess $^{15}\text{NH}_3$ (9 mmol, 250 mL at 1 atm and 25 °C) into 5.5 mL dry THF in a 20 mL heavy walled, high-pressure vessel. Before the transfer of $^{15}\text{NH}_3$, THF was subjected to 3 cycles of freeze/thaw degassing. The $^{15}\text{NH}_3$ /THF solution was thawed in a dry ice/ethanol bath. Before transfer to the electrochemical cell, the cold bath was removed, and the vessel was filled with argon. The Teflon plug was replaced with a Suba-Seal® septum under an argon counterflow and the solution was stirred for approximately 1 min under a static argon atmosphere after closing off the counterflow. Then, the required volume of the solution

was withdrawn by syringe and injected into the electrochemical cell while the solution was still cold.

2.4. Electrochemistry

All electrochemical experiments were conducted under inert atmosphere (N_2 and Ar for voltammetry and chronoamperometry experiments, respectively).

Note: Due to significant interference of residual water, it is crucial to rigorously dry all solvents and materials prior to electrolysis.

2.4.1. Cyclic Voltammetry (CV)

CV experiments were carried out using a Metrohm μ Autolab potentiostat, in dry THF containing either 0.1 M $[Bu_4N](PF_6)$ or 0.1 M $[NH_4](PF_6)$ as the supporting electrolyte. For electrochemical experiments in nitromethane (NM) 0.2 M $[NH_4](PF_6)$ was used as the supporting electrolyte. Glassy carbon (disk: geometric surface area = 0.07 cm^2 , plate: geometric surface area = 2.0 cm^2), a custom silver/ saturated silver nitrate/methanol and a platinum mesh were used as the working, reference and counter electrodes, respectively. The diagram of the electrochemistry cell is shown in Figure 2.4.1.

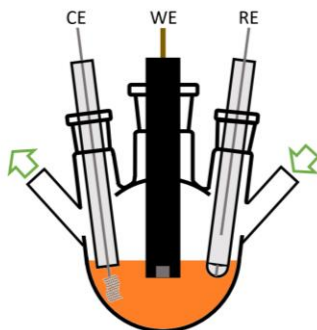


Figure 2.4.1 Diagram of the three-electrode electrochemical cell used for CV experiments. The side arms are inert gas inlet and outlets. CE: Counter Electrode, WE: Working Electrode and RE: Reference Electrode.

The potential of the reference electrode was measured versus ferrocene/ferrocenium ($\text{Fc}^{+/0}$) in each solvent. Figure 2.4.2 shows how $E_{1/2}$ of ferrocene was measured versus $\text{Ag}/\text{AgNO}_3/\text{methanol}$ reference electrode in THF and NM.

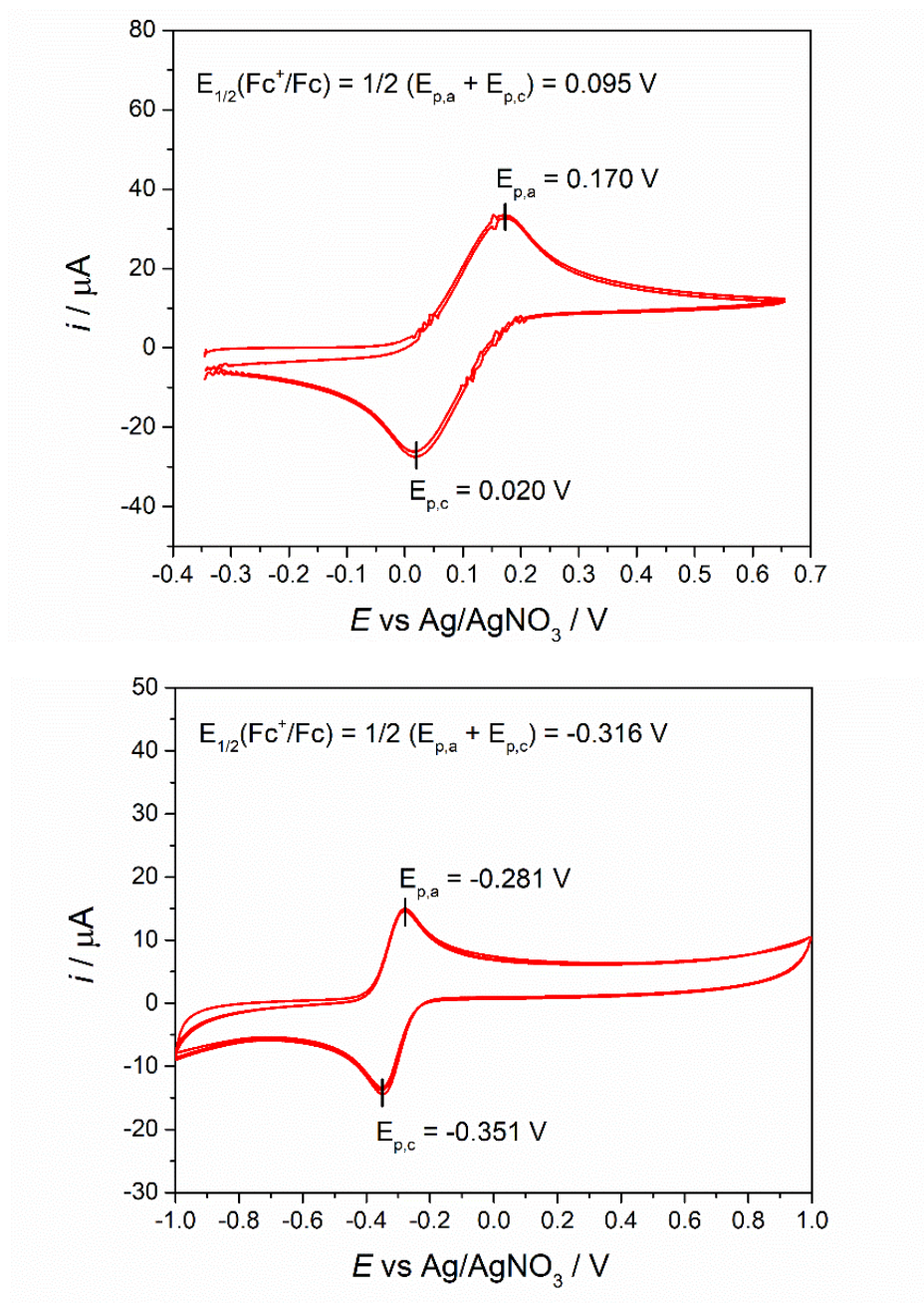


Figure 2.4.2 CVs (three cycles) of ferrocene in THF and NM using the Ag/AgNO_3 reference electrode. Top: $3.0 \times 10^{-3} \text{ M}$ ferrocene in THF, and Bottom: $1.6 \times 10^{-3} \text{ M}$ ferrocene in NM. CVs were obtained at 0.1 V s^{-1} scan rate. $E_{p,a}$ and $E_{p,c}$ stand for anodic and cathodic peak potentials, respectively. The $E_{1/2}$ is defined as the midpoint between $E_{p,a}$ and $E_{p,c}$ and is calculated as their arithmetic average.

2.4.2. Determination of the Onset Potential

The onset potential of the current is defined as the intersection of the baseline current with the linear portion of the oxidation current. Figure 2.4.3 represents the onset potential determination for non-catalytic oxidation of ammonia at the surface of the electrode in THF.

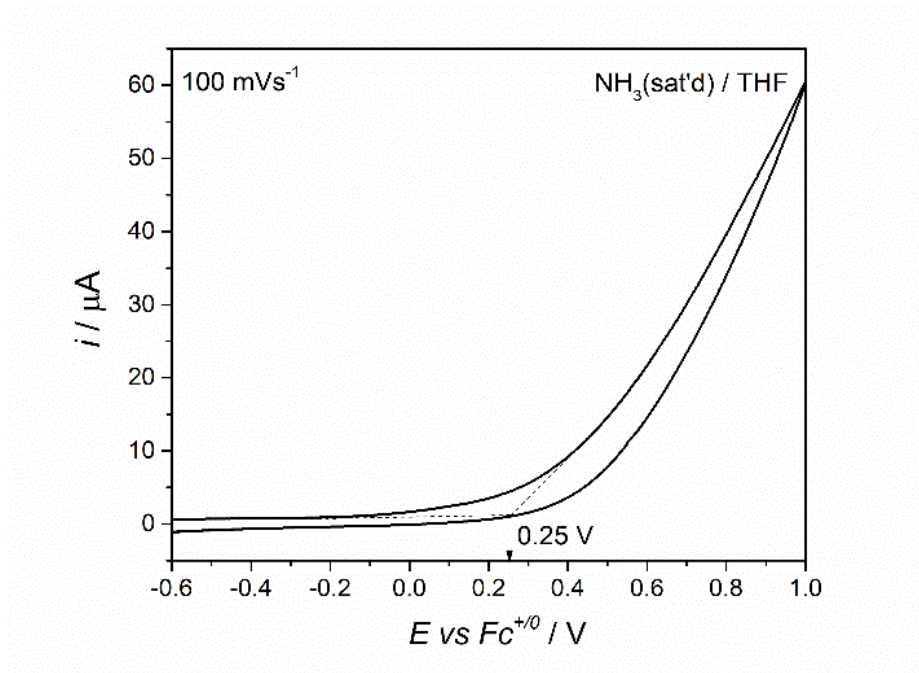


Figure 2.4.3 Determination of the onset potential for oxidation of ammonia at the surface of the glassy carbon electrode in THF. The potential of the cross-point between the baseline and the oxidation current is considered as the onset potential.

2.4.3. Hydrodynamic Voltammetry

Two types of hydrodynamic voltammetry experiments were used in this study, one with a rotating disk electrode (RDE) and the other with a rotating ring-disk electrode (RRDE). A flat bottom glass cell was used for those experiments (Figure 2.4.4). The speed of rotation was controlled remotely using an Autolab RDE consisted of the rotating mechanical unit (RDE-2) and the motor control unit (MCU).

RRDE electrodes (Autolab) were used as WE which the tip was fitted with a 5 mm glassy carbon electrode disk and a thin concentric platinum ring with 375 μm gap in between. Theoretical collection efficiency of the RRDE was 24.9%. The rotation speeds (ω) were applied in revolution per minute (rpm) and were converted to rad s^{-1} using the following calculation:

$$\omega\left(\frac{\text{rad}}{\text{s}}\right) = \omega\left(\frac{\text{rev}}{\text{min}}\right) \cdot 2\pi\left(\frac{\text{rad}}{\text{rev}}\right) \cdot \frac{1}{60}\left(\frac{\text{min}}{\text{s}}\right) \quad (1)$$

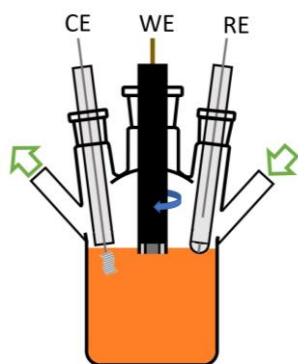


Figure 2.4.4 Diagram of the three-electrode electrochemical cell used in RDE and RRDE experiments. The side arms are inert gas inlet and outlets. CE: Counter Electrode, WE: Working Electrode and RE: Reference Electrode.

2.4.4. Controlled Potential Electrolysis (CPE)

CPE or Bulk electrolysis (BE) experiments were performed with a constant applied potential to the working electrode, while the solution was vigorously stirring. For the electrochemical synthesis of $[\text{Ru}(\text{trpy})(\text{dmabpy})\text{NH}_3]^{3+}$, **2b**, the counter electrode was consisted of a silver coil immersed in a solution of 0.1 M AgNO_3 and 0.1 M $[\text{Bu}_4\text{N}](\text{PF}_6)$ in acetonitrile. This solution was separated from the electrolysis solution with a fritted glass bridge. For the bulk electrolysis of ammonia in THF in the presence of the catalyst, the counter electrode was platinum mesh and was directly inserted into the electrolysis solution in order to allow the reduction of anodically produced protons. Desired masses of the catalyst and $[\text{NH}_4](\text{PF}_6)$ were weighed out and placed in the cell

(Figure 2.4.5). The cell was sealed and kept under a slow flow of Ar overnight. Prior to solvent transfer, the cell was disconnected from the Ar line and was kept closed for 3 hours, during which 100 μL samples of the cell headspace were injected to the gas chromatograph instrument (See Section 2.5) every hour to check for leaks. Then 2.5 mL of saturated NH_3/THF was transferred to the cell by injecting through the injection/sampling port (Figure 2.4.5, inset). Three steps of BE were performed by applying a constant potential of 0.15 V versus $\text{Fc}^{+/0}$ to the working electrode for 60 min, while the solution was vigorously stirred. Before and after each BE step, 100 μL of the headspace was sampled, CVs of the solution were taken and 30 μL aliquots of the solution were taken out with a glass syringe for UV-Vis measurements. Bulk electrolysis experiments using isotopic labeled reagents were performed in the same fashion. Some other BE experiments were conducted in a cell set up similar to what is represented in Figure 2.4.1.

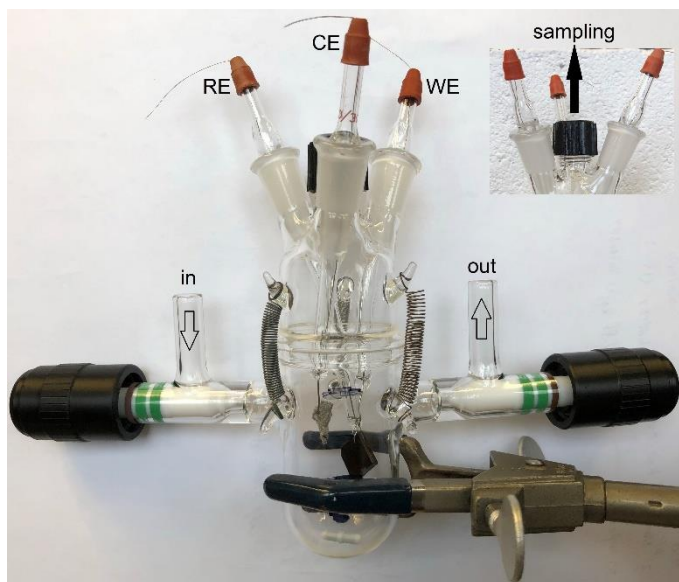


Figure 2.4.5 The cell used in some controlled potential electrolysis experiments. An empty cell is presented here for better visibility. The counter electrode is Pt mesh, and working is glassy carbon plate. The inset shows the position of the sampling port.

2.5. Gas Chromatography (GC)

Gas quantifications were conducted with a gas chromatograph (Agilent 7820A) equipped with an Agilent-PLOT/U capillary column (Agilent 19095P-UO4PT 30 m \times 350 μ m \times 20 μ m), a CP-molsieve 5Å capillary column (Agilent CP7539 50 m \times 530 μ m \times 50 μ m) and a thermal conductivity detector (TCD). Argon was used as the carrier gas. The PLOT/U capillary column is connected to the injector and exits to a pneumatic valve that switches between the CP-molsieve 5Å capillary column and the detector. Ten minutes after injection, the pneumatic valve switches to isolate the faster eluting, volatile diatomic gases in the molsieve column, allowing the slower eluting volatiles THF and NH₃ to pass from the PLOT/U column directly to the detector. At ca. 17 min, the valve resets, and the diatomics in the molsieve column then elute to the detector. The full chromatogram is shown in Figure 2.5.1.

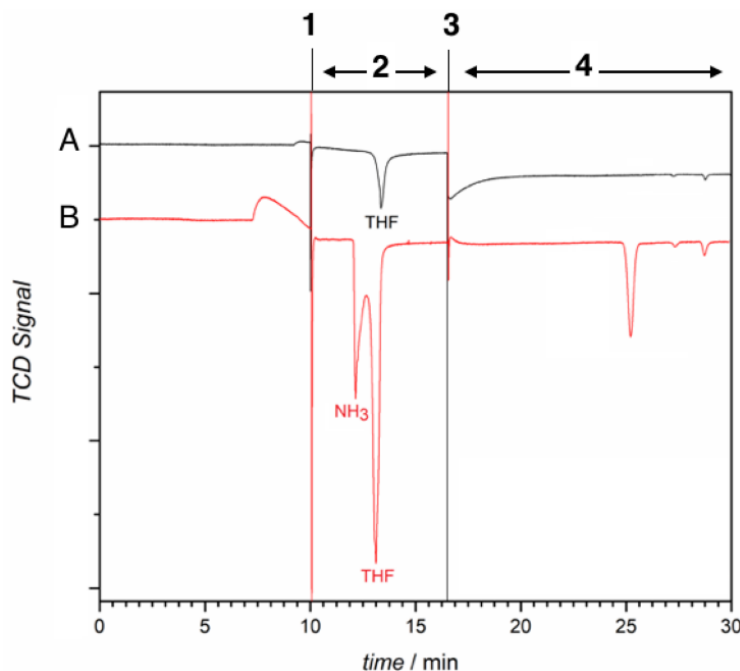


Figure 2.5.1 Full TCD Chromatograms obtained for two headspace injections. Injection A (black): Headspace of a cell containing THF and the catalyst. Injection B (red): Headspace of the cell after 2 h of electrolysis in the presence of NH₃ and the catalyst. At point 1, a GC column valve switches to isolate N₂, H₂, and residual O₂ in the molsieve column, while heavier volatiles, THF, and NH₃, elute through the PLOT/U column to the detector during time window 2. At time point 3, the column isolation valve resets and diatomic gases elute through the molsieve column to the thermal conductivity detector as seen in time window 4.

2.5.1. GC Calibration

Evolution of H₂ and N₂ was quantified based on an independent calibration obtained separately for each gas by direct injection of known volumes of a gaseous mixture of 5% V hydrogen and 95% V nitrogen (Airgas, USA) to the GC. The moles of N₂ and H₂ are calculated using the ideal gas law with T = 293 K and P = 1 atm (Table 2.1). The data points for 0 mol N₂ and H₂ in Figure 2.5.2 correspond to 100 µL injections of argon gas (Blank), corrected for residual N₂ in the argon gas used in during electrolysis giving a peak with an area of 28.84.

Table 2.1 Experimental data used for GC signal calibration for moles of injected N₂ and H₂. Red and blue colored numbers are used to construct the corresponding calibration lines in Fig. 2.5.2.

Volume of gas injected (µL)	Volume of H ₂ in the injection (µL)	Volume of N ₂ in the injection (µL)	Moles of H ₂ injected ^a	Moles of N ₂ injected ^a	H ₂ peak area	N ₂ peak area	Corrected N ₂ peak area ^b
50	2.5	47.5	1.04×10 ⁻⁷	1.97×10 ⁻⁶	98.62	295.32	266.48
80	4.5	76.0	1.66×10 ⁻⁷	3.16×10 ⁻⁶	157.67	466.79	437.95
100	5.0	95.0	2.08×10 ⁻⁷	3.95×10 ⁻⁶	207.20	589.95	561.11

^aCalculated as $n = (PV)/(RT)$.
^bCorrected N₂ peak area = N₂ peak area – 28.84.

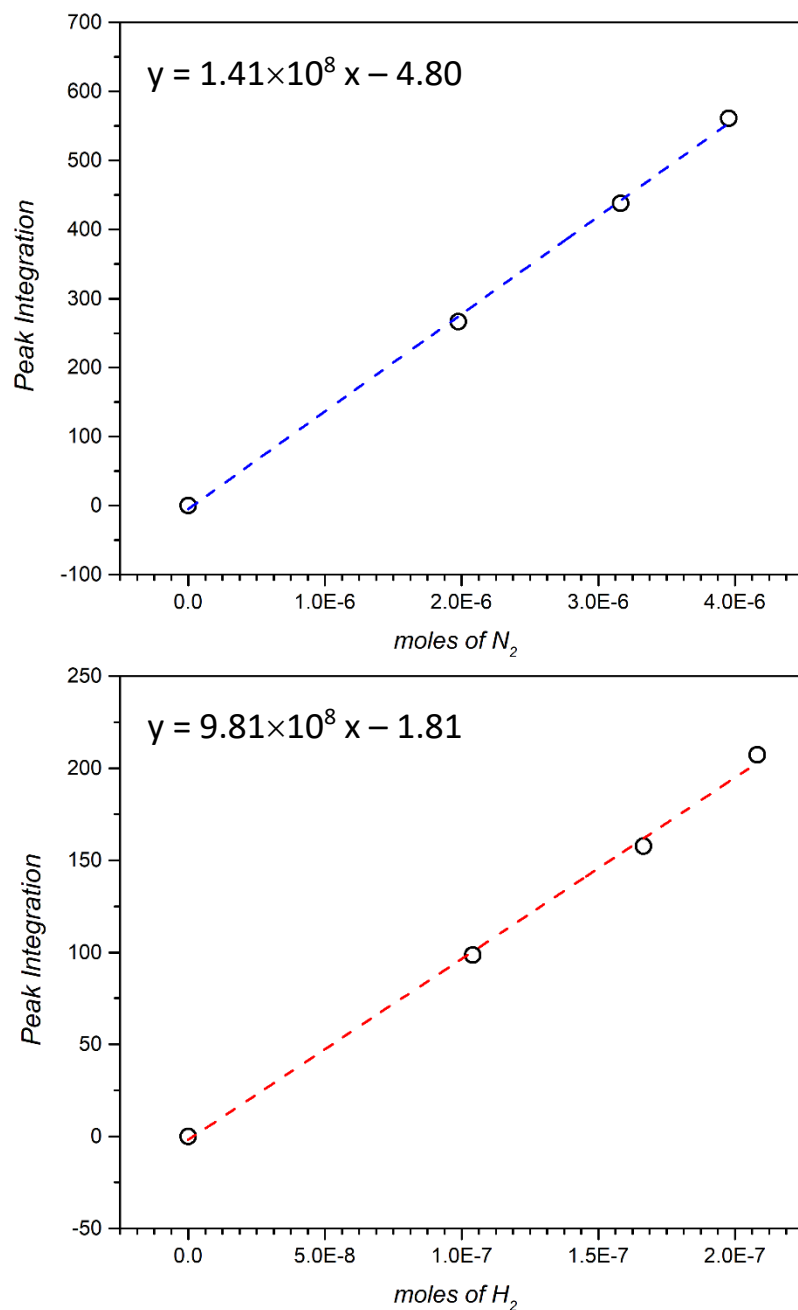


Figure 2.5.2 Gas Chromatography calibration lines obtained for N₂ (top, blue) and H₂ (bottom, red) based on data in Table 2.1.

2.6. GC-MS Experiment

Isotopic N₂ production was monitored by mass spectrometry with a Shimadzu QP2010SE GC/MS spectrometer modified with an Agilent J & W CP-molecular sieve column installed (5Å, 50 m ×

530 $\mu\text{m} \times 50 \mu\text{m}$) and helium as the carrier gas. The N_2 was chromatographically separated from other gases in the mixture, and then mass-to-charge values of 28 ($^{14}\text{N}^{14}\text{N}$), 29 ($^{15}\text{N}^{14}\text{N}$) and 30 ($^{15}\text{N}^{15}\text{N}$) were determined by quantitative integration of parent peak intensities. The amounts of gases were not quantified in GC-MS experiments. The instrument was modified, and the analysis was carried out according to the following description. An Agilent J & W CP-molecular sieve column was installed (CP7539 50 m \times 530 $\mu\text{m} \times 50 \mu\text{m}$) and fitted with a 3 m guard column of 0.25 mm ID into the detector. The guard column was cut from a Varian FactorFour WCOT fused silica 0.25 mm ID column and connected with a Silitek treated MXT union connector. The injection volume of the cell headspace was 100 μL with split ratio 50:1 and a flow rate of 3 mL min^{-1} , with an injector temp = 100 $^{\circ}\text{C}$.

2.7. X-Ray Spectroscopy

Scanning Electron Microscope (SEM) images were obtained using a Carl Zeiss EVO LS25 microscope. Energy-dispersive X-ray spectroscopy (EDS) measurements of selected areas were performed using an EDAX instrument equipped with a Pegasus camera.

REFERENCES

REFERENCES

- (1) Armarego, W. L. T. *Purification of Laboratory Chemicals*, 6th ed.; Butterworth-Heinemann, 2009.

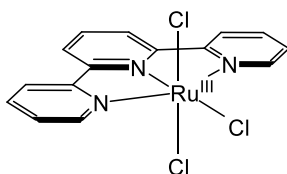
CHAPTER 3: CATALYTIC ACTIVITY OF $[\text{Ru}(\text{TRPY})(\text{DMABPY})\text{NH}_3]^{2+}$ IN THF

Inspired by Meyer and Thompson results using $\text{Ru}(\text{trpy})(\text{bpy})\text{NH}_3](\text{PF}_6)_2$,¹ we started this study based off of the similar ruthenium (II) ammine complex and investigated the chemistry when it was exhaustively oxidized in the presence of ammonia in organic solvents. This chapter focuses on initial electrochemical studies of complexes $[\text{Ru}(\text{trpy})(\text{bpy})\text{NH}_3](\text{PF}_6)_2$ (**1a**) and $[\text{Ru}(\text{trpy})(\text{dmabpy})\text{NH}_3](\text{PF}_6)_2$ (**2a**) with and without ammonia in THF.

3.1. Synthesis of $[\text{Ru}(\text{trpy})(\text{bpy})\text{NH}_3](\text{PF}_6)_2$ (**1a**)

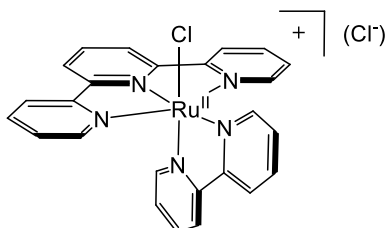
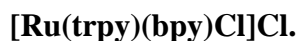
1a was synthesized in three steps as described below.

3.1.1. Synthesis of (2,2':6',2''-terpyridyl) trichloro ruthenium (III), $[\text{Ru}(\text{trpy})\text{Cl}_3]$.



$[\text{Ru}(\text{trpy})\text{Cl}_3]$ was prepared by a literature procedure and characterized by ESI⁺-MS: m/z: 404.9 $[\text{M}-\text{Cl}]^+$.² Trichloro complexes of ruthenium (III) with other derivatives of trpy were synthesized by the same procedure.

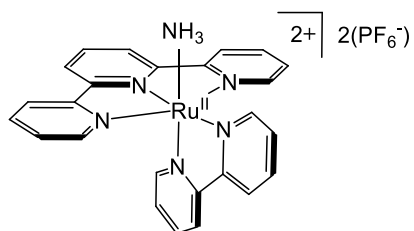
3.1.2. (2,2':6',2''-terpyridyl) (2,2'-bipyridyl) chloro ruthenium (II) chloride,



[Ru(trpy)(bpy)Cl]Cl was synthesized from [Ru(trpy)Cl₃] using a previously reported procedure.³

¹H NMR (500 MHz, DMSO-*d*₆) δ 10.09 (dd, *J* = 5.6, 1.5 Hz, 1H), 8.91 (d, *J* = 8.1 Hz, 1H), 8.82 (d, *J* = 8.1 Hz, 2H), 8.70 (d, *J* = 8.0 Hz, 2H), 8.64 (d, *J* = 8.1 Hz, 1H), 8.36 (td, *J* = 7.9, 1.6 Hz, 1H), 8.22 (t, *J* = 8.1 Hz, 1H), 8.07 (ddd, *J* = 7.3, 5.6, 1.3 Hz, 1H), 7.99 (td, *J* = 7.8, 1.5 Hz, 2H), 7.78 (td, *J* = 7.8, 1.4 Hz, 1H), 7.62 (dd, *J* = 5.6, 1.5 Hz, 2H), 7.38 (ddd, *J* = 7.2, 5.5, 1.3 Hz, 2H), 7.32 (dd, *J* = 5.8, 1.4 Hz, 1H), 7.08 (ddd, *J* = 7.3, 5.7, 1.3 Hz, 1H).

3.1.3. (2,2':6',2''-Terpyridyl)(2,2'-bipyridyl)ruthenium(II) ammine dihexafluoro phosphate, [Ru(trpy)(bpy)NH₃](PF₆)₂, (1a).



[Ru(trpy)(bpy)NH₃](PF₆)₂ was synthesized from [Ru(trpy)(bpy)Cl]Cl and characterized by ¹H NMR spectroscopy using a previously reported procedure.⁴

3.2. Catalytic Activity of 1a in THF

Cyclic voltammetry of [Ru(trpy)(bpy)NH₃](PF₆)₂ in THF shows a reversible one-electron redox process at $E_{1/2} = 0.40$ V *versus* Fc^{+/0} corresponding to oxidation of Ru(II) center to Ru(III) (Figure 3.2.1). In this CV experiments, as the potential is scanned in the positive direction, oxidation of the analyte results in an anodic current. In the reverse scan, reduction gives rise to a cathodic current. The half-potential of the redox process ($E_{1/2}$) is determined as the midpoint between the potentials corresponding to the maximum anodic and cathodic currents (*i*_{p,a} and *i*_{p,c}, respectively).

Scans to more positive potentials were constrained by the oxidation potential window of the THF solvent.

Plots of the anodic and cathodic peak currents in μA *versus* square root of the scan rate are linear with a ratio of 1.03. From the slope of the anodic line, a diffusion coefficient, D_{ox} , of $4.06 \times 10^{-6} \text{ cm}^2 \text{ s}^{-1}$ was calculated according to equation 1.⁵

$$i_p = 0.4463 \left(\frac{F^3}{RT} \right)^{\frac{1}{2}} n^{\frac{3}{2}} A D_{\text{ox}}^{\frac{1}{2}} C^{\text{bulk}} \nu^{\frac{1}{2}} \quad (1)$$

Where n is number of transferred electrons ($1 e^-$), A is the surface area of the working electrode (0.07 cm^2), C^{bulk} is the bulk concentration of $[\text{Ru}(\text{trpy})(\text{bpy})\text{NH}_3](\text{PF}_6)_2$ ($2.13 \times 10^{-6} \text{ mol cm}^{-3}$), ν is the scanning rate (V s^{-1}), $T = 23 \text{ }^\circ\text{C}$, $R = 8.314 \text{ J mol}^{-1} \text{ K}^{-1}$ and $F = 96485 \text{ C}$.

The onset potential of the current arising from direct oxidation of NH_3 at the glassy carbon working electrode was measured vs. $\text{Fc}^{+/0}$ as shown in Figure 3.2.2. Electro-oxidation of saturated solutions of NH_3 in THF ($[\text{NH}_3] = 0.34 \text{ M}$) in the presence of $2.13 \times 10^{-3} \text{ M}$ $[\text{Ru}(\text{trpy})(\text{bpy})\text{NH}_3](\text{PF}_6)_2$ results in an enhanced current (red solid line curve in Figure 3.2.2) with an onset potential lower than the direct NH_3 oxidation in the absence of the complex.

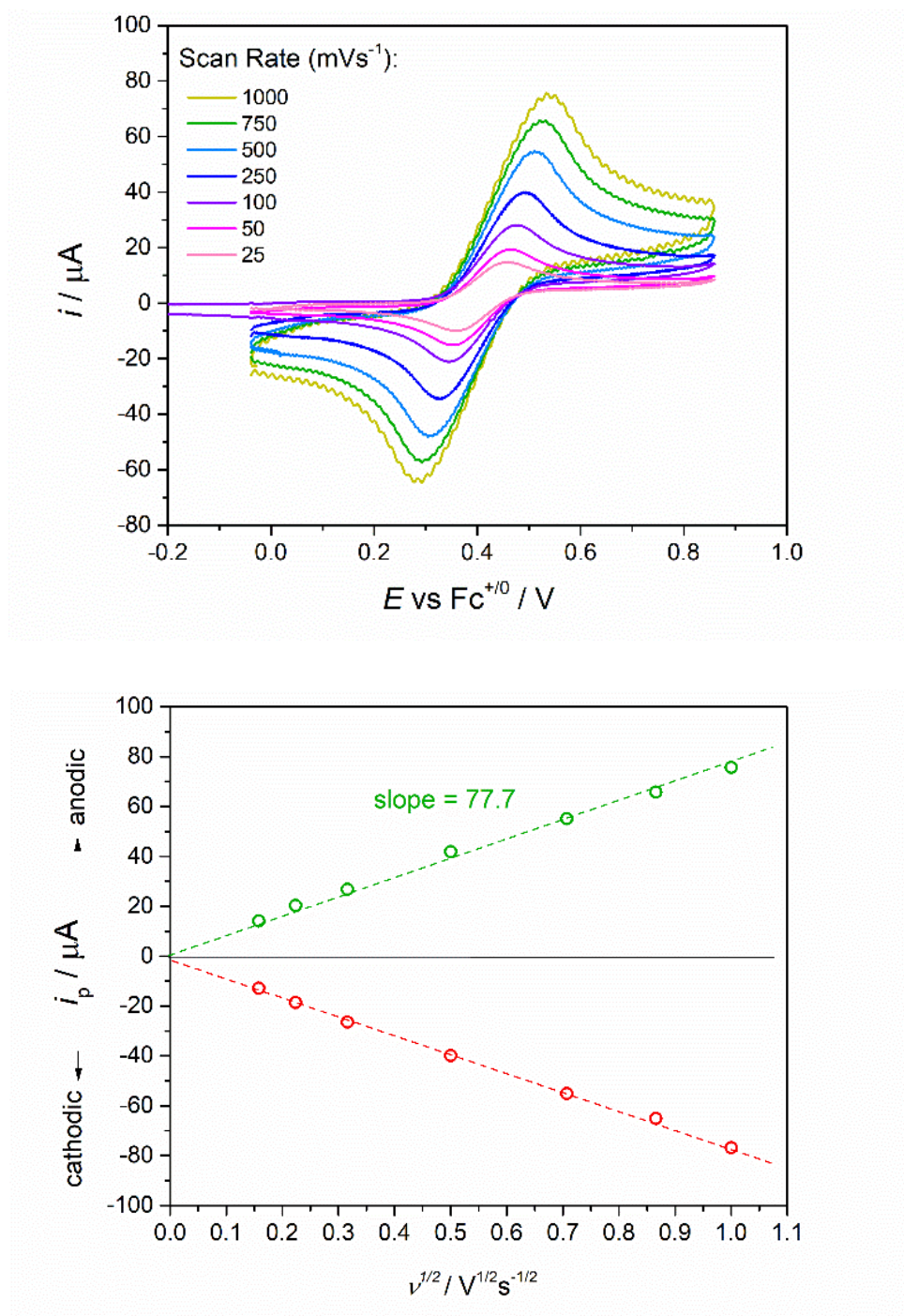


Figure 3.2.1 Top: Scan rate dependence of the current in $2.13 \times 10^{-3} \text{ M}$ $[\text{Ru}(\text{trpy})(\text{bpy})\text{NH}_3](\text{PF}_6)_2$ (**1a**) in THF shown for seven scan rates. Bottom: Plots of anodic and cathodic peak currents obtained from CVs on the top *versus* square root of the scan rate. From the slope of the anodic branch a diffusion coefficient of $D_{\text{ox}} = 4.06 \times 10^{-6} \text{ cm}^2 \text{ s}^{-1}$ is calculated for **1a**.

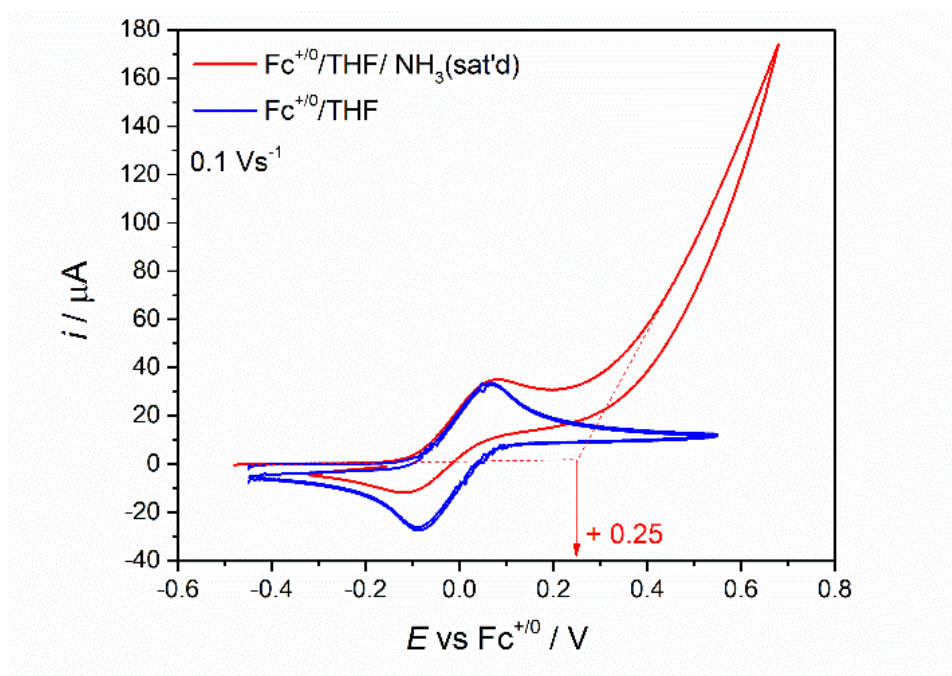


Figure 3.2.2 Cyclic voltammograms for a solution containing ferrocene in THF with (red) and without (blue) NH_3 (0.34M). The onset of the direct ammonia oxidation was measured as +0.25 V vs. ferrocene. In solutions that do not contain ferrocene, the oxidation of ammonia appears at the same potential using an Ag/AgNO_3 reference electrode that is separately calibrated with $\text{Fc}^{+/0}$ in THF.

The disappearance of the return current in the CV of $[\text{Ru}(\text{trpy})(\text{bpy})\text{NH}_3](\text{PF}_6)_2$ (**1a**) and the lower onset potential both are consistent with the enhanced current being catalytic and not merely being the mathematical summation of currents for $[\text{Ru}(\text{trpy})(\text{bpy})\text{NH}_3](\text{PF}_6)_2$ (**1a**) and direct NH_3 oxidation. Additionally, when the currents are normalized for the scan rate, the catalytic activity appears to be improved for longer time scales, *i.e.* slower scan rates, suggesting that the current is controlled by a slow reaction which is improved when the time scale of the reaction is increased (Figure 3.2.3, bottom).

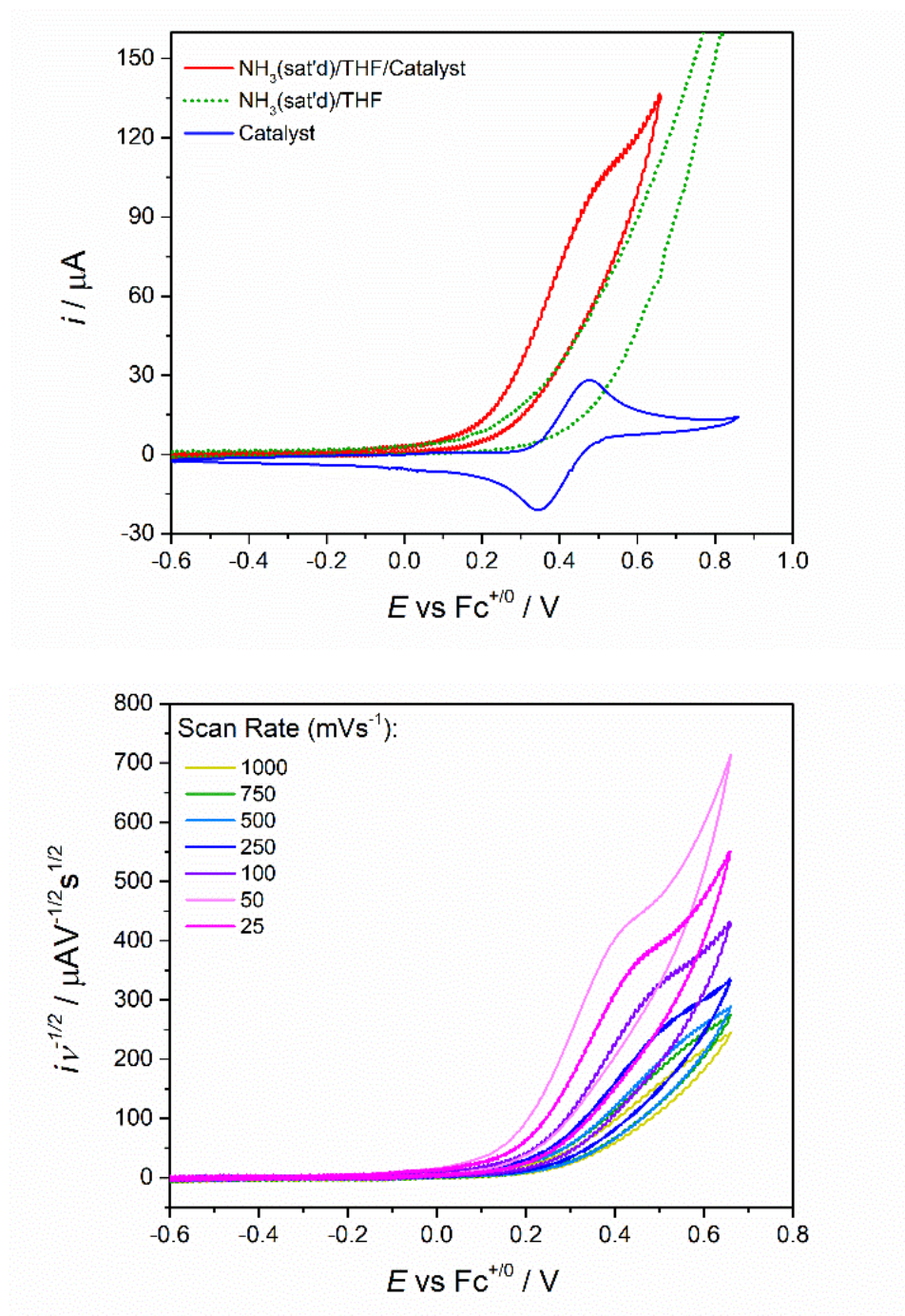


Figure 3.2.3 Top: Cyclic voltammograms for THF solutions of 2.13×10^{-3} M catalyst **1a** (blue), 0.34 M NH_3 added to the solution of 2.13×10^{-3} M catalyst **1a** (red) and direct NH_3 oxidation in THF in the absence of **1a** (dotted green). Scan rate 0.1 V s^{-1} . Bottom: Normalized catalytic ($i/\sqrt{\nu}$) currents when NH_3 (0.34 M) is added to a solution of 2.13×10^{-3} M **1a** obtained for mentioned scan rates. The magnitude and the onset of the normalized currents are being improved as the scan rate is decreasing.

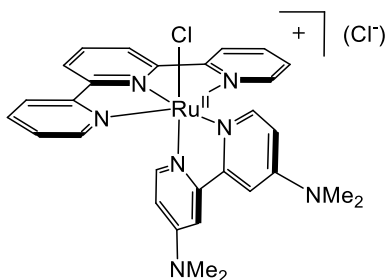
Since the onset of the catalytic current is only 80 mV more negative than noncatalytic ammonia oxidation, it is hard to assess the catalytic current without the interference of background NH_3 oxidation. All these factors are related to the relatively positive $E_{1/2}$ for $[\text{Ru}(\text{trpy})(\text{bpy})\text{NH}_3](\text{PF}_6)_2$ (**1a**). It is expected that catalysts with redox potentials more negative than 0.25 V *versus* $\text{Fc}^{+/0}$ (NH_3 oxidation onset) could enable a clear observation of a background-free catalytic current and hence more precise insights to the catalysis mechanism. Controlling the electron density at the ruthenium metal center *via* structural modifications of the polypyridyl ligands is a well-established approach to tune the catalytic activity of ruthenium polypyridyl catalysts.^{6,7} Installing electron-donating substituent groups on the trpy and bpy moieties, directly affects the redox potential of the complex and therefore the catalytic activity *via* making the higher oxidation states of the metal more accessible.² Aiming to lower the redox potential, $[\text{Ru}(\text{trpy})(\text{dmabpy})\text{NH}_3](\text{PF}_6)_2$ (**2a**) was employed by utilizing a more electron rich 4,4'-bis(dimethylamino)-2,2'-bipyridine (dmabpy) ligand.

3.3. Synthesis of $[\text{Ru}(\text{trpy})(\text{dmabpy})\text{NH}_3](\text{PF}_6)_2$ (**2a**)

2a was synthesized from $[\text{Ru}(\text{trpy})\text{Cl}_3]$ in two steps as described below.

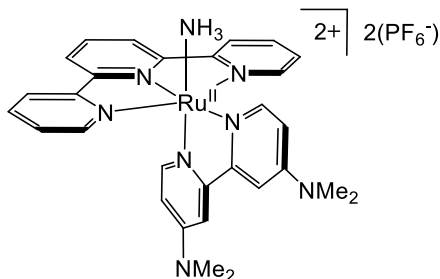
3.3.1. (2,2':6',2''-Terpyridyl)(4,4'-bis(N,N-dimethylamino)-2,2'-bipyridyl)chloro

ruthenium(II) chloride, $[\text{Ru}(\text{trpy})(\text{bdmabpy})\text{Cl}]\text{Cl}$.



(2,2':6',2''-Terpyridyl)trichloro ruthenium (200 mg, 0.45 mmol, 1 equiv.), 4,4'-bis(N,N-dimethylamino)-2,2'-bipyridine (110 mg, 0.45 mmol, 1 equiv.), and LiCl (95 mg, 2.25 mmol, 5 equiv.) were weighed into a 150 mL round bottom flask equipped with a stir bar. A 1:1 mixture of methanol/water (50 mL) was added as a solvent, and the resulting dark slurry was stirred under a positive pressure of N₂. Triethylamine (0.5 mL) was added by syringe. The reaction was heated to gentle reflux under nitrogen with stirring for 4 hours. The volume of the solution was reduced by half on a rotary evaporator, resulting in the precipitation of dark, red-brown solids. The flask was cooled in an ice bath, and the dark solid was collected by suction filtration. The solid was washed with 1 mL of ice-cold 3 M HCl, then 3 × 1 mL portions of cold acetone followed by 3 × 1 mL diethyl ether. A black-purple crystalline solid was collected with mass of 230 mg (0.36 mmol) after drying under high vacuum at 50 °C for 12 hours. (79% yield). **¹H NMR (500 MHz, DMSO-*d*₆)** δ 8.75 (d, *J* = 6.7 Hz, 1H), 7.77 (d, *J* = 8.1 Hz, 2H), 7.67 (d, *J* = 8.0 Hz, 2H), 7.21 (t, *J* = 8.0 Hz, 1H), 7.13 – 7.00 (m, 5H), 6.74 (d, *J* = 2.9 Hz, 1H), 6.55 (t, *J* = 6.6 Hz, 2H), 6.42 (dd, *J* = 6.8, 2.8 Hz, 1H), 5.69 (d, *J* = 6.9 Hz, 1H), 5.39 (dd, *J* = 6.9, 2.8 Hz, 1H), 2.56 (s, 6H), 2.19 (s, 6H).

3.3.2. (2,2':6',2''-Terpyridyl)(4,4'-bis(N,N-dimethylamino)-2,2'-bipyridyl)ruthenium(II) ammine dihexafluoro phosphate, [Ru(trpy)(dmabpy)NH₃](PF₆)₂, (2a).



[Ru(tpy)(dmabpy)Cl]Cl was weighed into a 25 mL heavy walled reaction flask equipped with a stir bar (200 mg, 0.31 mmol, 1 equiv.). Concentrated aqueous ammonium hydroxide was added as

solvent (10 mL, excess). The reaction was closed with a Teflon screw plug and heated as a closed system for 2 h at 90 °C. After heating was complete, the reaction and stir bar were poured into a 125 mL beaker open to air in a fume hood. Excess ammonium hexafluorophosphate (100 mg, 0.6 mmol, 2 equiv.) was added as a solid into the beaker with stirring. The mixture was stirred for an hour until a thick slurry of precipitated brown solids resulted. The solid was collected by filtration and was washed with small portions of deionized water until the initial brown filtrate ran a lighter tan color. The mass of the resultant brown solid was 239 mg (0.27 mmol) after vacuum drying, 88 % isolated yield. **¹H-NMR (500 MHz; CD₃CN):** δ 8.72 (d, *J* = 6.7 Hz, 1H), 8.49 (d, *J* = 8.1 Hz, 2H), 8.38 (d, *J* = 8.0 Hz, 2H), 8.09 (t, *J* = 8.1 Hz, 1H), 7.94 (td, *J* = 7.8, 1.3 Hz, 2H), 7.88 (d, *J* = 5.5 Hz, 2H), 7.69 (d, *J* = 2.8 Hz, 1H), 7.41-7.38 (m, 3H), 7.17 (dd, *J* = 6.7, 2.8 Hz, 1H), 6.48 (d, *J* = 6.8 Hz, 1H), 6.16 (dd, *J* = 6.9, 2.8 Hz, 1H), 3.35 (s, 6H), 2.99 (s, 6H), 1.65 (s, 3H). **¹³C NMR (126 MHz; CD₃CN):** δ 159.4, 159.1, 157.0, 156.0, 154.9, 153.8, 152.7, 149.7, 148.6, 137.0, 133.2, 127.4, 123.4, 122.6, 109.1, 108.6, 105.8, 105.2, 39.2, 38.9. **¹⁹F NMR (470 MHz; CD₃CN):** δ -72.8 (d, *J*_{F-P} = 706 Hz). **³¹P NMR (202 MHz; CD₃CN):** δ -144.6 (septet, *J*_{P-F} = 706 Hz). **Anal.** **Calcd** for C₂₉H₃₂F₁₂N₈P₂Ru: C, 39.42 H, 3.65; N, 12.68. **Found:** C, 39.37; H, 3.66; N, 12.52.⁸

3.4. Catalytic Activity of **2a** in THF

3.4.1. Assessment of the Catalytic Current by Cyclic Voltammetry

In dry THF, the *E*_{1/2} of the Ru(III)/Ru(II) couple for [Ru(trpy)(dmabpy)NH₃](PF₆)₂ (**2a**) appears at 0.095 V vs. Fc^{+/0} (See Appendix, Figure A3.2.1), 305 mV more negative than the *E*_{1/2} of [Ru(trpy)(bpy)NH₃](PF₆)₂ (**1a**) and 155 mV more negative than the onset of direct NH₃ oxidation at the working electrode. An enhanced current is observed for solutions containing **2a** and NH₃(sat'd) in THF, with an onset potential of approximately -0.025 V vs. Fc^{+/0} (Figure 3.4.1).

Similar to what was observed for **1a**, a negative shift in the onset potential as well as an increase in the normalized currents for slow scan rates, agree with a complicate catalytic mechanism which enhances with longer experiment time scales at low scan rates (See Appendix, Figure A3.2.2).

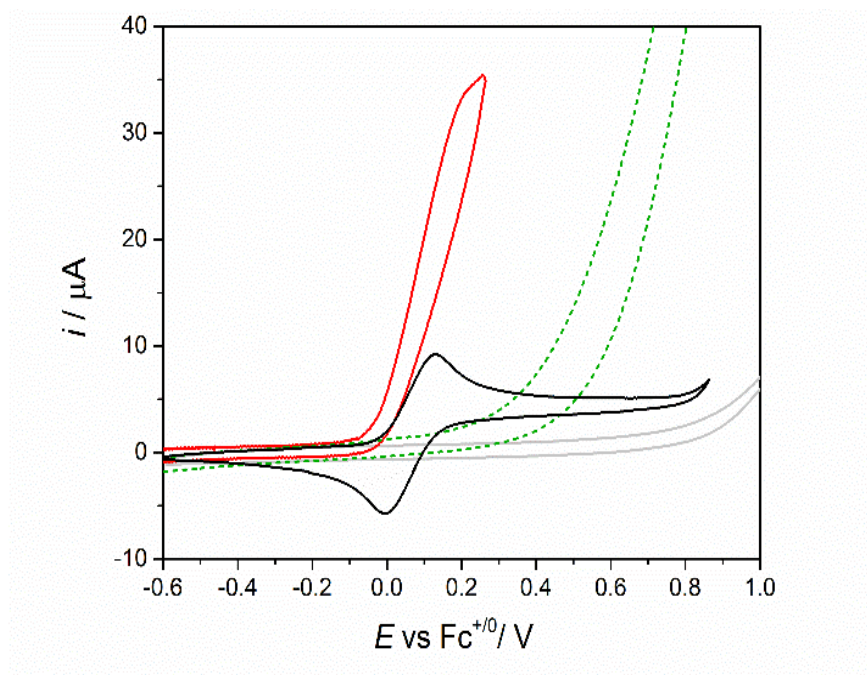


Figure 3.4.1 Cyclic voltammograms for THF solutions of 2.5×10^{-3} M **2a** (black), 2.5×10^{-3} M **2a** and 0.34 M NH_3 (red), uncatalyzed NH_3 oxidation in THF, 0.34 M (green) and the electrolyte background (gray). Scan rate 0.1 Vs^{-1} . This figure shows that upon the presence of the catalyst **2a**, a catalytic current is appeared at lower overpotentials relative to direct oxidation of ammonia in THF.

The catalytic current has a linear dependence on the concentration of $[\text{Ru}(\text{trpy})(\text{dmabpy})\text{NH}_3](\text{PF}_6)_2$ catalyst (See Appendix, Fig. A3.2.3). To assess the dependence of the catalytic current on the concentration of ammonia, THF solutions of 2.5×10^{-3} M **2a** in NH_3 were prepared while maintaining the $[\text{NH}_3]$ larger than 3-fold excess to assure that pure catalytic conditions are held. A plot of the catalytic currents at 0.2 V *versus* concentration of ammonia (Figure 3.4.2) shows a nonlinear trend.

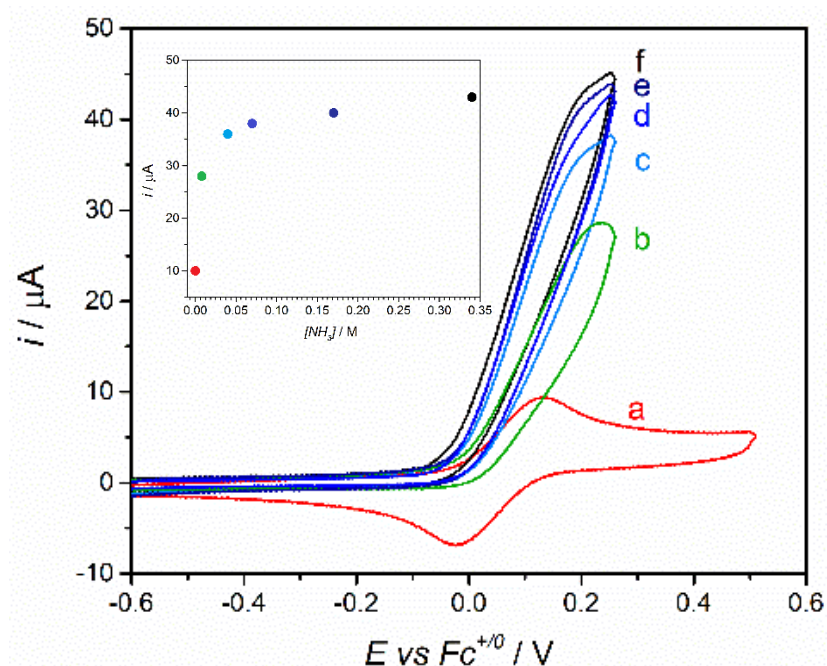


Figure 3.4.2 Dependence of catalytic current on the concentration of ammonia when $[\mathbf{2a}] = 2.5 \times 10^{-3} \text{ M}$, $[\text{NH}_3] =$ (a) 0 M, (b) 0.008 M, (c) 0.04 M, (d) 0.07 M, (e) 0.17 M and (f) 0.34 M. Inset: Peak currents (at 0.90 V for catalytic currents) *versus* concentration of ammonia. The first data point (gray) is the anodic peak current for the catalyst in the absence of ammonia and is shown for comparison. Scan rate 100 mV s^{-1} .

3.4.2. Quantification of the Products of the Electrolysis Using Gas Chromatography

Controlled potential electrolysis of NH_3 saturated THF solutions were performed under argon in the presence of $[\text{Ru}(\text{trpy})(\text{dmabpy})\text{NH}_3](\text{PF}_6)_2$ (**2a**) ($2.7 \times 10^{-3} \text{ M}$, $6.8 \times 10^{-6} \text{ mol}$). A potential of 0.15 V vs. $\text{Fc}^{+/0}$ was applied to the working electrode that was immersed in the solution for a total time of 180 min, during which 9.1 C of charge (9.4×10^{-5} moles of electrons) was passed (Figure 3.4.3).

The ^1H NMR of the solution, after the electrolysis only contains $[\text{Ru}(\text{trpy})(\text{dmabpy})\text{NH}_3](\text{PF}_6)_2$ (**2a**) (See Appendix, A3.5.1) and when the concentration of the catalyst **2a** was measured before, and after the electrolysis by UV-Vis spectrophotometry, a modest decrease of 6.7% in **2a** was calculated (See Appendix, A3.5.2). So, the gradual decrease in the current with time could be attributed to the consumption of the substrate, NH_3 , as opposed to the catalyst degradation.

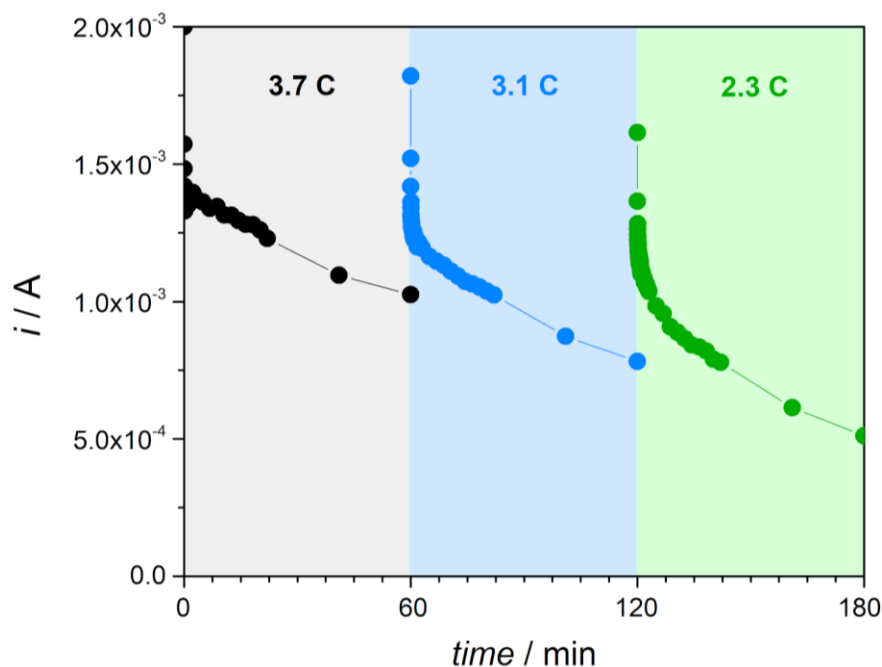


Figure 3.4.3 Current passing during three steps of controlled potential electrolysis (each 3600 s) while the solution was being stirred under argon. $[2a] = 2.7 \times 10^{-3}$ M, $[NH_3] = 0.34$ M, 0.1 M $[NH_4](PF_6)$ in dry THF. Numbers show the amount of charge (q , in coulombs) passed in each step, calculated based on the integration of the area under each curve ($q = i \times t$).

Comparison of the cyclic voltammograms of the solution obtained before the electrolysis and after each 30 min interval also shows a decrease in current, as well as slight reappearance of a cathodic return current at higher scan rates (See Appendix, A3.5.3), suggesting that upon consumption of the NH_3 substrate the CVs do not further depict the characteristics of a pure kinetic regime. Consistently, when NH_3 is bubbled in the solution after 180 min of electrolysis, the catalytic current is restored (See Appendix, Figure A3.5.3.2).

For the electrolysis experiment shown in Figure 3.4.4, the headspace gas was analyzed at 60-minute intervals by gas chromatography.

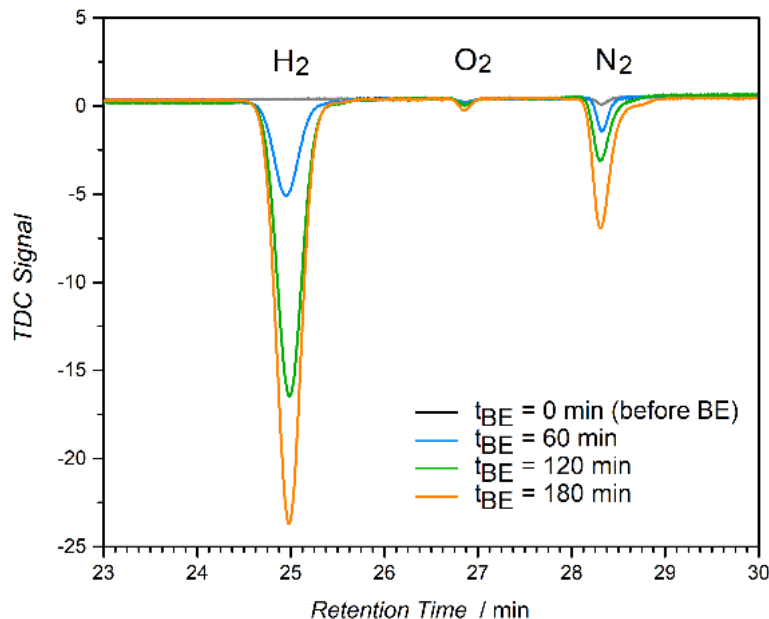


Figure 3.4.4 Gas chromatograms obtained after injection of 100 μ L of the electrolysis headspace before applying potential and after 60, 120 and 180 min of electrolysis. The peaks associated with N₂ and H₂ are growing in after each step. The residual O₂ in the headspace sample is attributed to the leaks. For full chromatogram See Appendix, Figure A3.4.4.1.

Quantification of the products in the gaseous phase shows that after 180 min of electrolysis, 1.4×10^{-5} moles of N₂ and 3.9×10^{-5} moles of H₂ were evolved at 86% and 77.6% faradaic efficiencies for the respective anodic and cathodic reactions with the H₂:N₂ ratio equal to 2.74:1. Similar faradaic efficiencies and H₂:N₂ ratio results were obtained for a few bulk electrolysis replicate experiments that were carried out with different [2a] and duration of electrolysis (See Appendix, A3.5.4). Control electrolysis experiment in which electro-oxidation of NH₃ in THF was conducted at 0.15 V *versus* Fc⁺⁰ in the absence of the catalyst did not generate N₂ and H₂ in the gaseous headspace.

3.5. Homogeneous vs. Heterogeneous Catalysis

To verify the homogenous nature of the catalysis, the surface of the glassy carbon electrode was examined with XPS. The Ru3d peak appears at 280 eV, overlapping with the C1s peak at 284.8 eV. Because the electrode is glassy carbon, the very large C1s peak obscures unambiguous identification of the Ru3d peak. However, when the region between 270 to 300 eV is scanned separately, the characteristic peak for Ru3d is not evident (Figure 3.5.1, bottom).

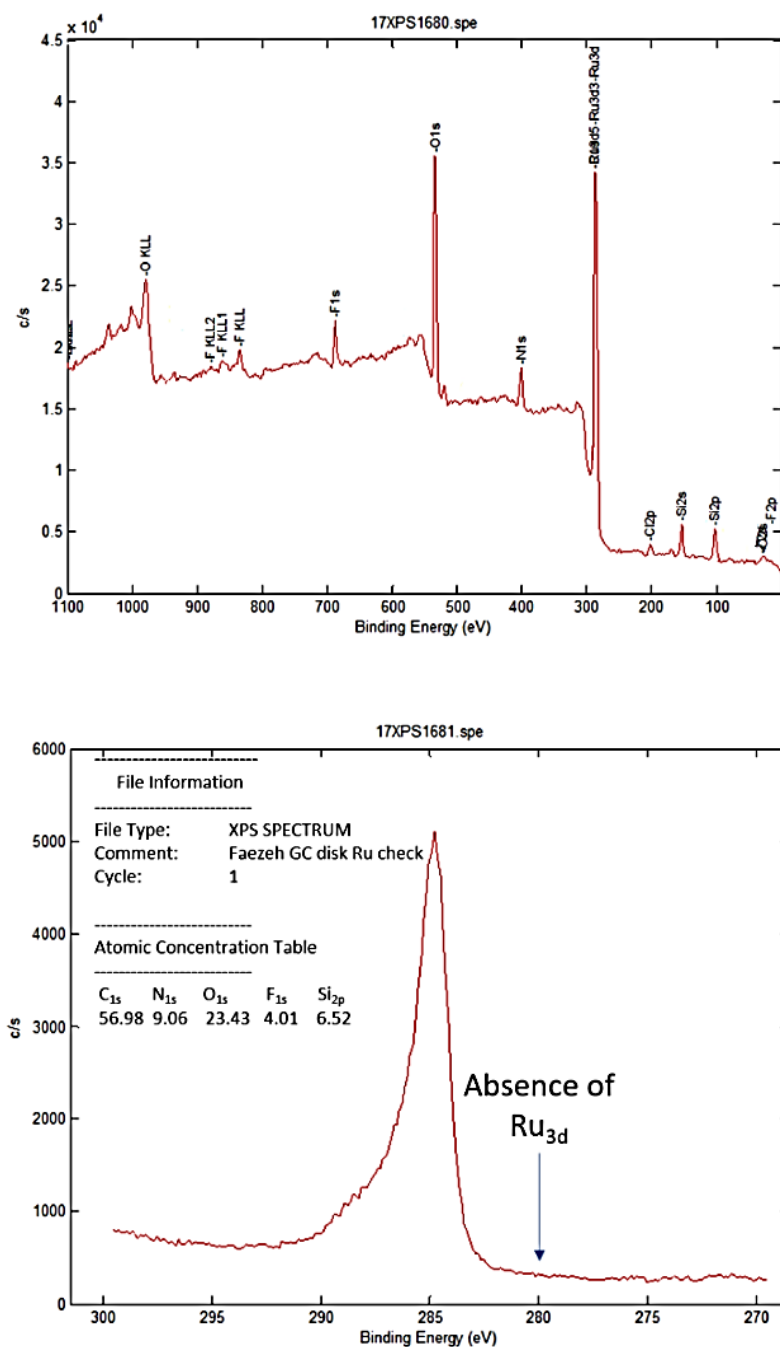


Figure 3.5.1 XPS spectra of the glassy carbon electrode after the BE. Top: full spectrum. The source of silicon and oxygen is electrode contamination with silicon grease during the removal of the electrode from the electrolysis cell. The grease was heavily applied around the joints to prevent leaks. Bottom: the scan around 285 eV where the characteristic peak for ruthenium is expected to appear if depositions have had taken place.

Additionally, a rinse test was performed by removing the glassy carbon electrode from the electrolysis solution, rinsing with dry THF and then inserting it into a cell containing a fresh $\text{NH}_3/\text{THF}/0.1 \text{ M } [\text{NH}_4](\text{PF}_6)$ solution. No enhanced catalytic current was passed at an applied potential of 0.15 V versus $\text{Fc}^{+/0}$, and the headspace sampling of the electrolysis cell at the end of 3 hours of electrolysis showed no formation of N_2 and H_2 (Figure 3.5.2). These results confirm that the catalytic activity is not due to electrodeposition of ruthenium species on to the surface of the glassy carbon electrode.

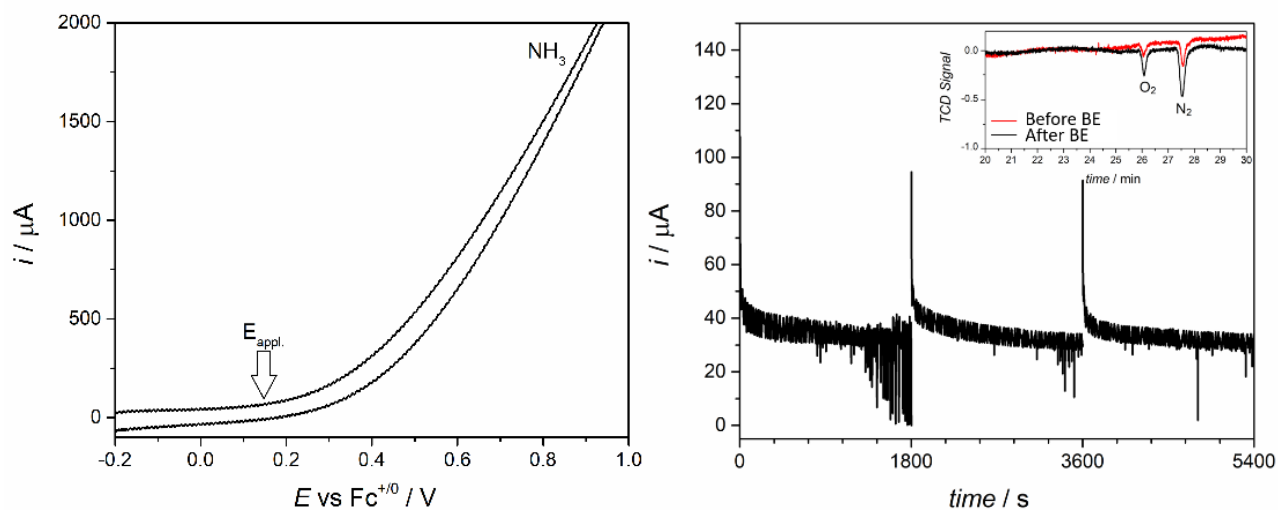


Figure 3.5.2 Rinse test results. Left: The CV recorded for a solution of $\text{NH}_3(\text{sat'd})/\text{THF}$ in which the rinsed glassy electrode was immersed. Scan rate 0.1 Vs^{-1} . Right: Current vs. times for three electrolysis steps of electrolysis. The inset is the gas chromatogram of the cell headspace injected to GC before the electrolysis and after the third hour of electrolysis. No H_2 is generated and the $\text{N}_2:\text{O}_2$ ratio matches with leaks from the air.

Examination of the glassy carbon electrode by SEM after the rinse test reveals a ruthenium-deposition free surface and the EDS measurements of the selected areas do not show any ruthenium depositions on the surface (See Appendix, A3.5.5). Such depositions, when existent, are very easily noticeable. For instance, in an electrolysis experiment which failed due to the presence of water residuals in the NH_3/THF solution, microscopic examination of the surface showed that large

grains of a ruthenium-containing material have developed on to the surface. This layer is visible with naked eye in the form of a thin orange layer on the electrode that does not get rinsed with THF (Figure 3.5.3). To prevent this issue, extensive care should be taken regarding the dryness of the reagents and equipment.

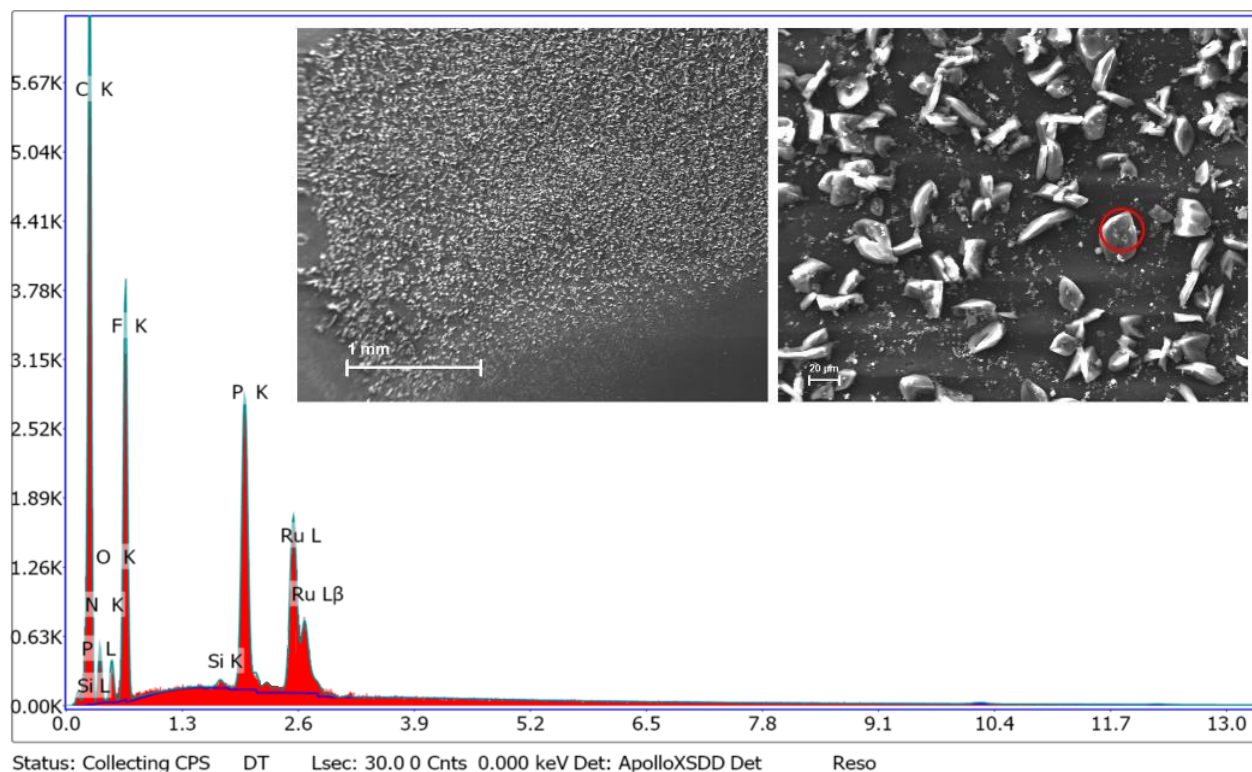


Figure 3.5.3 EDS analysis of the selected area (red circle in the inset) on the glassy carbon electrode at the end of a failed electrolysis experiment. The insets are the SEM images of the electrode with two different magnifications. These results show that a ruthenium containing material has deposited on the surface, possibly acting as an active catalytic surface.

3.6. Isotopic Labeling Experiments

In order to understand the origin of the evolved N_2 in bulk electrolysis experiments, nitrogen-labeling experiments were performed. In these experiments, electrolysis of $^{15}NH_3$ was conducted in the presence of ^{15}N -labeled catalyst under the same conditions applied in section 3.4.1.

3.6.1. Synthesis of [Ru(trpy)(dmabpy)¹⁵NH₃](PF₆)₂ (¹⁵N-2a)

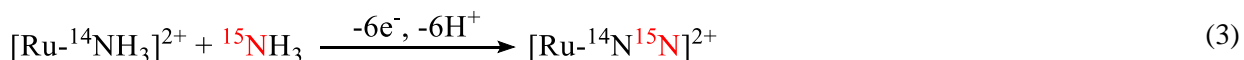
(2,2':6',2''-terpyridyl)(4,4'-bis(*N,N*-dimethylamino)-2,2'-bipyridyl) chloro ruthenium(II) chloride was weighed into a 25 mL heavy walled reaction flask (160 mg, 0.25 mmol, 1 equiv.) containing 10 mL deionized water. ¹⁵NH₄Cl (670 mg, 12.5 mmol, 50 equiv.) was weighed and added to the solution as a solid. Pellets of KOH (690 mg, 12.5 mmol, 50 equiv.) were transferred into the solution and the flask was capped and sealed immediately. The reaction was heated for 2 h at 100 °C while stirring. After 2 h, the flask was cooled down to room temperature and the solution was transferred to a beaker. Ammonium hexafluorophosphate (80 mg, 0.5 mmol, 2 equiv.) was added as a solid and the precipitate was collected on a glass filter. The solid was washed with portions of deionized water and dried overnight in a vacuum oven at 60 °C. The mass of product was 182 mg (0.20 mmol), 83 % isolated yield. ¹H NMR (500 MHz, CD₃CN): δ 8.69 (d, *J* = 6.7 Hz, 1H), 8.45 (d, *J* = 8.1 Hz, 2H), 8.35 (d, *J* = 8.1 Hz, 2H), 8.06 (t, *J* = 8.1 Hz, 1H), 7.91 (td, *J* = 7.8, 1.4 Hz, 2H), 7.85 (d, *J* = 5.4 Hz, 2H), 7.65 (d, *J* = 2.8 Hz, 1H), 7.37-7.35 (m, 3H), 7.14 (dd, *J* = 6.7, 2.8 Hz, 1H), 6.45 (d, *J* = 6.8 Hz, 1H), 6.12 (dd, *J* = 6.9, 2.8 Hz, 1H), 3.31 (s, 6H), 2.96 (s, 6H), 1.61 (d, *J* = 68.3 Hz, 3H). ¹³C NMR (126 MHz; CD₃CN): δ 159.4, 159.1, 157.0, 156.0, 154.9, 153.8, 152.7, 149.7, 148.6, 137.0, 133.2, 127.4, 123.4, 122.6, 109.1, 108.6, 105.8, 105.2, 39.2, 38.9.

3.6.2. Electrolysis of ¹⁵NH₃ using 2a and ¹⁵N-2a

Controlled potential electrolysis of a ¹⁵NH₃ saturated THF solution containing ¹⁵N-2a generated ¹⁵N≡¹⁵N (*m/z* = 30) judged by GC-MS analysis (See Appendix, Figure A3.5.6.2). As described by reaction 2 below (polypyridyl ligands are not shown), ¹⁵N≡¹⁵N (*m/z* = 30) is expected to be the result of the N-N bond formation between the coordinated ammonia nitrogen and the free ammonia in the solution:



Bulk electrolysis of a $^{15}\text{NH}_3$ saturated THF solution with non-labeled **2a** generated N_2 that was initially $^{15}\text{N}^{14}\text{N}$ ($m/z = 29$) and was eventually dominated by $^{15}\text{N}^{15}\text{N}$ ($m/z = 30$) as the $^{14}\text{NH}_3$ ligand in the complex was displaced by $^{15}\text{NH}_3$ in the solution over the course of the electrolysis (See Appendix, Fig. A3.5.6.3). Reactions 3-5 describe these pathways:



This finding is of a great importance because it precludes the possibility of coupling pathways and provides evidence for a single ruthenium site catalytic mechanism. Incorporation of the NH_3 substrate in the N-N bond formation step also suggests that this step is governed by a nucleophilic-electrophilic mechanism, guiding us towards the essentiality of an intermediate bearing a very electrophilic nitrogen. Insights to the possible intermediates are discussed in the following chapters.

3.7. Conclusions

The catalytic activity of two complexes **1a** and **2a** were confirmed by cyclic voltammetry. More detailed studies on the electro-oxidation of NH_3 in THF solutions in the presence of **2a** shows that N_2 and H_2 are generated while the substrate NH_3 is being consumed throughout the electrolysis. Isotope labeling experiments provide evidence that the generated nitrogen is the product of the anodic reaction and the possibility of a heterogeneous catalytic layer was ruled out via control

experiments. In the next two chapters, our findings towards the mechanistic details of the catalysis are discussed.

APPENDIX

A3.1. ^1H NMR Spectra

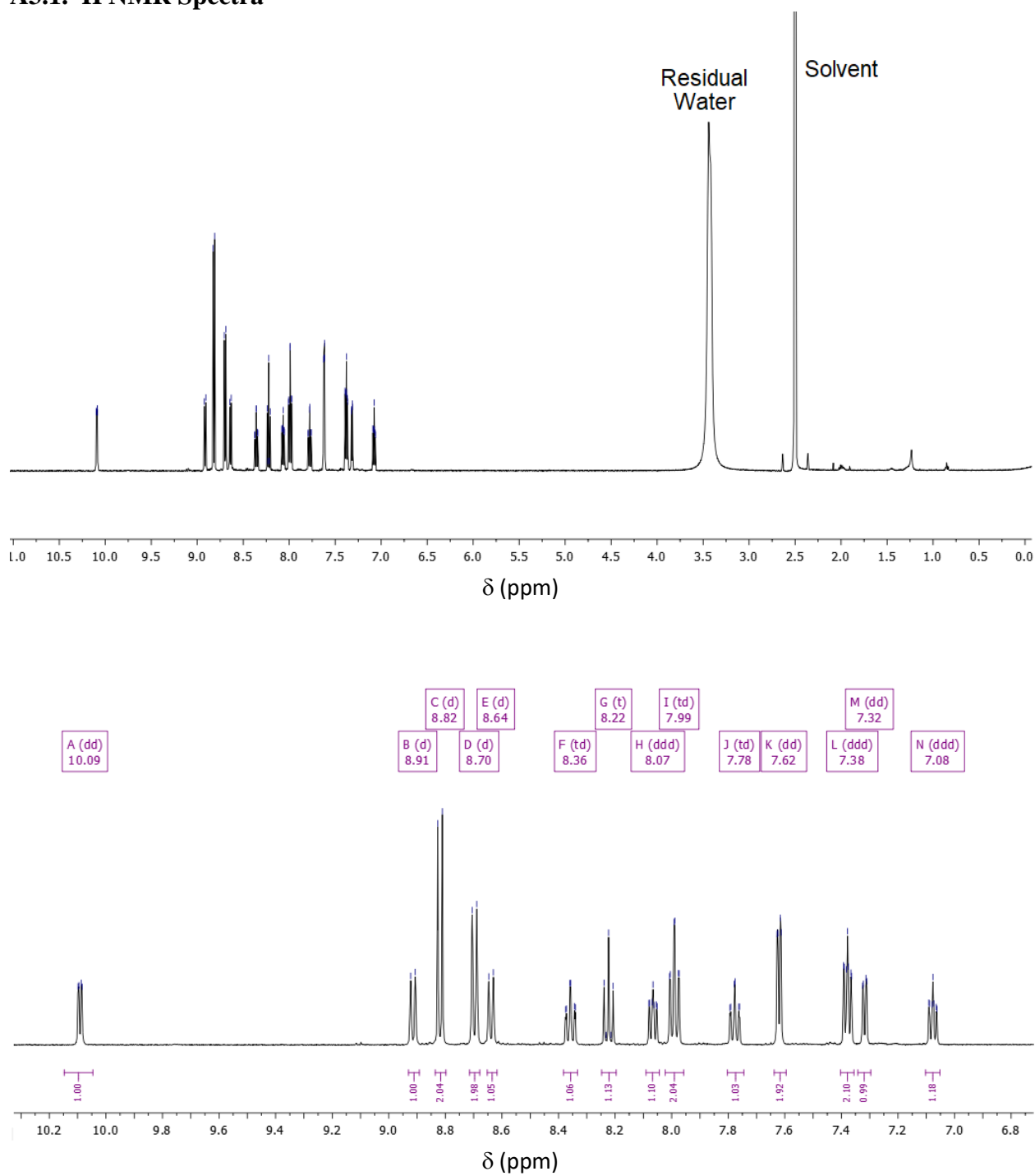


Figure A0.1.1. ^1H NMR spectrum of $[\text{Ru}(\text{trpy})(\text{bpy})\text{Cl}]\text{Cl}$ in $\text{DMSO-}d_6$. Top: full spectrum, Bottom: magnified aromatic region.

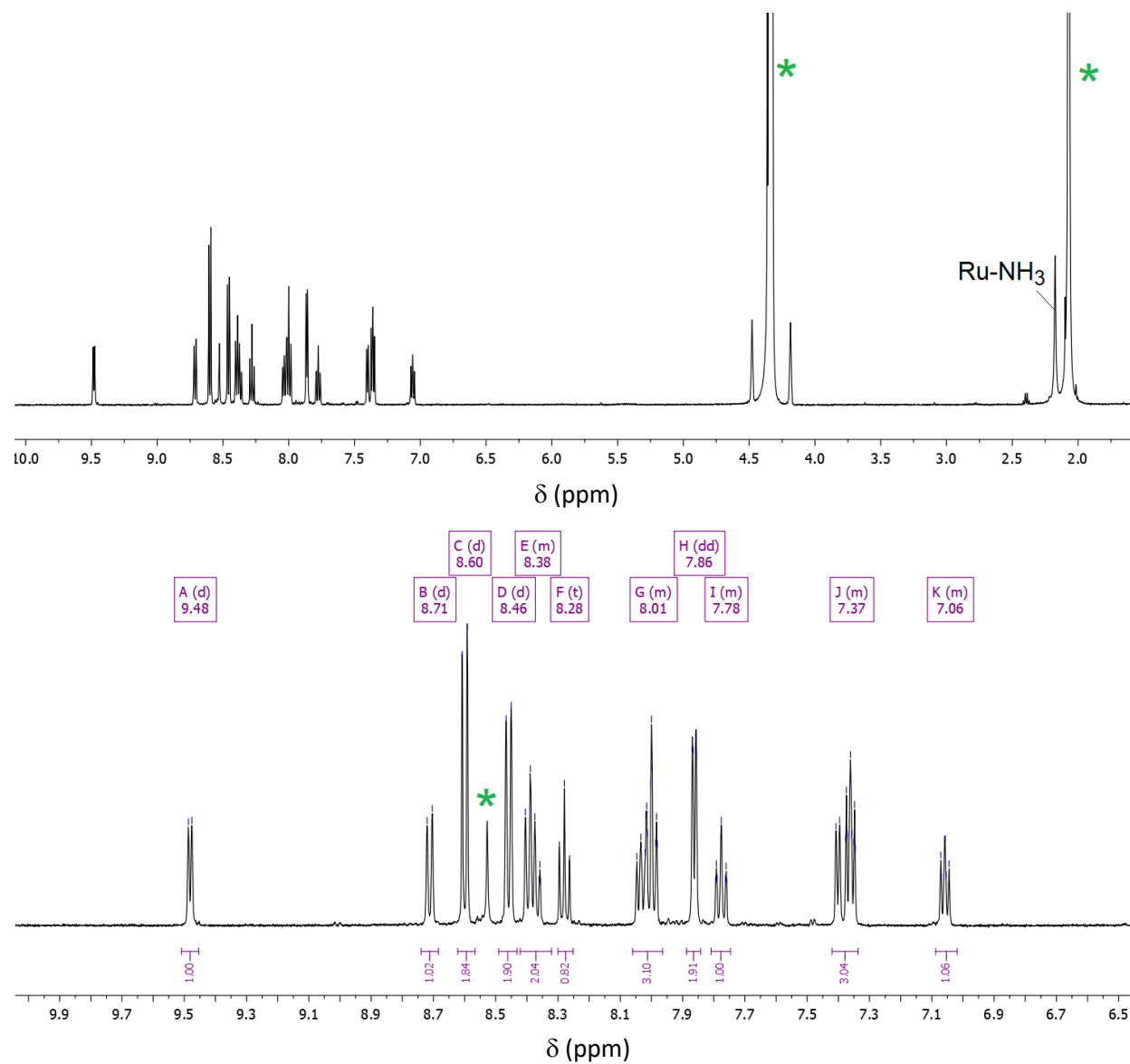


Figure A3.1.2. ¹H NMR spectrum of [Ru(trpy)(bpy)NH₃](PF₆)₂ in NM-*d*₃. Top: full spectrum, Bottom: blow-up of the aromatic region. Starred peaks are solvent related.

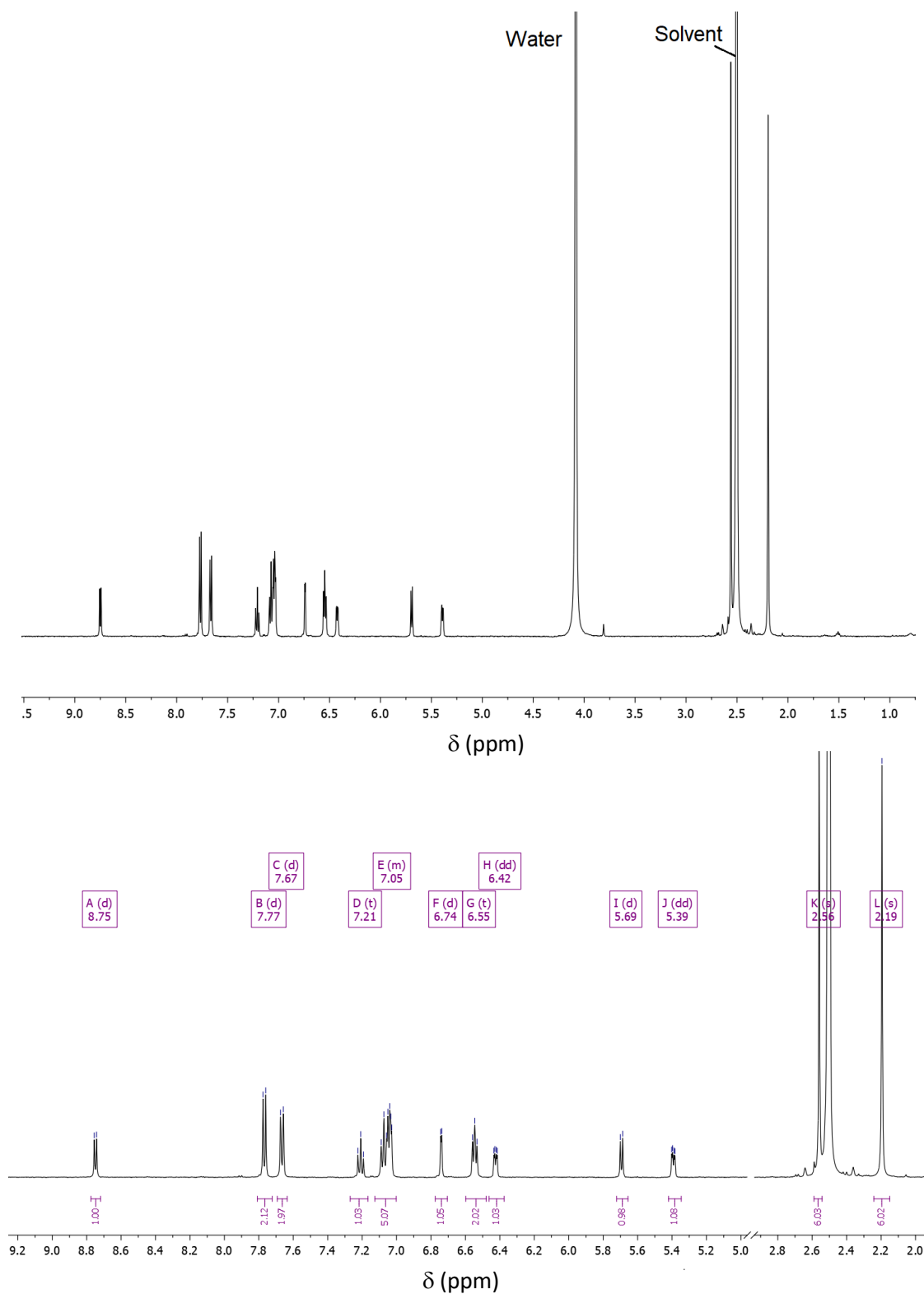


Figure A3.1.3 ^1H NMR spectrum of $[\text{Ru}(\text{trpy})(\text{dmabpy})\text{Cl}]\text{Cl}$ in $\text{DMSO-}d_6$. Top: full spectrum, Bottom: blow-up of the aromatic region.

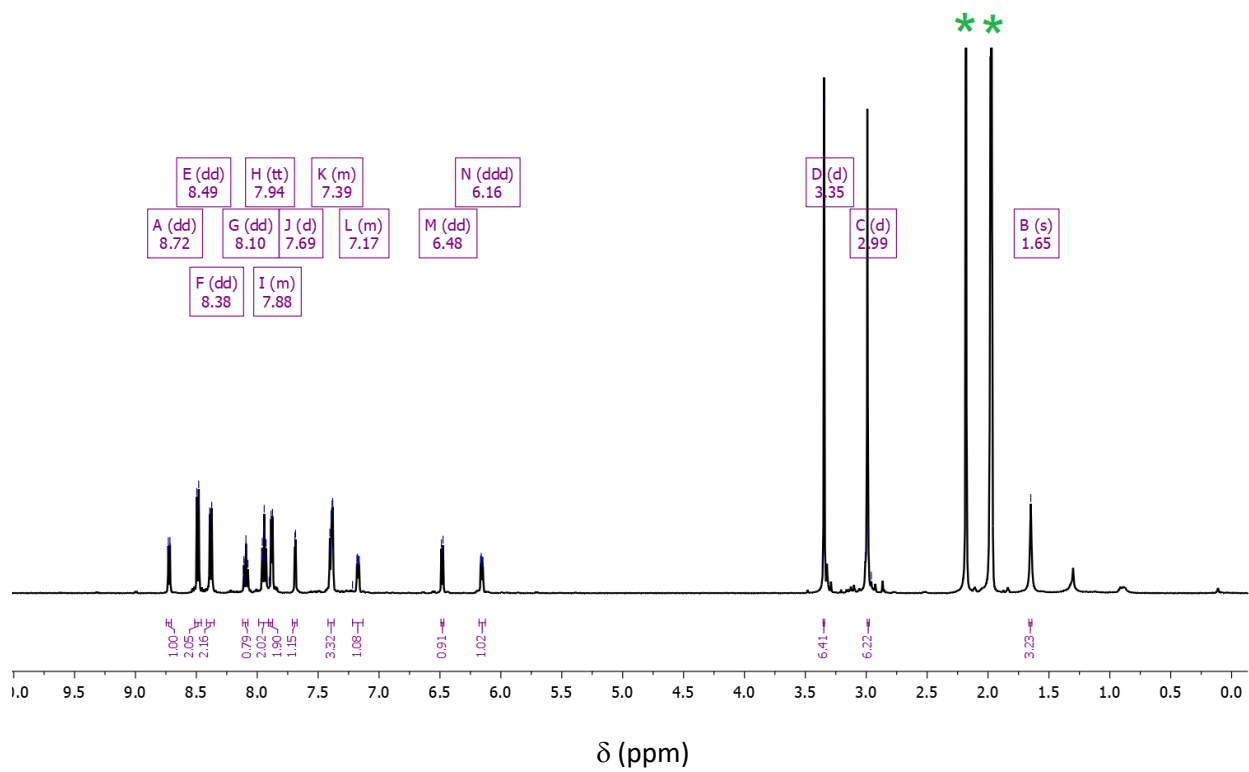


Figure A3.1.4 ^1H NMR spectrum of $[\text{Ru}(\text{trpy})(\text{dmabpy})\text{NH}_3](\text{PF}_6)_2$ in acetonitrile- d_3 . Top: full spectrum, Bottom: blow-up of the aromatic region. Starred peaks are solvent related.

A3.2. Cyclic Voltammetry Studies of **2a** in THF.

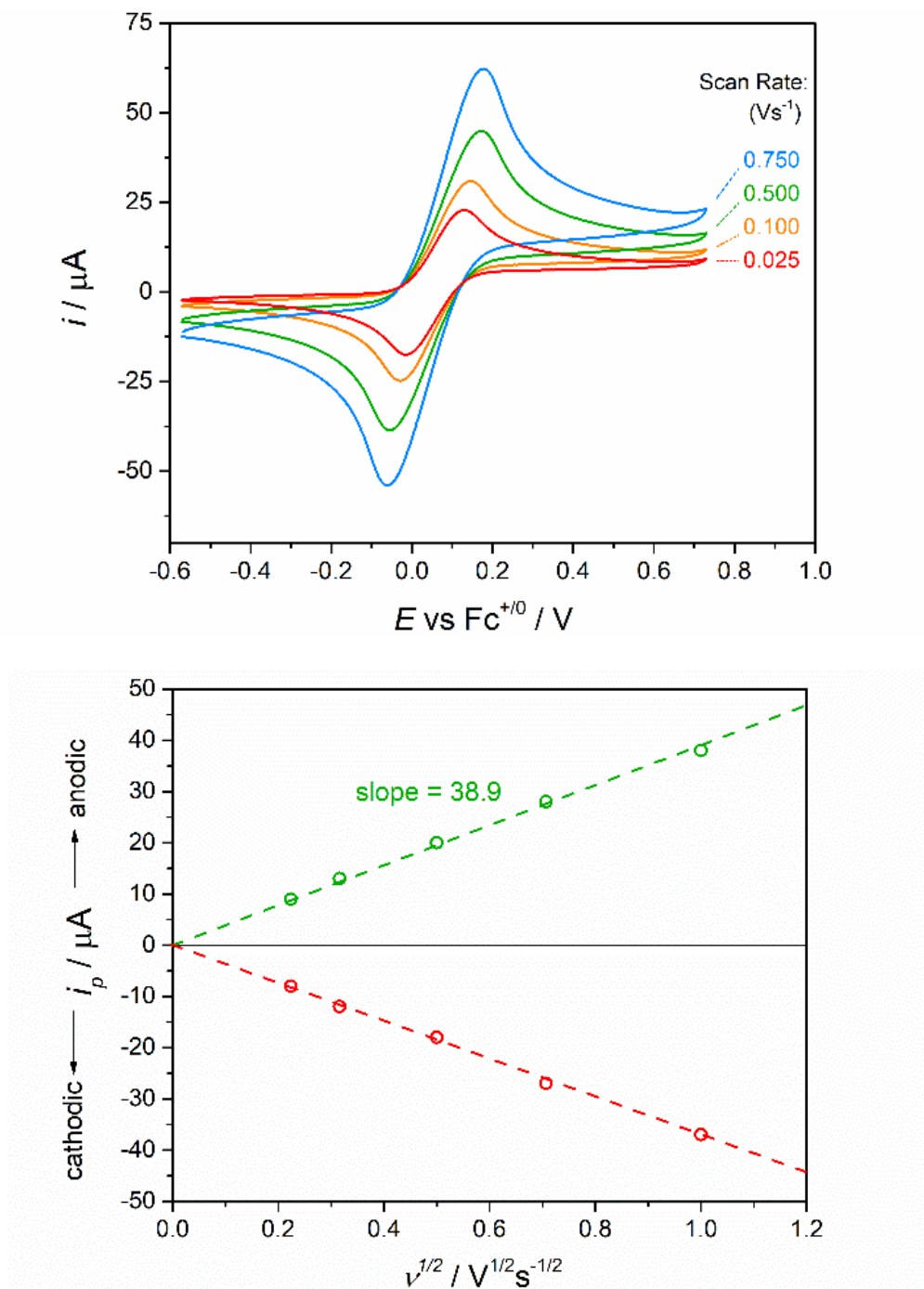


Figure A3.2.1 Top: Scan rate dependence of the current in $5.2 \times 10^{-3} \text{ M}$ **2a** in THF for (a) 50, (b) 100, (c) 250, (d) 500 and (e) 1000 mV s^{-1} . Bottom: Plots of anodic and cathodic peak currents obtained from CVs on the top versus square root of the scan rate. From the slope of the anodic branch a diffusion coefficient of $D_{\text{ox}} = 4.26 \times 10^{-6} \text{ cm}^2 \text{ s}^{-1}$ was calculated for **2a**.

A3.3. Scan Rate Dependence of the Catalytic Current

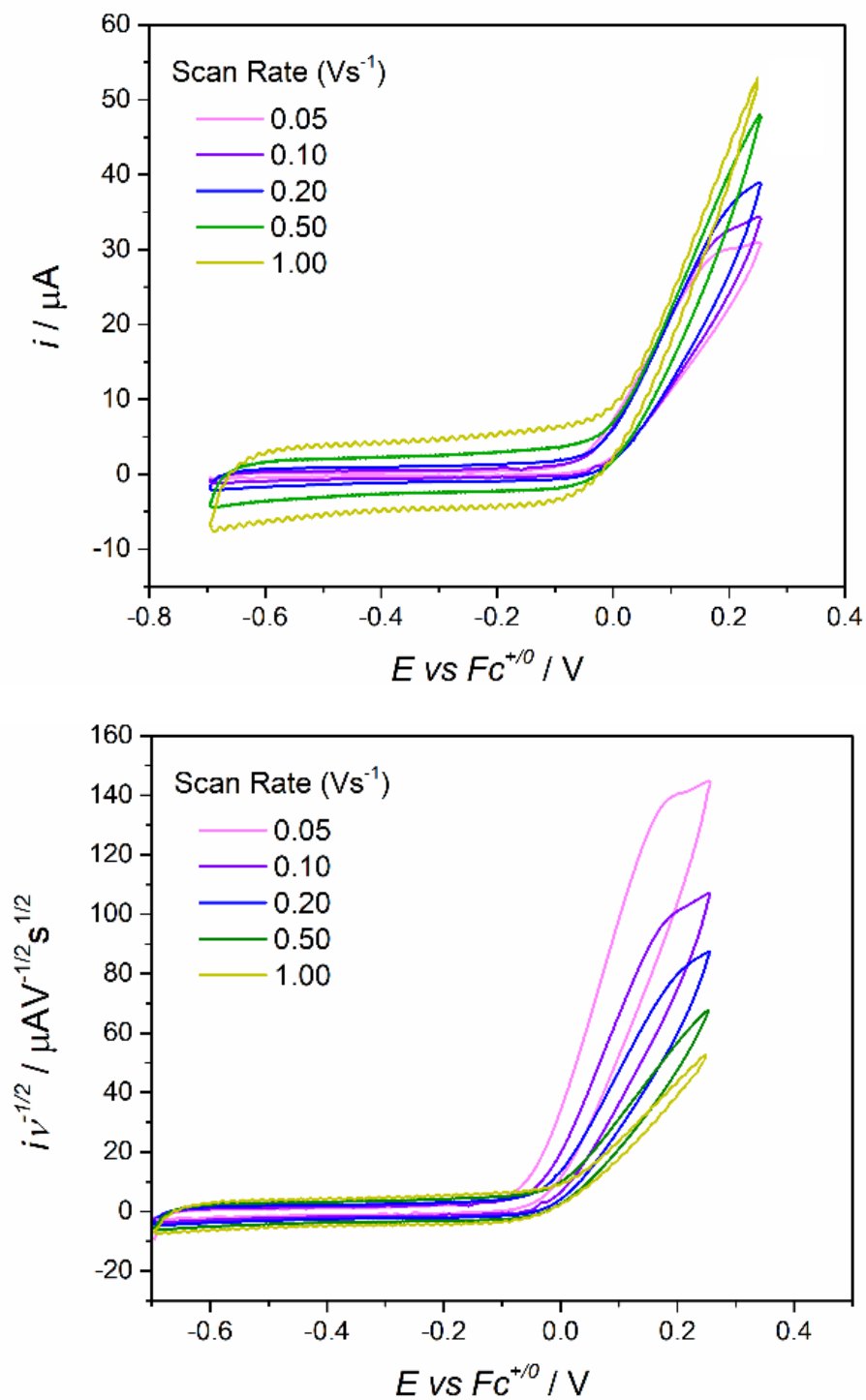


Figure A3.3.1 Top: CVs collected for 2.5×10^{-3} M **2a** in saturated ammonia solutions in THF, with different scan rates, Bottom: Normalized catalytic currents in the solution of 2.5×10^{-3} M **2a** and NH_3 (0.34 M). Both magnitude and the onset of the normalized currents are improved at lower scan rates.

A3.4. Concentration Dependence of the Catalytic Current

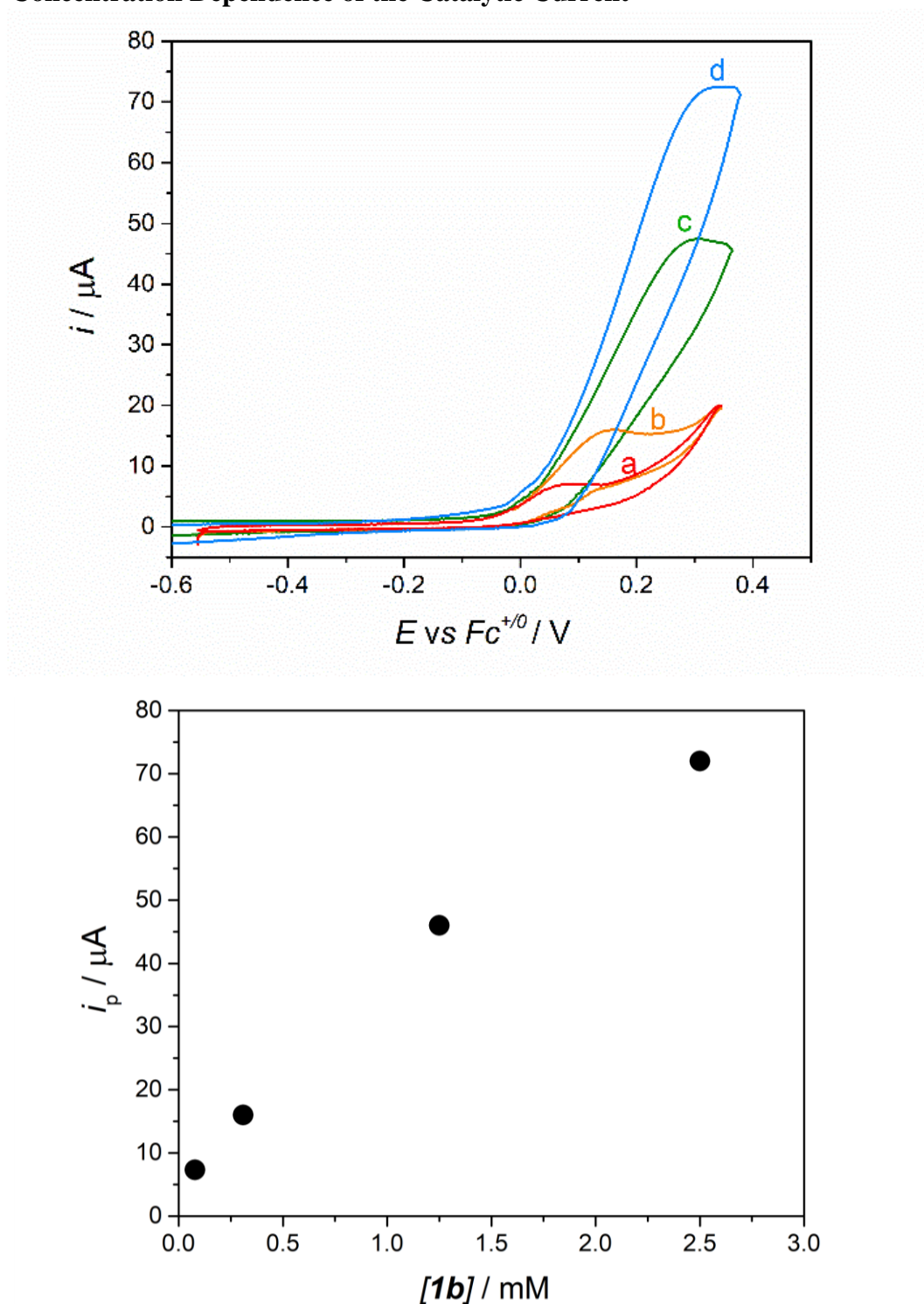


Figure A3.4.1 Top: Catalytic current *versus* concentration of **2a**. In all cases $[\text{NH}_3] = 0.34 \text{ M}$. Bottom: Catalytic peak currents *versus* concentration of the catalyst **2a**. (a) $7.8 \times 10^{-5} \text{ M}$ catalyst, (b) $3.1 \times 10^{-4} \text{ M}$ catalyst, (c) $1.2 \times 10^{-3} \text{ M}$ catalyst and (d) $2.5 \times 10^{-3} \text{ M}$ catalyst. Scan rate 0.1 V s^{-1} . The correlation between the catalytic current and the concentration of the catalyst is almost linear.

A3.5. Catalytic Electrolysis of NH_3 in THF

A3.5.1. ^1H NMR Spectrum of the Solution After the Electrolysis

After the electrolysis, the solvent was pumped out for 3 hours, and the residual solids were dissolved in acetonitrile- d_3 .

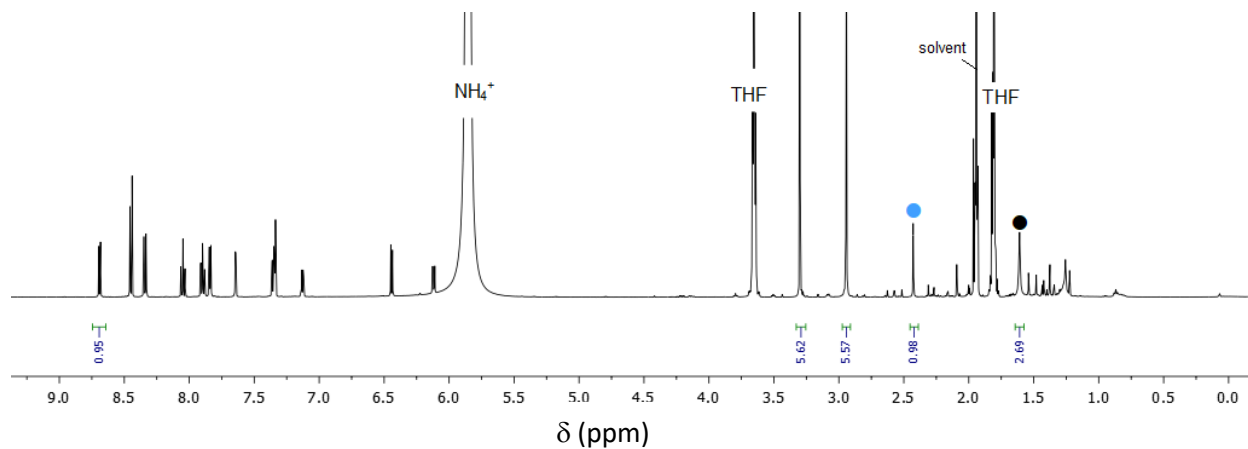


Figure A3.5.1.1 Room temperature ^1H NMR spectrum of the electrolysis sell contents in acetonitrile- d_3 . The resonance for the coordinated ammine is labeled with a black circle. The singlet at 2.46 ppm (blue circle) is unidentified.

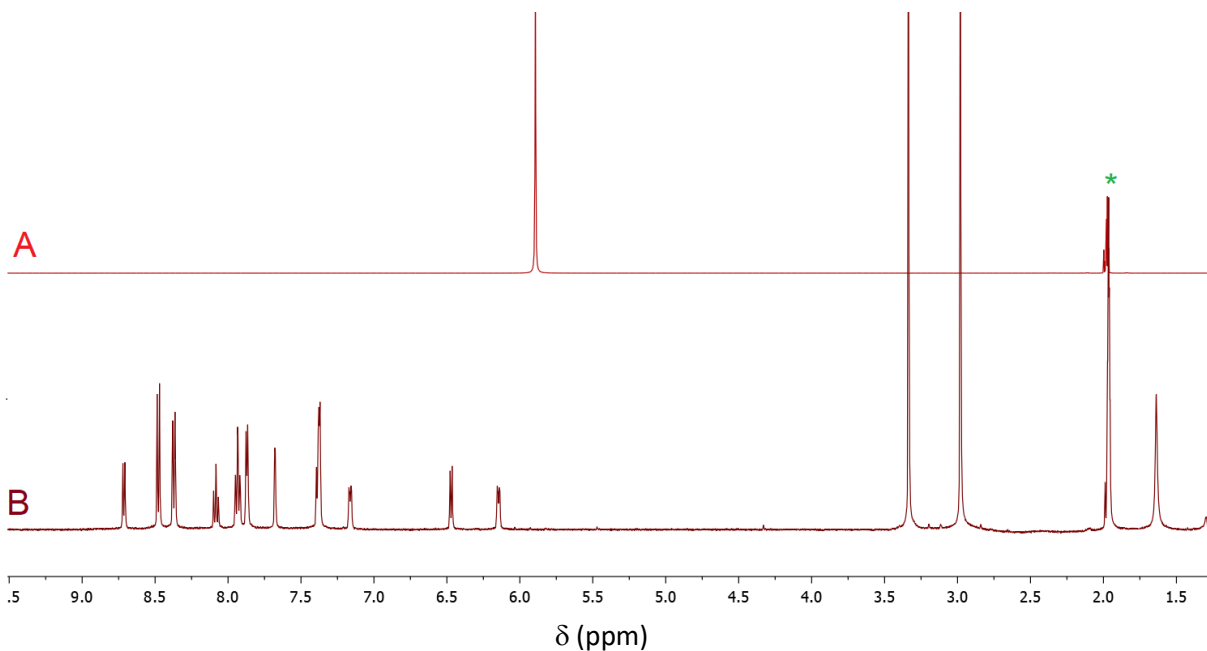


Figure A3.5.1.2 ^1H NMR spectra of (A) $[\text{NH}_4](\text{PF}_6)$ and (B) an authentic sample of **2a** in acetonitrile- d_3 . This figure could be used to identify the species observed in the spectrum in Figure A3.5.1.1. The starred peak is due to solvent residuals.

A3.5.2. Spectrophotocchemical Determination of [2a] Before and After Electrolysis

To obtain the electronic absorption spectra, 30 μL of the solution was drawn before and after the electrolysis (“soln.1”) using a glass syringe and was transferred to a 5 mL volumetric flask. The volume was made up to the volume by THF (“soln.2”). The electronic spectra of these solutions were collected against a THF reference, and the absorbance values at 490 nm were converted to concentration using the absorption coefficient of **2a** in THF ($\epsilon = 9945 \text{ M}^{-1} \text{ cm}^{-1}$). The calculated concentration in the solution after BE is with the consideration of the change in the solution volume during the electrolysis. Calculations are summarized in Table A3.5.2.1.

Table A3.5.2.1 The spectrophotocchemical measurement of **2a** concentration before and after BE.

sample	Abs. @496 nm	[2a] ^a in soln.2	mol 2a in soln. 2	mol 2a in BE solution	% loss
b (t=0)	0.149	$1.49 \times 10^{-5} \text{ M}$	7.49×10^{-8}	$6.24 \times 10^{-6} \text{ }^b$	
a (t=180 min)	0.151	$1.51 \times 10^{-5} \text{ M}$	7.59×10^{-8}	$5.82 \times 10^{-6} \text{ }^c$	$\frac{(6.24-5.82)}{6.24} \times 100 = 6.7\%$

^ausing $A = \epsilon b C$, where $b = 1 \text{ cm}$ and $\epsilon = 9945 \text{ M}^{-1} \text{ cm}^{-1}$ at 496 nm.
^btotal volume of the solution at t=0 is 2.5 mL.
^ctotal volume of the solution at t=180 min is 2.3 mL.

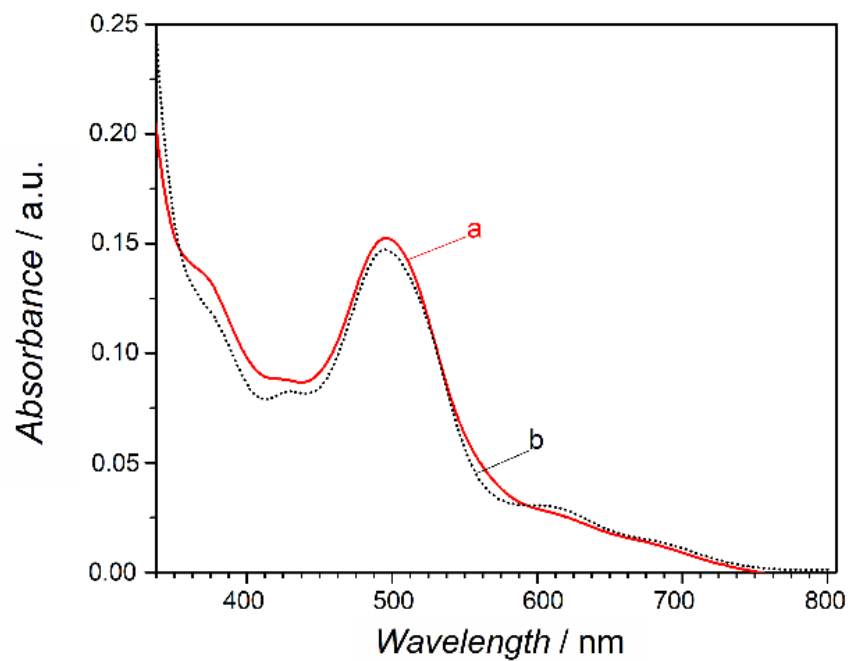
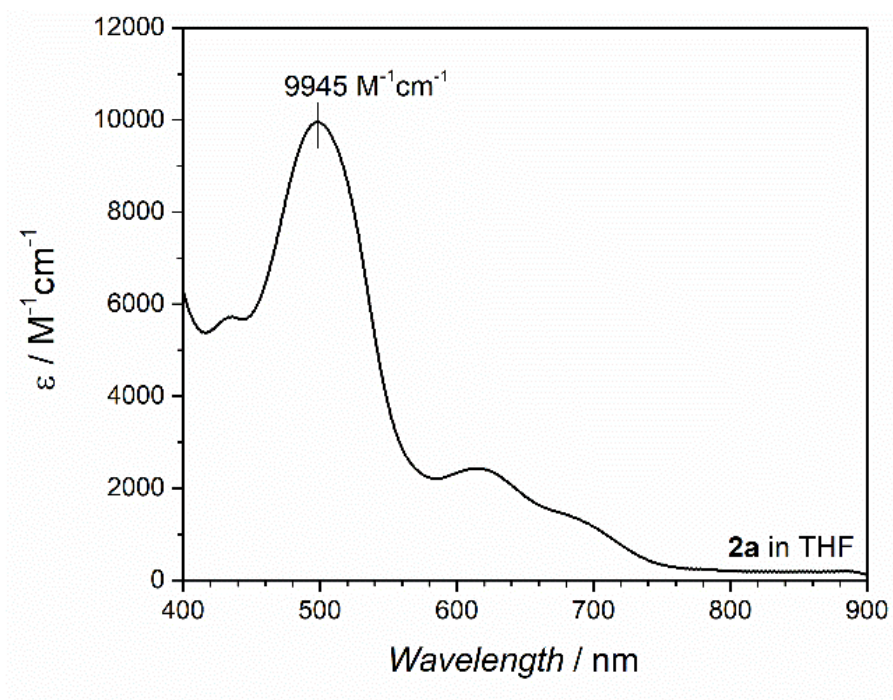


Figure A3.5.2.1 Top: Electronic absorption spectrum of **2a** in THF. Bottom: Absorption spectra of the solution used in the electrolysis of NH_3 (a) after the electrolysis ($t=180 \text{ min}$) and (b) before the electrolysis ($t=0$).

A3.5.3. CVs of the Solution Over the Course of Electrolysis

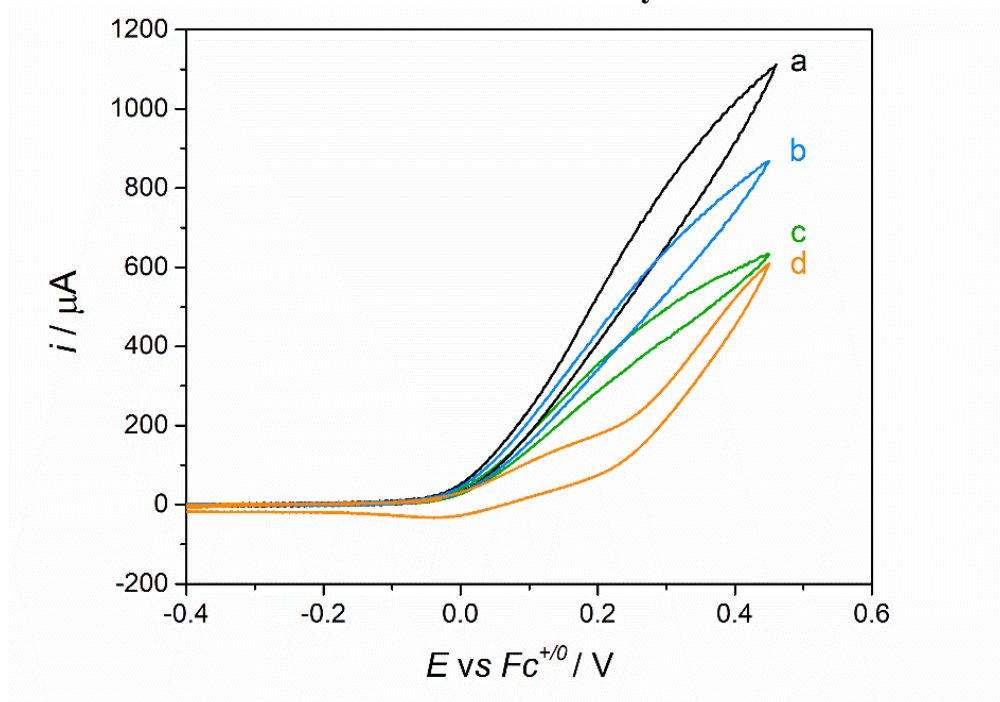


Figure A3.5.3.1 Cyclic voltammograms of the electrolysis solution obtained under static conditions (without stirring). (a) before electrolysis, (b) after 60 min, (c) after 120 min, (d) after 180 min of electrolysis. $[\mathbf{2a}] = 2.7 \times 10^{-3} \text{ M}$, Scan rate 0.1 V s^{-1} . $A = 2.0 \text{ cm}^2$. The change in the CVs are related to the consumption of ammonia with time.

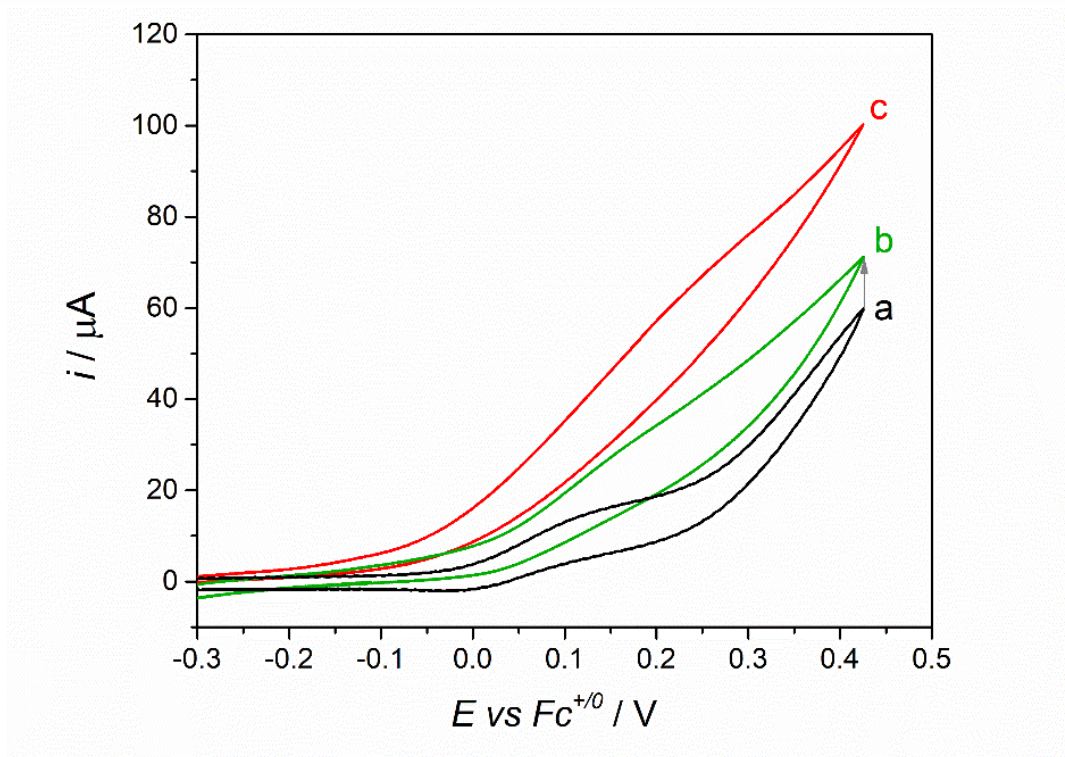
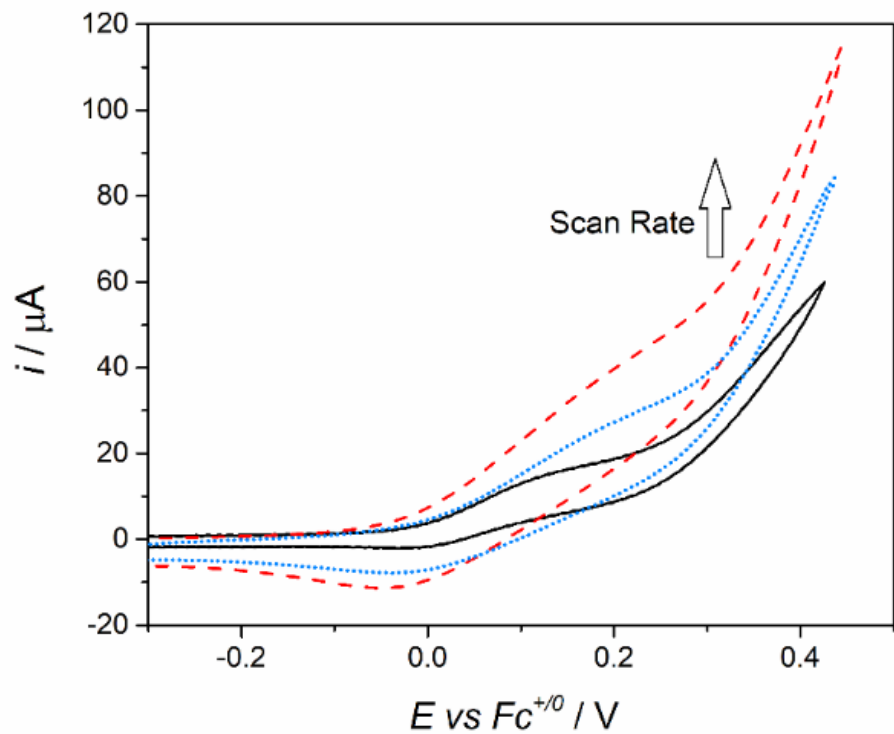


Figure A3.5.3.2 Top: CVs of the solution at the end of a bulk electrolysis experiment (6.1 C charge passed, $1 \times 10^{-6} \text{ mol } \mathbf{2a}$) with different scan rates. Solid black: 100 mV s^{-1} , dotted blue: 500 mV s^{-1} and dashed red: 1000 mV s^{-1} . Bottom: Effect of NH_3 addition on the anodic current in the solution after the electrolysis (scan rate 100 mV s^{-1}). (a) CV of the solution after BE is complete, (b) current recovery after NH_3 is bubbled through the solution in (a), and (c) CV of the solution before electrolysis. $A = 0.07 \text{ cm}^2$.

A3.5.4. Quantification of the Gaseous Products of the Electrolysis in the Headspace

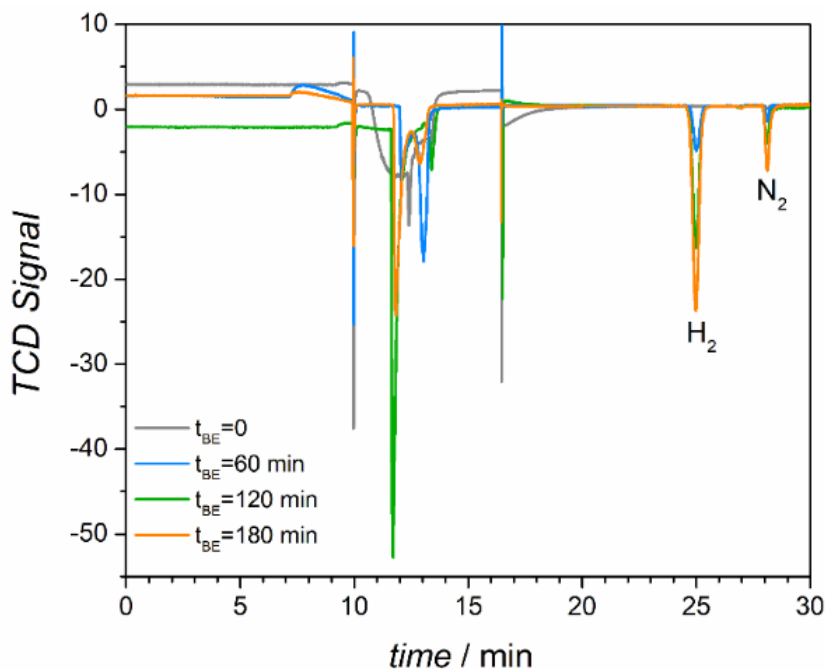


Figure A3.5.4.1 Full gas chromatograms from 100 microliter injections of cell headspace gases during electrolysis. (i) Before electrolysis ($t=0$), and after (blue) 60 min, (green) 120 min, and (orange) 180 min of electrolysis. The two peaks between 10 and 15 min are THF and NH_3 . The baselines are superimposed on top of each other for the time $17 \text{ min} < t < 30 \text{ min}$ window.

Prior to the experiment, the ratio of $\text{N}_2:\text{O}_2$ in the lab air was obtained by injecting 100 μL volumes of air to the instrument and finding the peak integral ratios. For the BE experiments discussed in 3.4.2, the $\text{N}_2:\text{O}_2$ ratio was found to be 2.98. The peak integrals for N_2 in the cell headspace samples were corrected for leaks and N_2 residuals in argon gas according to equation A1,

$$\text{N}_2(\text{sample})_{\text{corr.}} = \text{N}_2(\text{sample}) - \text{N}_2(\text{blank}) - \left[\text{O}_2(\text{sample}) \cdot \frac{\text{N}_2(\text{air})}{\text{O}_2(\text{air})} \right] \quad (\text{A1})$$

Where the $\text{N}_2(\text{sample})$ is the peak area of N_2 measured in the injection, $\text{N}_2(\text{blank})$ is the nitrogen gas present in the headspace before the electrolysis begins ($=0.88$), $\text{O}_2(\text{sample})$ is the oxygen observed in the sample injection which is coming in to the cell through leakage over time, and the

$\frac{N_2(\text{air})}{O_2(\text{air})}$ is the 2.98 that was obtained experimentally. The term in the bracket in equation A1 is to eliminate the amounts of N_2 that is brought in to the cell via air leaks. No correction was applied to H_2 signals since no H_2 was present in the air and blank samples.

Table A3.5.4.1. Actual signals obtained for each gas and the corrected signals for N_2 (in the gray-shaded column).

Duration of Electrolysis (min)	Peak Integrals			
	H_2	O_2	N_2	Corrected N_2
t=0	0	0	0.88	0
t=60	135.38	1.06	12.05	8.01
t=120	286.51	1.18	19.52	15.12
t=180	550.28	1.72	34.95	28.95

The H_2 and corrected N_2 signals were converted to the number of moles in the 100 μL injections using the calibration lines that were obtained for each gas (Chapter 2). The number of moles of each gas was then back-calculated for the 6.5 mL headspace of the BE cell that was employed for the experiment. Faradaic efficiencies (FE) were calculated by dividing the theoretical number of moles of each gas (based on the transferred charge) by their corresponding experimental values. Results are shown in Table A3.5.4.2.

Table A3.5.4.2. Results of the Electrolysis Experiment.^a

Duration of electrolysis	Charge passed (C)	Measured in Headspace		$H_2:N_2$	% FE	
		H_2 (μmol)	N_2 (μmol)		H_2	N_2
60 min	3.7	8.9	3.8	2.34	46.8	59.3
120 min	6.8	19.0	7.0	2.71	54.2	59.8
180 min	9.1	36.5	13.4	2.72	77.6	86.0

^a 6.8×10^{-6} mol **2a**

Two other BE experiments were also performed, and the results were analyzed in the same way:

Table A3.5.4.3. Results of the Electrolysis Experiments #2 and #3.

Experiment	Duration of electrolysis	Charge passed (C)	Measured in Headspace		H ₂ : N ₂	% FE	
			H ₂ (μmol)	N ₂ (μmol)		H ₂	N ₂
#2 ^a	120 min	7.2	29.5	11.2	2.63	79.0	90.3
#3 ^b	240 min	8.0	32.4	13.8	2.67	78.2	87.6

^a 5.9×10^{-6} mol **2a**, ^b 5.6×10^{-6} mol **2a**

A3.5.5. Microscopic Examination of the Surface of the Glassy Carbon Electrode

The surface of the working electrode was examined with XPS and EDS for possible precipitation of catalytic layers.

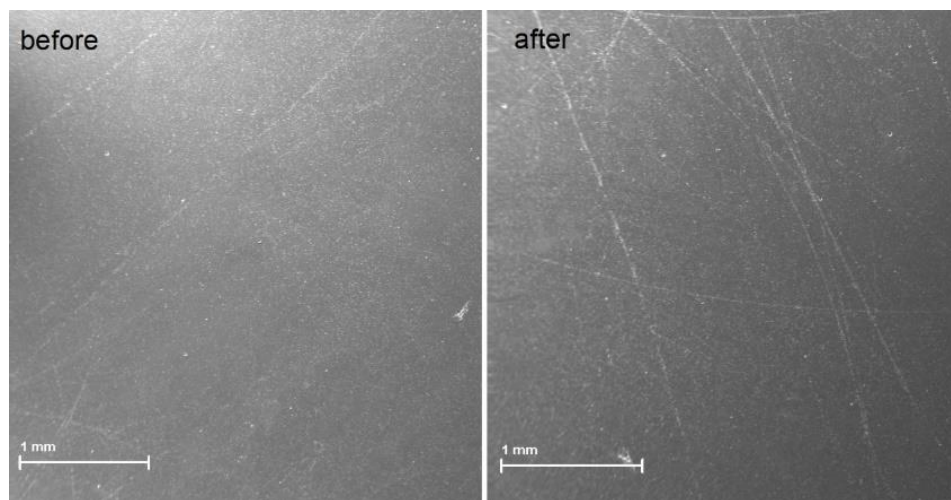


Figure A3.5.5.1 SEM images of the glassy carbon electrode before and after being used in the electrolysis.

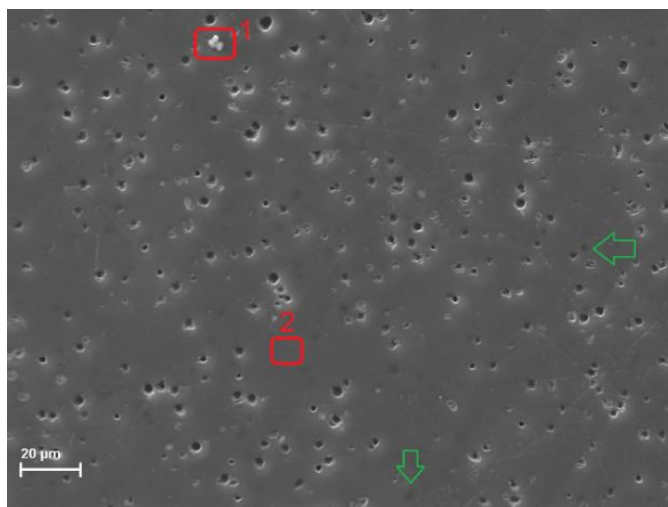
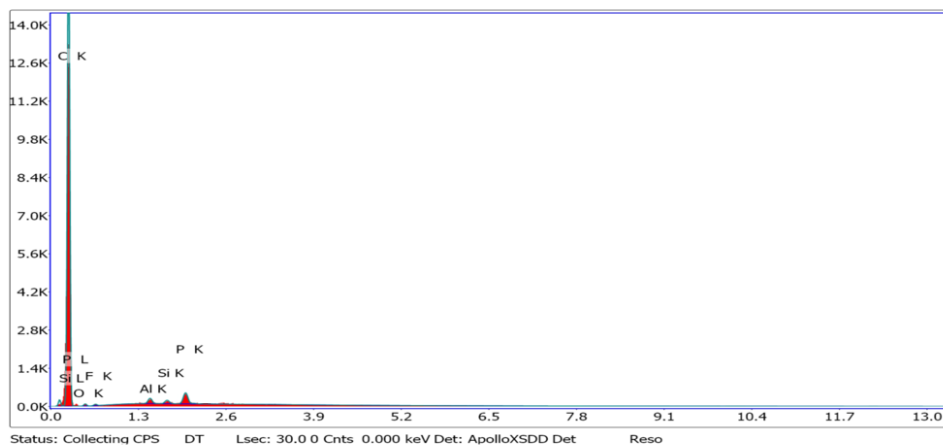


Figure A3.5.5.2 A more magnified SEM image of the working electrode after the electrolysis. The pores in the electrode were present before the electrolysis and are remains of the unknown history of various uses. The green arrows show that the pores are not only on the surface but are visible underneath the surface. These buried pores may be exposed in the future upon polishing. The areas 1 and 2 are selected for EDS measurements.

kV: 20 Mag: 20 Takeoff: 33 Live Time(s): 30 Amp Time(μs): 3.2 Resolution:(eV)125.9



kV: 20 Mag: 200 Takeoff: 33.1 Live Time(s): 30 Amp Time(μs): 3.2 Resolution:(eV)125.9

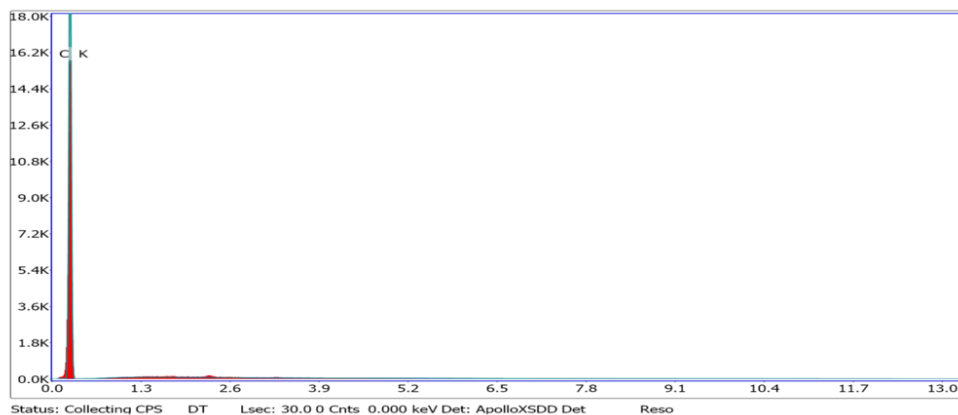


Figure A3.5.5.3 EDS analysis of selected areas 1 (top) and 2 (bottom). Al, P, and F are probably from polishing paste and PF_6 salts. The source of Si and oxygen is probably the silicon grease.

A3.5.6. Data of the Double and Single Labeling Experiments

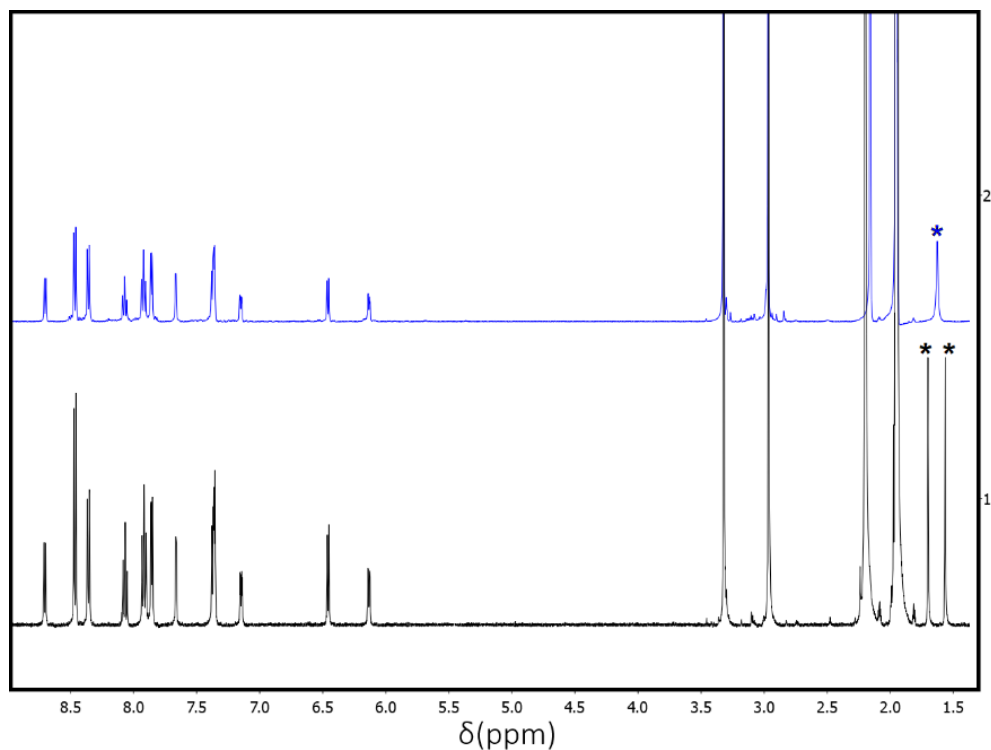


Figure A3.5.6.1 ^1H NMR spectra for unlabeled **2a** (top, blue) and ^{15}N -**2a** (bottom, black) in acetonitrile- d_3 . The starred resonances are associated with the coordinated NH_3 ligand.

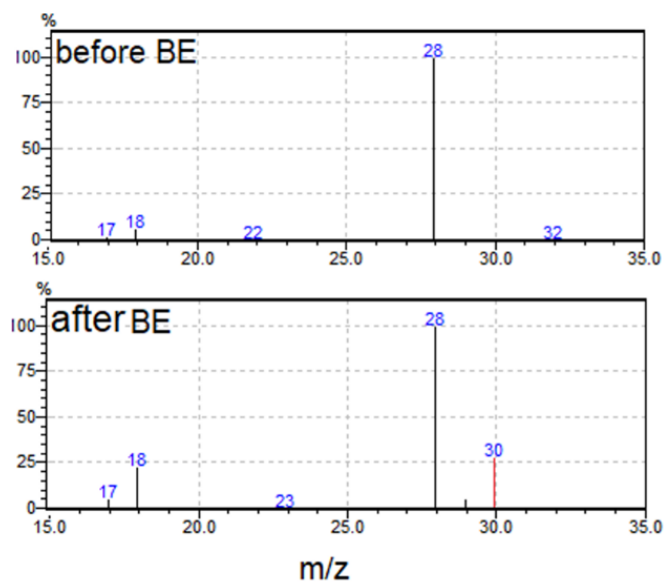


Figure A3.5.6.2 Mass spectrometry data for two injections of headspace mixture of the bulk electrolysis experiments of $^{15}\text{NH}_3$ solutions before and after passing 3.58 C.

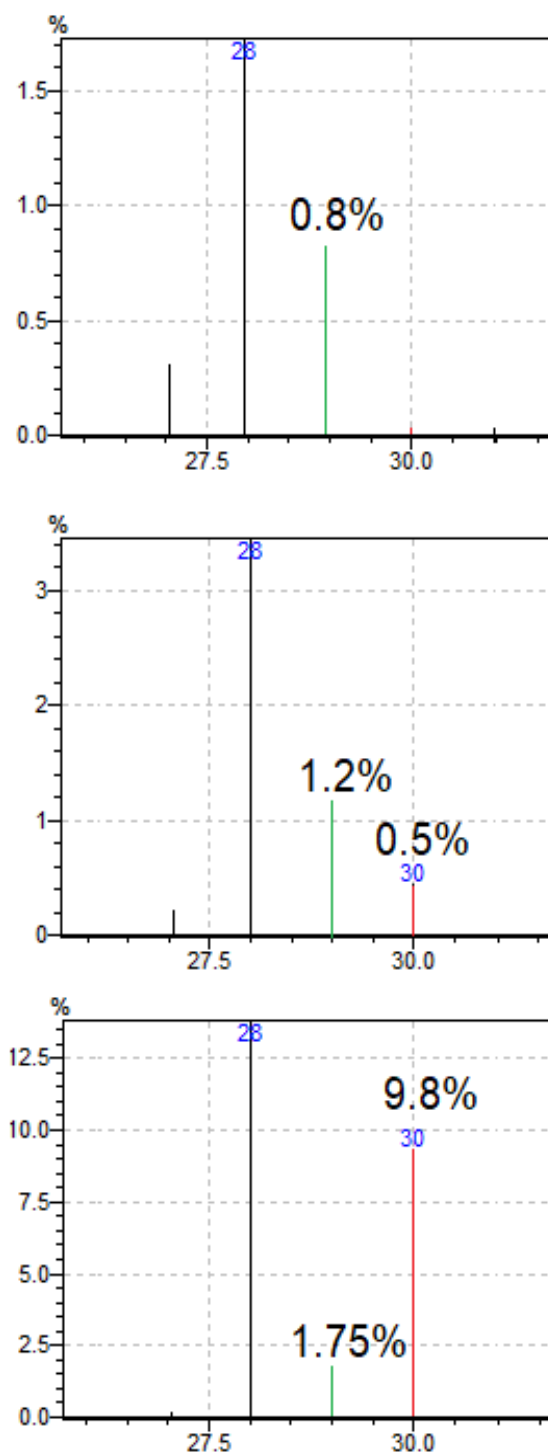


Figure A3.5.6.3 MS spectra for the injections of the headspace mixture of an electrolysis experiment when $^{15}\text{NH}_3$ was electrolyzed in the presence of 4.5×10^{-5} M **2a**. Top: The headspace of the blank cell. The peak at $m/z=29$ (green) shows an abundance of 0.8% relative to N_2 ($m/z=28$), the natural abundance of $m/z=29$ in the air. Middle: The percent of $m/z=29$ has increased to 1.2% after passing 1.34 C. $m/z=30$ (red) is also growing. Bottom: After 6.47 C charge is passed the generated N_2 is dominantly $m/z=30$

REFERENCES

REFERENCES

- (1) Murphy, W. R.; Takeuchi, K.; Barley, M. H.; Meyer, T. J. *Inorg. Chem.* **1986**, 25 (9), 1041–1053.
- (2) Wasylenko, D. J.; Ganesamoorthy, C.; Henderson, M. A.; Koivisto, B. D.; Osthoff, H. D.; Berlinguette, C. P. *J. Am. Chem. Soc.* **2010**, 132 (45), 16094–16106.
- (3) Takeuchi, K.; Thompson, M.; Pipes, D. W.; Meyer, T. J. *Inorg. Chem.* **1984**, 23 (13), 1845–1851.
- (4) Ridd, M. J.; Keene, F. R. *J. Am. Chem. Soc.* **1981**, 103 (19), 5733–5740.
- (5) Bard, A. J.; Faulkner, L. R. *Electrochemical Methods: Fundamentals and Applications*, 2nd Edition, Wiley Global Education, 2000.
- (6) Yagi, M.; Tajima, S.; Komi, M.; Yamazaki, H. *Dalt. Trans.* **2011**, 40, 3802–3804.
- (7) Hetterscheid, D. G. H.; Reek, J. N. H. *Angew. Chem. Int. Ed* **2012**, 51, 9740–9747.
- (8) Habibzadeh, F.; Miller, S. L.; Hamann, T. W.; Smith, M. R. *Proc. Natl. Acad. Sci.* **2019**, 3 (1), 2–6.

CHAPTER 4: THE RU(III) INTERMEDIATE

With the redox potential of $[\text{Ru}(\text{trpy})(\text{dmabpy})\text{NH}_3]^{+2}$ (**2a**) being more negative than the direct oxidation of ammonia at the glassy carbon electrode in THF, we can conclude that the oxidation of Ru(II) to Ru(III) occurs under catalytic conditions to give the first intermediate of the catalytic cycle, $[\text{Ru}(\text{trpy})(\text{dmabpy})\text{NH}_3]^{3+}$ (**2b**). In the presence of a base, such as NH_3 , $[\text{Ru}(\text{trpy})(\text{dmabpy})\text{NH}_3]^{3+}$ is unstable and reacts further to give other intermediates, but it eventually goes back to $[\text{Ru}(\text{trpy})(\text{dmabpy})\text{NH}_3]^{+2}$ at the end of the cycle. However, when the electrolysis was performed in the absence of a base, $[\text{Ru}(\text{trpy})(\text{dmabpy})\text{NH}_3]^{3+}$ was produced upon one-electron oxidation of $[\text{Ru}(\text{trpy})(\text{dmabpy})\text{NH}_3]^{+2}$ and, was isolated as a green solid in dichloromethane (DCM), with Ag^+ ion serving as the sacrificial oxidant in a separated compartment. Alternatively, $[\text{Ru}(\text{trpy})(\text{dmabpy})\text{NH}_3]^{+3}$ was synthesized from $[\text{Ru}(\text{trpy})(\text{dmabpy})\text{NH}_3]^{+2}$ using a chemical oxidant in DCM and was thoroughly characterized using a variety of techniques.

4.1. Synthesis of $[\text{Ru}(\text{trpy})(\text{dmabpy})\text{NH}_3](\text{PF}_6)_3$, (2b**)**

4.1.1. Electrochemical Synthesis

Exhaustive oxidation of solutions containing $[\text{Ru}(\text{trpy})(\text{dmabpy})\text{NH}_3]^{+2}$ in DCM at the applied constant potential of 0.35 V versus $\text{Fc}^{+/0}$ afforded a green precipitate adhered to the surface of the glassy carbon electrode. To perform this experiment, a 1.2×10^{-3} M solution of $[\text{Ru}(\text{trpy})(\text{dmabpy})\text{NH}_3]^{+2}$ in DCM was prepared with 0.1 M $[\text{Bu}_4\text{N}](\text{PF}_6)$ serving as the supporting electrolyte. The counter electrode was prepared by inserting a freshly polished silver coil in a solution of 0.5 M AgPF_6 in acetonitrile, containing 0.1 M $[\text{Bu}_4\text{N}](\text{PF}_6)$. The CE silver coil and solution were separated from the electrolysis solution using a fritted glass membrane (Figure

4.1.1). A glassy carbon plate with a large surface area was used as the working electrode, and the solution was stirred during the electrolysis.

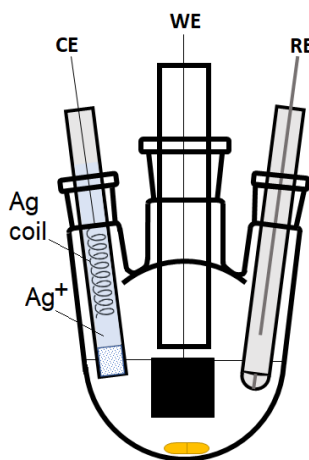


Figure 4.1.1 The diagram of the three-electrode electrolysis cell used for chemical oxidation of **2a** to **2b**.

Every 10 min the glassy carbon electrode was removed from the cell, rinsed with fresh DCM and the solid precipitate was scraped off the electrode into a centrifuge tube. At the end of the experiment, 5 mL fresh DCM was added to the collected solid in the centrifuge tube, the tube was placed in a centrifuge machine and was spun at a speed of 60 rpm for 20 min. Then the solvent was slowly decanted, and the rinsing step was repeated three times. The washed solid was then dried under vacuum overnight. Since these experiments were never performed to completion, *i.e.*, to the point where all $[\text{Ru}(\text{trpy})(\text{dmabpy})\text{NH}_3]^{+2}$ were oxidized, a yield was not calculated.

4.1.2. Chemical Synthesis

Addition of 1 equiv. of the chemical oxidant tris(*para*-bromophenyl) ammonium cation radical, $[\text{N}(\text{pBr-ph})_3]\text{PF}_6$, to solutions of $[\text{Ru}(\text{trpy})(\text{dmabpy})\text{NH}_3]^{+2}$ in DCM yielded a green precipitate after 30 min of stirring under nitrogen. The solid was collected on a Fine glass filter and was rinsed several times with fresh DCM. For a starting solution of 1.13×10^{-2} M

[Ru(trpy)(dmabpy)NH₃](PF₆)₂ (100 mg, 1.13×10⁻⁴ mol **2a** in 10 mL DCM) a yield of 94% (110 mg, 1.06×10⁻⁴ mol **2b**) was obtained.

4.2. Characterization of **2b**

4.2.1. Proton NMR

Complex [Ru(trpy)(dmabpy)NH₃]⁺³ as a hexafluorophosphate salt is not soluble in dry THF or DCM and reacts (judged by the color change from green to orange upon mixing) with electron donating solvents such as methanol or dimethyl sulfoxide (DMSO). On the other hand, it fully dissolves in solvents with slight acidic properties such as dry acetonitrile and nitromethane (NM). However, ¹H NMR experiments show that while the solutions of [Ru(trpy)(dmabpy)NH₃]⁺³ in dry acetonitrile remain green, the coordinated NH₃ is replaced by the solvent to some extent (See Appendix, Figure A4.1.1). Addition of a small concentration of nitric acid to the acetonitrile prevents ligand displacement and affords clear ¹H NMR spectra of [Ru(trpy)(dmabpy)NH₃]⁺³ that reflect the paramagnetic nature of the complex (See Appendix, Figure A4.1.2). **¹H NMR (500 MHz, 0.1% HNO₃/ CD₃CN):** δ 90.07 (s, 6 H), 61.54 (s, 3 H), 52.58 (s, 2 H), 48.85 (s, 6 H), 41.50 (s, 2 H), 12.99 (s, 1 H), 9.34 (s, 2 H), 7.99 (s, 2 H), 4.67 (s, 2 H), -18.20 (s, 1 H), -20.53 (s, 1 H), -23.14 (s, 1 H), -23.31 (s, 1 H), -35.59 (s, 1 H), -43.30 (s, 1 H).

4.2.2. Elemental Analysis

The results of CHN analysis for both electrochemically and chemically made [Ru(trpy)(dmabpy)NH₃]⁺³ samples are identical and are as follows: Anal. Calcd. for C₂₉H₃₂N₈P₃F₁₈Ru: C, 33.81; H, 3.13; N, 10.88. Found: C, 33.65; H, 3.10; N, 10.98.

4.2.3. Magnetic Susceptibility

The Evans method was used to calculate the effective magnetic moment, μ_{eff} , for $[\text{Ru}(\text{trpy})(\text{dmabpy})\text{NH}_3]^{+3}$ using ferrocene as the standard.¹ A standard solution of saturated ferrocene in nitromethane- d_3 was prepared and transferred to a glass capillary. The capillary tube was sealed and inserted into an NMR tube containing 0.40 ml nitromethane- d_3 . A sample solution was prepared by dissolving 3.0 mg of $[\text{Ru}(\text{trpy})(\text{dmabpy})\text{NH}_3](\text{PF}_6)_3$ (2.91 μmol **2b**) in 0.25 mL nitromethane- d_3 . 240 μL of this sample solution was transferred to the NMR tube using a 100 μL gas-tight glass syringe and the NMR spectrum was acquired after the addition. The shift in the ferrocene ^1H resonance upon addition of **2b** was measured (Hz) and used to calculate the molar magnetic susceptibility (χ_M) using equation 1.

$$\chi_M = \frac{3000\Delta\nu}{4\pi\nu_0 C} - \chi_D \quad (1)$$

Where $\Delta\nu$ is the observed frequency shift of the reference resonance (Hz), ν_0 is the spectrometer frequency (500 MHz), and C is the concentration of $[\text{Ru}(\text{trpy})(\text{dmabpy})\text{NH}_3]^{+3}$ (mol L^{-1}). The experimental value for $\Delta\nu$ was 10.25 Hz for the $4.37 \times 10^{-6} \text{ M}$ solution of the sample in the NMR tube (Figure 4.2.1).

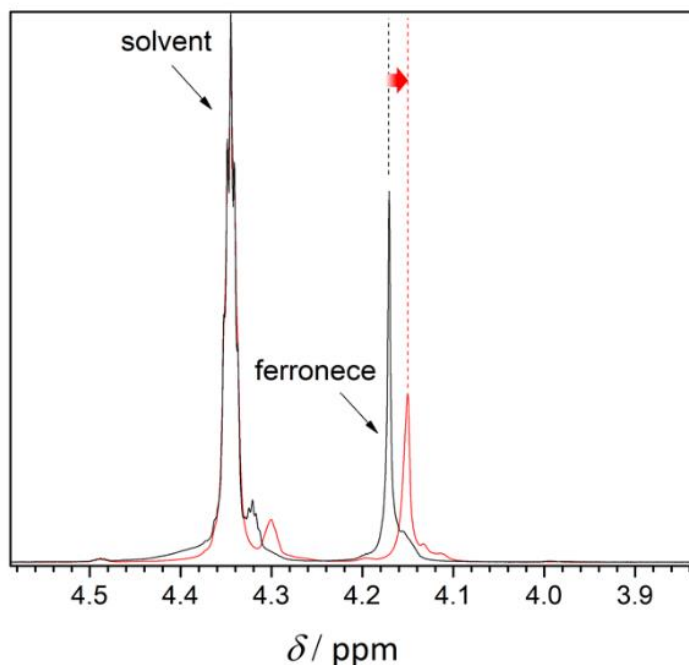


Figure 4.2.1 The ^1H NMR resonance shift observed for the standard ferrocene after addition of paramagnetic **2b**.

The diamagnetic contribution to the magnetic susceptibility, χ_D , was calculated using tabulated Pascal's constants, as shown below.²

$$\chi_D(\text{Ru}^{3+}) = -23 \times 10^{-6} \text{ mol}^{-1} \quad (2)$$

$$\chi_D(\text{tpy}) = 15\chi_D(\text{C}_{\text{ring}}) + 3\chi_D(\text{N}_{\text{ring}}) + 11\chi_D(\text{H}) + 3\lambda(\text{py}) + 2\lambda(\text{Ar} - \text{Ar}) = -139.14 \times 10^{-6} \text{ mol}^{-1} \quad (3)$$

$$\chi_D(\text{dmabpy}) = \chi_D(\text{bpy}) + 2\chi_D(\text{C}) + 4\chi_D(\text{N}) + 12\chi_D(\text{H}) + 4\lambda(\text{Ar} - \text{CNH}_2) = -180.44 \times 10^{-6} \text{ mol}^{-1} \quad (4)$$

$$\chi_D(\text{NH}_3) = -18 \times 10^{-6} \text{ mol}^{-1} \quad (5)$$

$$\chi_D(\text{Complex 2b}) = \chi_D(\text{Ru}^{3+}) + \chi_D(\text{tpy}) + \chi_D(\text{dmabpy}) + \chi_D(\text{NH}_3) \quad (6)$$

$$\chi_D(\text{Complex 2b}) = -360.58 \times 10^{-6} \text{ mol}^{-1} \quad (7)$$

The appropriate substitutions in eq. 1 yield

$$\chi_M = 1110.0 \times 10^{-6} - (-360.58 \times 10^{-6}) = 1470.5 \times 10^{-6} \text{ mol}^{-1} \quad (8)$$

The effective magnetic momentum, μ_{eff} , was therefore determined directly from χ_M according to equation 9 with $T = 21\text{ }^{\circ}\text{C}$ for the sample temperature.

$$\mu_{eff} = 2.828\sqrt{\chi_M T} = 1.84\ \mu_B \quad (9)$$

The experimental value for μ_{eff} is slightly higher than the spin-only value of $1.73\ \mu_B$ for one unpaired electron and is typical for low spin d^5 complexes.³

4.2.4. Electrochemistry

CVs of $[\text{Ru}(\text{trpy})(\text{dmabpy})\text{NH}_3]^{+3}$ in NM show a reversible redox process at $E_{1/2} = 0.085\text{ V}$ versus $\text{Fc}^{+/0}$, identical to the redox potential of $[\text{Ru}(\text{trpy})(\text{dmabpy})\text{NH}_3]^{+2}$ in NM (Figure 4.2.2, top). NM acts as an excellent solvent for electrochemical studies of $[\text{Ru}(\text{trpy})(\text{dmabpy})\text{NH}_3]^{+3}$ since it provides a very wide working oxidation potential window. When the scanning potential in the cyclic voltammetry experiments of $[\text{Ru}(\text{trpy})(\text{dmabpy})\text{NH}_3]^{+3}$ in NM are extended to almost 1.5 V versus $\text{Fc}^{+/0}$, another redox wave is evident (Figure 4.2.2, bottom, wave II). Hydrodynamic linear scan voltammograms (See Appendix, Figure A4.3.1) of $[\text{Ru}(\text{trpy})(\text{dmabpy})\text{NH}_3]^{+3}$ in NM reveal that the first redox process corresponds to the reversible reduction of $[\text{Ru}(\text{trpy})(\text{dmabpy})\text{NH}_3]^{+3}$ to $[\text{Ru}(\text{trpy})(\text{dmabpy})\text{NH}_3]^{+2}$, while the second process is an oxidative process that was assigned to quasi-reversible one-electron oxidation of Ru(III) to Ru(IV) which was not observable in solvents with a smaller potential window such as THF or dichloromethane.

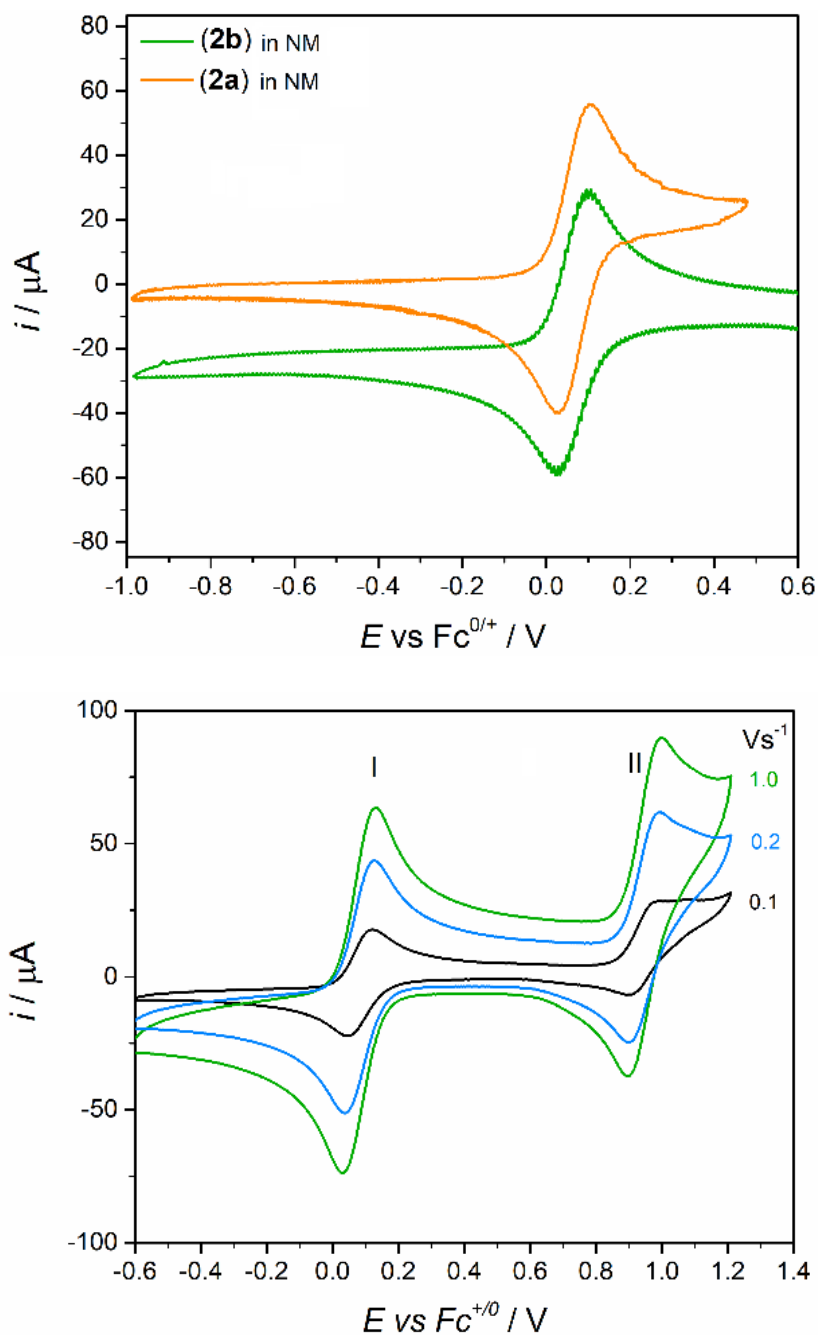


Figure 4.2.2 Top: CV of $4.5 \times 10^{-3} \text{ M}$ **2b** (green) compared to the CV of $4.12 \times 10^{-3} \text{ M}$ **2a** (orange) in NM. Both complexes appear at the same $E_{1/2}$. Bottom: Extended potential window CVs of $2.10 \times 10^{-3} \text{ M}$ **2b** in NM shown for three scan rates. Here a second oxidation process is seen at 0.95 V vs. $\text{Fc}^{+/0}$ (labeled as II).

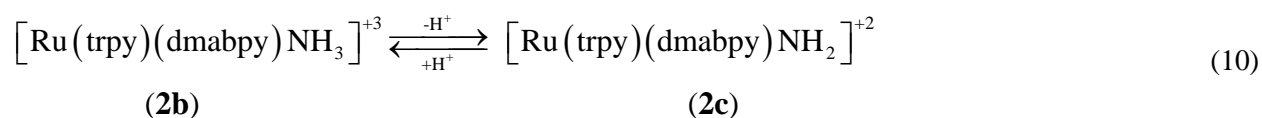
Bulk electro-reduction of $[\text{Ru}(\text{trpy})(\text{dmabpy})\text{NH}_3]^{+3}$ back to $[\text{Ru}(\text{trpy})(\text{dmabpy})\text{NH}_3]^{+2}$ was also performed in THF, using a similar cell diagram as shown in Figure 4.1.1, to further investigate the

relation between these two complexes. In this case, the counter electrode was modified to a platinum wire immersed in a solution of decamethyl ferrocene (Me_{10}Fc) in acetonitrile ($E_{1/2} = -0.51$ V versus $\text{Fc}^{+/0}$, See Appendix, Figure A4.4.1), so that the oxidation of decamethyl ferrocene occur during the reduction of $[\text{Ru}(\text{trpy})(\text{dmabpy})\text{NH}_3]^{+3}$. The glassy carbon plate working electrode was replaced with a rotating disk electrode after 1000, 2000 and 5000 s of electrolysis while a slow flow of Ar was maintained to keep the solution from exposure to air, and hydrodynamic CVs were taken to track the changes in each complex after electrolysis. However, due to the low solubility of $[\text{Ru}(\text{trpy})(\text{dmabpy})\text{NH}_3]^{+3}$ in THF, the hydrodynamic currents associated with $[\text{Ru}(\text{trpy})(\text{dmabpy})\text{NH}_3]^{+3}$ do not reflect the actual concentration. 1.03 equivalent of electrons were transferred for the full conversion of $[\text{Ru}(\text{trpy})(\text{dmabpy})\text{NH}_3]^{+3}$ to $[\text{Ru}(\text{trpy})(\text{dmabpy})\text{NH}_3]^{+2}$ along with the color of the solution changing to orange. The $E_{1/2}$ of the final product is also the same as what is measured for $[\text{Ru}(\text{trpy})(\text{dmabpy})\text{NH}_3]^{+2}$ in the THF solvent (See Appendix, Figures A4.4.2 and A4.4.3).

4.3. Deprotonation of $[\text{Ru}(\text{trpy})(\text{dmabpy})\text{NH}_3]^{+3}$

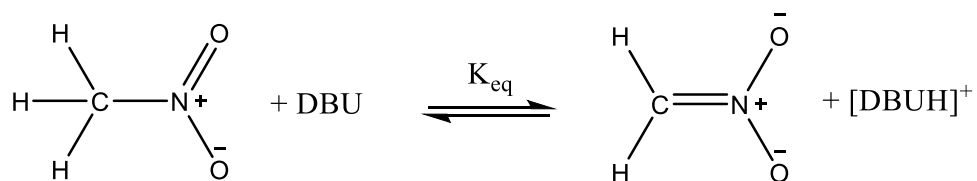
Addition of NH_3 to solutions of $[\text{Ru}(\text{trpy})(\text{dmabpy})\text{NH}_3]^{+3}$ in NM (or suspensions in case of THF) leads to a rapid reaction which changes the color of the solution (or the suspension in case of THF) from green to orange. Therefore, $[\text{Ru}(\text{trpy})(\text{dmabpy})\text{NH}_3]^{+3}$ could not be detected from the solution under catalytic conditions where the concentration of NH_3 is very large because the presence of the base promotes further reactions. As discussed in chapter 1, the acidity of the complexes increases with the oxidation state of the ruthenium metal center. The acidic $[\text{Ru}(\text{trpy})(\text{dmabpy})\text{NH}_3]^{+3}$ (compared to $[\text{Ru}(\text{trpy})(\text{dmabpy})\text{NH}_3]^{+2}$) is expected to undergo deprotonation in the presence of a base of suitable strength. With $[\text{Ru}(\text{trpy})(\text{dmabpy})\text{NH}_3]^{+2}$ having

a oxidation potential within the applied potential for the catalytic electrolysis experiments, it is speculated that the first step towards N₂ formation, is the one electron oxidation of [Ru(trpy)(dmabpy)NH₃]⁺² to [Ru(trpy)(dmabpy)NH₃]⁺³. The latter, **2b**, is stable in the absence of a base and was isolated as discussed earlier. The reversibility of the [Ru(II/III)NH₃]^{2+/3+} couple in THF suggests that the pK_a of [Ru(trpy)(dmabpy)NH₃]⁺³ is not low enough to be deprotonated by THF and changing the electrolyte from [Bu₄N](PF₆) to more acidic [NH₄](PF₆) does not affect the *E*_{1/2}. However, when a base such as NH₃ is added, [Ru(trpy)(dmabpy)NH₃]⁺³ undergoes deprotonation to give an amido complex, [Ru(trpy)(dmabpy)NH₂]⁺², **2c**.



The acid-base equilibrium constant for reaction (10) depends on the strength and concentration of the proton acceptor and the nature of the solvent due to its effects on the K_b of the base. Relatively acidic [Ru(trpy)(dmabpy)NH₂]⁺³ is unstable when NH₃ is present in the solution and reacts further to give other intermediates that were formed *via* nucleophilic attack of the free NH₃ (*vide infra*). However, with a suitable adjustment of the type and concentration of the base, as well as the nature of the solvent it might be possible to observe [Ru(trpy)(dmabpy)NH₂]⁺². To do so, the sterically hindered 1,8-diazabicyclo [5.4.0] undec-7-ene (DBU) was selected as the noncoordinating proton acceptor to prevent possible nucleophilic/electrophilic reactions since the bulky structure of DBU limits the approach of the base to the electron deficient intermediates which leads to the formation of other products. Nitromethane was chosen as the solvent due to complete solubility of [Ru(trpy)(dmabpy)NH₃]⁺³. Being an acidic solvent, NM may compete with [Ru(trpy)(dmabpy)NH₃]⁺³ in losing protons to DBU. In solutions containing DBU and NM, the

amounts of deprotonated DBU is defined by the equilibrium constant of the reaction represented below:



Scheme 4.1 The acid-base equilibrium between DBU ($\text{pK}_{\text{a}} = 11.9$ (DMSO)) and NM ($\text{pK}_{\text{a}} = 17.2$ (DMSO)). pK_{a} values from Refs. 14 and 15. Based on the pK_{a} values, this equilibrium is more towards the reactants. However, a slight yellow color is observed when DBU is added to NM, which might indicate the some reaction occurs between the two.

Direct infusion of a diluted solution consisting of $[\text{Ru}(\text{trpy})(\text{dmabpy})\text{NH}_3]^{+3}$ in anhydrous nitromethane mixed with sub-stoichiometric concentrations of DBU to an ESI⁺ QTOF mass spectrometer ⁽¹⁾ shows the presence of four ruthenium-based species (Figure 4.3.1). For this experiment stock solutions of 1.16×10^{-3} M $[\text{Ru}(\text{trpy})(\text{dmabpy})\text{NH}_3]^{+3}$ (6 mg in 5 mL NM) and 1.34×10^{-3} M DBU (2 μL DBU in 10 mL NM) were prepared in the glove box. 4 mL of the DBU solution was diluted to a final volume of 5 mL to give a secondary stock solution of 1.07×10^{-3} M. 1 μL of each of these solutions were transferred to a 1 mL volumetric flask containing NM and then the volume was made up by adding fresh NM. The final concentrations for $[\text{Ru}(\text{trpy})(\text{dmabpy})\text{NH}_3]^{+3}$ and DBU were 1.16×10^{-6} M and 1.072×10^{-6} M, respectively (DBU:**2b** = 0.92:1). 100 μL of this solution was then diluted to 1 mL in a glass vial equipped with a septum cap, the vial was wrapped with Teflon tape and was taken to the mass spectrometer, and the content was directly injected to the instrument.

¹ Positive mode electrospray ionization (ESI⁺) quadrupole time-of-flight (QTOF) mass spectrometer

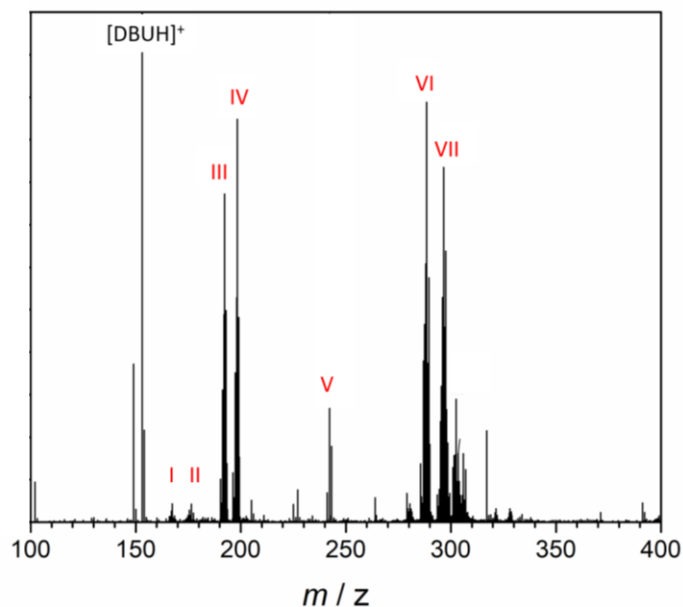


Figure 4.3.1 Total ion spectrum obtained for a solution containing 1.16×10^{-7} M **2b** and 1.072×10^{-7} M DBU in NM.

Peaks 1 and II, and VI and VII are related to doubly charged species, while peaks III and IV are triply charged species. Peak V is matching with the dmabpy ligand, which comes off in the mass analyzer. The dmabpy-less complexes are seen as in signals I and II. The mass to charge (m/z) values observed for ruthenium species that are expected to be existent in the solution and their assignments to observed signals III, IV, VI and VII are listed in Figure 4.3.2. For other assignments see Appendix, A4.5.

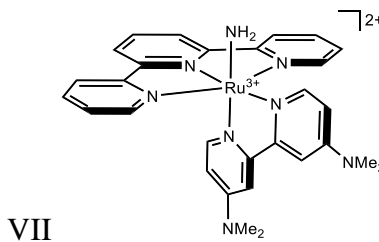
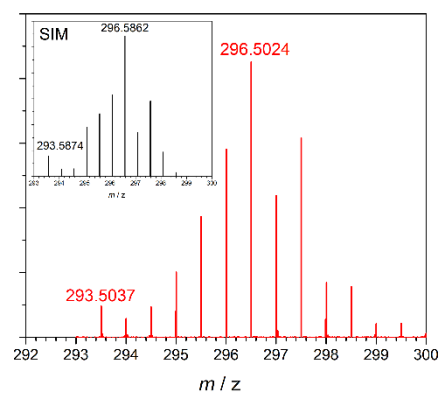
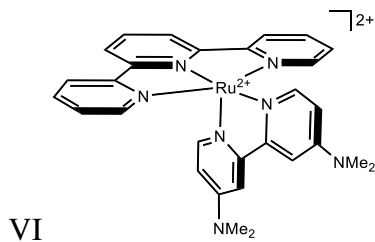
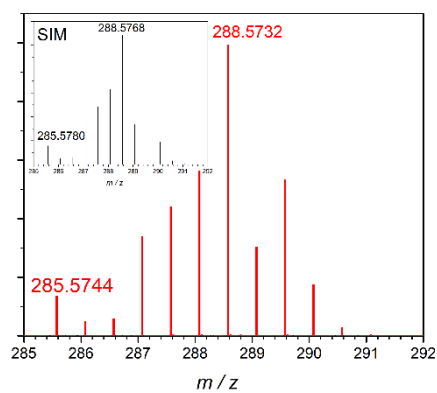
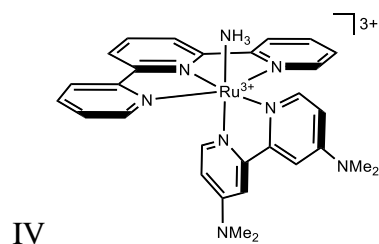
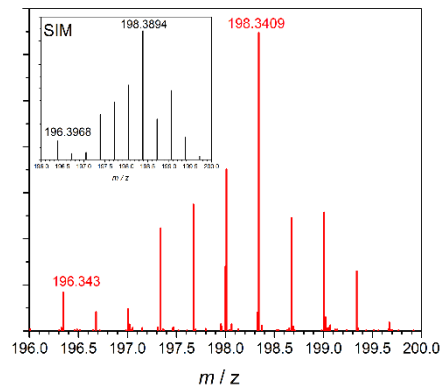
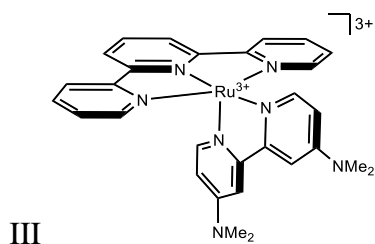
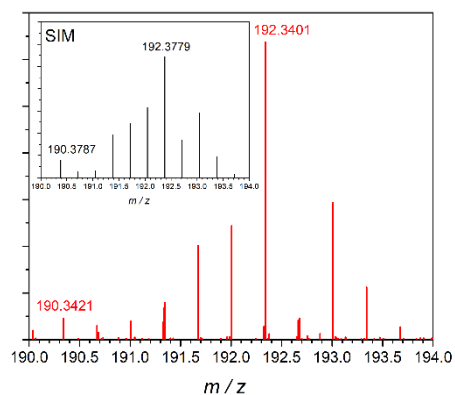


Figure 4.3.2 Assignments to four selected m/z values III, V, VI, and VII. The spectra in red are the experimentally obtained spectra and the inset shows the simulated spectra.

Direct infusion techniques, even when integrated with high-resolution mass analyzers such as QTOF, suffer from inevitable matrix effects since the samples are infused together without separation. This may result in reduced sensitivity and vague accuracy for analyte identification.⁴ Nevertheless, direct infusion of control samples containing $[\text{Ru}(\text{trpy})(\text{dmabpy})\text{NH}_3]^{+2}$ and $[\text{Ru}(\text{trpy})(\text{dmabpy})\text{NH}_3]^{+3}$ in NM result in the formation of ion fragments IV and VI, respectively (See Appendix, A4.5). Thus, III and VII are species generated under experimental conditions, *i.e.*, presence of DBU. These peaks are close to fragmentations of $[\text{Ru}(\text{trpy})(\text{dmabpy})\text{NH}_2]^{+2}$, the deprotonated form of $[\text{Ru}(\text{trpy})(\text{dmabpy})\text{NH}_3]^{+3}$ in the presence of a base, so they were cautiously assigned to $[\text{Ru}(\text{trpy})(\text{dmabpy})\text{NH}_2]^{+2}$.

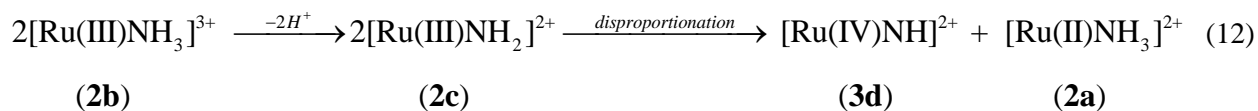
4.4. Regeneration of 2a from 2b

One of the products detected by mass spectrometry was $[\text{Ru}(\text{trpy})(\text{dmabpy})\text{NH}_3]^{+2}$. Regeneration of $[\text{Ru}(\text{trpy})(\text{dmabpy})\text{NH}_3]^{+2}$ upon treatment of $[\text{Ru}(\text{trpy})(\text{dmabpy})\text{NH}_3]^{+3}$ with a base has a significant role in elucidating the reaction mechanism. Similar results have already been observed and reported for ruthenium catalysts used for water oxidation. According to Shaffer *et al.*, for two ruthenium complexes $[\text{Ru}^{\text{II}}(\text{trpy})(\text{bpm})(\text{OH}_2)]^{2+}$ and $[\text{Ru}^{\text{II}}(\text{trpy})(\text{bpz})(\text{OH}_2)]^{2+}$ (bpm= 2,2'-bipyrimidine, bpz= 2,2'-bipyrazine), addition of one equivalent of an oxidizing agent yielded $[\text{Ru}(\text{III})\text{OH}]^{2+}$ (polypyridyl ligands are omitted) as the dominant species even at low pHs.¹⁶ They further discussed that while the $\text{Ru}(\text{II})\text{OH}_2/\text{Ru}(\text{III})\text{OH}_2$ redox potential was relatively high due to the electron withdrawing effects of the bpm and bpz ligands, the oxidation of $[\text{Ru}(\text{III})\text{OH}]^{2+}/[\text{Ru}(\text{II})\text{O}]^{2+}$ occurred at lower potentials, a phenomenon that thermodynamically enables a rapid disproportionation reaction to take place following the formation of $[\text{Ru}(\text{III})\text{OH}]^{2+}$:



Coia *et al.* have also reported similar chemistry for $[\text{Os}(\text{trpy})(\text{bpy})\text{NH}_3]^{2+}$ in aqueous conditions with $\text{pH} \geq 10$.⁵

A redox disproportionation reaction is a reasonable rationale for the regeneration of $[\text{Ru}(\text{trpy})(\text{dmabpy})\text{NH}_3]^{+2}$ from $[\text{Ru}(\text{trpy})(\text{dmabpy})\text{NH}_3]^{+3}$ in the presence of a base (NH_3 or DBU) when a chemical oxidant is absent (polypyridyl ligands are omitted in eq. 12):



This reaction should show second-order kinetics in $[\text{Ru}(\text{trpy})(\text{dmabpy})\text{NH}_3]^{+3}$ and is easy to monitor by spectrophotometry since the electronic spectra of the reactant ($[\text{Ru}(\text{trpy})(\text{dmabpy})\text{NH}_3]^{+3}$) and one of the products ($[\text{Ru}(\text{trpy})(\text{dmabpy})\text{NH}_3]^{+2}$) is fully known. The Ru(IV)imido complex, $[\text{Ru}(\text{trpy})(\text{dmabpy})\text{NH}]^{+2}$, **3d**, is isoelectronic to analogous Ru(IV) oxo intermediates that are reported for catalytic water oxidation reactions. Huynh and Meyer, summarize the Ru(IV/III) redox behavior with pH in aqueous systems for $[\text{Ru}(\text{bpy})_2(\text{py})\text{H}_2\text{O}]^{2+}$ (py = pyridine) catalysts using Pourbaix diagrams as described briefly below:

At $\text{pH} = 0.8$, the redox couple is $\text{cis-}[\text{Ru}^{\text{IV}}(\text{bpy})_2(\text{py})(\text{O})]^{2+}/\text{cis-}[\text{Ru}^{\text{III}}(\text{bpy})_2(\text{py})(\text{H}_2\text{O})]^{3+}$. As the pH is increased above 0.85, the couple becomes $\text{cis-}[\text{Ru}^{\text{IV}}(\text{bpy})_2(\text{py})(\text{O})]^{2+}/\text{cis-}[\text{Ru}^{\text{III}}(\text{bpy})_2(\text{py})(\text{OH})]^{2+}$. At $\text{pH} = 12.8$, the pH-dependent Ru(IV/III) and pH-independent Ru(III/II) couples intersect. As the pH is increased further, $E_{1/2}$ of Ru(III/II) becomes more positive than the $E_{1/2}$ of Ru(IV/III) and $\text{cis-}[\text{Ru}^{\text{III}}(\text{bpy})_2(\text{py})(\text{OH})]^{2+}$ is unstable due to disproportionation. In this pH region, $\text{cis-}[\text{Ru}^{\text{III}}(\text{bpy})_2(\text{py})(\text{OH})]^{2+}$ is a stronger oxidant than $\text{cis-}[\text{Ru}^{\text{IV}}(\text{bpy})_2(\text{py})(\text{O})]^{2+}$ because of the pH dependence of the Ru(IV/III) couple.⁶ Stabilization of a higher oxidation state by metal-ligand

multiple bonding or change in pH can become sufficient, so $E^\circ(\text{VI/III}) < E^\circ(\text{III/II})$ for sequential couples, which leads to $\Delta E^\circ = E^\circ(\text{VI/III}) - E^\circ(\text{III/II}) < 0$ (E° is the formal redox potential). If ΔE° is negative, the intermediate oxidation state in adjacent couples is “missing” thermodynamically because it is unstable with respect to disproportionation, *e.g.*, $2\text{Ru(III)} \rightarrow \text{Ru(II)} + \text{Ru(IV)}$.⁶

Examples of isolated Ru(IV) oxo species are existent in the literature. For instance, addition of excess concentrations of $(\text{NH}_4)_2[\text{Ce}^{\text{IV}}(\text{NO}_3)_6]$, CAN, oxidant to solutions of $[\text{Ru}(\text{TPA})(\text{bpy})]^{2+}$ (TPA=*tris*(2-pyridyl- methyl)amine, Figure 4.4.1) in H_2O (pH=2) at room temperature afforded light green paramagnetic $[\text{Ru}^{\text{IV}}(\text{O})(\text{H}^+\text{TPA})(\text{bpy})]^{3+}$ through partial ligand dissociation.⁷ The product was isolated and the structure was determined by X-ray diffraction. The electronic absorption spectra of $[\text{Ru}^{\text{IV}}(\text{O})(\text{H}^+\text{TPA})(\text{bpy})]^{3+}$ was featureless within the wavelength window of 400 – 700 nm and its ESI⁺-MS spectrum in CH_3CN contained a peak cluster at $m/z=709.1$ assigned to $\{[\text{Ru}(\text{O})(\text{H}^+\text{TPA})(\text{bpy})]^{3+} - \text{H}^+ - 2(\text{PF}_6^-)\}^+$.⁷

In another case, UV-Vis titration of $[\text{Ru}^{\text{II}}(\text{bpy})_2(\text{py})(\text{OH}_2)]^{2+}$ (Figure 4.4.1) with CAN in 1 M HClO_4 (aq) exhibited a decrease of the MLCT (metal to ligand charge transfer) band at 470 nm with occurrence of two isosbestic points at 322 and 585 nm.⁸ Upon addition of 1 equiv. of CAN, a weak band was observed at 587 nm, which was assigned to the LMCT (ligand to metal charge transfer) band of the Ru(III) complex, $[\text{Ru}^{\text{III}}(\text{bpy})_2(\text{py})(\text{OH}_2)]^{3+}$. Further addition of CAN caused a decrease in the LMCT band at 587 nm and the reaction ended on the addition of 2 equiv. of CAN. The obtained Ru(IV)O complex, $[\text{Ru}^{\text{IV}}(\text{O})(\text{bpy})_2(\text{py})]^{2+}$, did not show any specific absorption bands in the visible region.⁹

Diamagnetic Ru(IV)=O species have also been reported. In seven-coordinated $[\text{Ru}^{\text{IV}}(\text{O})(\text{N4Py})(\text{OH}_2)]^{2+}$ (N4Py = (1, 1 – di (pyridin-2-yl) – N, N-bis (pyridin-2-ylmethyl)

methanamine), Figure 4.4.1) the splitting of degenerate $d\pi$ orbitals into a stable pair of d_{yz} and d_{zx} and unstable d_{xy} orbitals causes a singlet diamagnetic ground state.¹⁰

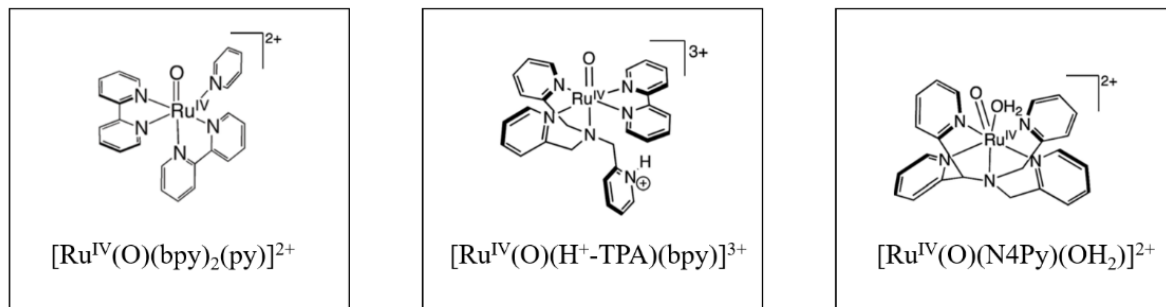


Figure 4.4.1 The structure of the mentioned Ru(IV)oxo species.

Compared to ruthenium (IV) oxo, the chemistry and characterization of terminal Ru(IV) imido complexes are less developed, which makes it difficult to investigate their potential role in the catalytic NH_3 oxidation cycle. While we were not successful in obtaining direct evidence for their generation in the catalytic cycle, the clues that direct us to the consideration of such intermediates would be discussed later in this chapter.

4.5. Reaction of $[\text{Ru}(\text{trpy})(\text{dmabpy})\text{NH}_3]^{+3}$ With Bases

4.5.1. Electrochemistry

Addition of DBU to solutions of $[\text{Ru}(\text{trpy})(\text{dmabpy})\text{NH}_3]^{+3}$ in NM results in a rapid color change from green to orange, and the voltammograms exhibit new redox features as shown in Figure 4.5.1.

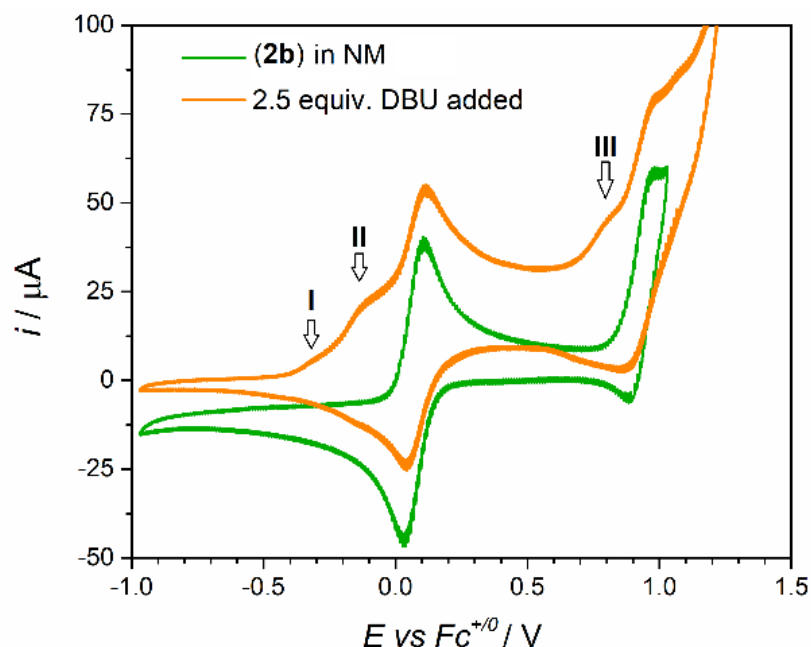


Figure 4.5.1 CVs of a solution of 5.36×10^{-3} M **2b** in NM before (green) and after (orange) addition of 1.34×10^{-2} M DBU. Scan rate 0.1 V s^{-1} . After the reaction with the base, the solution contains **2a** and three new redox active species labeled as I, II and III.

According to the starting currents being anodic, the solution after addition of DBU does not contain $[\text{Ru}(\text{trpy})(\text{dmabpy})\text{NH}_3]^{+3}$ but instead has two new species that are easier to be oxidized (irreversibly) than $[\text{Ru}(\text{trpy})(\text{dmabpy})\text{NH}_3]^{+2}$ (peaks I and II in Figure 4.5.1). These features are absent when excess concentrations of NH_3 is added as the base to solutions of $[\text{Ru}(\text{trpy})(\text{dmabpy})\text{NH}_3]^{+3}$ in NM, the case which the voltammograms resemble of catalytic oxidation of NH_3 by $[\text{Ru}(\text{trpy})(\text{dmabpy})\text{NH}_3]^{+2}$ (Figure 4.5.2). While due to the possibility of N-N bond formation, the chemistry is more complicated when NH_3 is used, the very negative onset potential of the catalytic current respect to the $E_{1/2}$ of $[\text{Ru}(\text{trpy})(\text{dmabpy})\text{NH}_3]^{+3}$ can be related to more feasible oxidative processes. In the following sections the reaction of $[\text{Ru}(\text{trpy})(\text{dmabpy})\text{NH}_3]^{+3}$ with the two bases, NH_3 and DBU are discussed in more details.

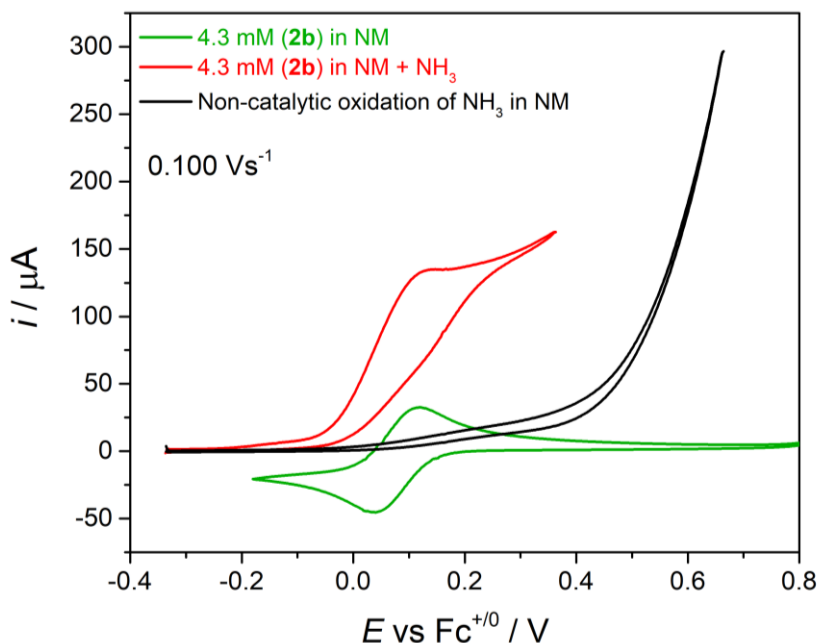


Figure 4.5.2 CVs of a solution containing 4.30×10^{-3} M $[\text{Ru}(\text{trpy})(\text{dmabpy})\text{NH}_3]^{+3}$, **2b**, in NM before (green) and after (red) addition of NH_3 (saturated, 0.93 M, determined by NMR measurements). The black curve shows the non-catalytic oxidation of NH_3 in NM.

By adding stoichiometric concentrations of NH_3 to solutions of $[\text{Ru}(\text{trpy})(\text{dmabpy})\text{NH}_3]^{+3}$ in NM, another redox peak appears at 0.26 V versus $\text{Fc}^{+/0}$ (Figure 4.5.3), corresponding to a new species in a lower concentration than the starting $[\text{Ru}(\text{trpy})(\text{dmabpy})\text{NH}_3]^{+3}$, judged by the relative anodic peak currents of the newly appeared peak and the redox peak for $[\text{Ru}(\text{trpy})(\text{dmabpy})\text{NH}_3]^{+3}$. Due to the possibility of N-N formation in the presence of ammonia which would lead to a hydrazine intermediate, CVs of an authentic ruthenium hydrazine complex were taken in NM. Two redox processes with matching $E_{1/2}$ potentials are observed for the $\text{Ru}(\text{II})\text{-N}_2\text{H}_4$, suggesting that its formation under reaction conditions has to be considered. The hydrazine intermediates are discussed in chapter 5 in more details.

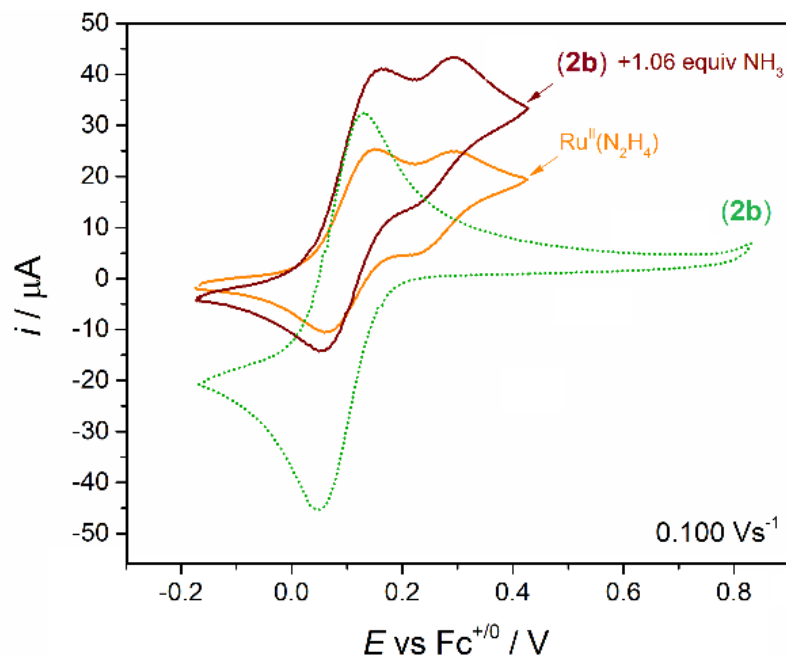


Figure 4.5.3 Vs of 4.30×10^{-3} M $[\text{Ru}(\text{trpy})(\text{dmabpy})\text{NH}_3]^{+3}$ in NM without NH_3 (green), and after addition of NH_3 (4.60×10^{-3} M, 1.06 equiv.) (brown). CV obtained for 2.80×10^{-3} M $[\text{Ru}(\text{trpy})(\text{dmabpy})\text{N}_2\text{H}_4](\text{PF}_6)_2$ in NM in the absence of NH_3 .

4.5.2. ^1H NMR Studies

Addition of DBU to solutions of $[\text{Ru}(\text{trpy})(\text{dmabpy})\text{NH}_3]^{+3}$ in $\text{NM}-d_3$, as mentioned before, is followed by a fast color change and the NMR spectrum shows $[\text{Ru}(\text{trpy})(\text{dmabpy})\text{NH}_3]^{+2}$ as the only diamagnetic ruthenium-based species present (Figure 4.5.4). When NH_3 is bubbled into an NMR tube containing $[\text{Ru}(\text{trpy})(\text{dmabpy})\text{NH}_3]^{+3}$, the final red solution has two ruthenium species appeared in the room temperature ^1H NMR spectrum, with the major one having resonances matching with $[\text{Ru}(\text{trpy})(\text{dmabpy})\text{NH}_3]^{+2}$ except for the singlet at δ 1.65 ppm being moved to δ 2.20 ppm in the presence of NH_3 . The resonances related to the minor species are modestly close to the hydrazine complex, $[\text{Ru}(\text{trpy})(\text{dmabpy})\text{N}_2\text{H}_4]^{+2}$, **2e** (Figure 4.5.5).

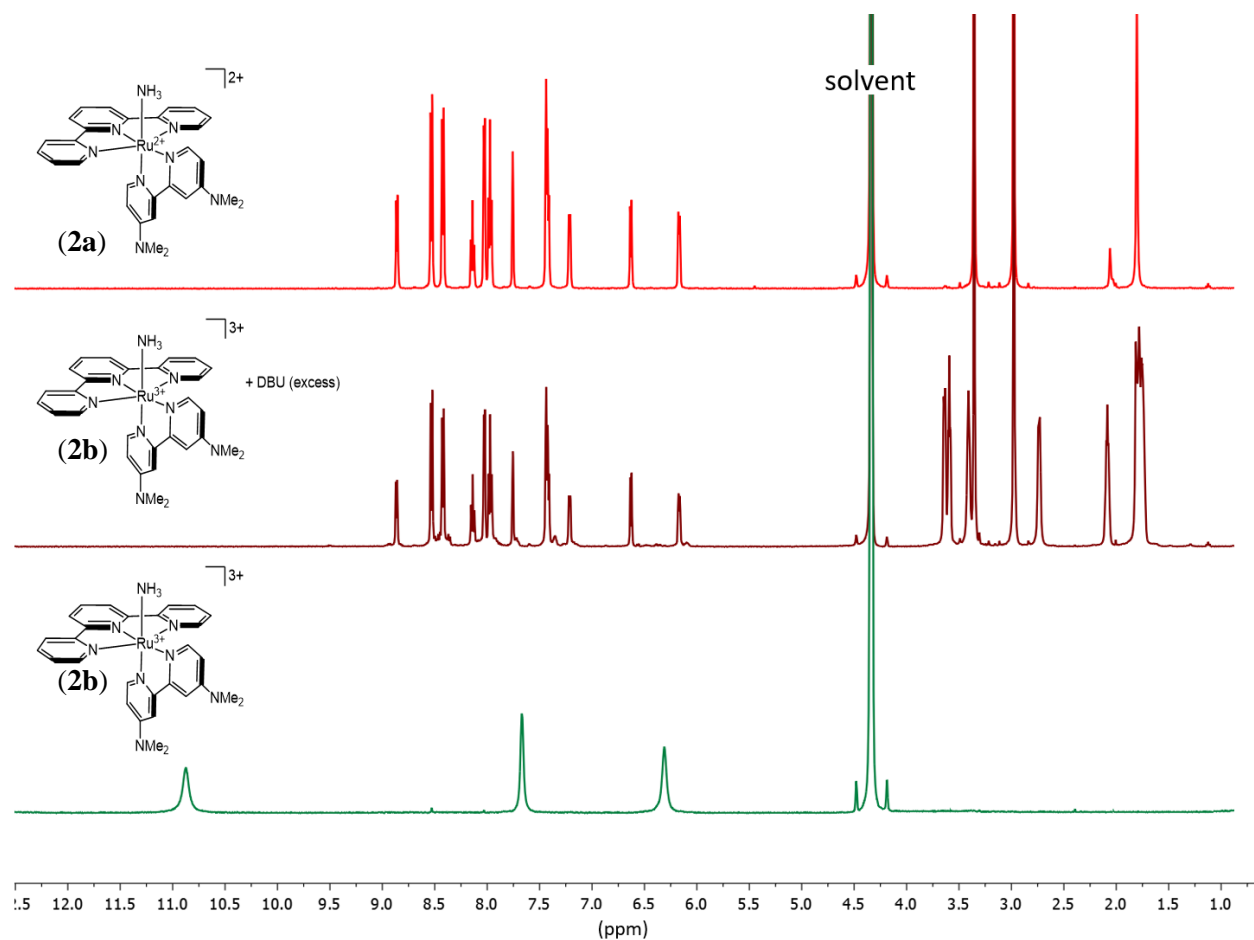


Figure 4.5.4 ^1H NMR spectra (rt, 500 MHz, nitromethane- d_3) of **2b** (bottom, green), **2b** + excess DBU (middle, brown) and **2a** (top, red). Comparison between the spectrum obtained after addition of NH_3 to **2b** and the spectrum of **2a** in NM, shows that **2a** is the main product of the reaction at room temperatures. The resonances at δ 1.65, 2.05, 2.97, 3.51 and 3.46 ppm are related to the added DBU.

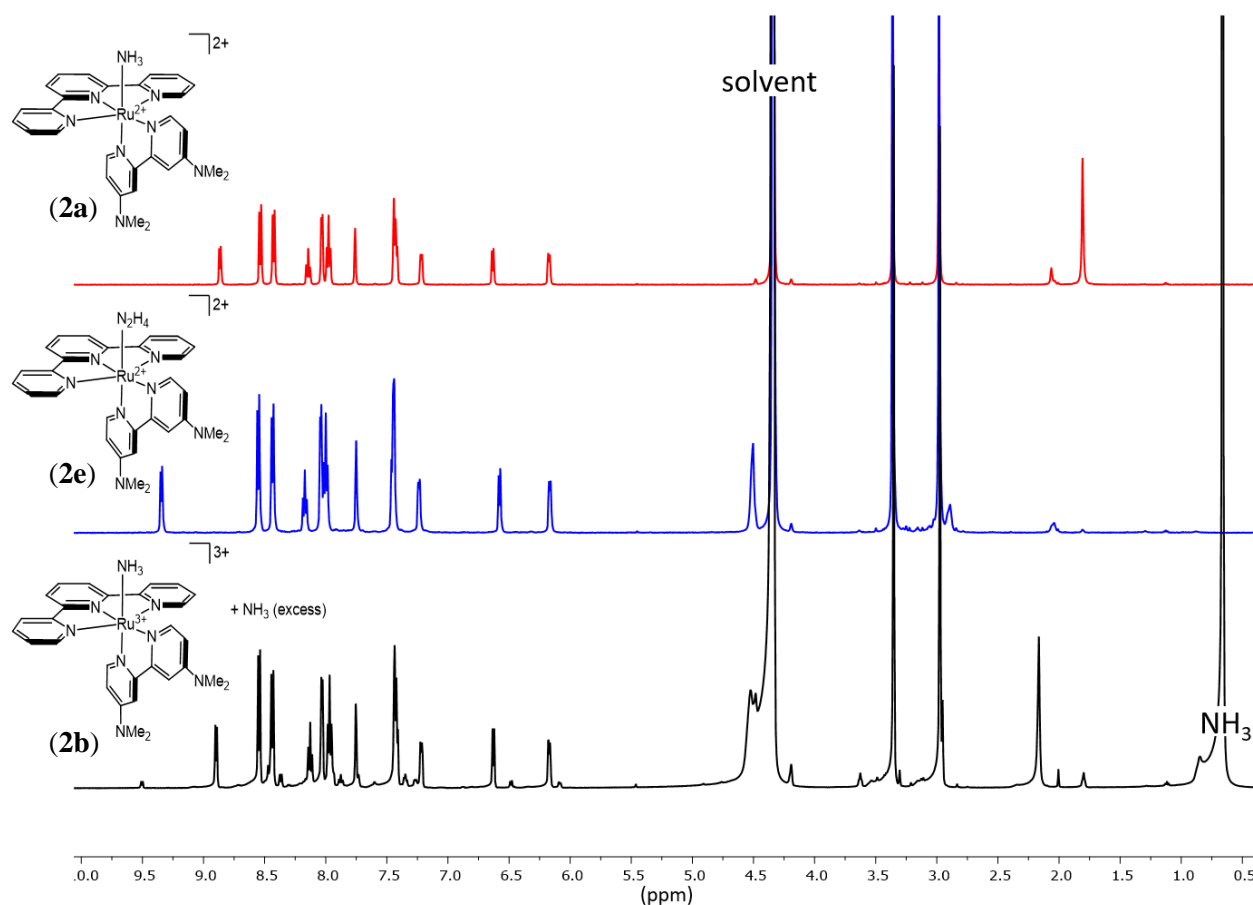


Figure 4.5.5 ^1H NMR spectra (rt, 500 MHz, nitromethane- d_3) of **2b** + excess NH_3 (bottom, black), **2e** (middle, blue) and **2a** (top, red). By comparing the spectra, the major product of the reaction between **2b** and NH_3 in NM is **2a**.

4.5.3. UV-Vis Spectrophotometric Titrations

Monitoring the regeneration of $[\text{Ru}(\text{trpy})(\text{dmabpy})\text{NH}_3]^{+2}$, **2a**, from $[\text{Ru}(\text{trpy})(\text{dmabpy})\text{NH}_3]^{+3}$, **2b**, *via* treatment with bases, provides us with a great tool to investigate the mechanistic details. In this section we focus on titration of $[\text{Ru}(\text{trpy})(\text{dmabpy})\text{NH}_3]^{+3}$ with DBU in NM and in chapter 5, similar titrations are discussed when NH_3 is used as the base.

Absorption spectra of $[\text{Ru}(\text{trpy})(\text{dmabpy})\text{NH}_3]^{+3}$ in dry NM has two LMCT bands¹¹ at 730 nm ($\epsilon = 5600 \text{ M}^{-1} \text{ cm}^{-1}$) and 840 nm ($\epsilon = 5800 \text{ M}^{-1} \text{ cm}^{-1}$). Electronic absorption spectrum of $[\text{Ru}(\text{trpy})(\text{dmabpy})\text{NH}_3]^{+2}$ in NM has a characteristic $\text{Ru}(\text{d}\pi) \rightarrow \text{dmabpy}(\pi^*)$ MLCT band at 490

nm ($\epsilon = 15660 \text{ M}^{-1} \text{ cm}^{-1}$) (See Appendix, Figure A4.6.1).¹² The decrease and increase in the absorption values at 730 nm and 490 nm were used to track the fates of species $[\text{Ru}(\text{trpy})(\text{dmabpy})\text{NH}_3]^{+3}$ and $[\text{Ru}(\text{trpy})(\text{dmabpy})\text{NH}_3]^{+2}$, respectively, in spectrophotocatalytic titrations of $[\text{Ru}(\text{trpy})(\text{dmabpy})\text{NH}_3]^{+3}$ with DBU in NM.

For this experiment, a stock solution of $1.11 \times 10^{-3} \text{ M}$ $[\text{Ru}(\text{trpy})(\text{dmabpy})\text{NH}_3]^{+3}$ (5.7 mg **2b** in 5 mL NM) was prepared initially. 150 μL of this stock solution was transferred to a cuvette containing 2.0 mL NM to give 2.15 mL of a final solution of $7.73 \times 10^{-5} \text{ M}$ $[\text{Ru}(\text{trpy})(\text{dmabpy})\text{NH}_3]^{+3}$. Based on the absorption reading at 730 nm and using the molar absorptivity of $[\text{Ru}(\text{trpy})(\text{dmabpy})\text{NH}_3]^{+3}$ in NM, the actual concentration was determined as $7.65 \times 10^{-5} \text{ M}$ $[\text{Ru}(\text{trpy})(\text{dmabpy})\text{NH}_3]^{+3}$. The cuvette was capped and sealed in the glove box. A solution of DBU in NM was also prepared by adding 1 μL DBU to 5 mL NM (solution1) which was further diluted by a factor of 50 to give a final solution of $2.68 \times 10^{-5} \text{ M}$ DBU (solution2). Aliquots of these solutions (solution2 for the first 10 additions, then solution1 until the end of the titration) were added step by step to the cuvette containing $[\text{Ru}(\text{trpy})(\text{dmabpy})\text{NH}_3]^{+3}$ during the experiment and the spectra were recorded after each addition. The changes in the spectral features are shown in Figure 4.5.6.

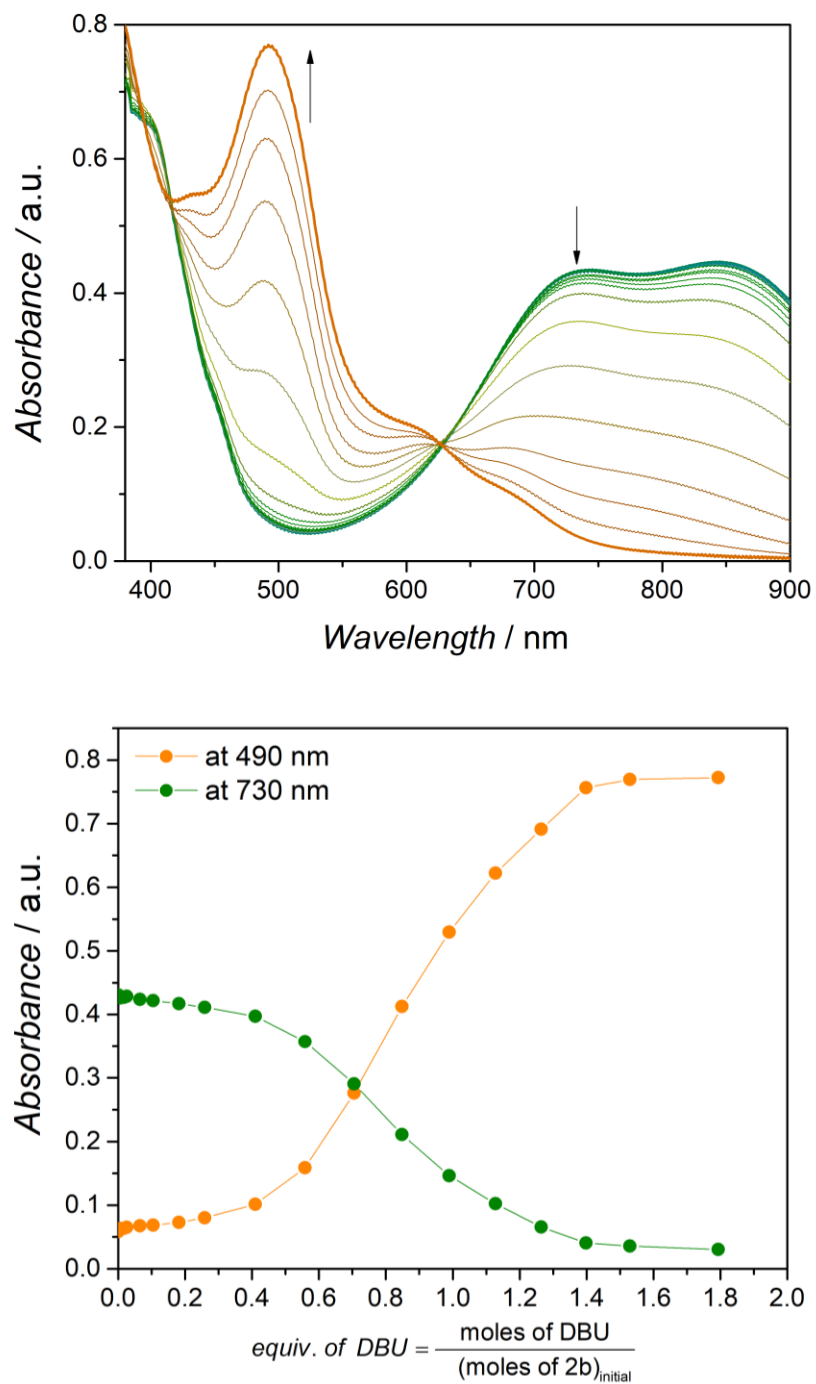


Figure 4.5.6 Top: Changes in the electronic absorption spectra of a green “starting solution” of 7.65×10^{-5} M **2b** with the addition of DBU to the orange “final solution”. Bottom: Increase in the absorbance at 490 nm due to generation of **2a** happens simultaneously with the decrease in absorbance at 730 nm due to consumption of **2b**.

As data in Figure 4.5.6 (top) represents, the LMCT bands of $[\text{Ru}(\text{trpy})(\text{dmabpy})\text{NH}_3]^{+3}$ gradually disappears with addition of base, and the reappearance of a new band at 490 nm occurs simultaneously. The negligible initial change in the absorbances in the plot of absorbance (at 730 nm and 490 nm) versus the equivalent of added DBU (=moles of DBU present in the solution divided by the starting moles of $[\text{Ru}(\text{trpy})(\text{dmabpy})\text{NH}_3]^{+3}$) (Figure 4.5.6, bottom) is attributed to the acid-base equilibrium that is established between the solvent and the base, DBU. The reaction is complete when approximately 1.4 equiv. of DBU is present in the solution, judging by the spectra not changing with further additions of DBU. Based on room temperature NMR results which showed $[\text{Ru}(\text{trpy})(\text{dmabpy})\text{NH}_3]^{+2}$ as the product of the reaction between $[\text{Ru}(\text{trpy})(\text{dmabpy})\text{NH}_3]^{+3}$ and excess DBU, the absorption spectrum obtained at 1.4 equiv. of DBU (Figure 4.5.7, orange) was compared to the spectrum of a solution of $[\text{Ru}(\text{trpy})(\text{dmabpy})\text{NH}_3]^{+2}$ in NM. If it is considered that regeneration of $[\text{Ru}(\text{trpy})(\text{dmabpy})\text{NH}_3]^{+2}$ is *via* the deprotonation of $[\text{Ru}(\text{trpy})(\text{dmabpy})\text{NH}_3]^{+3}$, followed by redox disproportionation of $[\text{Ru}(\text{trpy})(\text{dmabpy})\text{NH}_2]^{+2}$, we can estimate the concentration of the produced $[\text{Ru}(\text{trpy})(\text{dmabpy})\text{NH}_3]^{+2}$ at the end of the titration to be 3.46×10^{-5} M in the final solution with the volume of 2.402 mL, based on the stoichiometry of equation 12. The comparison between the constructed absorption spectrum for 3.46×10^{-5} M $[\text{Ru}(\text{trpy})(\text{dmabpy})\text{NH}_3]^{+2}$ (Figure 4.5.7, red) and the spectrum collected at the end point of the titration (1.4 equiv. DBU) is shown in Figure 4.5.7 (red and orange spectra).

To account for the effect of DBU, a solution of $[\text{Ru}(\text{trpy})(\text{dmabpy})\text{NH}_3]^{+2}$ and DBU in NM was made and its absorption spectrum was recorded. To prepare this solution, a stock solution of 2.68×10^{-3} M DBU was made by adding 2 μL DBU to 5 mL NM. 250 μL of this solution was further diluted to a final volume of 5 mL to give a solution of 1.34×10^{-4} M. 50 μL of a solution containing 4.2×10^{-4} M $[\text{Ru}(\text{trpy})(\text{dmabpy})\text{NH}_3]^{+2}$ (3.7 mg **2a** in 10 mL NM) was diluted to 0.5 mL by the

1.31×10^{-4} M DBU in NM as the solvent. The final concentrations of $[\text{Ru}(\text{trpy})(\text{dmabpy})\text{NH}_3]^{+2}$ and DBU in this solution were 4.20×10^{-5} M and 1.21×10^{-4} M, respectively (**2a** : DBU = 1 : 2.80 or 0.5 : 1.40). The absorption spectrum for this solution was obtained by dividing the absorbance by [**2a**] ($=4.20 \times 10^{-5}$ M) (See Appendix, Figure A4.6.2) and was used to construct the spectrum that mimics the final solution of the titration by multiplying molar absorptivity by 3.46×10^{-5} M (Figure 4.5.7, black).

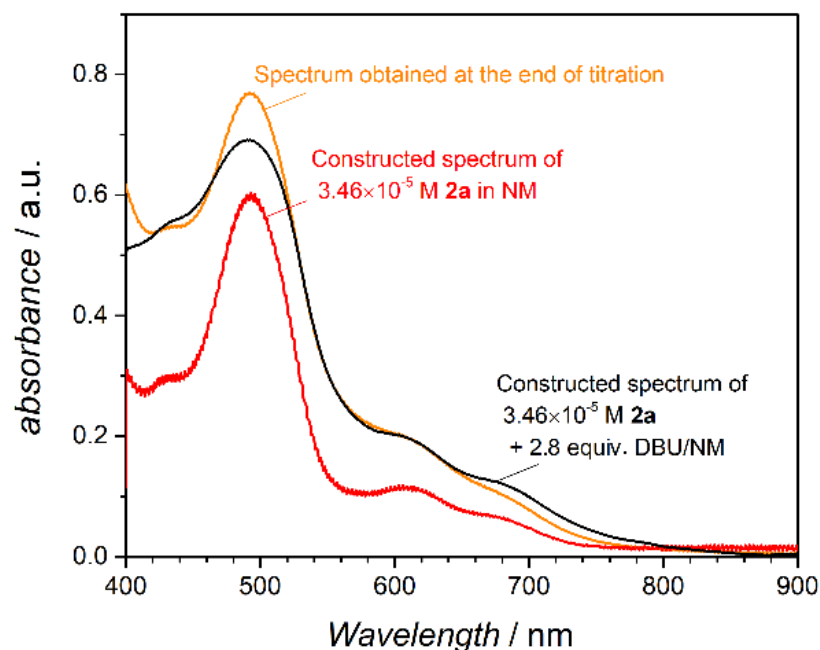


Figure 4.5.7 Comparing the electronic absorption spectra obtained at the end of the titration, *i.e.* 1.4 equiv. DBU added (orange) with the constructed spectrum for 0.5 equiv. **2a** in NM (red) and constructed spectrum for 0.5 equiv. **2a** + DBU in NM (black).

As seen in Figure 4.5.7, neither of the simulated spectra perfectly match with that of the final solution, implying that some other absorbing species are present in the solution. Mathematical subtraction of the constructed spectra (red and black curves in Figure 4.5.7) from the spectrum of the endpoint solution results in residual absorption spectra (See Appendix, Figure A4.6.3). While the identities of such co-products are not known at this point, the observations in the steady-state titrations of $[\text{Ru}(\text{trpy})(\text{dmabpy})\text{NH}_3]^{+3}$ with DBU in NM are consistent with a half equivalence of

[Ru(trpy)(dmabpy)NH₃]⁺² being generated by this reaction, supporting the concept of the redox disproportionation.

4.6. Rotating Ring Disk Electrode (RRDE) Experiments

Electrochemical experiments using two working electrodes in the solution provide invaluable information about the intermediates of a reaction. Those experiments are performed under hydrodynamic conditions achieved by enforced convection to overcome migration-related mass transport limitations, thus leaving diffusion to be the only factor affecting the mass transport. Under such circumstances, when an intermediate is generated at one working electrode it can be detected at the other closely-positioned working electrode. The potential of the second working electrode is often set to a constant value at which the intermediate could undergo another redox reaction, generating a current that carries information about that desired species. Commercially available RRDEs are as excellent tools for such experiments since the two working electrodes are closely positioned respect to each other and the rotation of the electrodes is precisely controlled. The RRDE used in this study consisted of a glassy carbon disk electrode (WE1) embedded into a Teflon shaft. Concentric to the disk, a platinum ring electrode was placed (WE2). The micrometer scale gap between the two electrodes allows the flow of the disk products to the ring (Figure 4.6.1). The shaft was connected to an electric motor that enabled a very fine control of the electrode's angular speed. A bipotentiostat controlled the potential of both WE2 and WE1 separately and the current of the of each electrode was measured against a platinum mesh counter electrode.

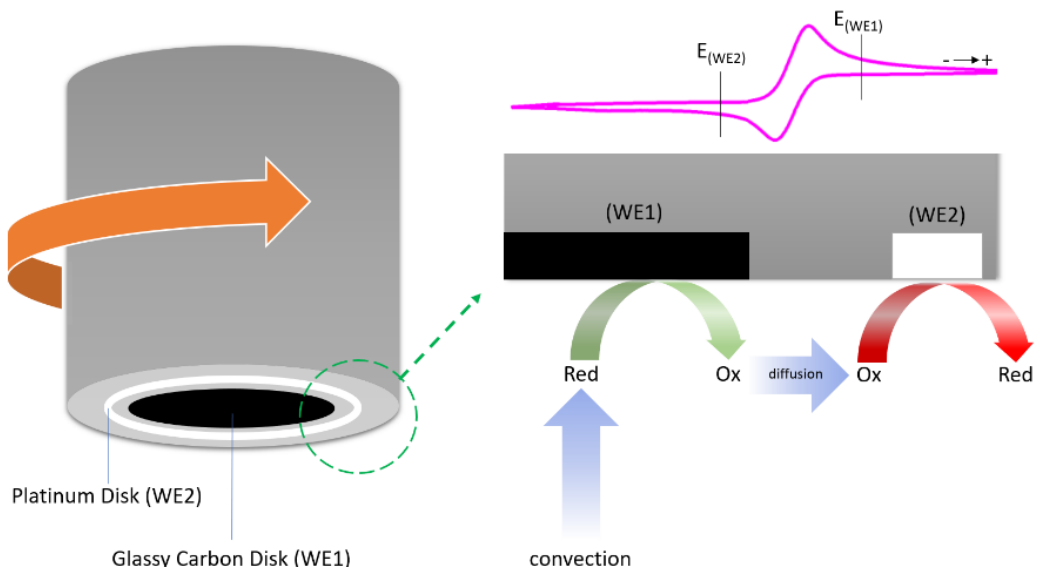


Figure 4.6.1 The schematic structure of an RRDE electrode is illustrated on the left. On the right, the redox events at the disk and ring are displayed for a redox active species with a generic CV response as shown on the top.

As shown in Figure 4.6.1, for a solution containing a reducing species, *Red*, the rotation of the electrode provides a steady state flow of *Red* to the diffusion layer of the disk electrode through convection. When the potential of the disk (WE1) is positive respect to the $E_{1/2}$, e.g., $E(WE2)$ in Figure 4.6.1, *Red* undergoes oxidation to produce *Ox* at the surface of the electrode. The redox events at the disk electrode are normally unaffected by the ring; while the current at the ring is totally determined by the products of the disk reaction. If the lifetime of the species *Ox* is $\sim \frac{d^2}{D}$ (d = the gap between the disk and the ring in cm, D = diffusion constant of *Ox* in cm^2s^{-1}), it would reach to the ring electrode. In cases where the potential of the ring, WE2 is set to a value more negative than the $E_{1/2}$, e.g., $E(WE1)$ in Figure 4.6.1, *Ox* can be reduced back to *Red*, causing a reductive current to be observed for the ring. However, not all of the generated *Ox* could reach to WE2 (ring) and only a fraction of the disk products is collected by the ring. The term collection efficiency, N , is used to describe the fraction of the collected products at the ring and is defined as

the ratio of the ring limiting current to the disk limiting currents (where the current is plateaued). N is governed by the geometry of the RRDE or more specifically the gap between the two electrodes and should be independent from the rotation. If in an experiment, the observed N is rotation speed dependent, one can conclude that the lifetime of the intermediates are short and major losses occur within the gap between the disk and the ring.¹³

In this work, two types of experiments were performed in RRDE measurements. In one set of experiments, the RRDE was immersed in a solution containing $[\text{Ru}(\text{trpy})(\text{dmabpy})\text{NH}_3]^{+2}$ in THF and the potential of the disk electrode was scanned linearly. The ring was set a constant potential, and the redox events at the rings were studied. The other set of experiments were carried out by applying a constant potential at the disk while the ring's potential was being scanned linearly. Both experiments were running both in the absence and presence of DBU base. For these experiments, the potentials are reported vs. NHE (conversion was done based on $\text{Fc}^{+/0}$ in THF).

4.6.1. Titration with DBU: Scanning E_D , Constant E_R

Before the addition of the DBU, CVs were taken in a solution of 5.57×10^{-4} M $[\text{Ru}(\text{trpy})(\text{dmabpy})\text{NH}_3]^{+2}$ in THF at both disk and ring electrodes (Figure 4.6.2, top). The same redox potentials were observed for Ru(II/III)NH_3 couple at each electrode, with the ring showing less currents due to its smaller surface area. Then, the electrodes were rotated with three rotation speeds, and the potential of the disk (E_D) was scanned at a rate of 10 mVs^{-1} , exhibiting a typical hydrodynamic steady-state i - E curve (Figure 4.6.2, bottom) for the disk. The potential of the ring (E_R) was set at a constant value of 0.00 V vs. NHE, negative to the $E_{1/2}$ of $[\text{Ru}(\text{trpy})(\text{dmabpy})\text{NH}_3]^{+2}$ to collect the products of the disk reaction. Under these conditions, for $E_D < E_{1/2}$ no oxidation occurred at the disk ($i_D=0$), consequently no currents were observed for the ring because there was

no products to be collected. When $E_D > E_{1/2}$, oxidation of $[\text{Ru}(\text{trpy})(\text{dmabpy})\text{NH}_3]^{+2}$ to $[\text{Ru}(\text{trpy})(\text{dmabpy})\text{NH}_3]^{+3}$ took place at the disk and produced $[\text{Ru}(\text{trpy})(\text{dmabpy})\text{NH}_3]^{+3}$ was reached to the ring and reduced back to $[\text{Ru}(\text{trpy})(\text{dmabpy})\text{NH}_3]^{+2}$, exhibiting a reductive current (i_R).

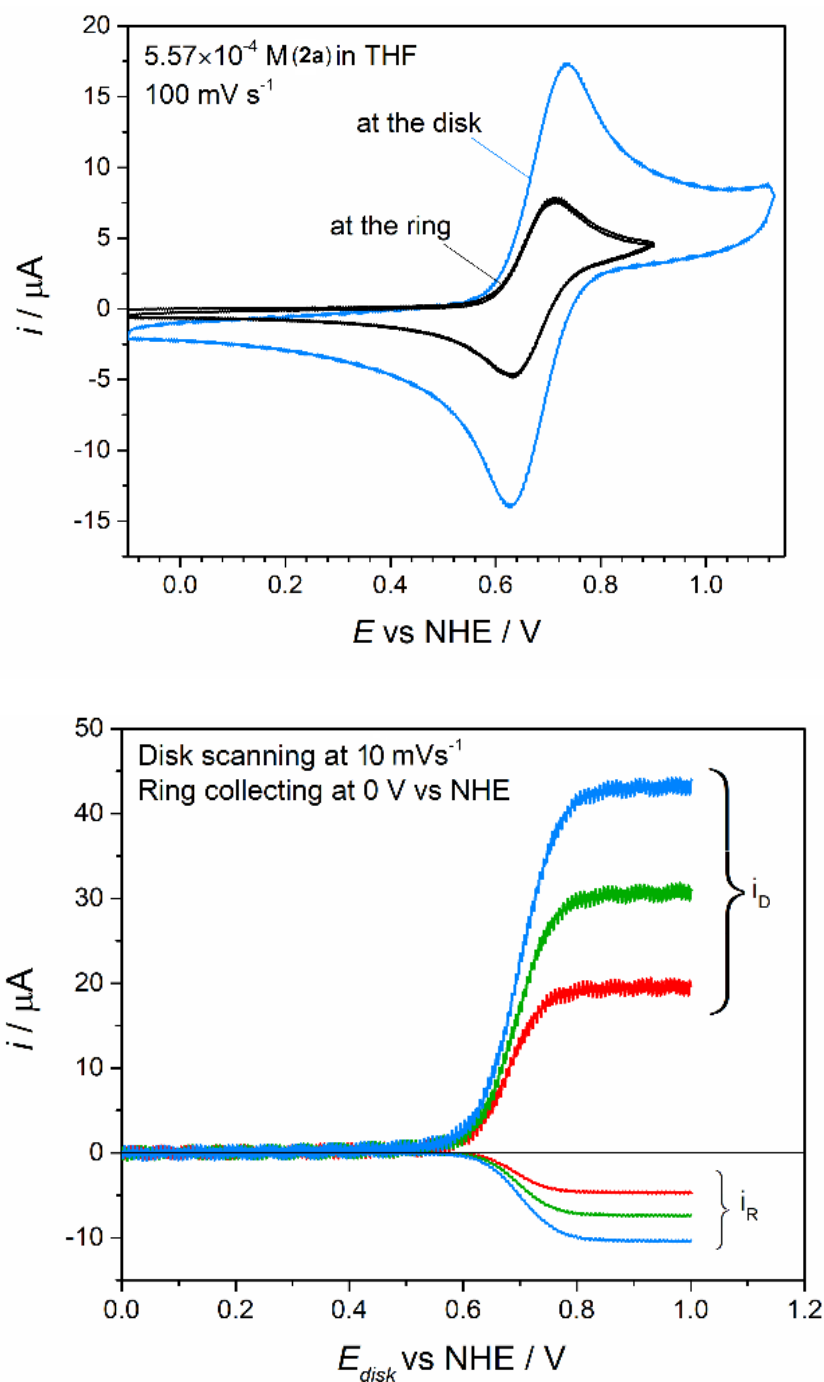


Figure 4.6.2 Top: CVs obtained for a solution containing $5.57 \times 10^{-4} \text{ M}$ **2a** in THF collected at the ring and the disk show that the $E_{1/2}$ of the complex does not change with the material of the electrode. Bottom: The currents associated with the disk (i_D) and ring (i_R), when the potential of the disk is being scanned linearly and the ring is set at a constant reductive potential of 0.00 V vs. NHE. Three rotation speeds are shown: 200 rpm (red), 500 rpm (green) and 1000 rpm (blue). $N = 24\%$ (rotation speed independent), consistent with the value reported by the manufacturer.

Step by Step addition of aliquots of a DBU solution in THF to the electrochemistry cell resulted in the appearance of a pre-peak in the CVs of the disk (Figure 4.6.3, top). The magnitude of the pre-peak current increased linearly with the concentration of DBU (See Appendix, Figure A4.7.1) while its potential demonstrated a positive shift as [DBU] was increasing. Linear scan voltammograms (LSVs) were then obtained after each addition. For instance, for the first addition of DBU where $[\text{DBU}] = 1.10 \times 10^{-5} \text{ M}$, the potential of the disk was scanned and the reduction of the products of the disk reaction(s) were collected reductively at the ring (Figure 4.6.3, bottom).

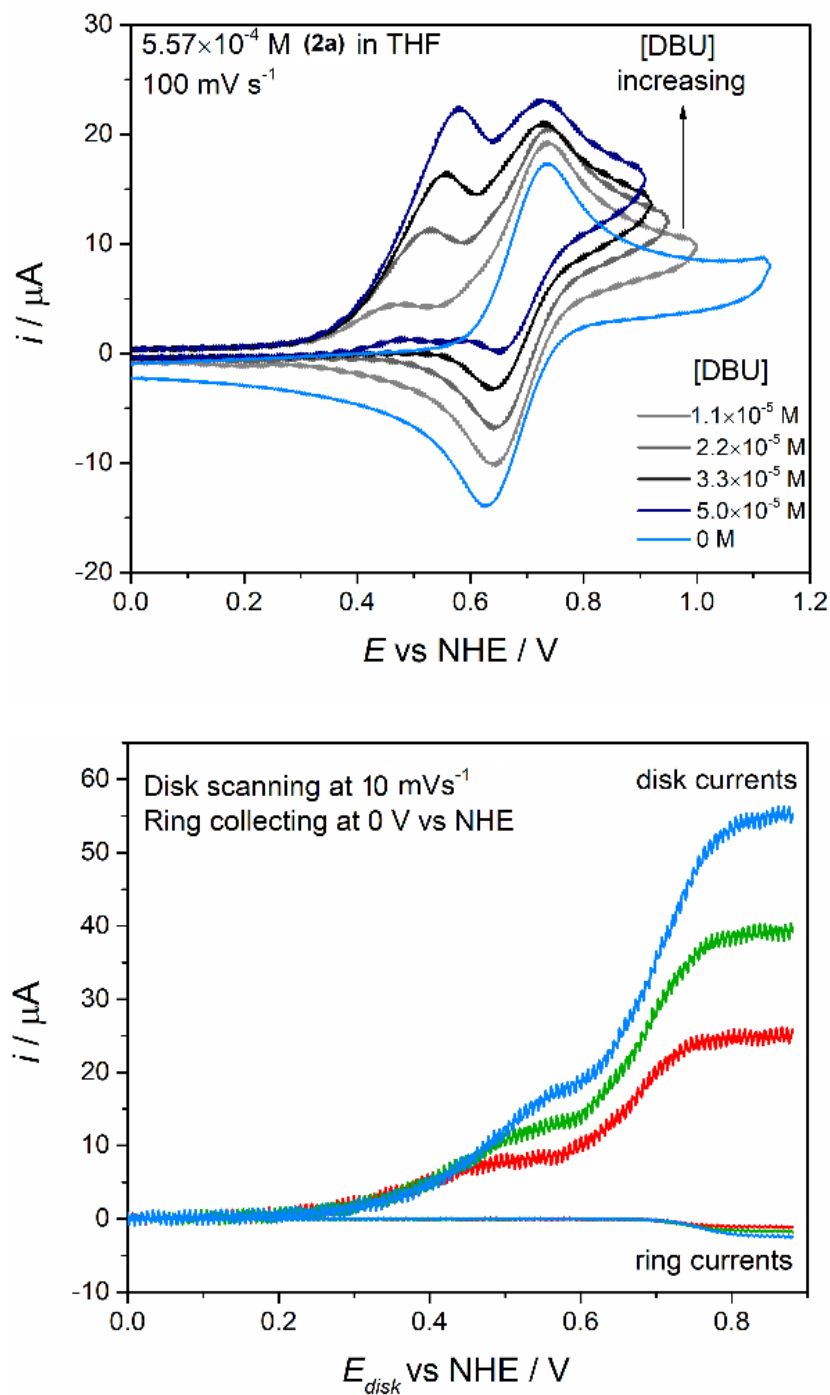


Figure 4.6.3 Top: CVs obtained after addition of DBU to the solution containing 5.57×10^{-4} M **2a** in THF collected at the disk. Bottom: The currents associated with the disk and ring for the experiment with $[\text{DBU}] = 1.10 \times 10^{-5}$ M. Three rotation speeds are shown: 200 rpm (red), 500 rpm (green) and 1000 rpm (blue). $N < 24\%$ (rotation speed independent).

As seen in Figure 4.6.3, bottom the LSVs of the disk show two diffusion limited currents, similar to the CVs in Figure 4.6.3, top. However, the behavior of the ring's current is significantly different

when compared to Figure 4.6.2, bottom. The product(s) of the process responsible for the pre-peak are not reduced at the ring. This could be either due to their instability and very short lifetimes (being consumed in a rapid coupled chemical reaction) or because their reduction takes place at more negative potentials and is not observable within the selected potential window. The ring, however, shows small reductive currents at potentials more positive than 0.7 V versus NHE. Since the Ru(II/III)NH₃ peak still has a return peak in the corresponding CV, this reductive ring current might be due to the reduction of Ru(III)NH₃ species. However, the very low collection efficiencies and the more positive onset potential of the ring's current compared to what was seen in the control experiment (Figure 4.6.2, bottom) may be indications of the reduction of a new species.

4.6.2. Titration with DBU: Scanning E_R, Constant E_D

In another experiment, the potential of the disk electrode was held at a constant oxidative potential of 1.00 V vs NHE ($E_D > E_{1/2}(\mathbf{2a})$) in a solution containing [Ru(trpy)(dmabpy)NH₃]⁺² in THF.⁽¹⁾ At this potential, oxidation of Ru(II) to Ru(III) occurred, thus a constant, mass transport-limited oxidative current was seen for the disk electrode. Meanwhile, the potential of the ring was scanned linearly to phish for any redox-active products of the disk reaction. As seen in Figure 4.6.4, when $E_R < E_{1/2}(\mathbf{2a})$, reduction of [Ru(trpy)(dmabpy)NH₃]⁺³ product (**2b**) was taking place at the ring. At $E_R > E_{1/2}(\mathbf{2a})$, oxidation of the [Ru(trpy)(dmabpy)NH₃]⁺², **2a**, to [Ru(trpy)(dmabpy)NH₃]⁺³, **2b**, happened at the ring.

¹ See Appendix A4 for experiments with different E_D values.

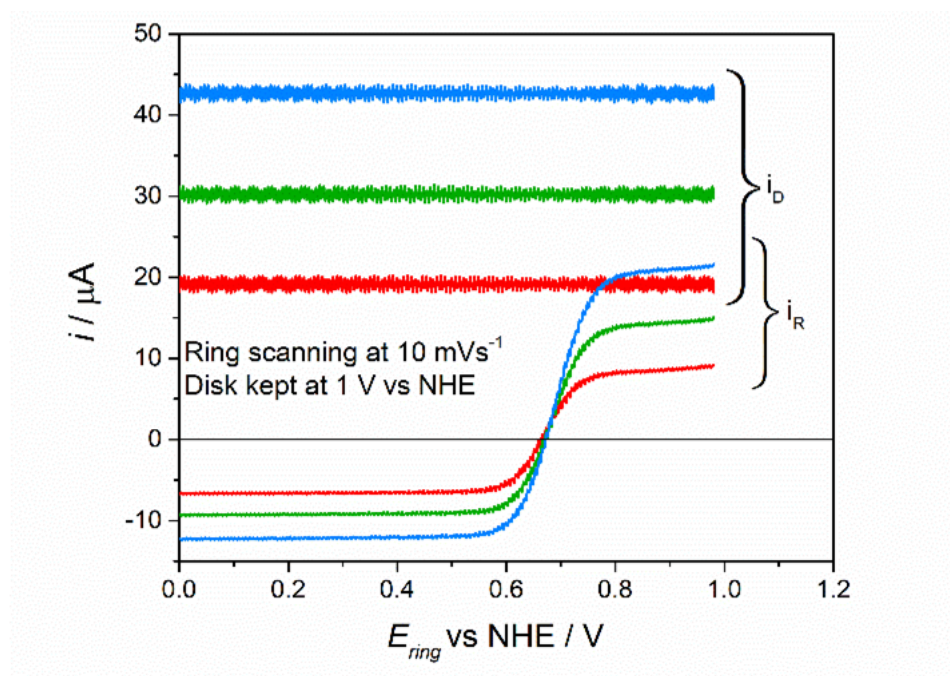


Figure 4.6.4 RRDE LSVs for 5.57×10^{-4} M **2a** in THF with the disk being held at a potential more positive than the $E_{1/2}$ of **2a**. Constant oxidative disk currents are labeled as i_D . The product of the disk oxidation is being collected and reduced at the ring when E_{ring} is lower than $E_{1/2}$ of **2a**. Three rotation speeds are shown: 200 rpm (red), 500 rpm (green) and 1000 rpm (blue). $N = 24\%$ (rotation speed independent).

Applying the same electrochemical conditions to a solution containing 5.57×10^{-4} M $[\text{Ru}(\text{trpy})(\text{dmabpy})\text{NH}_3]^{+2}$ and 1.10×10^{-5} M DBU results in LSV responses that are shown in Figure 4.6.5. First, we noticed that while the currents at the disk remain almost constant, they do not change with rotation speed and their magnitude is smaller than what was observed for the control experiment in Figure 4.6.4. One possible scenario is that the disk current is controlled by a sluggish kinetically controlled process. The currents at the ring also do appear to be independent from the events at the disk.

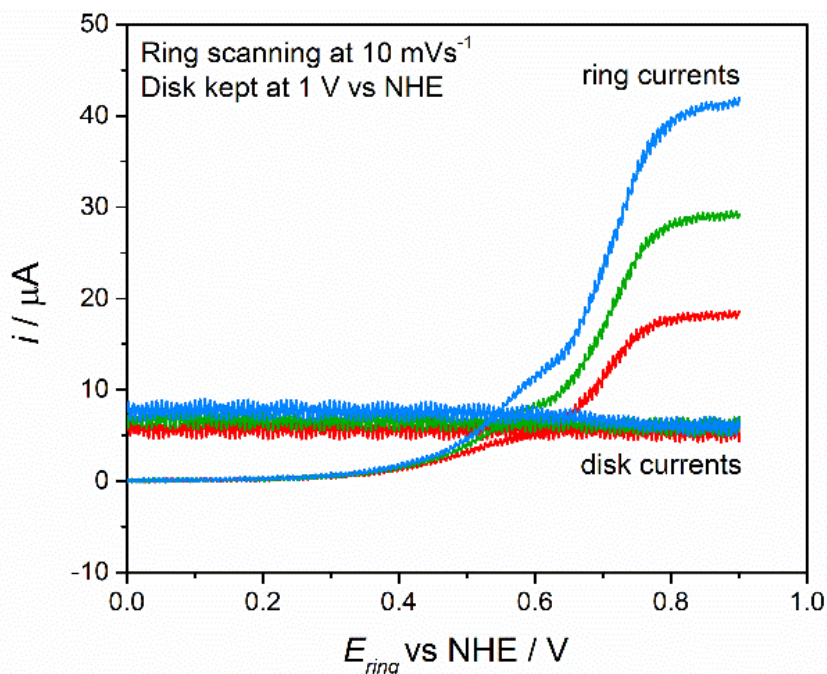


Figure 4.6.5 RRDE LSVs for the experiment with 5.57×10^{-4} M **2a** and $[\text{DBU}] = 1.10 \times 10^{-5}$ M in THF. Three rotation speeds are shown: 200 rpm (red), 500 rpm (green) and 1000 rpm (blue). The potential of the disk is held at the constant value of 1.0 V vs. NHE, while the potential of the ring was scanned linearly at a rate of 10 mVs^{-1} .

It has to be noted that only in RRDE experiments, a positive shift was observed after each addition of DBU. Figure 4.6.6, top shows that with increasing $[\text{DBU}]$, the redox potentials are shifted positively. This, reduces the accuracy of the applied E_D . When the peaks are moved so that the second (Figure 4.6.6, bottom), reversible peaks lay on top of each other, the CVs match with other experiments that were conducted using a stationary (different) glassy carbon electrode (no ring) (See Appendix, Figure A4.7.5). It is still unclear that whether these issues are related to the instability of the reference electrode or the conditions of the RRDE experiments, *i.e.*, presence of a platinum ring (since it might catalyze the production of interfering species) or convection which might affect the electrochemistry at the glassy carbon disk. More careful RRDE experiments need to be conducted, specifically polishing of the electrodes in between DBU additions and performing EDX examinations of the surface of the disk at the end of the experiment are strongly

recommended. Nevertheless, multiple LSV measurements were performed between every two DBU additions and the CVs taken before and after each RRDE experiments do not agree with depositions on to the surface. Still, more investigations regarding these experiments have to be done.

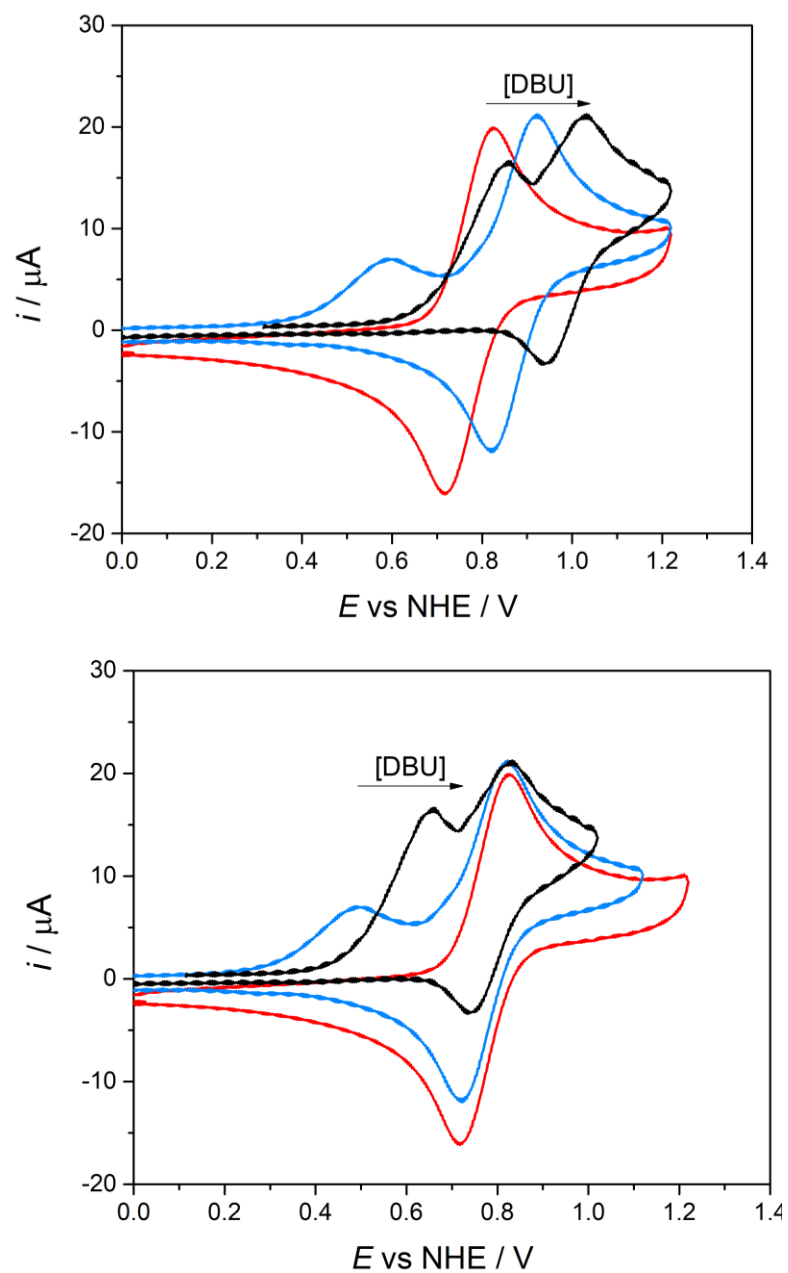


Figure 4.6.6 CVs taken at the disk without DBU (red) and after two additions of DBU. Top: raw data, Bottom: after the reversible processes (second peaks) were superimposed.

4.7. Conclusions

Chemical synthesis of the compound $[\text{Ru}(\text{trpy})(\text{bdmabpy})\text{NH}_3](\text{PF}_6)_3$, **2b**, as the first intermediate in the catalytic cycle provided a convenient path to investigate the role of this complex in the catalytic cycle. Treatment of **2b** with DBU as a non-coordinating base resulted in regeneration of $[\text{Ru}(\text{trpy})(\text{bdmabpy})\text{NH}_3](\text{PF}_6)_2$, **2a**, which was related to a redox disproportionation following the deprotonation of **2b**. Reactions of **2b** with NH_3 , yielded another intermediate with characteristics similar to a hydrazine complex as observed in CV experiments. These findings would confirm the one electron oxidation of **2a** to **2b** to be the initial step in the catalytic cycle. Under catalytic conditions this intermediate would rapidly react with ammonia to form a hydrazine complex. Since the selected solvent, NM, was not innocent towards the added base, overcoming the solubility of **2b** in solvents such as THF or DCM is recommended.

Additionally, reactions of **2a** with DBU were conducted using RRDE experiments in THF, which initially suggested that very short-living intermediates were generated. RRDE experiments with NH_3 as the base (not presented in this dissertation) were also performed, however the results were complicated, probably due to the material of the ring (Pt) which seems to have a catalytic effect on hydrazine decomposition. Thus, for those conditions a RRDE with both the disk and the ring being made of glassy carbon are required.

APPENDIX

A4.1. ^1H NMR Spectra

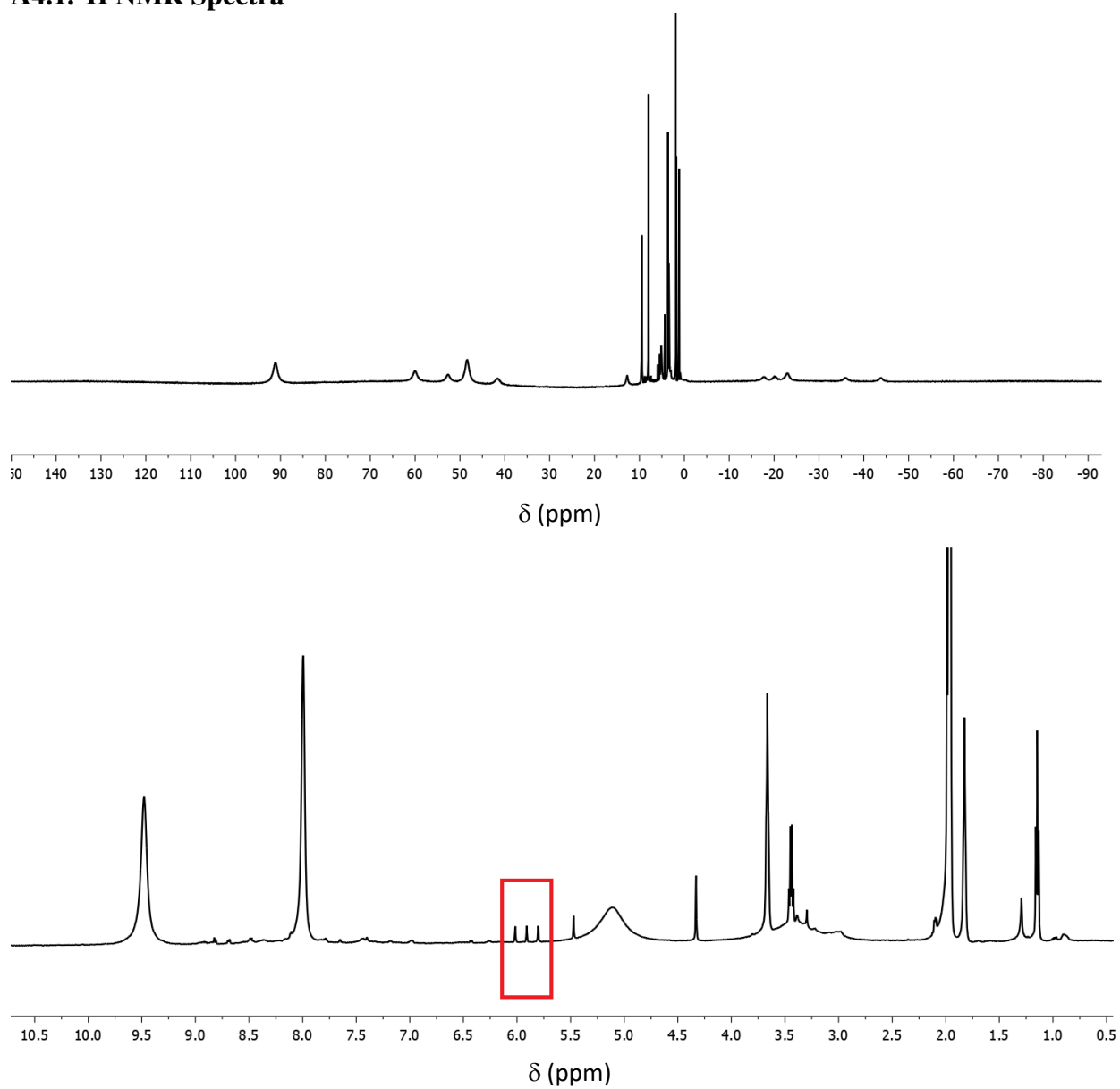


Figure A4.1.1 Full ^1H NMR spectrum (500 MHz, $\text{acetonitrile-}d_3$, 25 $^\circ\text{C}$) of **2b** (top) and the magnified region between 5 and 10 ppm (bottom). The red square highlights the resonances related to ammonium that is produced after the coordinated NH_3 was replaced with acetonitrile.

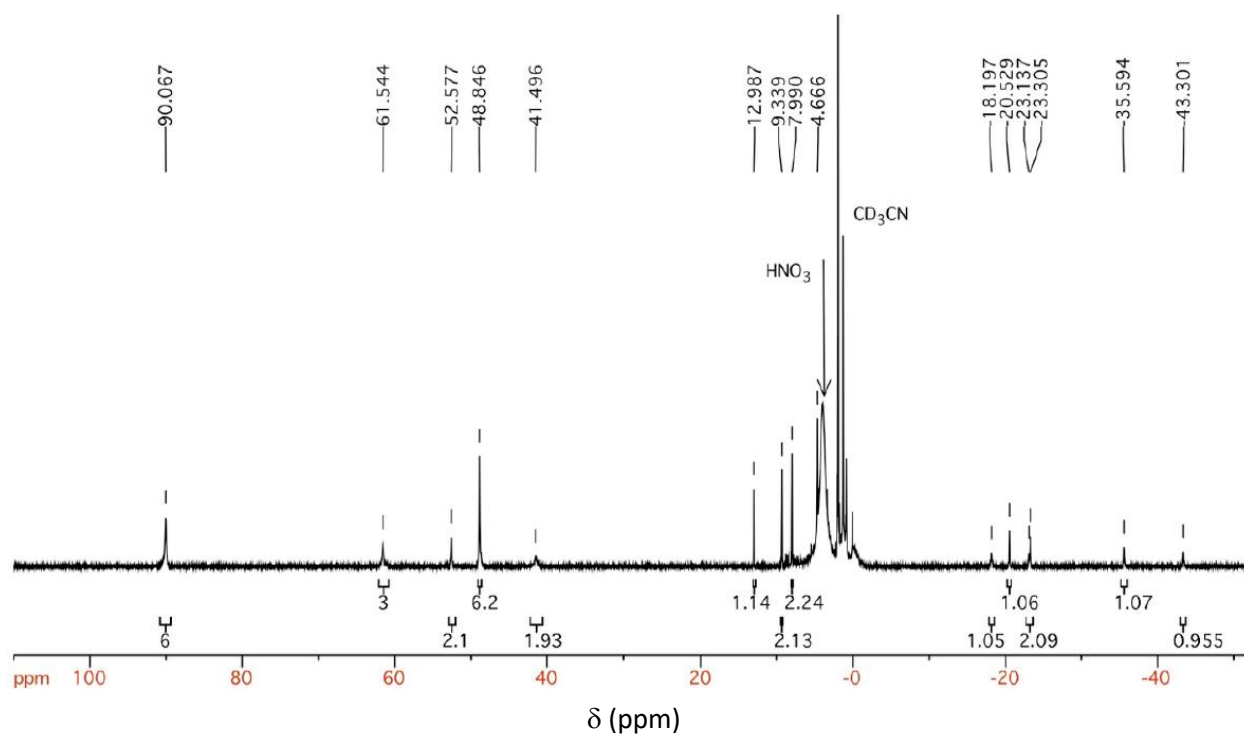


Figure A4.1.2 ^1H NMR spectrum (500 MHz, acetonitrile- d_3 with 0.1% HNO_3 , 25 $^\circ\text{C}$) of the paramagnetic complex **2b** added to prevent redox disproportionation.¹⁷

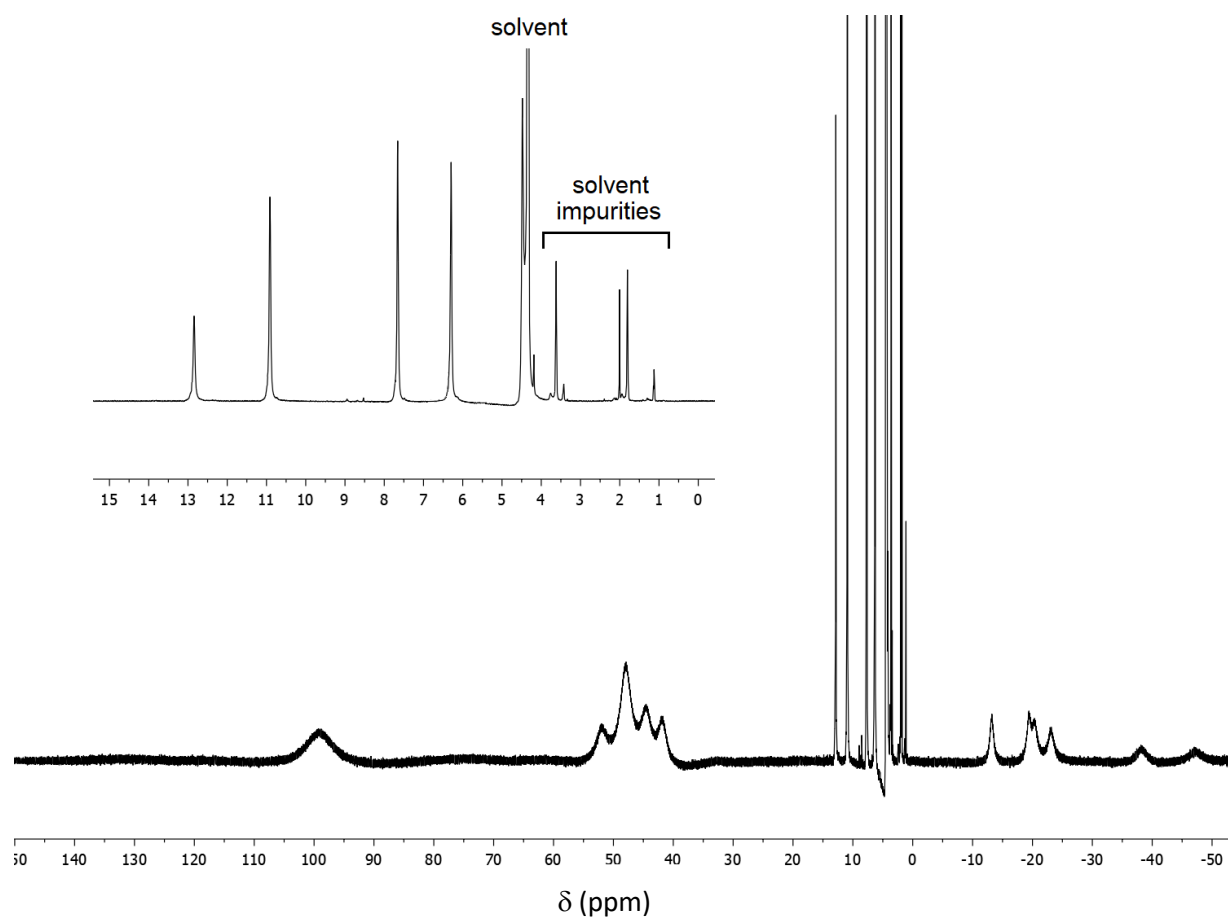


Figure A4.1.3 ^1H NMR spectrum (500 MHz, nitromethane- d_3) of **2b**. The Inset shows the magnified upfield region between δ 0 to 15 ppm.

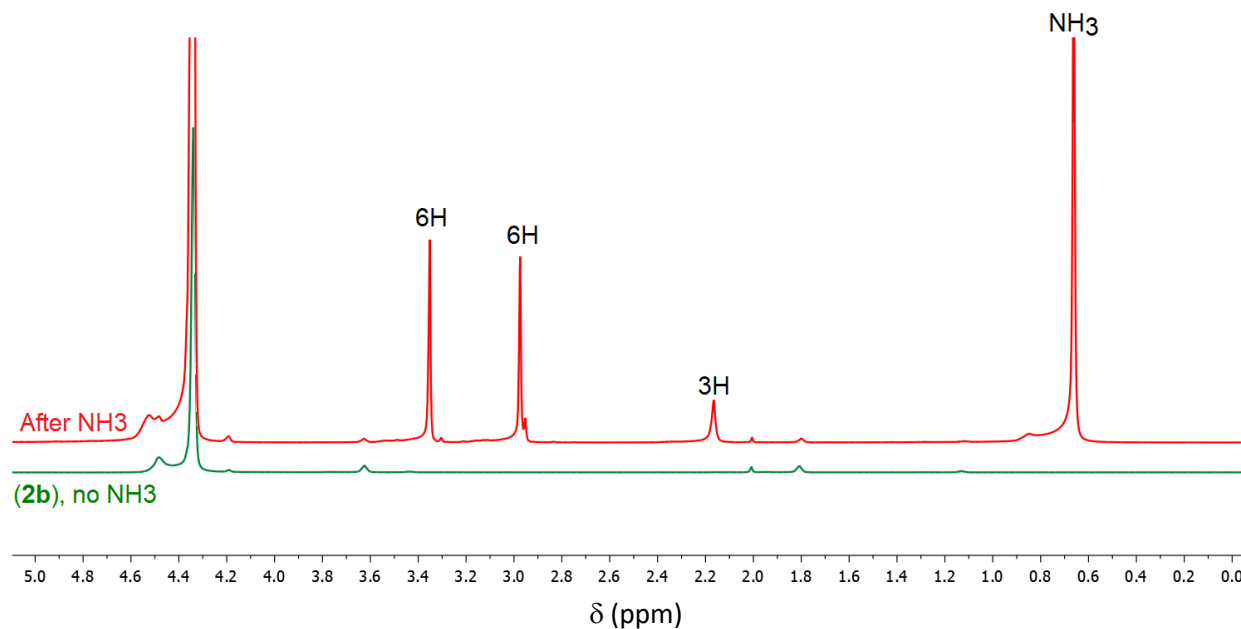


Figure A4.1.4 The upfield region of the ^1H NMR spectrum (500 MHz, nitromethane- d_3) of **2b** before (green) and after (red) addition of NH_3 , which shows the reappearance of methyl and amine proton resonances, related to regeneration of **2a**.

A4.2. Infrared Spectroscopy

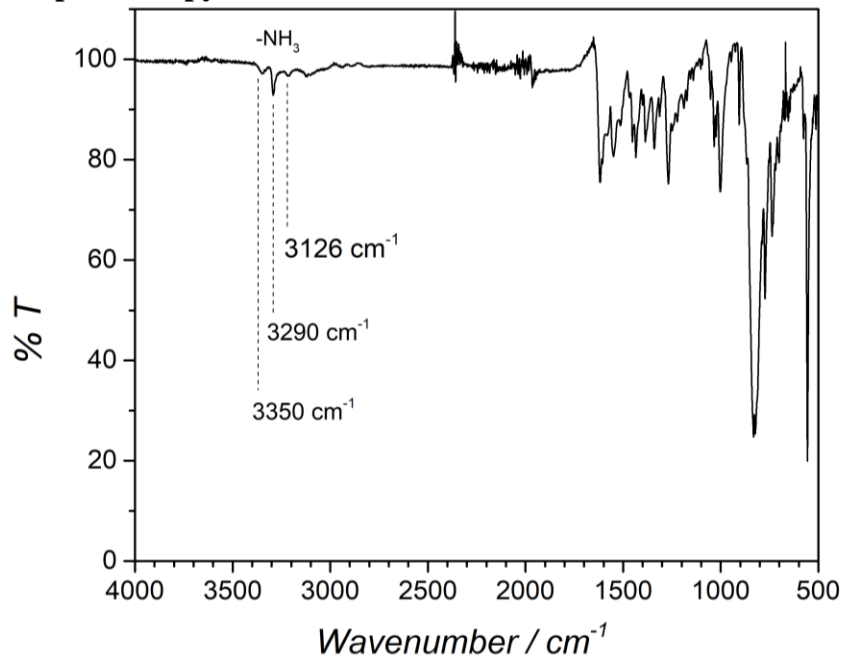


Figure A4.2.1 ATIR Spectrum obtained for a solid sample of **2b**. The stretches associated to the coordinated ammine are shown.

A4.3. Hydrodynamic Linear Scan Voltammetry of **2b** in NM Using an RDE

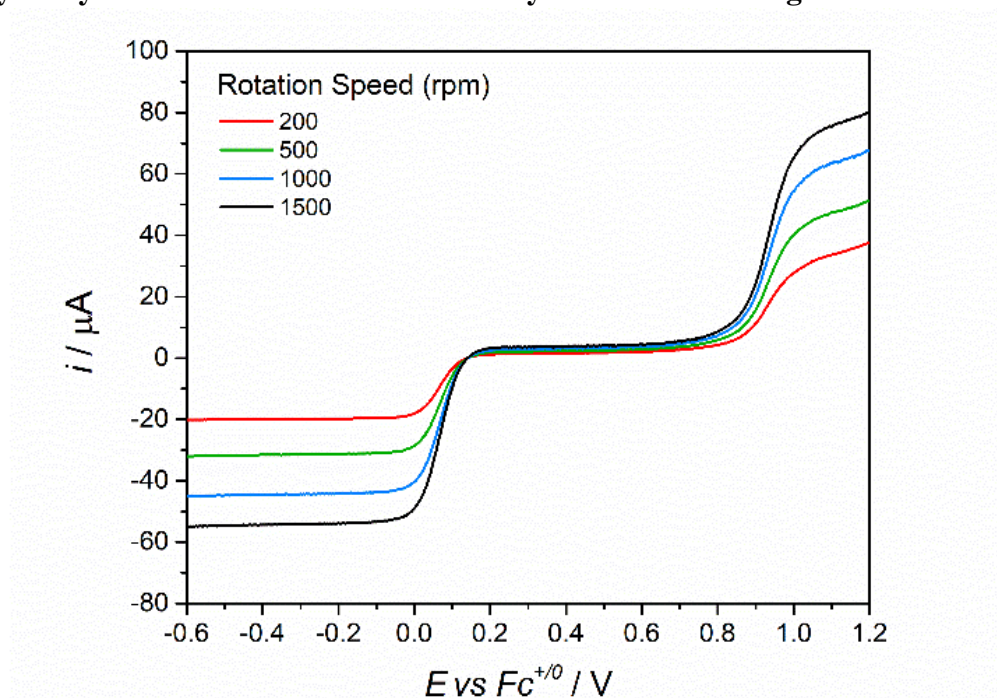


Figure A4.3.1 RDE linear scan voltammograms of a solution of 2.10×10^{-3} **2b** in NM, scan rate 0.01 V s^{-1} . The first process ($E_{1/2}=0.085 \text{ V vs. Fc}^{+/0}$) is the reduction of Ru(III) to Ru(II) and the second process at $0.96 \text{ V vs. Fc}^{+/0}$ is oxidation of Ru(III) to Ru(IV).

A4.4. Bulk Electro-Reduction of 2b to 2a

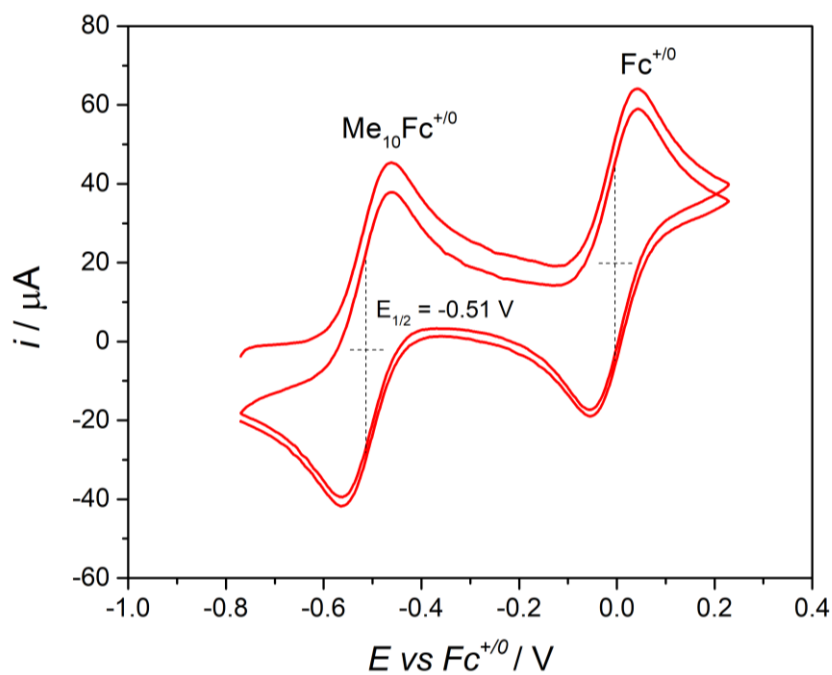


Figure A4.4.1 Half potential of $\text{Me}_{10}\text{Fc}^{+/0}$ measured by CV (two successive cycles) versus $\text{Fc}^{+/0}$ in acetonitrile. Scan rate 0.1 V s^{-1} .

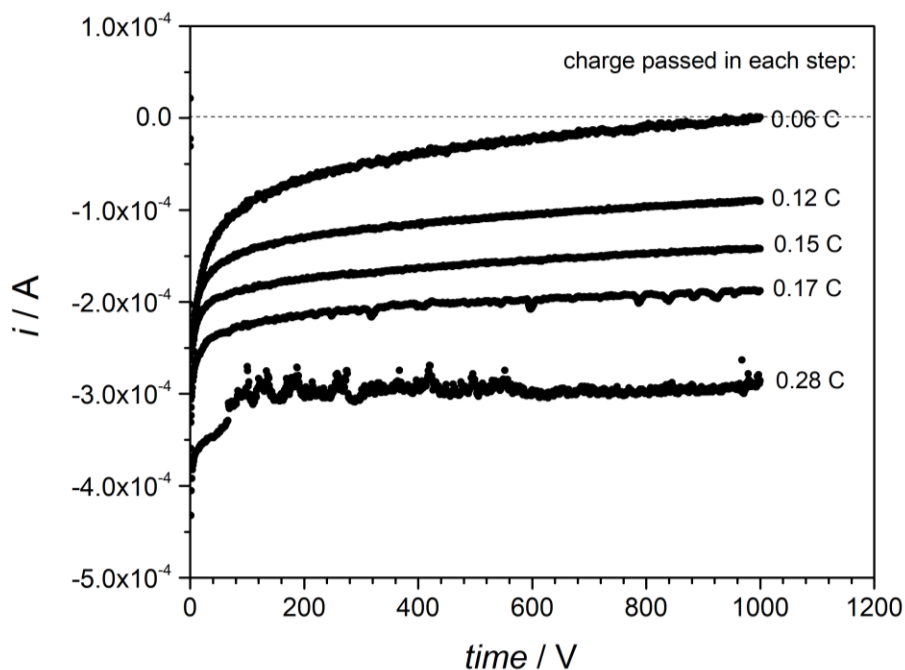


Figure A4.4.2 Currents passing for five steps of electrolysis of 8.0 mg **2b** in 10 mL THF (7.77×10^{-4} M) at a constant potential of -0.25 V versus $E_{1/2}$. A total of 0.78 C charge (1.03 equiv. of electrons) was passed at the end of the electrolysis.

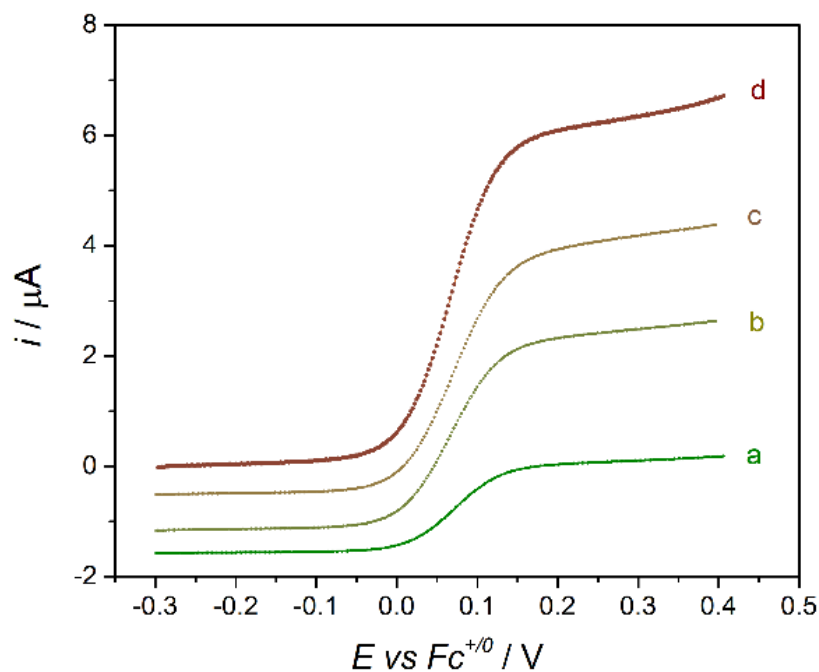


Figure A4.4.3 Hydrodynamic linear scans obtained using a rotating disk electrode after three steps of reduction of **2b** (7.7×10^{-6} mol) in THF. (a) 0, (b) 0.28, (c) 0.45 and (d) 0.78 C charge passed. Scan rate 10 mV s^{-1} .

A4.5. DI-MS Data

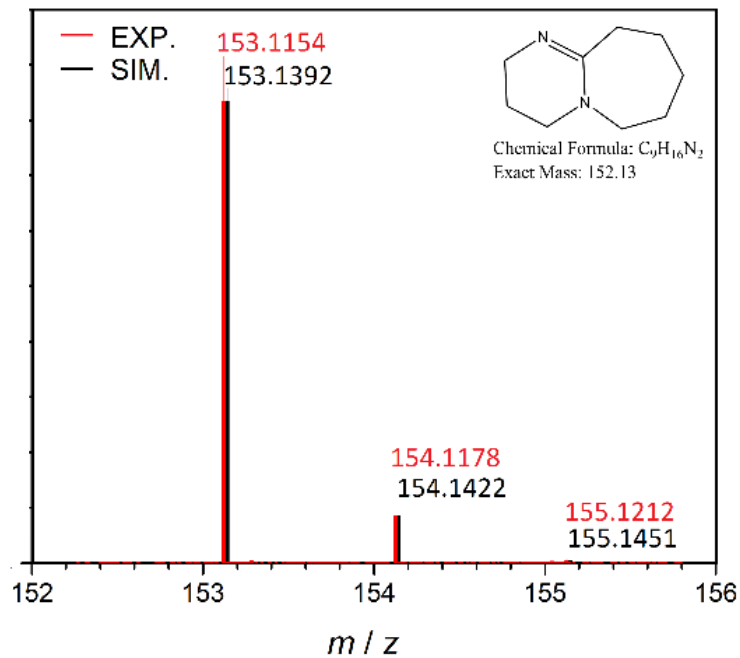


Figure A4.5.1 Fragmentation pattern for protonated DBU. red: experimental and black: simulated spectra. This data shows that for DI-MS results, there is an almost significant difference between observed and simulated m/z values.

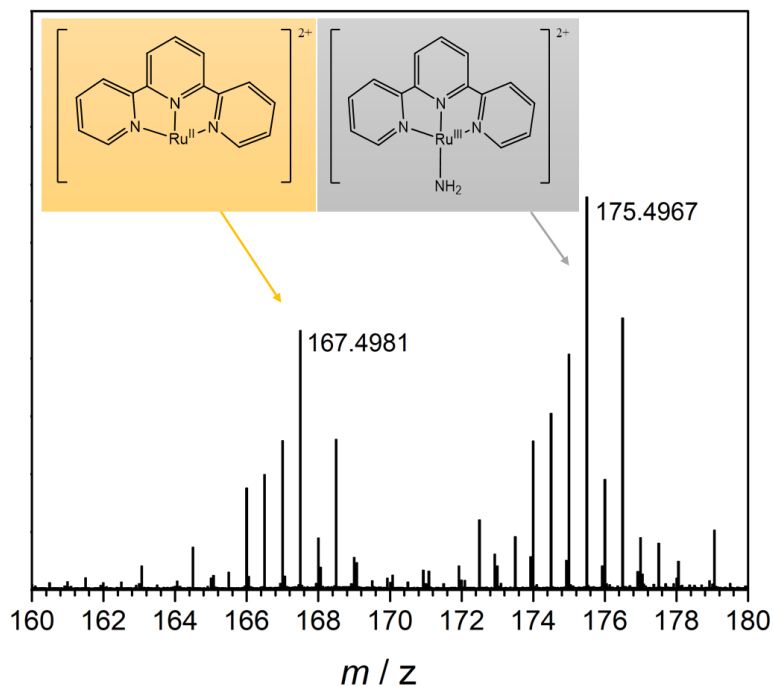


Figure A4.5.2 Ions assigned to charge-to-mass values observed for peaks I and II in Figure 4.3.1.

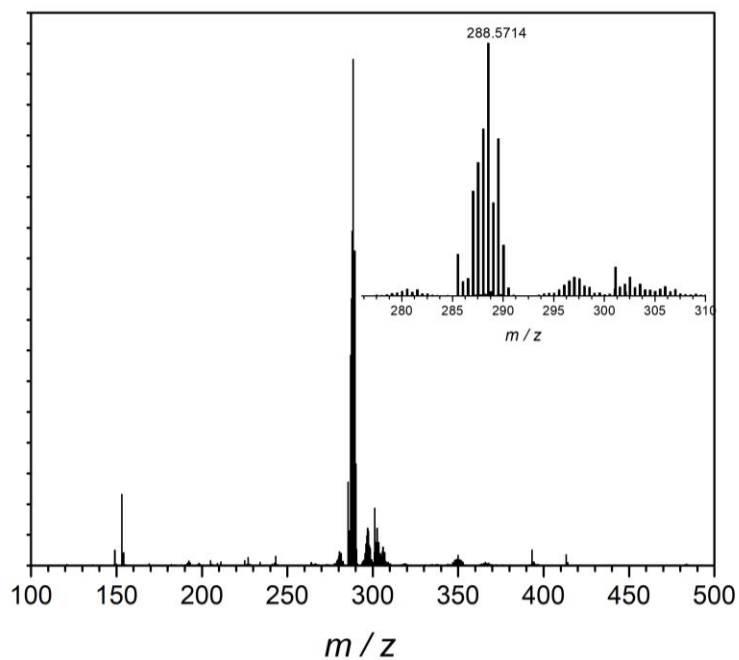


Figure A4.5.3 Mass spectra obtained for direct infusion of a sample containing **2a** in NM. The inset is mass-to-charge 280 -310 the region magnified. This is similar to peak cluster VI in Figure 4.3.1.

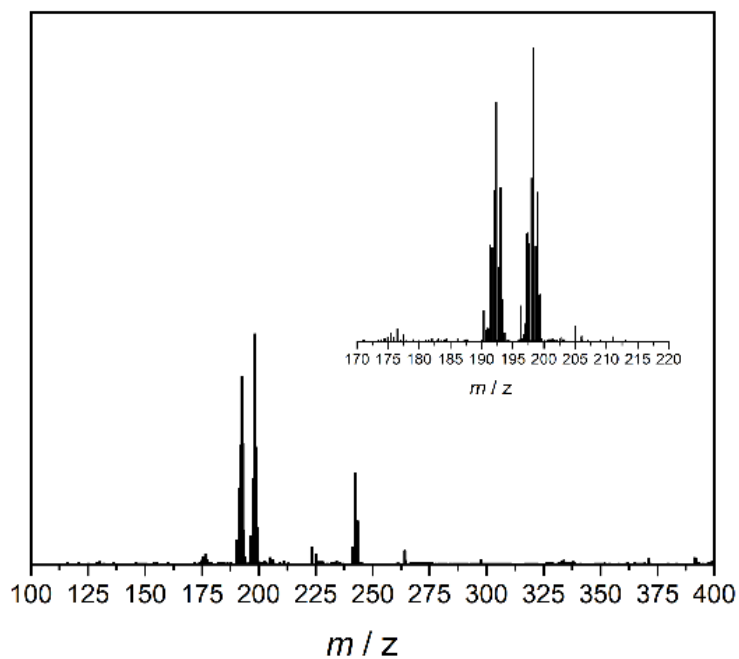


Figure A4.5.4 Mass spectra obtained for direct infusion of a sample containing **2b** in NM. The inset is mass-to-charge 170 -220 the region magnified. This is similar to peak clusters III and IV in Figure 4.3.1 (triply charges fragmentations).

A4.6. Vis-Spectrophotometric Data

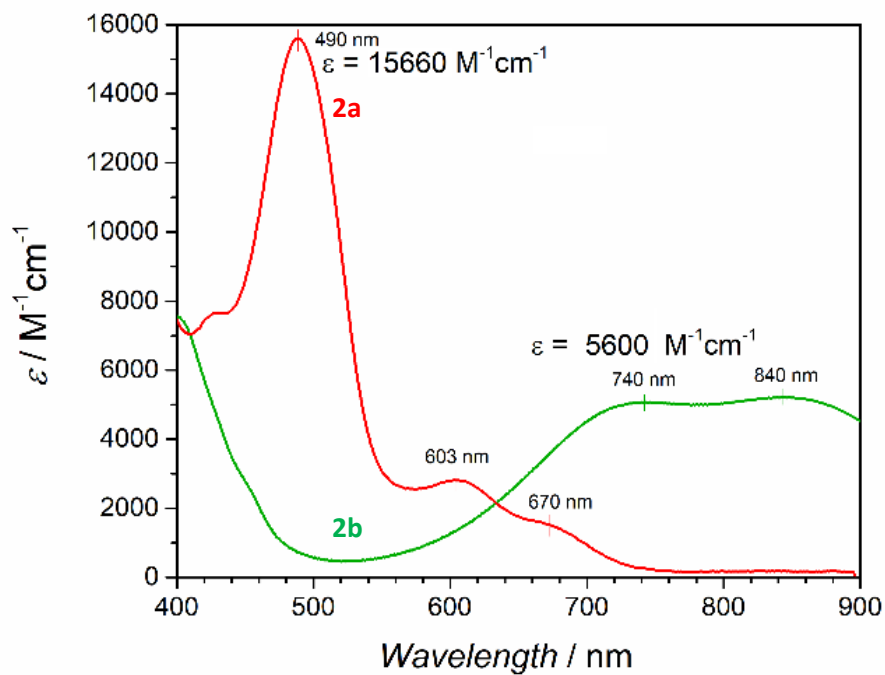


Figure A4.6.1 Electronic absorption spectra of $7.10 \times 10^{-6} \text{ M}$ **2a** (red) and $7.65 \times 10^{-5} \text{ M}$ **2b** (green) in NM.

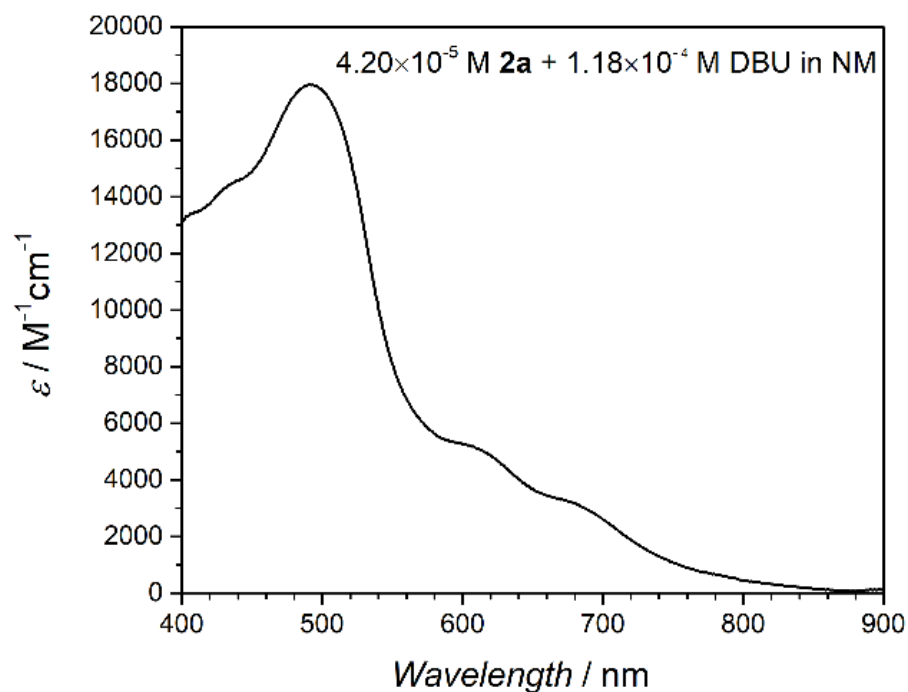


Figure A4.6.2 Electronic absorption spectrum of a solution containing $4.20 \times 10^{-5} \text{ M}$ **2a** and $1.18 \times 10^{-4} \text{ M}$ DBU in NM.

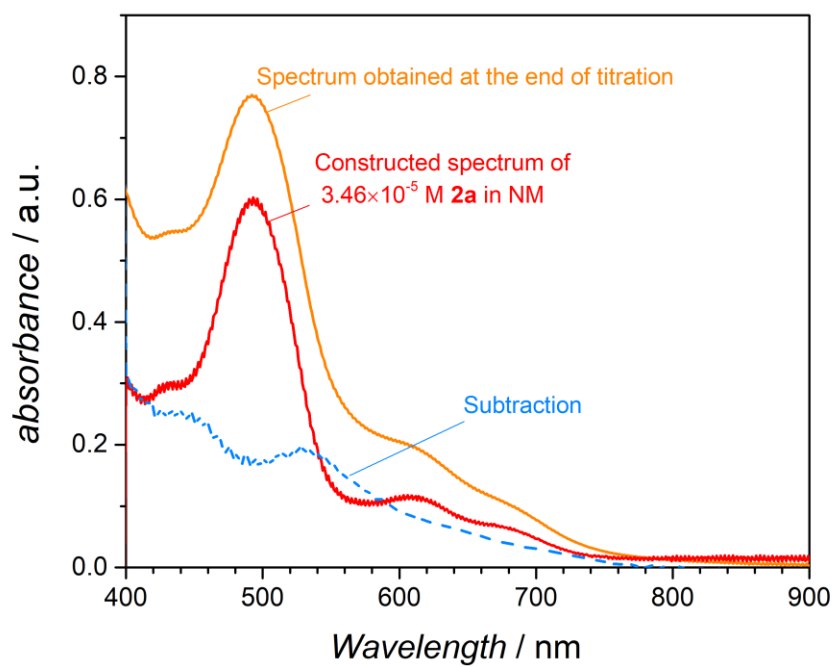
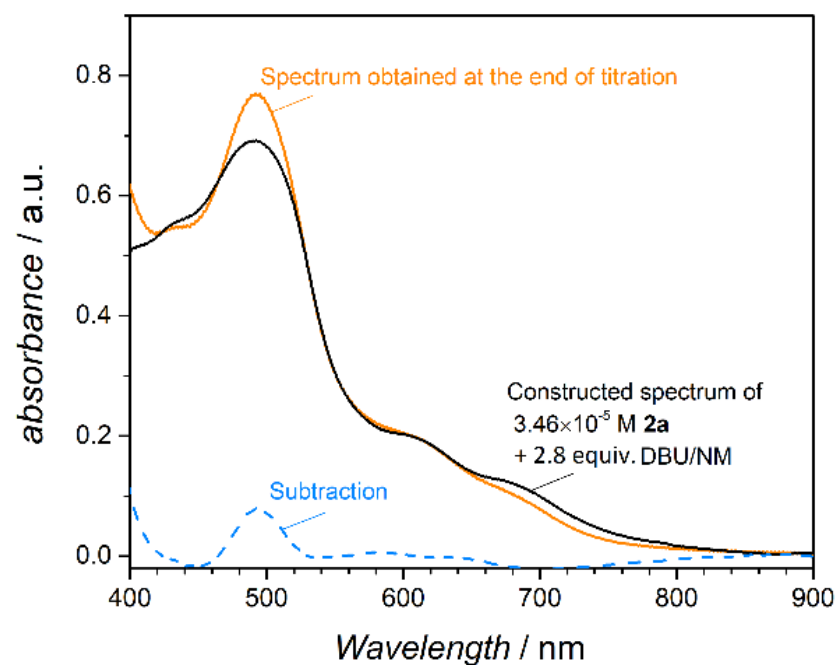


Figure A4.6.3 Subtraction spectra (blue) for two cases: Top: The simulated spectrum for 0.5 equiv. **2a** plus 2.8 (=2×1.4) equiv. DBU (black) is subtracted from the final absorption spectrum (orange), Bottom: The simulated spectrum for 0.5 equiv. **2a** (red) is subtracted from the final absorption spectrum (orange).

A4.7. RRDE Experiments

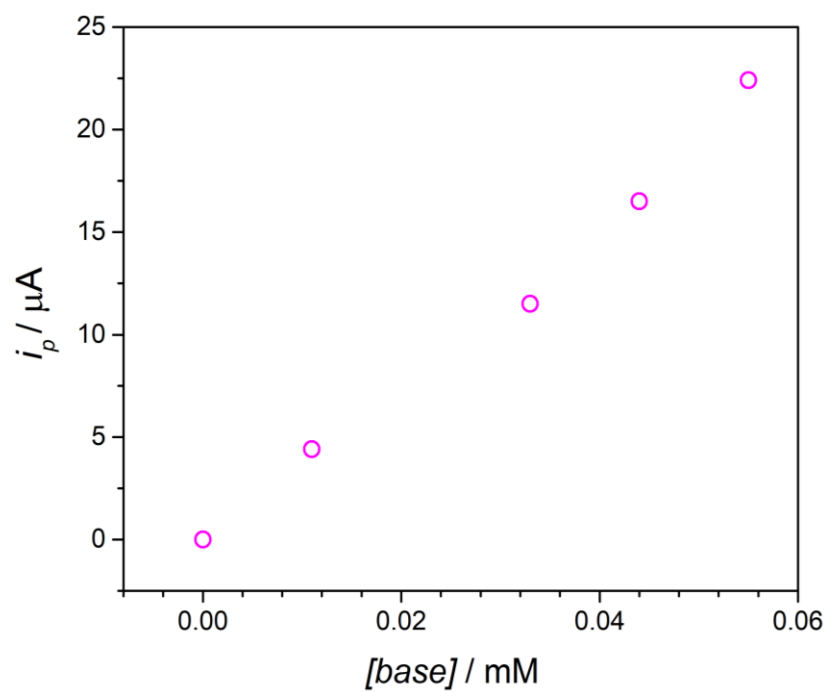


Figure A4.7.1 Dependence of the pre-peak current (i_p) on the concentration of DBU. Data extracted from Fig. 4.14.

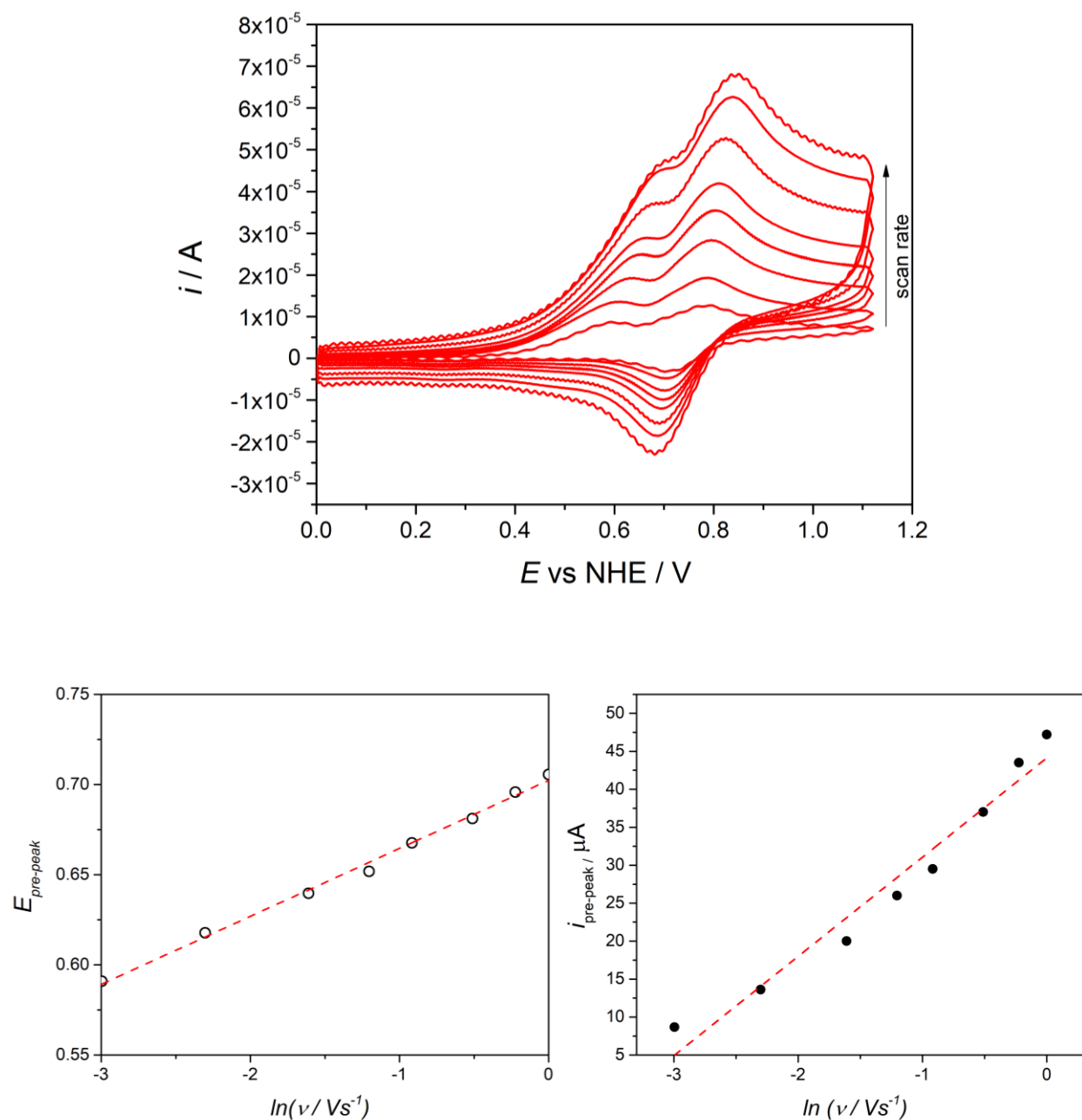


Figure A4.7.2 Top: CVs dependence on the scan rate on solution containing 4.58×10^{-4} M **2a** and 1.55×10^{-4} M DBU. Scan rates are 0.05, 0.1, 0.2, 0.3, 0.4, 0.6, 0.8 and 1.0 Vs^{-1} . Bottom: dependence of the pre-peak potential in V vs. NHE (left) and current (bottom) on the scan rate.

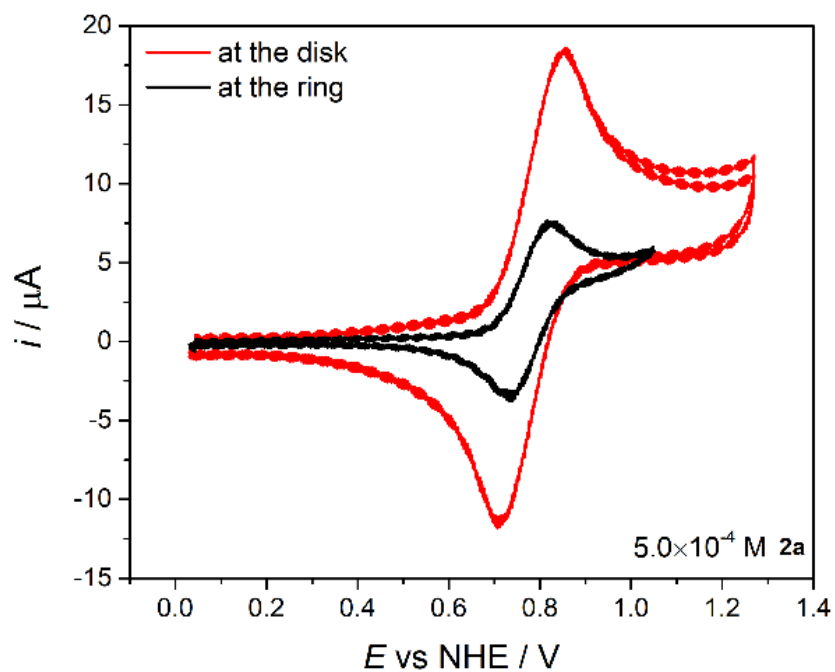


Figure A4.7.3 CVs obtained for a solution containing $5.0 \times 10^{-4} \text{ M } 2a$ in THF collected at the ring and the disk. Scan rate 0.1 Vs^{-1} . This CVs was taken prior to the RRDE control experiments shown in Figure A4.7.4.

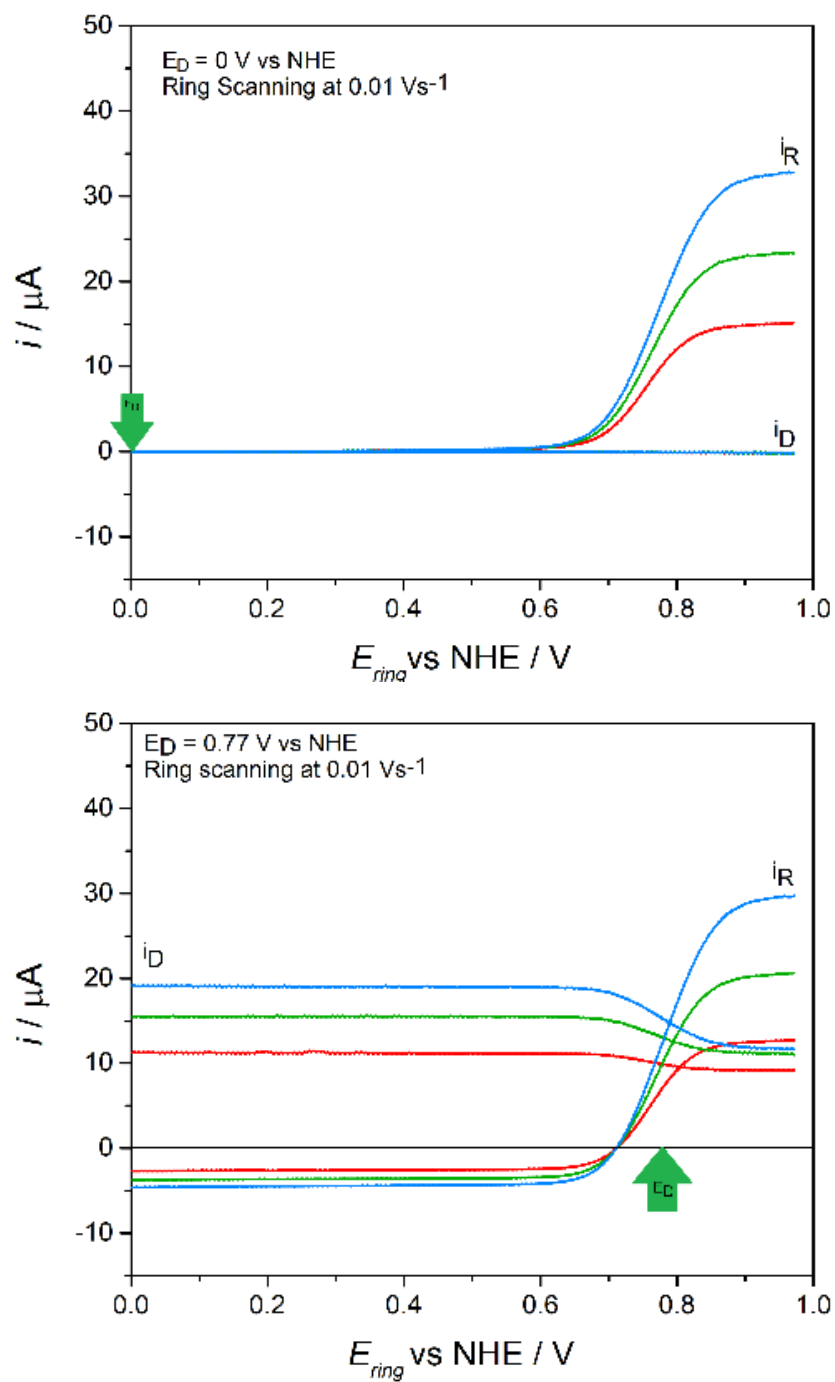
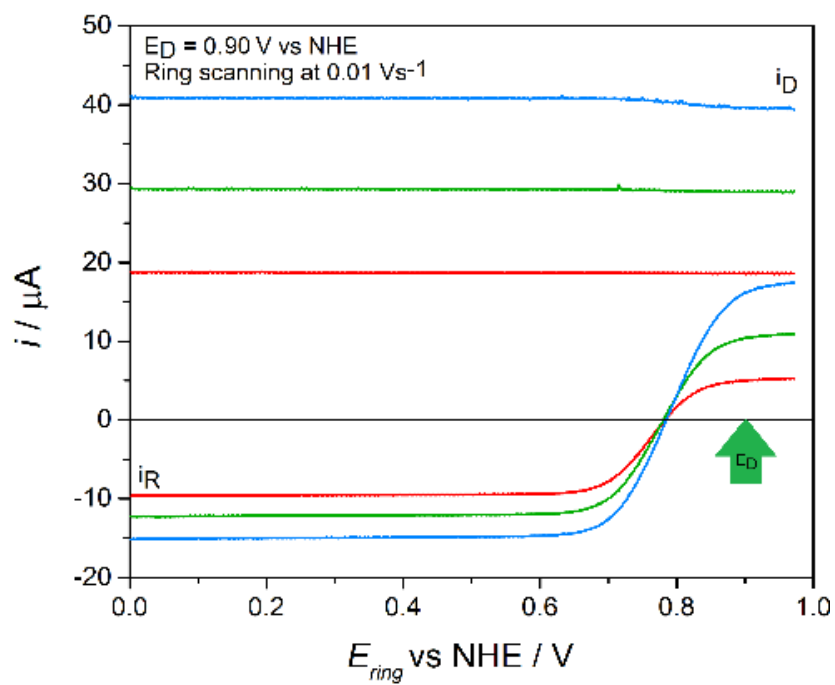


Figure A4.7.4 RRDE LSVs obtained for a solution containing $5.0 \times 10^{-4} \text{ M}$ **2a** in THF. The disk was set at a constant potential of 0 (top), 0.77 (bottom) and 0.9 V (next page) vs. NHE while the ring was scanned. Rotation speeds: 200 (red), 500 (green) and 1000 (blue) rpm.

Figure A4.7.4. (cont'd)



It appears that when the disk potential is almost equal to $E_{1/2}$, the disk potential is affected by the ring events!

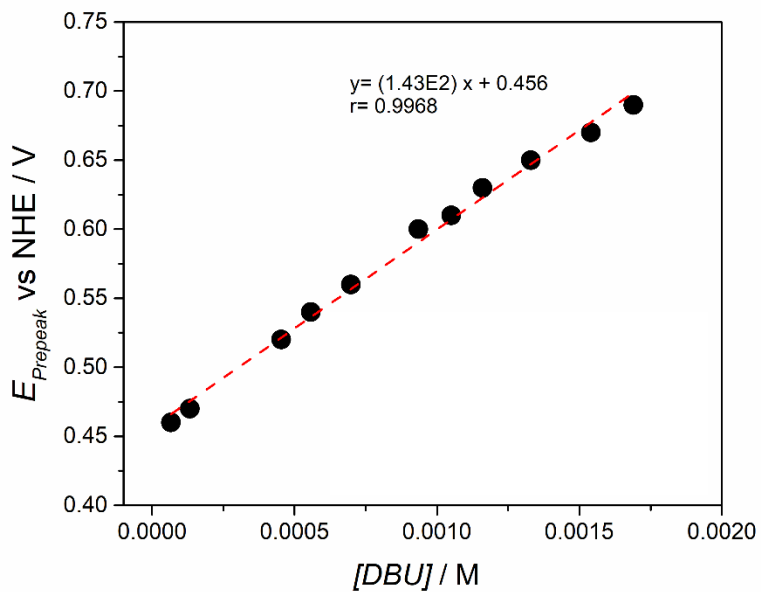
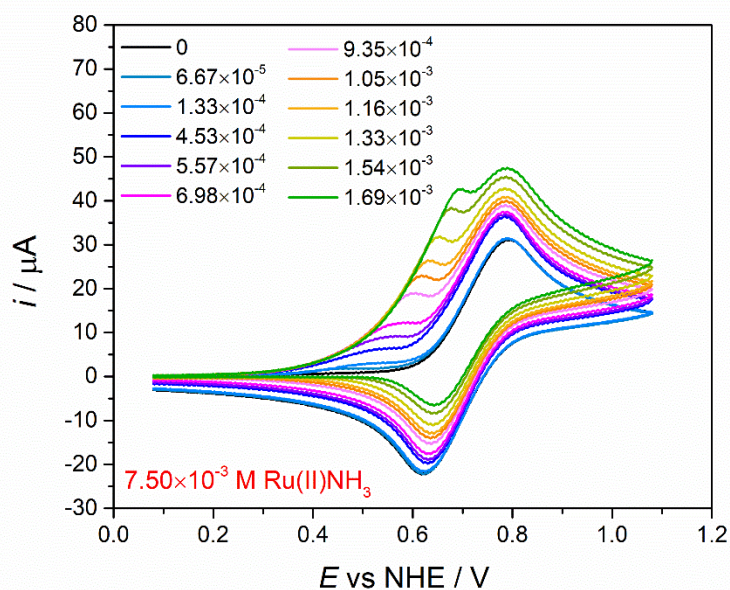
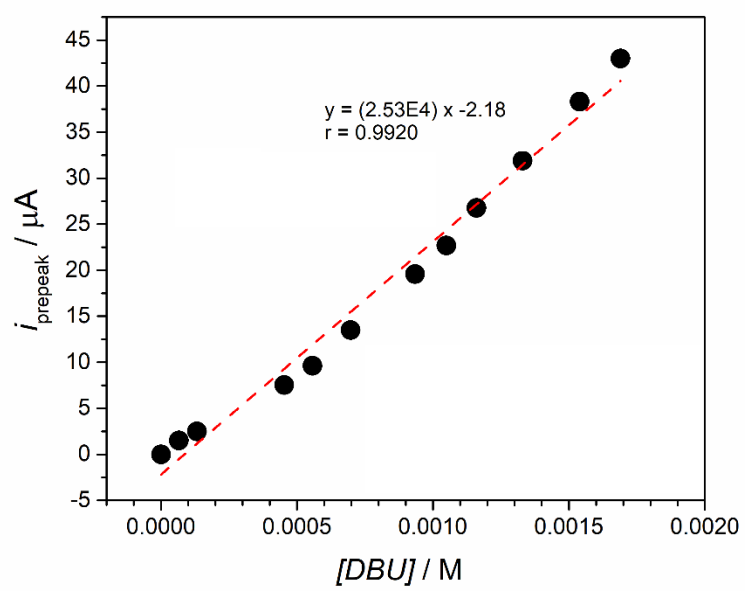


Figure A4.7.5 Raw CVs obtained after additions of DBU to a solution of 7.5 mM **2a** in THF, scan rate 0.1 Vs^{-1} (top). No shifting in the potentials were observed (compared to the CVs taken using a RRDE). The linear dependence of the pre-peak potential (bottom) and current (next page) to [DBU].

Figure A4.7.5 (Cont'd.)



REFERENCES

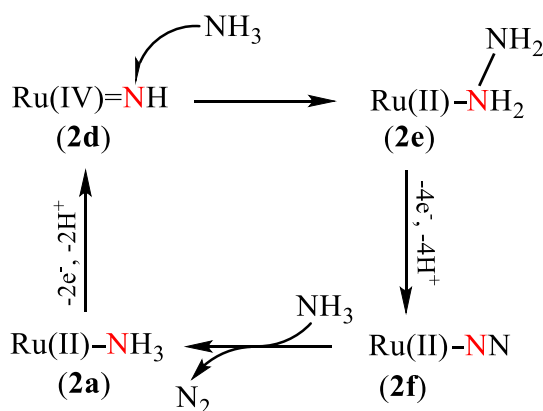
REFERENCES

- (1) Schubert, E. M. *J. Chem. Educ. Educ.* **1959**, 69 (1), 62.
- (2) Bain, G. A.; Berry, J. F. *J. Chem. Educ.* **2008**, 85 (4), 532.
- (3) Kettle, S. F. A. In *Physical Inorganic Chemistry*; Springer Berlin Heidelberg, 1996.
- (4) Lin, L.; Yu, Q.; Yan, X.; Hang, W.; Zheng, J.; Huang, B. *Analyst* **2010**, 135, 2970–2978.
- (5) Coia, G. M.; Demadis, K. D.; Meyer, T. J.; Carolina, N.; Hill, C.; Carolina, N.; January, R. V. **2000**, 2212–2223.
- (6) Huynh, M. H. V.; Meyer, T. J. *Chem. Rev.* **2007**, 107, 5004–5064.
- (7) Kojima, T.; Nakayama, K.; Ikemura, K.; Ogura, T.; Fukuzumi, S. *J. Am. Chem. Soc.* **2011**, 133, 11692–11700.
- (8) Meyer, T. J.; Moyer, B. a. *J. Am. Chem. Soc.* **1979**, No. 101, 1326–1328.
- (9) Ishizuka, T.; Kotani, H.; Kojima, T. *Dalt. Trans.* **2016**, 45, 16727–16750.
- (10) Ohzu, S.; Ishizuka, T.; Hirai, Y.; Jiang, H.; Miyuki, S.; Takashi, O.; Shunichi, F.; Kojima, T. *Chem. Sci.* **2012**, 3, 3421–3431.
- (11) Concepcion, J. J.; Tsai, M.-K.; Muckerman, J. T.; Meyer, T. J. *J. Am. Chem. Soc.* **2010**, 132 (14), 1545–1557.
- (12) Meyer, T. J.; Thompson, M. S. *J. Am. Chem. Soc.* **1981**, 103, 5579–5581.
- (13) Bard, a J.; Itaya, K.; Malpas, R. E.; Teherani, T. *J. Phys. Chem.* **1980**, 84 (1975), 1262–1266.
- (14) Matthews, W. S.; Bares, J. E.; Bartmess, J. E.; Bordwell, F. G.; Cornforth, F. J.; Drucker, G. E.; Margolin, Z.; Mccallum, R. J.; Mccollum, G. J.; Vanier, N. R. *J. Am. Chem. Soc.* **1975**, 97 (24), 7006–7014.
- (15) Bordwell pKa Table (Acidity in DMSO). <https://www.chem.wisc.edu/areas/reich/pkatable/>
- (16) Shaffer, D. W.; Xie, Y.; Concepcion, J. J. *Chem. Soc. Rev.* **2017**, 46, 6170–6193.
- (17) Habibzadeh, F.; Miller, S. L.; Hamann, T. W.; Smith, M. R. *Proc. Natl. Acad. Sci.* **2019**, 3 (1), 2–6.

CHAPTER 5: THE $[\text{Ru}(\text{TRPY})(\text{DMABPY})\text{N}_2\text{H}_4]^{2+}$ INTERMEDIATE

To elucidate the catalysis mechanism, identification of the possible intermediates in the catalytic cycle is very important. Such intermediates were not detected under catalytic conditions, *i.e.*, directly from the BE solution, since the spectrophotometric and NMR experiments after the electrolysis only showed the starting $[\text{Ru}(\text{trpy})(\text{dmabpy})\text{NH}_3]^{2+}$, **2a**. Thus, independent synthesis of some intermediates was pursued based on what was understood from the previous experiments. In the previous chapter $[\text{Ru}(\text{trpy})(\text{dmabpy})\text{NH}_3]^{3+}$, **2b**, as the first intermediate was discussed. Chapter 5 focuses on the chemistry of $[\text{Ru}(\text{trpy})(\text{dmabpy})\text{N}_2\text{H}_4]^{2+}$, **2e**.

The labeling experiments suggest that N-N bond formation is resulted from the nucleophilic attack of the ammonia to highly electrophilic nitrogen in of the intermediates. This provides evidence for a hydrazine pathway as illustrated in Scheme 5.1.



Scheme 5.1 The hydrazine pathway to formation of the N-N bond. The nucleophilic attack of the free NH_3 to an imido nitrogen leads into formation of a hydrazine intermediate. The polypyridyl ligands are omitted.

While existence of **2d** is not yet supported by direct evidences, it is speculated that an intermediate with a high-valent ruthenium should form to provide a highly electrophilic nitrogen. Attack of the ammonia's nitrogen to this nitrogen would lead to the formation of a bound hydrazine. Whether the N_2H_4 ligand remains coordinated or leaves the metal center under catalytic conditions is still

questionable. However, as we would discuss the formation of such hydrazine intermediates are very likely to be a part of the cycle.

Electrophilic-nucleophilic reactions between the catalyst and the substrate are reported and studied in several cases. The nucleophilic attack of the substrate water to Ru(V) or Ru(IV)oxo species is considered as the main path to O-O bond formation in homogeneous catalytic oxidation of water when single site ruthenium catalysts are employed.¹⁻³ Meyer and Thompson observed that when the oxidation of $[\text{Ru}(\text{trpy})(\text{bpy})\text{NH}_3]^{2+}$ in aqueous medium at $\text{pH} > 6.8$ is monitored by UV-Vis spectrophotometry, full conversion of $[\text{Ru}(\text{trpy})(\text{bpy})\text{NH}_3]^{2+}$ to $[\text{Ru}(\text{trpy})(\text{bpy})\text{NH}_2\text{OH}]^{2+}$ is occurring.⁴ Additionally, Os(V) hydrazido complexes were isolated from electrolysis solution in which $[\text{Os}(\text{trpy})(\text{bpy})\text{NH}_3]^{2+}$ was exhaustively oxidized in the presence of primary amines.⁵ These findings are shedding light on the mechanistic details of reactions that fit into the hydrazine pathway. In this chapter, the experimental results suggesting similar hydrazine pathways in N_2 formation in the introduced catalytic system are discussed.

5.1. Synthesis of an Authentic Sample of $[\text{Ru}(\text{trpy})(\text{bpy})\text{N}_2\text{H}_4]^{2+}$ Complex (2e)

2e was synthesized from the chloro complex following the procedure below:

$[\text{Ru}(\text{trpy})(\text{dmabpy})\text{Cl}]\text{Cl}$ weighed into a heavy walled reaction flask equipped with a stir bar (100 mg, 0.15 mmol, 1 equiv.). Hydrazine monohydrate was added as solvent (10 mL, excess). The reaction flask was closed with a Teflon screw plug and heated as a closed system for 2 h at 90 °C. After heating was complete, the reaction mixture was poured into a 125 mL beaker open to the air in a fume hood. The residue in the reaction flask was rinsed into the beaker with ~1 mL deionized water. Excess ammonium hexafluorophosphate (100 mg, 0.6 mmol, 4 equiv.) was added as a solid into the stirred mixture. After 1 h, brown solids precipitated. The solids were collected

by filtration with a disposable fritted Hirsch funnel of 10-micron pore size. The filter cake was washed with small, dropwise portions of deionized water until the initial brown filtrate ran a lighter pink-tan color. The brown filter cake was dried in the Hirsch funnel for two hours until a free-flowing powder resulted when broken up. The mass of the brown solid was 124 mg (0.138 mmol) after vacuum drying, 92 % isolated yield. **¹H NMR (500 MHz; CD₃CN):** δ 9.21 (d, J = 6.7 Hz, 1H), 8.50 (d, J = 8.1 Hz, 2H), 8.38 (d, J = 8.0 Hz, 2H), 8.12 (t, J = 8.1 Hz, 1H), 7.96 (td, J = 7.9, 1.5 Hz, 2H), 7.87 (dd, J = 5.5, 0.6 Hz, 2H), 7.68 (d, J = 2.8 Hz, 1H), 7.42-7.38 (m, 3H), 7.21 (t, J = 3.4 Hz, 1H), 6.42 (d, J = 6.8 Hz, 1H), 6.15 (t, J = 3.4 Hz, 1H), 4.41 (s, 2H), 3.35 (s, 6H), 2.99 (s, 6H), 2.62 (s, 2H). **¹³C NMR (126 MHz; CD₃CN):** δ 160.4, 160.0, 157.8, 156.9, 155.9, 154.9, 153.7, 151.8, 149.3, 138.2, 134.5, 128.7, 124.5, 123.8, 110.1, 109.5, 106.7, 106.1, 40.1, 39.8. **¹⁹F NMR (470 MHz; CD₃CN):** δ 72.9 (d, JF-P = 706.5 Hz). **³¹P NMR (202 MHz; CD₃CN):** δ -144.6 (septet, JP-F = 706.4 Hz). **HRMS (ESI⁺)** ⁽¹⁾ m/z [M - H]⁺ Calcd for C₂₉H₃₂N₉Ru 608.1824; Found 608.1834. **Anal.** Calcd for C₂₉H₃₃F₁₂N₉P₂Ru: C, 38.76; H, 3.70; N, 14.03. Found: C, 39.00; H, 3.63; N, 13.92. **IR (KBr)** 3378, 3371 cm⁻¹.⁵

5.2. Ligand Displacement in 2e / THF / NH₃

¹H NMR spectra of [Ru(trpy)(dmabpy)N₂H₄]²⁺ in THF-*d*₈ contains two singlets at δ 5.0 and δ 2.8 corresponding to the bound hydrazine (Figure 5.2.1)⁶. Addition of excess concentrations of ammonia to [Ru(trpy)(dmabpy)N₂H₄]²⁺ in THF-*d*₈ does not change the chemical shift of those resonances which suggests that the bound hydrazine is not likely to be replaced by ammonia. The possibility of replacement of the coordinated hydrazine under catalytic conditions would be further discussed.

¹ High Resolution Mass Spectrometry (Electro Spray Ionization – positive mode)

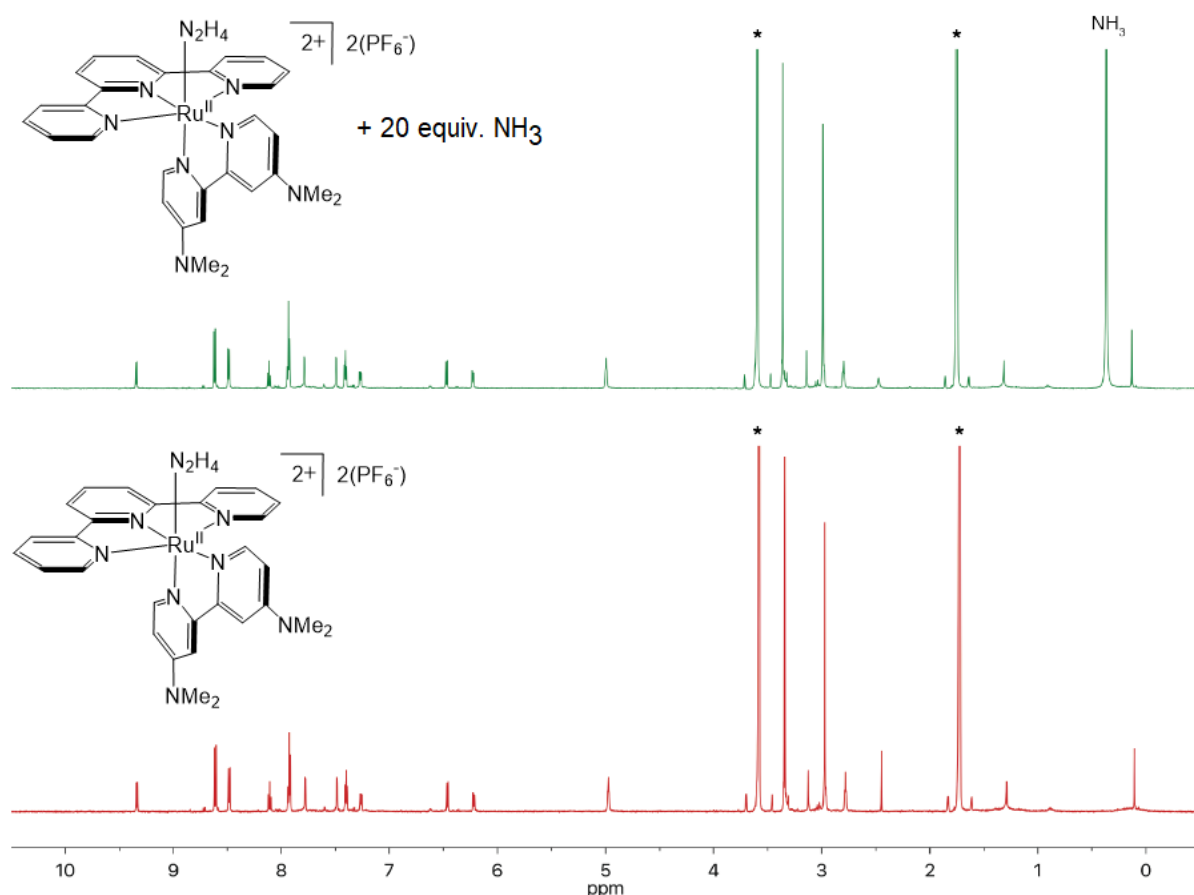


Figure 5.2.1 ^1H NMR reference spectrum (600 MHz, $\text{THF-}d_8$, 25 $^\circ\text{C}$) of complex **2e** with (top) and without (bottom) excess NH_3 . The starred peak is solvent residual. The displacement of the bound hydrazine with free ammonia was not observed.

5.3. Cyclic Voltammetry Studies

$[\text{Ru}(\text{trpy})(\text{dmabpy})\text{N}_2\text{H}_4]^{2+}$, when completely dry is not soluble in dry solvents without the help of sonication. The cyclic voltammograms of $[\text{Ru}(\text{trpy})(\text{dmabpy})\text{N}_2\text{H}_4]^{2+}$ in dry THF and DCM exhibit variable feature over time. The first CVs taken in a freshly made solution of $[\text{Ru}(\text{trpy})(\text{dmabpy})\text{N}_2\text{H}_4]^{2+}$ in DCM has two redox features, a quasi-reversible process at $E_{1/2}(\text{I}) = 0.30 \text{ V vs Fc}^{+/0}$ ($i_{p,a}/i_{p,c} = 1.35$) and an irreversible anodic process at $E_{1/2}(\text{II}) = 0.70 \text{ V vs Fc}^{+/0}$ (Figure 5.3.1, top). The origin of peak II is unknown, but peak I was assigned to $\text{Ru}^{\text{III/II}}(\text{N}_2\text{H}_4)$ couple. When another CV is taken following the first CV, a new redox process appears (Peak III in Figure 5.3.1,

bottom) which gradually vanishes with the number of scans. The position of this new peak matches with the $E_{1/2}$ of $[\text{Ru}(\text{trpy})(\text{dmabpy})\text{NH}_3]^{2+}$ but is not behaving reversibly. Peak III remains in the solutions and does not change with scan rate or potential window. It is only absent in the very first CV taken in the freshly made solution.

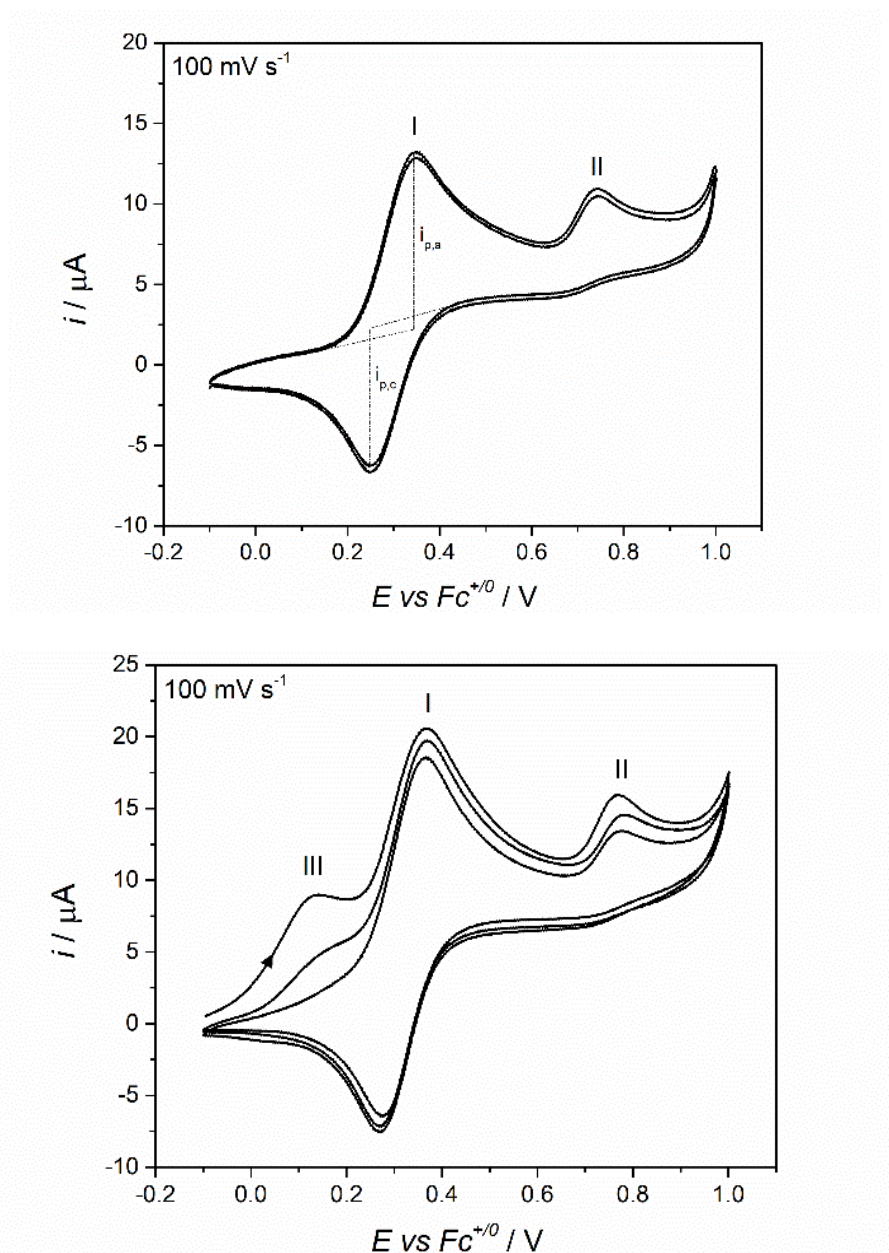


Figure 5.3.1 CVs of $M 1.85 \times 10^{-3} \text{ M } 2e$ in DCM. Top: the initial two cycles, Bottom: Three successive scans taken around 1 min after the CV in the top. Peak III appears after a couple scans are taken in a freshly made solution, but it goes away with successive cycling of the potential. CVs taken after the one shown in the bottom, behave the same way.

Upon bubbling NH_3 into the solution, an enhanced current is observed with an onset potential close to peak III (Figure 5.3.2). These results may suggest that the coordinated N_2H_4 ligand does not remain intact when oxidation of the metal center is enforced, and it is probable that $[\text{Ru}(\text{trpy})(\text{dmabpy})\text{N}_2\text{H}_4]^{2+}$ is converting to $[\text{Ru}(\text{trpy})(\text{dmabpy})\text{NH}_3]^{2+}$ under oxidative conditions.

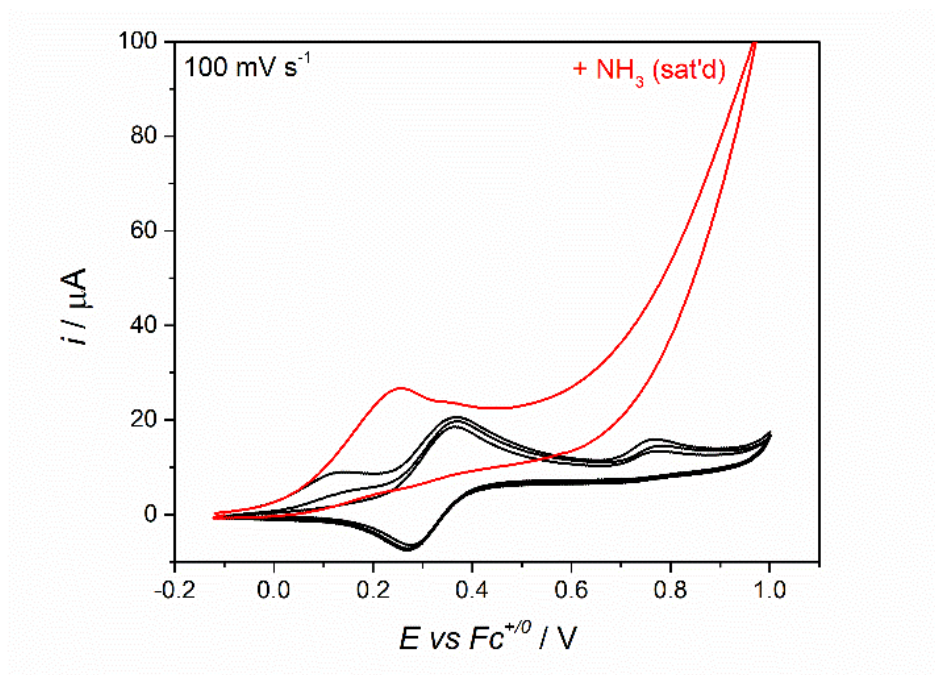


Figure 5.3.2 CVs of $1.85 \times 10^{-3} \text{ M } \mathbf{2e}$ in DCM in the absent (black. Three successive cycles) and presence of ammonia (red). The red curve is very similar to the catalytic oxidation of ammonia in the presence of $\mathbf{2a}$.

CV experiments were then performed in THF since it was the solvent used in the electrolysis. Three peaks were present from the beginning of the experiments as shown in Figure 5.3.3, top, with peak I being initially irreversible. The reversibility of peak I was restored at higher scan rates (Figure 5.3.3, bottom).

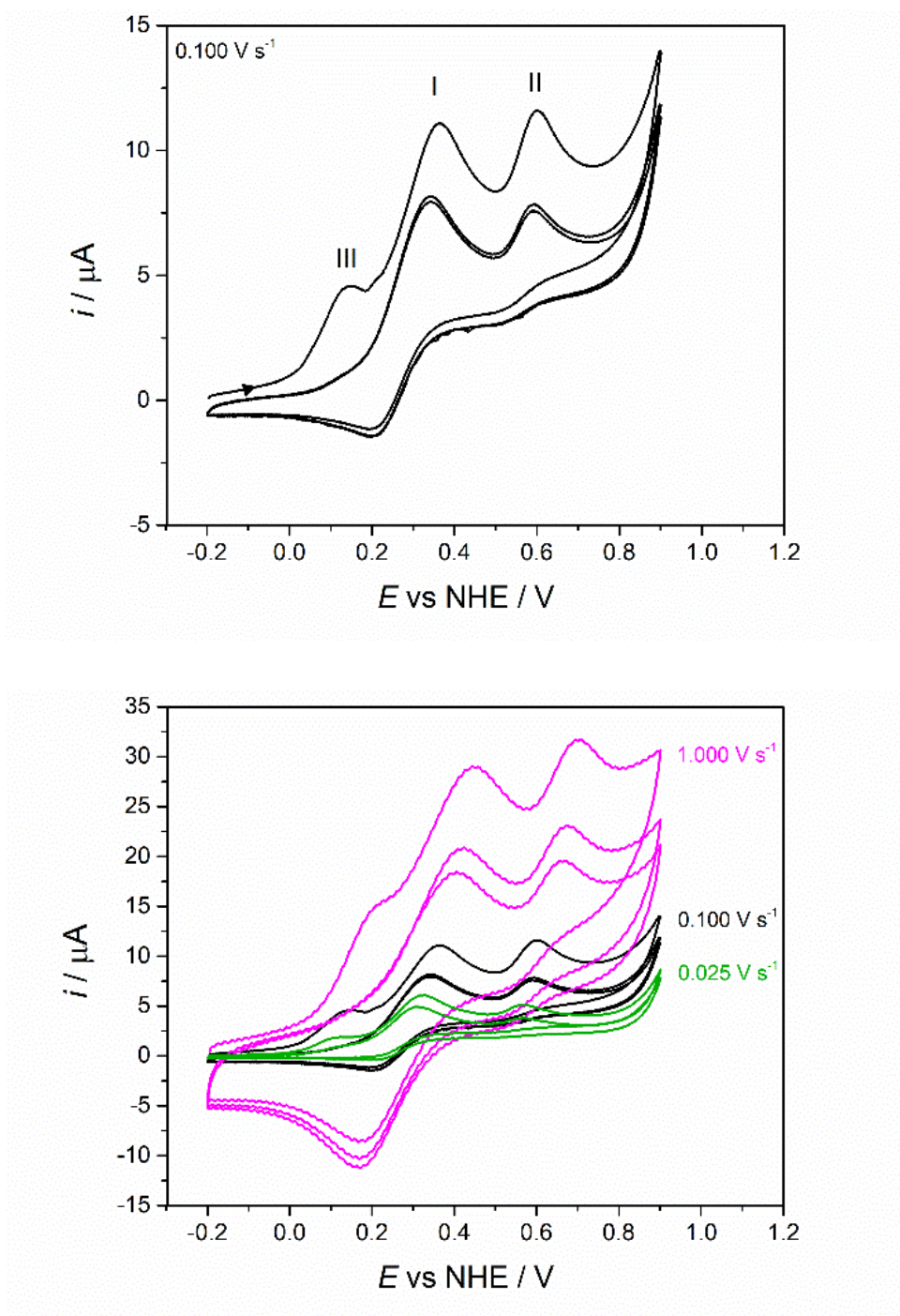


Figure 5.3.3 CVs of $1.22 \times 10^{-3} \text{ M}$ **2e** in THF. Top: three successive cycles in a freshly made solution. Bottom: Changes in the CVs with scan rate (three cycles are shown for each scan rate).

The differences in redox behavior of $[\text{Ru}(\text{trpy})(\text{dmabpy})\text{N}_2\text{H}_4]^{2+}$ in DCM and THF could be related to the basicity and/or coordinating ability of each solvent. When the potential window is changed

to -0.6 to 0.5 V vs. $\text{Fc}^{+/0}$, a very light shoulder was visible between -0.3 to -0.4 V (Figure 5.3.4, black). Similar to the experiments in DCM, the addition of NH_3 to the solution of $[\text{Ru}(\text{trpy})(\text{dmabpy})\text{N}_2\text{H}_4]^{2+}$ in THF resulted in an enhanced current with an onset potential close to peak III (Figure 5.3.4, red), while the shoulder at ~ -0.35 V disappeared.

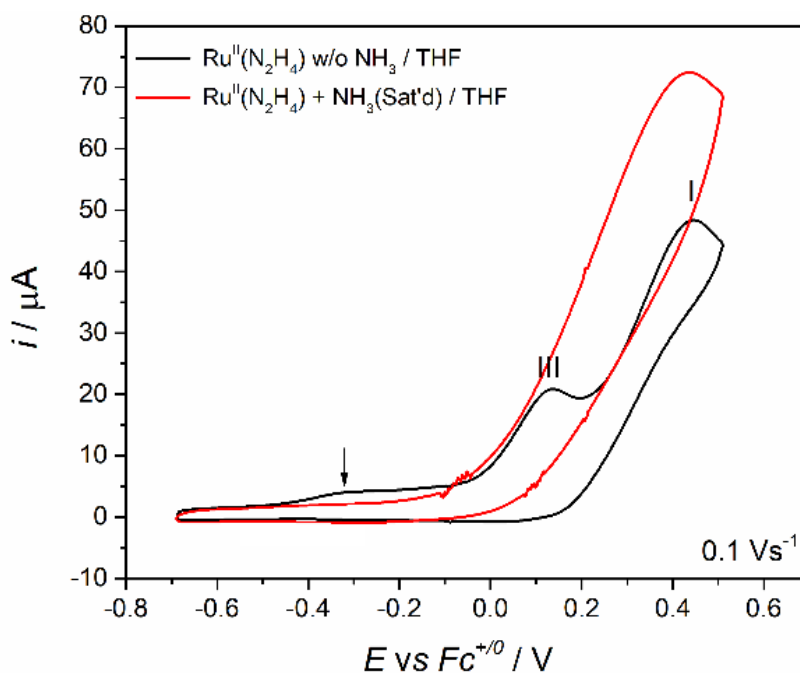


Figure 5.3.4 CVs of 2.50×10^{-3} M **2e** in THF in the absence (black) and presence (red) of NH_3 . A shoulder that is evident at around -0.35 is marked with an arrow.

By adding $[\text{Ru}(\text{trpy})(\text{dmabpy})\text{N}_2\text{H}_4]^{2+}$ to a solution containing $[\text{Ru}(\text{trpy})(\text{dmabpy})\text{NH}_3]^{2+}$ in THF, peaks I and II appeared in the voltammogram and the magnitude of the current associated with $[\text{Ru}(\text{trpy})(\text{dmabpy})\text{NH}_3]^{2+}$ increased (Figure 5.3.5, top), leading to the conclusions that first, peak II is related to $[\text{Ru}(\text{trpy})(\text{dmabpy})\text{N}_2\text{H}_4]^{2+}$ and second, peak III is very likely the amine complex, being generated from $[\text{Ru}(\text{trpy})(\text{dmabpy})\text{N}_2\text{H}_4]^{2+}$ under experimental conditions. Interestingly, very similar cyclic voltammograms were obtained when stoichiometric concentrations of NH_3 were added to a solution containing $[\text{Ru}(\text{trpy})(\text{dmabpy})\text{NH}_3]^{2+}$ (Figure 5.3.5, bottom).

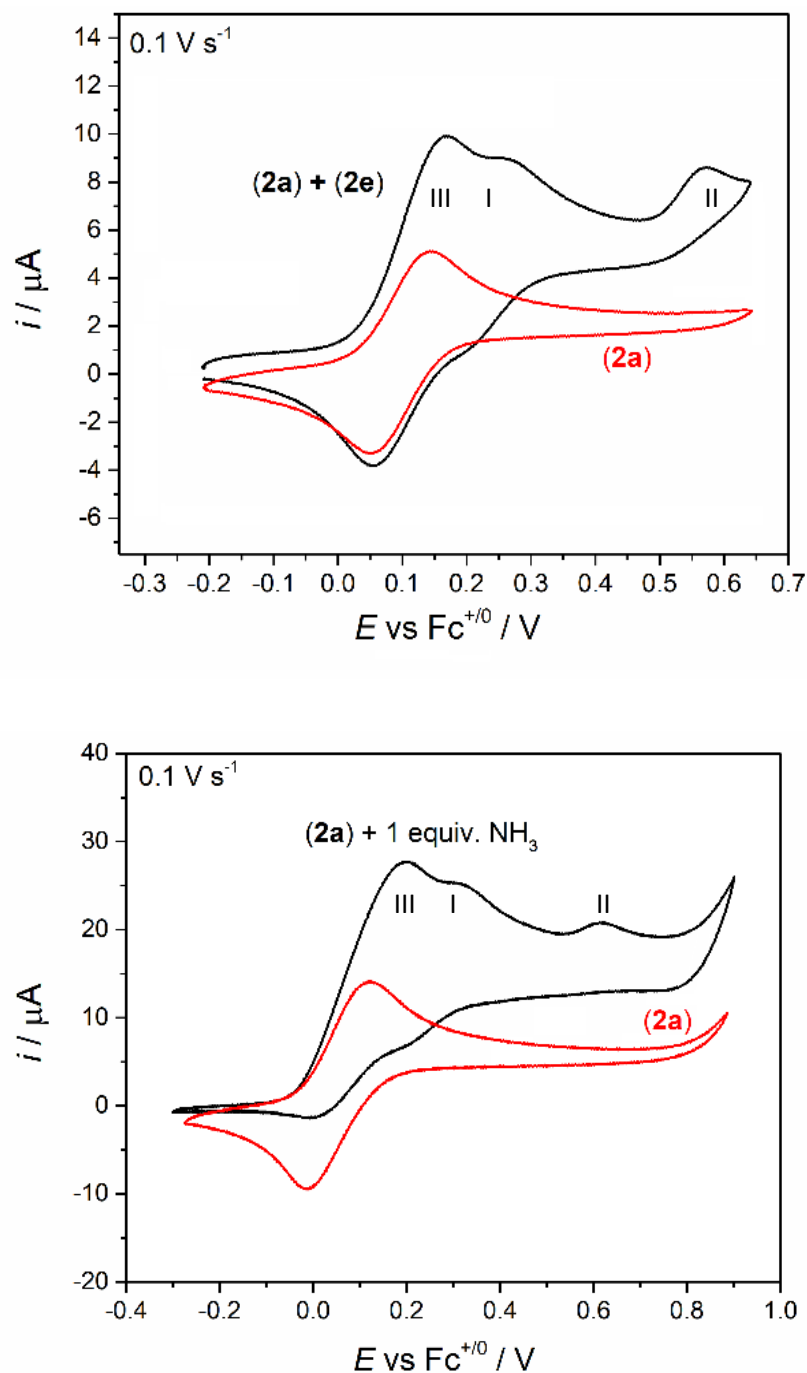


Figure 5.3.5 Cyclic voltammograms of a mixture solution of 1.05×10^{-3} M **2a** and 1.05×10^{-3} M **2e** in THF. Bottom: CVs of a mixture solution of **2a** and 1 equiv. NH_3 in THF.

Electro-oxidation of free hydrazine at the surface of the glassy carbon electrode in THF takes place at relatively low potentials (Figure 5.3.6, peak I). According to several studies on electrochemical

oxidation of N_2H_4 in non-aqueous media, hydrazine undergoes 2-electron oxidation in non-aqueous solutions to the final product diimide, N_2H_2 .⁷⁻⁹ Cao *et al.* argued that the reduction of the diimide product back to N_2H_4 is observed as a reductive peak. However, based on the number of electrons passed for the anodic process ($n = 0.67$), they inferred that only one-third of the hydrazine was converted to diimide in acetonitrile and the rest of the hydrazine molecules acted as the proton acceptor, according to equation 1:⁷



Upon addition of a strong base, triethylamine, to the hydrazine solutions in acetonitrile, the conversion of N_2H_4 to N_2H_2 was quantitative ($n=2$). While the oxidation of hydrazine in THF exhibits similar redox features (Figure 5.3.6), the anodic to cathodic current ratio is 1 : 1.5 (as opposed to 1: 3, reported in acetonitrile⁷), which could be related to the better proton accepting properties of THF compared to acetonitrile. However, what is worth noticing is that peak I in Figure 5.3.6 is at the same potential where the small shoulder appears in Figure 5.3.4, leaving us with the question of whether free hydrazine is generated under oxidative conditions or not.

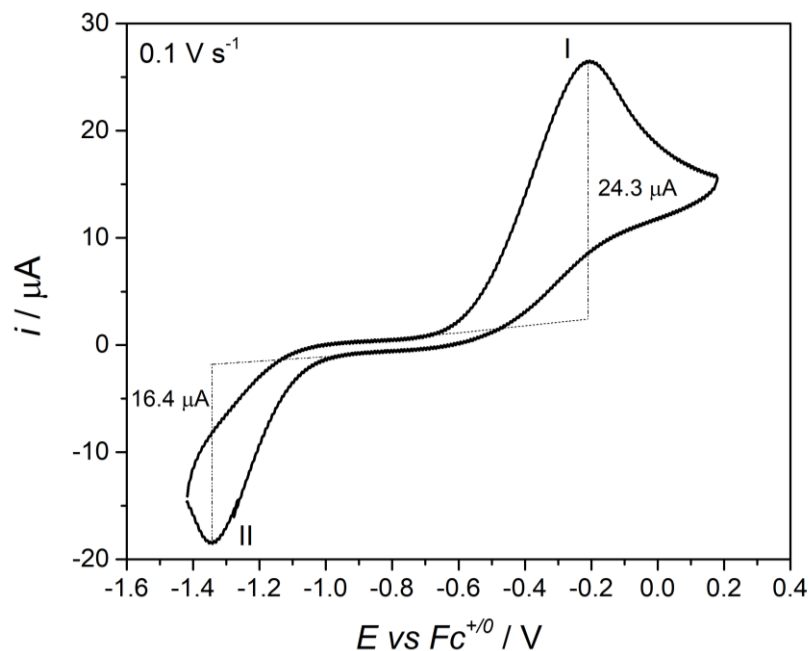


Figure 5.3.6 Electro-oxidation of 4.0×10^{-2} M N_2H_4 in THF at the glassy carbon electrode.

5.4. Variable Temperature (VT) ^1H NMR Experiments⁶

As mentioned in chapter 3, the ^1H NMR of the electrolysis solutions at room temperature only contains $[\text{Ru}(\text{trpy})(\text{dmabpy})\text{NH}_3]^{2+}$ as the ruthenium-based component. Treatment of $[\text{Ru}(\text{trpy})(\text{dmabpy})\text{NH}_3]^{3+}$ with NH_3 in $\text{THF}-d_8$ at room temperature gave the same results as well. Figure 5.4.1 compares the spectrum of the reaction mixture ($[\text{Ru}(\text{trpy})(\text{dmabpy})\text{NH}_3]^{3+} + \text{NH}_3$) with ^1H NMR spectra of authentic samples of the amine ($[\text{Ru}(\text{trpy})(\text{dmabpy})\text{NH}_3]^{2+}$) and hydrazine complexes ($[\text{Ru}(\text{trpy})(\text{dmabpy})\text{N}_2\text{H}_4]^{2+}$) to show that under experimental conditions no traces of $[\text{Ru}(\text{trpy})(\text{dmabpy})\text{N}_2\text{H}_4]^{2+}$ were observed in the product solution. However, when $[\text{Ru}(\text{trpy})(\text{dmabpy})\text{NH}_3]^{3+}$ is reacted with excess concentrations of ammonia in DCM other intermediates were captured at low temperatures (Figure 5.4.2).

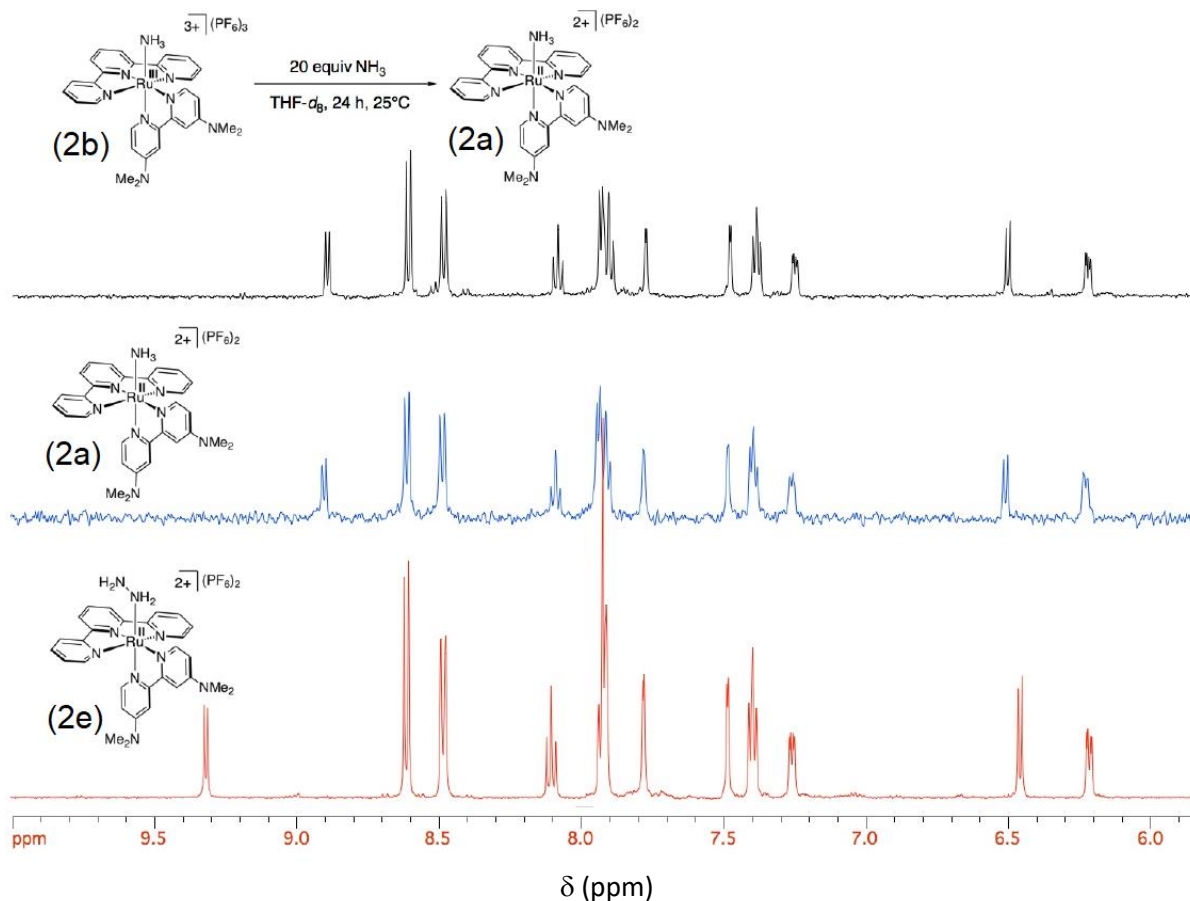


Figure 5.4.1 1H NMR spectrum (500 MHz, $THF-d_8$, $25^\circ C$) of the reaction solution of **2b** and excess NH_3 (top). 1H NMR spectra (500 MHz, $THF-d_8$, $25^\circ C$) of complex **2a** (middle) and **2e** obtained under same conditions, shown for comparison.

To do this experiment, $[Ru(trpy)(dmabpy)NH_3]^{3+}$ was weighed (5 mg, 4.9 μmol , 1 equiv.) into a gas-tight, medium pressure, high vacuum Teflon-valved NMR tube followed by addition of CD_2Cl_2 (0.5 mL) and the NMR tube was attached to a high vacuum manifold. Two cycles of freeze/pump/thaw were conducted in liquid nitrogen to de-gas the solvent. The NMR tube was maintained under static vacuum until a fixed volume of anhydrous, de-gassed ammonia was opened to the line and condensed into the NMR tube while in the Dewar of liquid nitrogen. The NMR tube was closed and removed from the line while behind a blast shield. The NMR tube was kept behind a blast shield in a Dewar of liquid nitrogen until ready to be inserted into the NMR

spectrometer. The resonances of one of the trapped intermediates at -75 °C matches with those obtained for $[\text{Ru}(\text{trpy})(\text{dmabpy})\text{N}_2\text{H}_4]^{2+}$ under the same experimental conditions.

Integration of the low-field resonances at δ 9.27 and δ 8.62 ppm in Figure 5.4.2 attributed to $[\text{Ru}(\text{trpy})(\text{dmabpy})\text{N}_2\text{H}_4]^{2+}$ and $[\text{Ru}(\text{trpy})(\text{dmabpy})\text{NH}_3]^{2+}$, respectively, gave a $[\text{Ru}(\text{trpy})(\text{dmabpy})\text{N}_2\text{H}_4]^{2+} : [\text{Ru}(\text{trpy})(\text{dmabpy})\text{NH}_3]^{2+}$ ratio of 1:5. However, the presence of other resonances in the spectrum in Figure 5.4.2 suggest that there are yet unidentified species that account for the remaining mass balance.

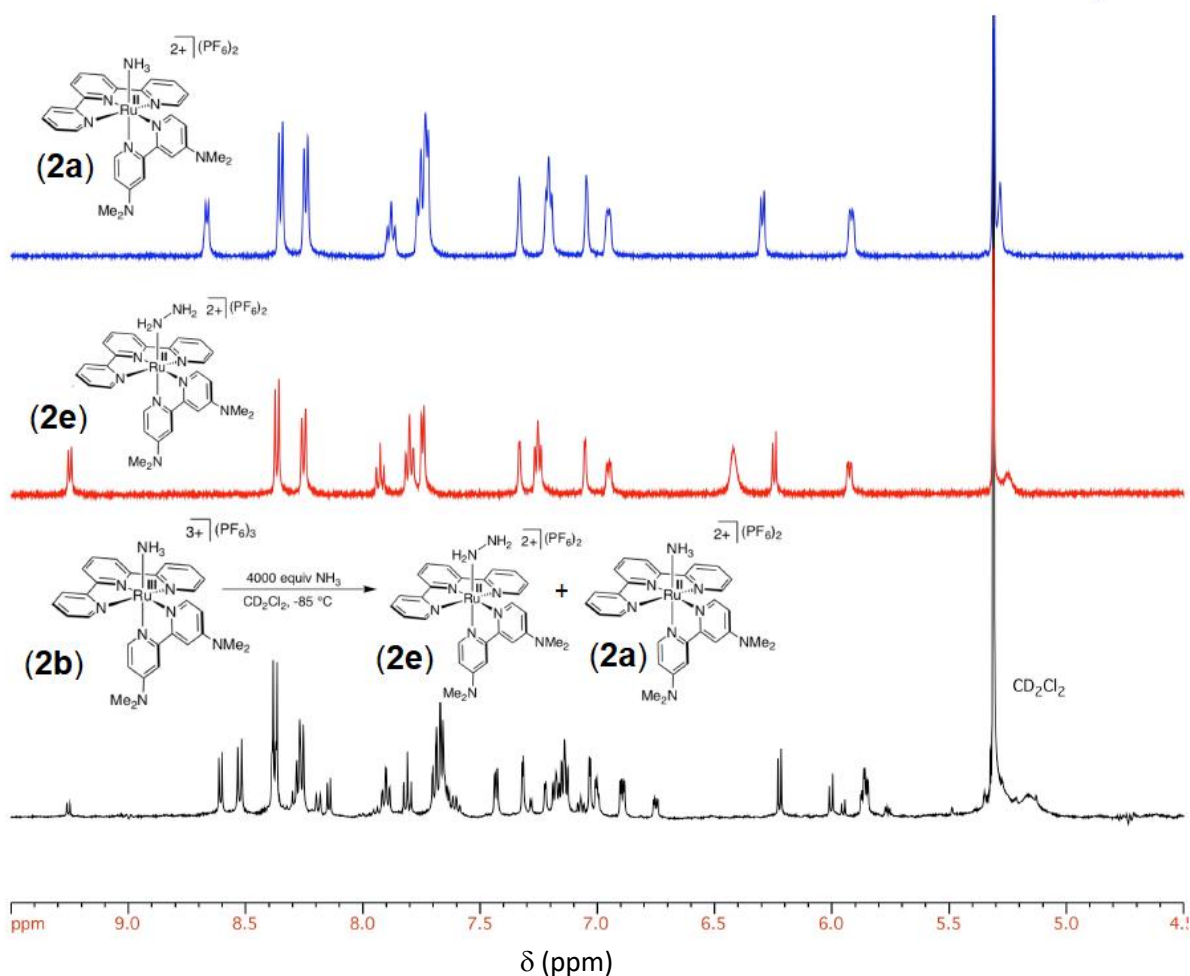


Figure 5.4.2 ^1H NMR spectra (500 MHz, CD_2Cl_2 , -75 °C) of complex **2a** with ~ 4000 equiv. NH_3 (top), complex **2e** with ~4000 equiv. NH_3 (middle), and the reaction mixture that results when ~ 4000 equiv. of NH_3 is added to **2b** at -85 °C.

It is still not fully understood why $[\text{Ru}(\text{trpy})(\text{dmabpy})\text{N}_2\text{H}_4]^{2+}$ does not appear in the NMR spectrum at room temperature, even though the solubility is expected to be enhanced compared to -75°C . Heating up the reaction mixture (Figure 5.4.2, bottom) gradually to room temperature shows that the resonances related to the hydrazine intermediate disappear and the final solution only shows $[\text{Ru}(\text{trpy})(\text{dmabpy})\text{NH}_3]^{2+}$ in the ^1H NMR spectrum (Figure 5.4.3).

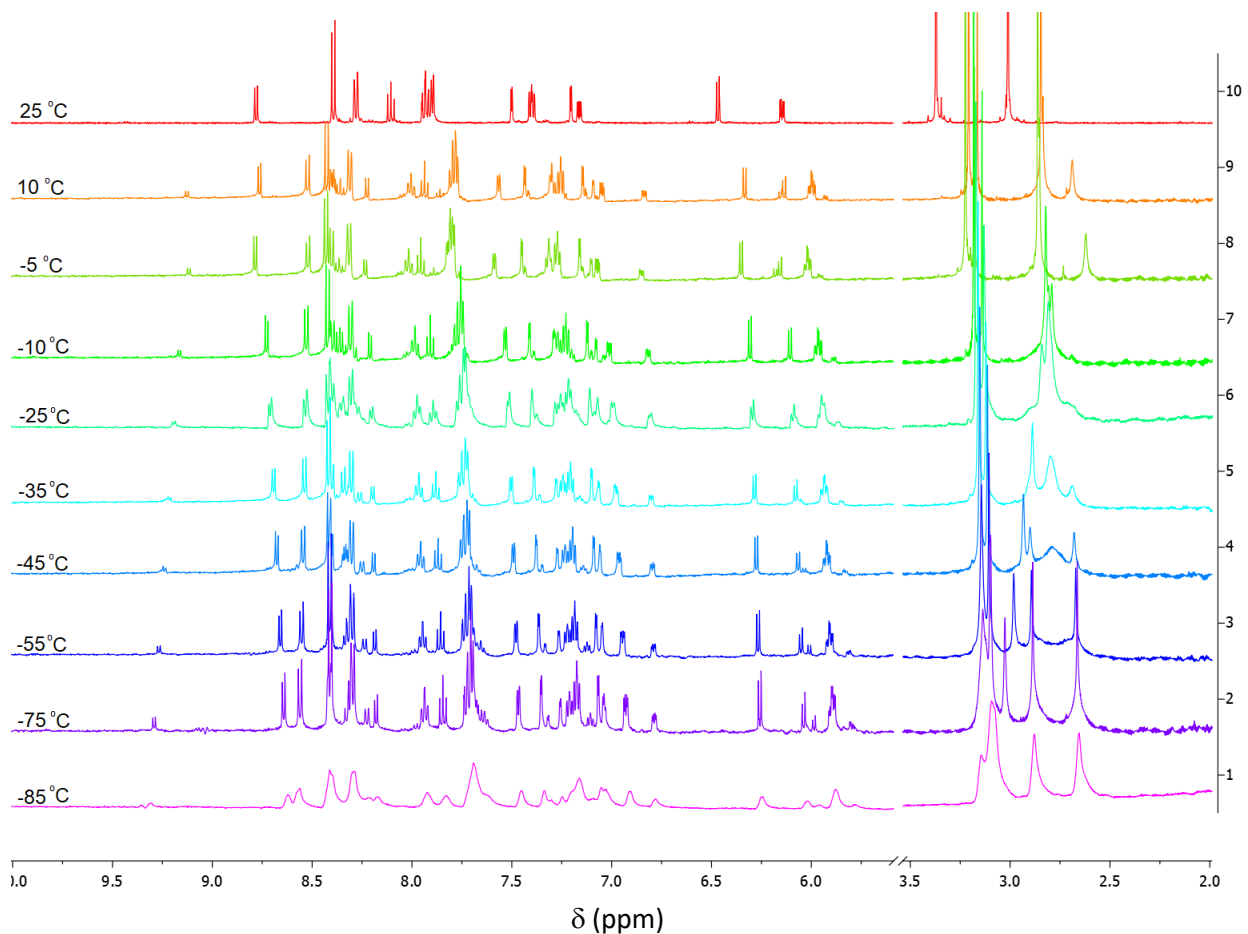


Figure 5.4.3 Change in the ^1H NMR (500 MHz, CD_2Cl_2) spectral features as the temperature of the solution containing **2b** and excess NH_3 is increasing. As the temperature is being increased, the resonances related to the hydrazine complex vanish and the NMR spectrum at room temperature only contains **2a**.

The mechanism of these conversions is unclear. Nevertheless, this phenomenon has to be considered when the treatment of $[\text{Ru}(\text{trpy})(\text{dmabpy})\text{NH}_3]^{3+}$ with NH_3 is being studied by other techniques specially spectrophotocatalytic titrations.

5.5. Spectrophotocatalytic Studies

The reaction between $[\text{Ru}(\text{trpy})(\text{dmabpy})\text{NH}_3]^{2+}$ and NH_3 was also studied by UV Vis-spectroscopy in THF containing 0.8% of NM to help the solubility of $[\text{Ru}(\text{trpy})(\text{dmabpy})\text{NH}_3]^{3+}$. Separate solutions of complexes $[\text{Ru}(\text{trpy})(\text{dmabpy})\text{NH}_3]^{2+}$, $[\text{Ru}(\text{trpy})(\text{dmabpy})\text{NH}_3]^{3+}$, and $[\text{Ru}(\text{trpy})(\text{dmabpy})\text{N}_2\text{H}_4]^{2+}$ in these solvent mixtures were prepared by diluting 40 μL of a stock solution of each complex in NM with THF to a final volume of 5 mL. Electronic absorption spectrum of $[\text{Ru}(\text{trpy})(\text{dmabpy})\text{NH}_3]^{2+}$ in NM(0.8% V)/THF has a characteristic $\text{Ru}(\text{d}\pi) \rightarrow \text{dmabpy}(\pi^*)$ MLCT band at 496 nm with a molar absorption coefficient (ϵ) of 10490 $\text{M}^{-1} \text{cm}^{-1}$ (See Appendix, Figure A5.1.1). This band is slightly shifted to higher energies for $[\text{Ru}(\text{trpy})(\text{dmabpy})\text{N}_2\text{H}_4]^{2+}$ and is almost non-existent for solutions of $[\text{Ru}(\text{trpy})(\text{dmabpy})\text{NH}_3]^{3+}$ in the solvent mixture (See Appendix, Figures A5.1.2, and A5.1.3). Since the UV cut-off of NM is 380 nm, the spectra collection was limited to wavelengths between 400-900 nm. Stock solutions of NH_3 (sat'd) in NM(0.8% V)/THF were prepared by bubbling dry ammonia gas through 5 mL of the solvent mixture for 5 min and the concentration was assumed to be 0.34 M. Aliquots of the NH_3 stock solutions were transferred to a cuvette containing 9.70×10^{-5} M $[\text{Ru}(\text{trpy})(\text{dmabpy})\text{NH}_3]^{3+}$ in the mixture solvent using a glass syringe. All absorbance spectra were collected against an NM (0.8% V)/THF reference solution. Right after the addition of ammonia to $[\text{Ru}(\text{trpy})(\text{dmabpy})\text{NH}_3]^{3+}$, the spectral features change and consumption of $[\text{Ru}(\text{trpy})(\text{dmabpy})\text{NH}_3]^{3+}$ is evident *via* gradual disappearing of the bands at 730 nm and 840 nm.

Simultaneously, a band is reappearing between 480-500 nm that suggests Ru(II) species are being generated as the products of the reaction (Figure 5.5.1).

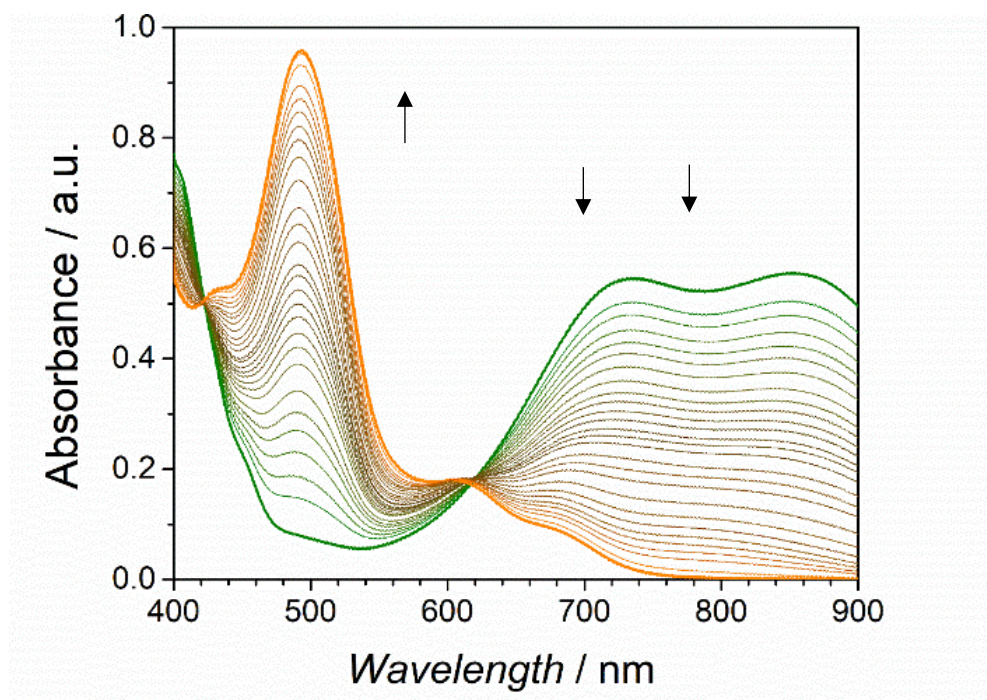


Figure 5.5.1 Changes in the absorption spectrum of a solution of 9.70×10^{-5} M **2b** with the addition of NH_3 . The green curve is the spectrum of the starting solution and the final orange spectrum is when the titration was ended (the point where the addition of NH_3 did not change the spectra). All absorption spectra are corrected for dilution.

Analysis of the results of the titration experiment, were performed based on the assumption that the product of the reaction between $[\text{Ru}(\text{trpy})(\text{dmabpy})\text{NH}_3]^{3+}$ and NH_3 is a mixture containing equal concentrations of $[\text{Ru}(\text{trpy})(\text{dmabpy})\text{NH}_3]^{2+}$ and $[\text{Ru}(\text{trpy})(\text{dmabpy})\text{N}_2\text{H}_4]^{2+}$. Here we assume that the presence of NH_3 in the solution triggers the redox disproportionation and 1 equiv. of $[\text{Ru}(\text{trpy})(\text{dmabpy})\text{N}_2\text{H}_4]^{2+}$ is formed along with each equiv. of $[\text{Ru}(\text{trpy})(\text{dmabpy})\text{NH}_3]^{2+}$ and it survives long enough to be seen by UV Vis-spectrophotometry. At the end of the titration 8.05×10^{-7} mol NH_3 is present in the solution, 4-fold excess with respect to the initial moles of $[\text{Ru}(\text{trpy})(\text{dmabpy})\text{NH}_3]^{3+}$, so the conversion of $[\text{Ru}(\text{trpy})(\text{dmabpy})\text{NH}_3]^{3+}$ to half equivalent of

each product $[\text{Ru}(\text{trpy})(\text{dmabpy})\text{NH}_3]^{2+}$ and $[\text{Ru}(\text{trpy})(\text{dmabpy})\text{N}_2\text{H}_4]^{2+}$ is expected to be quantitative. Based on the calculation, at the end of the titration the concentrations of $[\text{Ru}(\text{trpy})(\text{dmabpy})\text{NH}_3]^{2+}$ and $[\text{Ru}(\text{trpy})(\text{dmabpy})\text{N}_2\text{H}_4]^{2+}$ should be equal to $4.70 \times 10^{-5} \text{ M}$ ($=1.21 \times 10^{-7} \text{ mol} / 2.583 \times 10^{-3} \text{ L}$). The constructed absorption spectra for $4.70 \times 10^{-5} \text{ M}$ of $[\text{Ru}(\text{trpy})(\text{dmabpy})\text{NH}_3]^{2+}$ and $4.70 \times 10^{-5} \text{ M}$ $[\text{Ru}(\text{trpy})(\text{dmabpy})\text{N}_2\text{H}_4]^{2+}$ is compared to the final spectra in Figure 5.5.2.

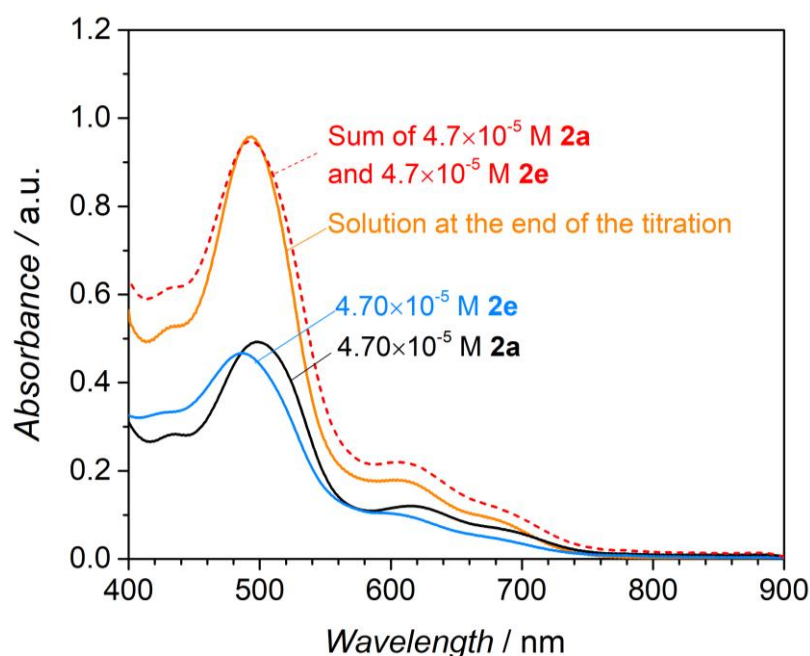


Figure 5.5.2 Comparison between the absorption spectra recorded at the end of titration (orange), the constructed spectra for 0.5 equiv. **2a** (black) and 0.5 equiv. **2e** (blue) and the arithmetic summation of the spectra of 0.5 equiv. **2a** (black) and 0.5 equiv. **2e** (blue) shown in dashed red.

When the constructed spectra for 0.5 equiv. of $[\text{Ru}(\text{trpy})(\text{dmabpy})\text{NH}_3]^{2+}$ and $[\text{Ru}(\text{trpy})(\text{dmabpy})\text{N}_2\text{H}_4]^{2+}$ were added together, the final spectrum of the solution after the titration was regenerated in terms of the position of bands. While this data is consistent with the formation of the hydrazine complex from $[\text{Ru}(\text{trpy})(\text{dmabpy})\text{NH}_3]^{3+}$ after treatment with NH_3 , it is still not

clear why $[\text{Ru}(\text{trpy})(\text{dmabpy})\text{N}_2\text{H}_4]^{2+}$ is not observed in quantitative concentrations by ^1H NMR measurements.

5.6. Conclusions

The formation of a hydrazine intermediate is experimentally supported. However, the fate of the hydrazine complex under catalytic conditions is still ambiguous. Future studies on an authentically synthesized $\text{Ru}(\text{II})\text{-N}_2$ complex would provide invaluable insights to the regeneration of the amine complex from the hydrazine complex.

APPENDIX

A5.1. Electronic absorption spectra in NM (0.8% V)/THF

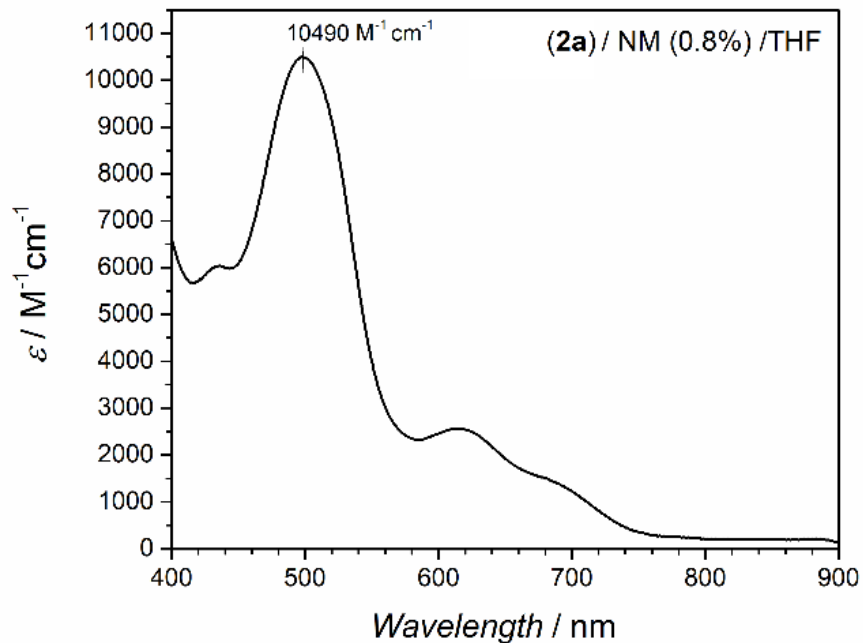


Figure A5.1.1 Absorption spectrum of $8.78 \times 10^{-5} \text{ M}$ **2a** in NM(0.8%)/THF.

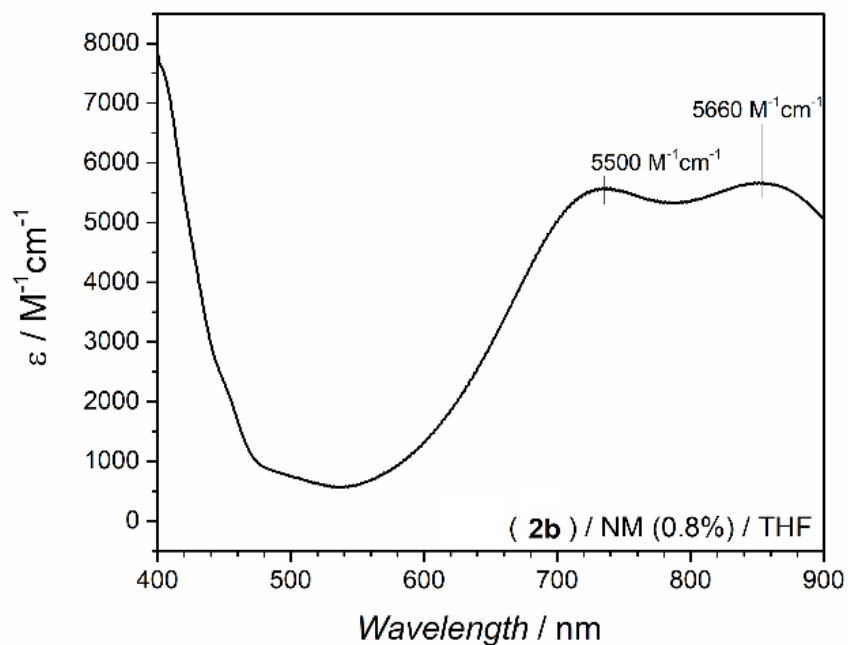


Figure A5.1.2 Absorption spectrum of $9.70 \times 10^{-5} \text{ M}$ **2b** in NM(0.8%)/THF.

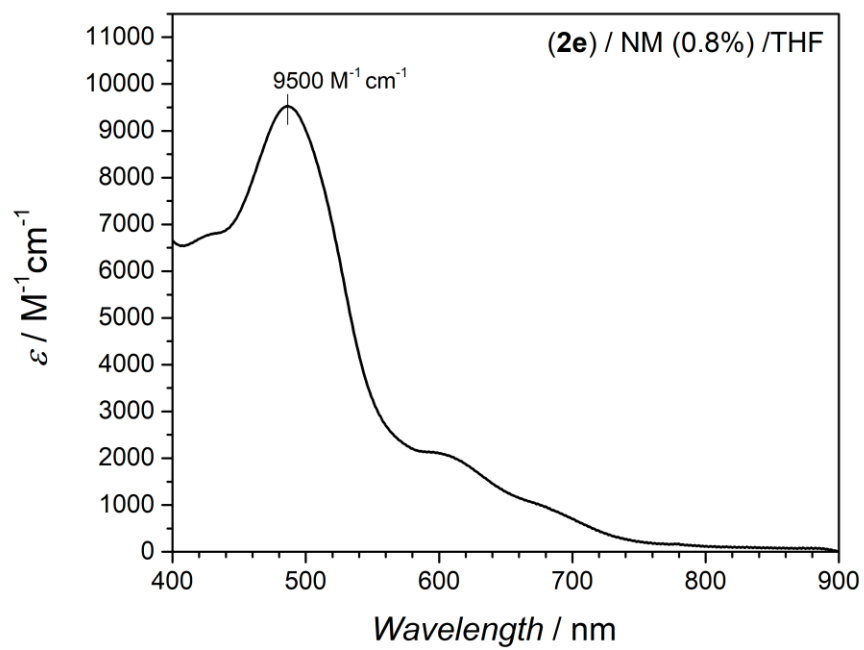


Figure A5.1.3 Absorption spectrum of 9.00×10^{-5} M **2e** in NM(0.8%)/THF.

REFERENCES

REFERENCES

- (1) Concepcion, J. J.; Tsai, M.-K.; Muckerman, J. T.; Meyer, T. J. *J. Am. Chem. Soc.* **2010**, *132* (14), 1545–1557.
- (2) Wasylenko, D. J.; Ganesamoorthy, C.; Kolvisto, B. D.; Henderson, M. A.; Berllinguetto, C. *P. Inorg. Chem.* **2010**, *49* (5), 2202–2209.
- (3) Kamdar, J. M.; Grotjahn, D. B. *Molecules* **2019**, *24* (3), 494–518.
- (4) Meyer, T. J.; Thompson, M. S. *J. Am. Chem. Soc.* **1981**, *103*, 5579–5581.
- (5) Coia, G. M.; White, P. S.; Meyer, T. J.; Wink, D. A.; Keefer, L. K.; Davis, W. M. *J. Am. Chem. Soc.* **1994**, *116* (4), 3649–3650.
- (6) Habibzadeh, F.; Miller, S. L.; Hamann, T. W.; Smith, M. R. *Proc. Natl. Acad. Sci.* **2019**, *3* (1), 2–6.
- (7) Cao, X.; Wang, B.; Su, Q. *J. Electroanal. Chem.* **1993**, *361* (1–2), 211–214.
- (8) Antoniadou, S.; Jannakoudakis, A. D.; Theodoridou, E. *Synth. Met.* **1989**, *30*, 295–304.
- (9) Michlmayr, M.; Sawyer, D. T. *J. Electroanal. Chem.* **1969**, *23*, 375–385.

**CHAPTER 6: PRELIMINARY ELECTROCHEMICAL STUDIES OF OTHER
RUTHENIUM POLYPYRIDYL AMINE CATALYSTS**

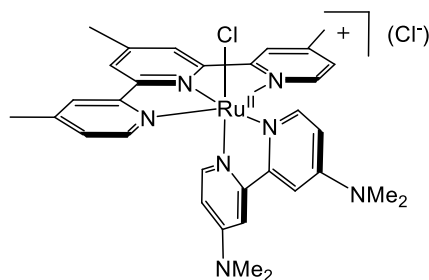
In order to prepare ruthenium complexes with $E_{1/2}$ potentials more negative than $[\text{Ru}(\text{trpy})(\text{bpy})\text{NH}_3](\text{PF}_6)_2$, **1a**, more ruthenium polypyridyl amine complexes were prepared. In these complexes, the same dmabpy ligands was used as in $[\text{Ru}(\text{trpy})(\text{dmabpy})\text{NH}_3](\text{PF}_6)_2$, **2a**, but various electron donating groups were placed on different positions on the trpy moiety. Three complexes were synthesized and their catalytic behavior towards oxidation of ammonia was studied using cyclic voltammetry methods.

6.1. $[\text{Ru}(\text{Me}_3\text{trpy})(\text{dmabpy})\text{NH}_3](\text{PF}_6)_2$, (**3a**).

6.1.1. Synthesis

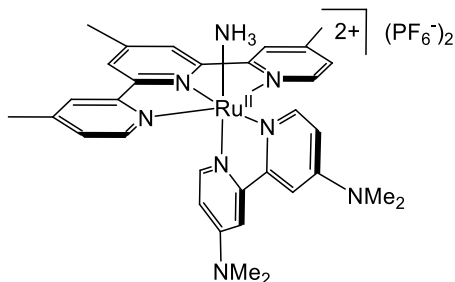
3a was synthesized in two steps as described below:

6.1.1.1. (4',4,4''-trimethyl-2,2':6',2''-terpyridine)(4,4'-bis(N,N-dimethylamino)-2,2'-bipyridyl) chloro ruthenium(II) chloride, $[\text{Ru}(\text{Me}_3\text{trpy})(\text{dmabpy})\text{Cl}]\text{Cl}$.



$[\text{Ru}(\text{Me}_3\text{trpy})(\text{dmabpy})\text{Cl}]\text{Cl}$ was synthesized following a procedure described in section 3.3.1 with 1:1 ethanol : water being used as the solvent. 78% yield. ^1H NMR (500 MHz, $\text{DMSO}-d_6$) δ 9.47 (d, $J = 6.7$ Hz, 1H), 8.57 (s, 2H), 8.45 (s, 2H), 7.84 (d, $J = 2.7$ Hz, 1H), 7.55 (dd, $J = 8.9, 4.2$ Hz, 3H), 7.25 (dd, $J = 6.9, 2.7$ Hz, 1H), 7.23 – 7.19 (m, 2H), 6.35 (d, $J = 6.8$ Hz, 1H), 6.23 (dd, $J = 7.0, 2.8$ Hz, 1H), 3.29 (s, 6H), 2.93 (s, 6H), 2.72 (s, 3H), 2.45 (s, 6H).

6.1.1.2. (4',4,4''-trimethyl-2,2':6',2''-terpyridine) (4,4'-bis(N,N-dimethylamino)-2,2'-bipyridyl) ruthenium (II) ammine dihexafluorophosphate, [Ru(Me₃trpy)(bdmabpy)NH₃](PF₆)₂, (3a).



[Ru(Me₃trpy)(bdmabpy)NH₃](PF₆)₂ was synthesized following the procedure described for **2a**. 85% yield. ¹H NMR (500 MHz, Acetonitrile-*d*₃): δ 8.72 – 8.65 (m, 1H), 8.31 (s, 2H), 8.19 (s, 2H), 7.64 (dd, *J* = 11.1, 4.3 Hz, 3H), 7.34 (d, *J* = 2.9 Hz, 1H), 7.17 (d, *J* = 5.7 Hz, 2H), 7.11 (dd, *J* = 6.7, 2.8 Hz, 1H), 6.44 (dd, *J* = 6.9, 1.1 Hz, 1H), 6.13 (dd, *J* = 7.0, 2.8 Hz, 1H), 3.30 (d, *J* = 1.1 Hz, 6H), 2.96 (d, *J* = 1.0 Hz, 6H), 2.77 (s, 3H), 2.50 (s, 6H), 1.60 (s, 3H).

6.1.2. Ammonia Oxidation Using 3a as the Catalyst

Cyclic voltammograms of a solution containing 2.70×10⁻³ M [Ru(Me₃trpy)(dmabpy)NH₃](PF₆)₂, **3a**, in THF has one reversible redox process at *E*_{1/2} = 0.12 V *versus* Fc⁺⁰ in the absence of ammonia. Bubbling NH₃ to this solution causes the loss of the reversibility of this redox process and an enhanced catalytic current is observed as shown in Figure 6.1.1. To evaluate the catalytic nature of the current after addition of ammonia, normalized catalytic currents were plotted and compared. As seen in Figure 6.1.2, the catalytic current is enhanced at lower scan rates as well as the potential of the current onset is also moved to more negative.

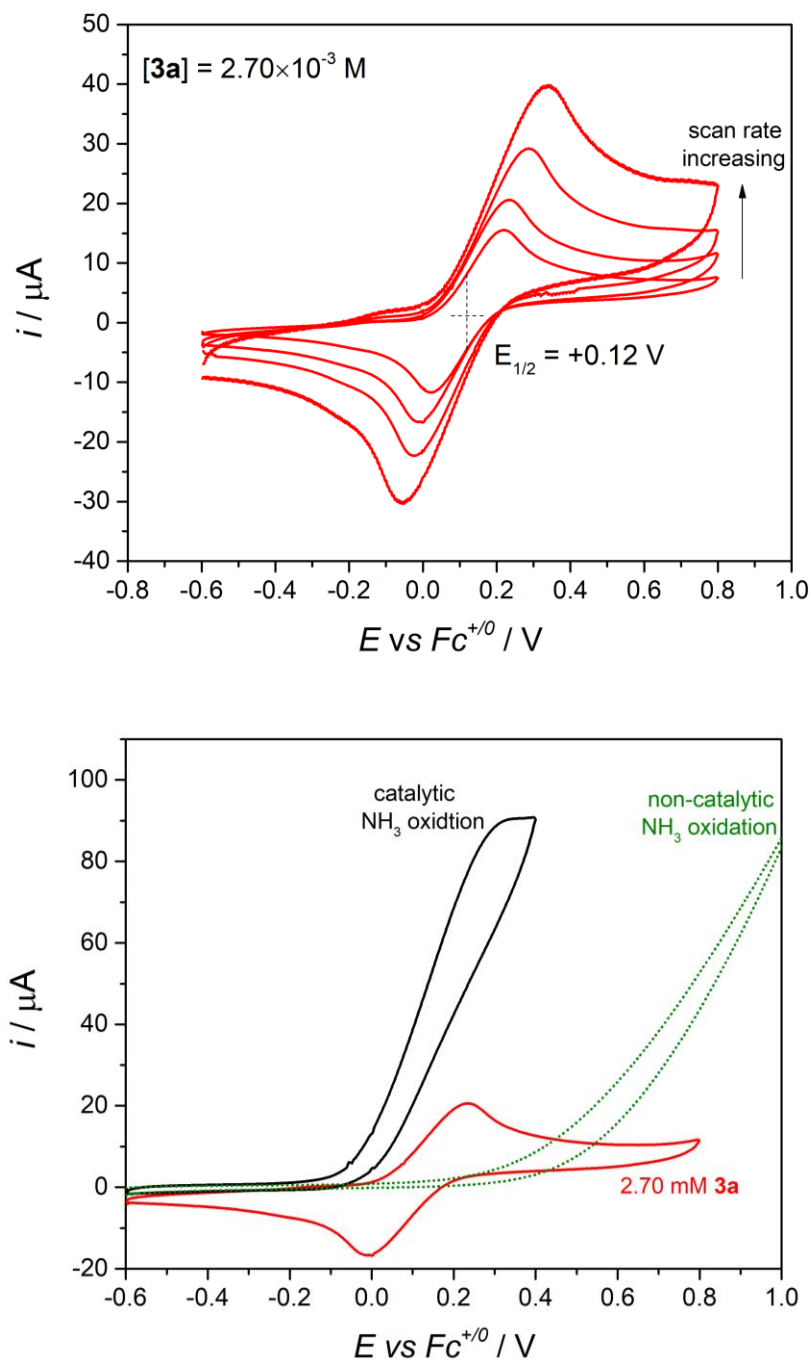


Figure 6.1.1 Top: CVs of **3a** in the absence of NH_3 (sat'd) in THF. Scan rates: 0.05, 0.1, 0.25 and 0.5 Vs^{-1} . Bottom: The catalytic current (black) in a solution 2.7 mM **3a** in THF. Dotted green line is the non-catalytic NH_3 oxidation. Scan rate is 0.1 Vs^{-1} and the onset of the catalytic current is -0.1 V versus $\text{Fc}^{+/0}$.

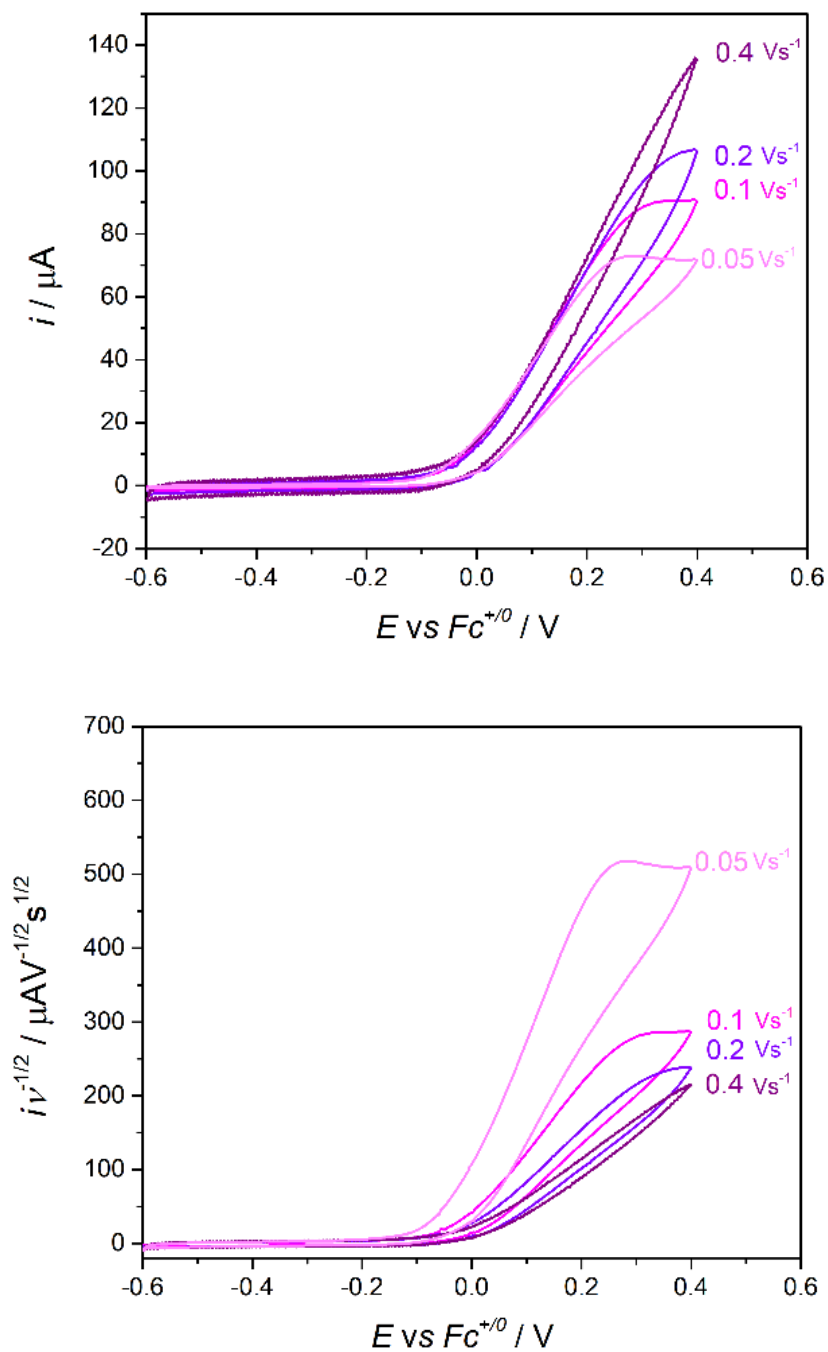


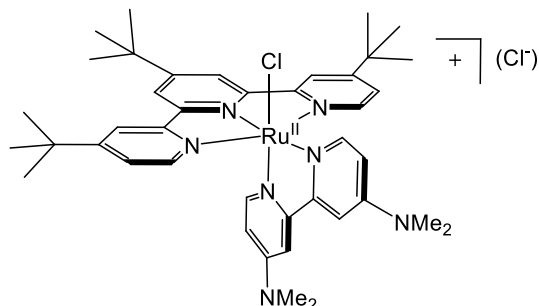
Figure 6.1.2 Top: Catalytic currents obtained in solutions of 2.7 mM **3a** and NH_3 (sat'd) in THF and their dependence on the scan rate. Bottom: the catalytic currents normalized for scan rate.

6.2. [Ru(^tBu₃trpy)(dmabpy)NH₃](PF₆)₂, (4a).

6.2.1. Synthesis

4a was synthesized in two steps as described below:

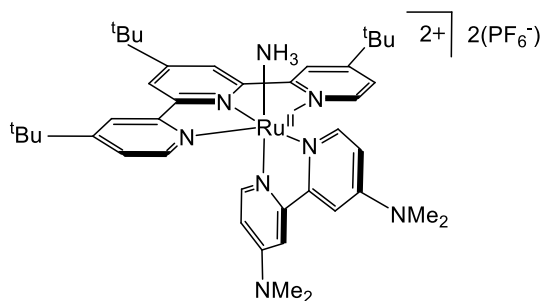
6.2.1.1. (4',4,4''-tri-tert-butyl-2,2':6',2''-terpyridine)(4,4'-bis(N,N-dimethylamino)-2,2'-bipyridyl) chloro ruthenium (II) chloride, [Ru(^tBu₃trpy)(dmabpy)Cl]Cl.



[Ru(^tBu₃trpy)(bdmabpy)Cl]Cl was synthesized following a procedure described in section 3.3.1.

86% yield. ¹H NMR (500 MHz, DMSO-*d*₆) δ 9.46 (d, *J* = 6.7 Hz, 1H), 8.77 (s, 2H), 8.67 (d, *J* = 2.1 Hz, 2H), 7.84 (d, *J* = 2.7 Hz, 1H), 7.57 (dd, *J* = 12.7, 4.4 Hz, 3H), 7.40 (dd, *J* = 6.0, 2.1 Hz, 2H), 7.26 (dd, *J* = 6.7, 2.7 Hz, 1H), 6.38 (d, *J* = 6.8 Hz, 1H), 6.31 – 6.17 (m, 1H), 3.30 (s, 6H), 2.94 (s, 6H), 1.63 (s, 9H), 1.34 (s, 18H).

6.2.1.2. (4',4,4''-tri-tert-butyl-2,2':6',2''-terpyridine)(4,4'-bis(N,N-dimethylamino)-2,2'-bipyridyl) ruthenium(II) ammine dihexafluorophosphate, (4a).



[Ru(^tBu₃trpy)(dmabpy)NH₃](PF₆)₂ was synthesized using the same procedure that was followed for **2a**. Yield 83%. ¹H NMR (500 MHz, Acetonitrile-*d*₃): δ 8.70 (d, J = 6.7 Hz, 1H), 8.50 (s, 2H), 8.37 (dd, J = 2.2, 0.7 Hz, 2H), 7.71 (dd, J = 6.0, 0.6 Hz, 2H), 7.64 (d, J = 2.7 Hz, 1H), 7.36 – 7.33 (m, 3H), 7.12 (dd, J = 6.7, 2.8 Hz, 1H), 6.44 (d, J = 6.8 Hz, 1H), 6.14 (dd, J = 6.9, 2.8 Hz, 1H), 3.31 (s, 6H), 2.96 (s, 6H), 1.64 (s, 9H), 1.59 (s, 3H), 1.37 (s, 18H).

6.2.2. Ammonia Oxidation Using **4a** as the Catalyst

One reversible redox process is observed in cyclic voltammograms at $E_{1/2} = -0.03$ V versus Fc^{+/0} in of a solution containing 2.51×10⁻³ M [Ru(^tBu₃trpy)(dmabpy)NH₃](PF₆)₂, **4a**, in THF the absence of ammonia (Figure 6.2.1, top). Saturation of the solution with NH₃ changes the electrochemical response to a purely anodic catalytic current as shown in Figure 6.2.1, bottom. The dependence of the catalytic currents to the scan rate is shown in Figure 6.2.2.

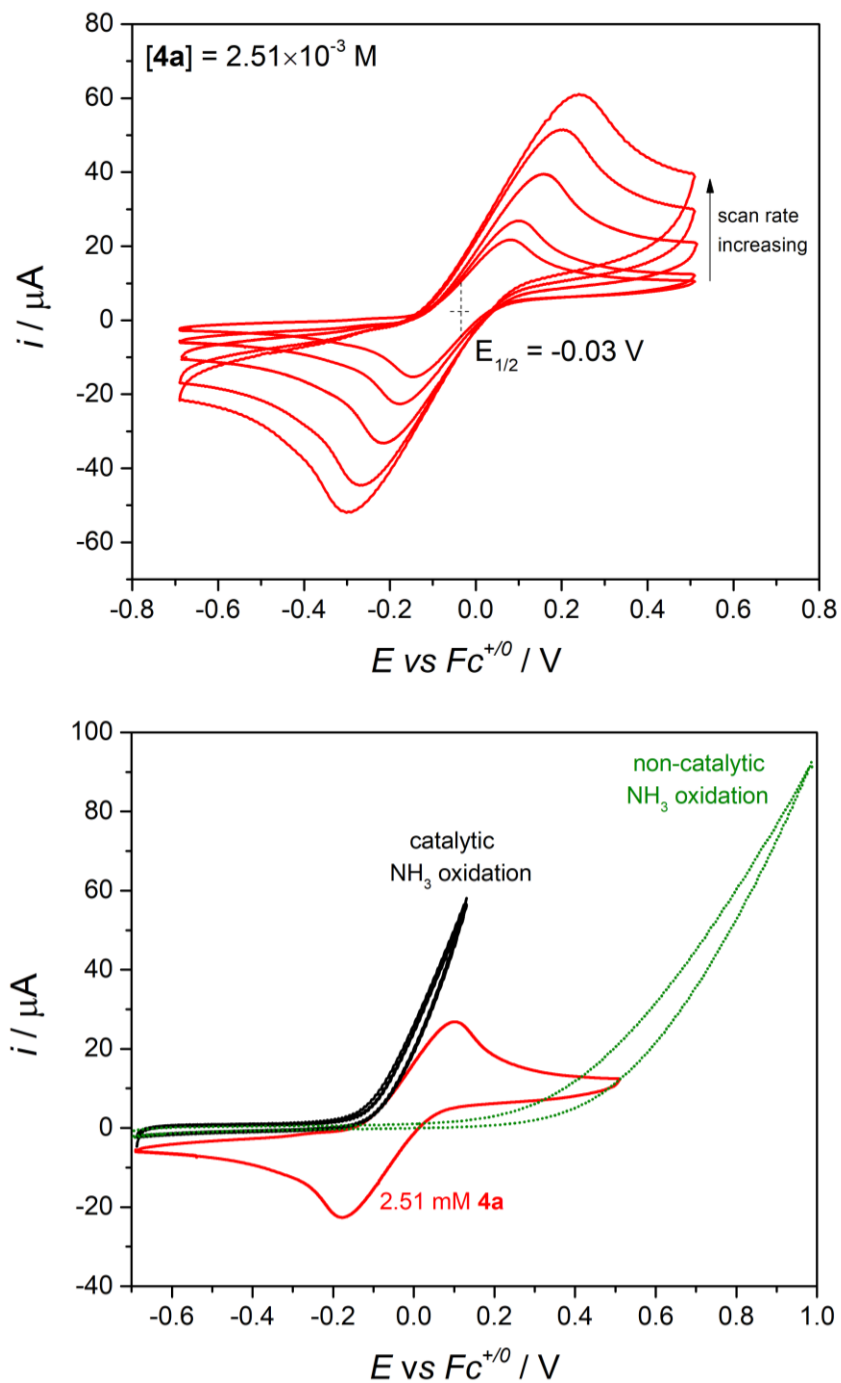


Figure 6.2.1 CVs of **4a** in the absence (top) and presence (bottom) of NH_3 (sat'd) in THF. Scan rates for the CVs on the top: 0.05, 0.1, 0.25, 0.5 and 0.8 Vs^{-1} . On the bottom, the scan rate is 0.1 Vs^{-1} and the onset of the catalytic current is -0.15 V versus $\text{Fc}^{+/0}$.

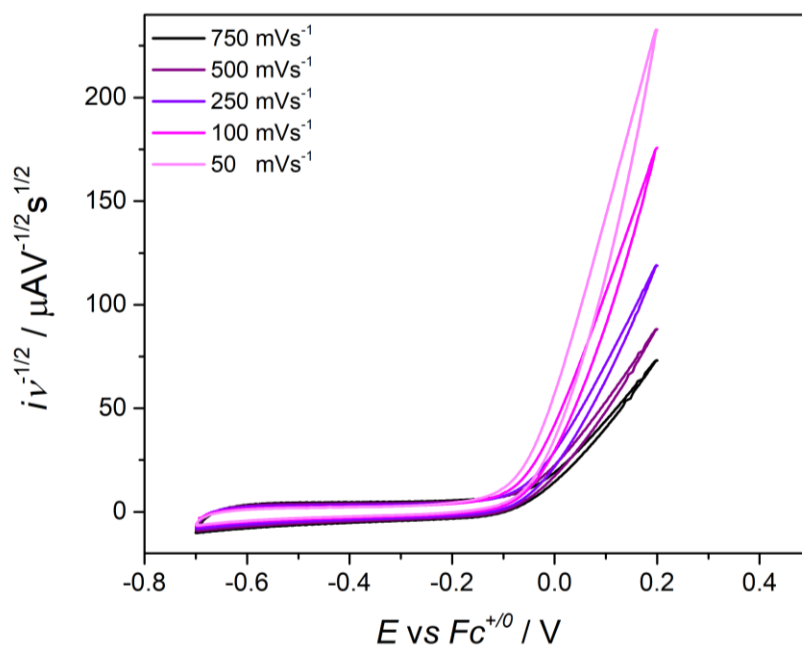
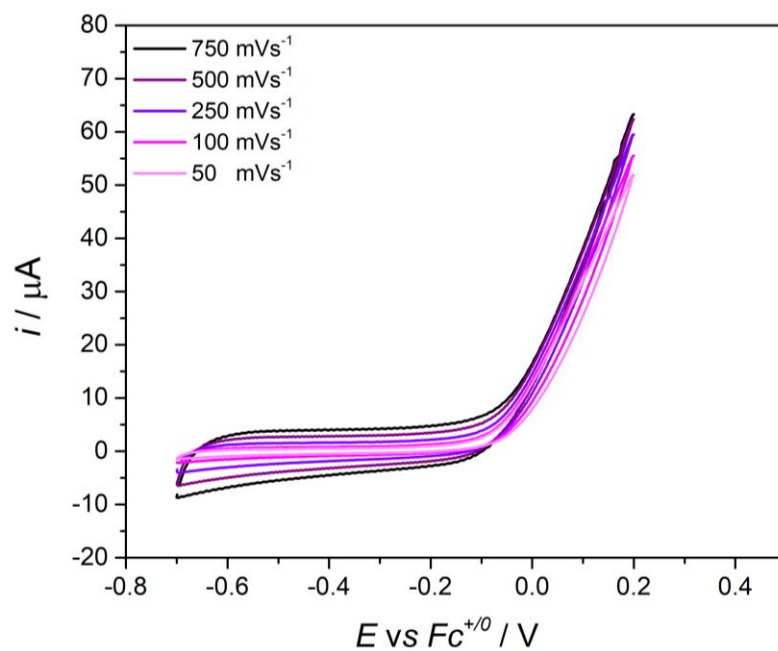


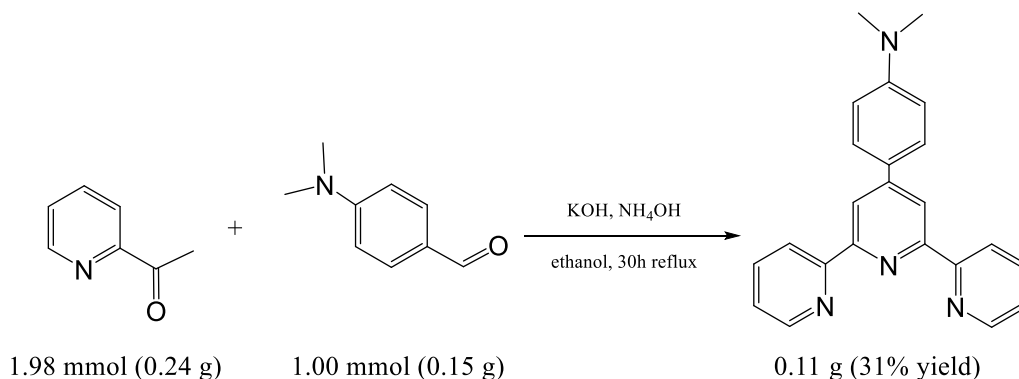
Figure 6.2.2 Top: Catalytic currents obtained in solutions of 2.51 mM **4a** and $\text{NH}_3(\text{sat'd})$ in THF and their dependence on the scan rate. Bottom: the catalytic currents normalized for scan rate.

6.3. [Ru(dmaptrpy)(dmabpy)NH₃](PF₆)₂, (5a).

6.3.1. Synthesis

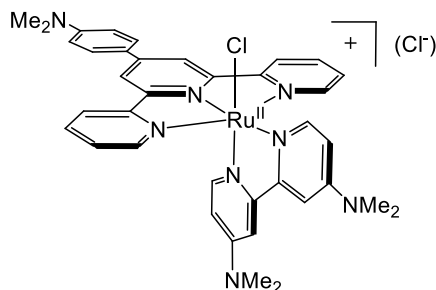
6.3.1.1. (4-N,N-dimethylaminophenyl)-2,2',6',2''-terpyridine, dmaptrpy.

The dmaptrpy ligand was synthesized initially using a one-step literature method:¹ 2-acetylpyridine (0.25 g, 2.06 mmol, 2 equiv.) and 4-dimethylaminobenzaldehyde (0.15 g, 1.00 mmol, 1 equiv.) were added to a round bottom flask containing a solution consisting of 0.12 g (2.14 mmol, 2 equiv.) KOH and 0.15 mL concentrated NH₄OH(aq) (2.17 mmol, 2 equiv.) in 200 mL ethanol. The solution was refluxed for 30h. The yellow solid product was collected by filtration and was washed with ethanol (5×10 mL) and diethyl ether (5×10 mL) and dried under vacuum overnight. Recrystallization from chloroform-methanol solutions yielded 0.110 g of bright yellow crystals (31% yield). ¹H NMR (500 MHz, methylene chloride-*d*₂) δ 8.74 – 8.71 (m, 4H), 8.67 (dt, J = 8.0, 1.1 Hz, 2H), 7.88 (dd, J = 7.2, 1.3 Hz, 2H), 7.87 – 7.84 (m, 2H), 7.36 (ddd, J = 7.5, 4.8, 1.2 Hz, 2H), 6.87 – 6.83 (m, 2H), 3.04 (s, 6H).



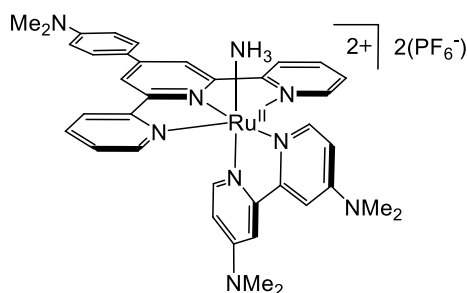
Scheme 6.1 Synthesis of the dmaptrpy ligand.

6.3.1.2. ((4-N,N-dimethylaminophenyl)-2,2',6',2''-terpyridine)(4,4'-bis(N,N-dimethylamino)-2,2'-bipyridyl) chloro ruthenium (II) chloride, [Ru(dmaptrpy)(dmabpy)Cl]Cl.



[Ru(dmaptrpy)(dmabpy)Cl]Cl was synthesized following a procedure described in section 3.1.2.

6.3.1.3. ((4-N,N-dimethylaminophenyl)-2,2',6',2''-terpyridine)(4,4'-bis(N,N-dimethylamino)-2,2'-bipyridyl) ruthenium(II) ammine dihexafluorophosphate, (5a).



[Ru(dmaptrpy)(dmabpy)NH₃](PF₆)₂ was synthesized following the procedure described for **2a**.

Yield 88%. ¹H NMR (500 MHz, CD₂Cl₂-d₂) δ 8.77 (d, J = 6.6 Hz, 1H), 8.50 (s, 2H), 8.32 (d, J = 8.1 Hz, 2H), 7.96 – 7.86 (m, 6H), 7.47 (d, J = 2.8 Hz, 1H), 7.36 (ddd, J = 7.2, 5.5, 1.3 Hz, 2H), 7.19 (d, J = 2.8 Hz, 1H), 7.13 (dd, J = 6.7, 2.8 Hz, 1H), 6.96 – 6.93 (m, 2H), 6.58 (d, J = 6.9 Hz, 1H), 6.12 (dd, J = 6.9, 2.8 Hz, 1H), 3.34 (s, 6H), 3.13 (s, 6H), 2.99 (s, 6H), 2.12 (s, 3H).

6.3.2. Ammonia Oxidation Using **5a** as the Catalyst

Unfortunately, the solubility of $[\text{Ru}(\text{dmaptrpy})(\text{dmabpy})\text{NH}_3](\text{PF}_6)_2$, **5a**, is very low in THF and DCM. Thus, the cyclic voltammetry experiments were conducted in NM. Addition of 4.05×10^{-3} M **5a** to solutions of NH_3 in NM, shows a dramatic negative shift in the onset potential for the NH_3 oxidation current (Figure 6.3.1).

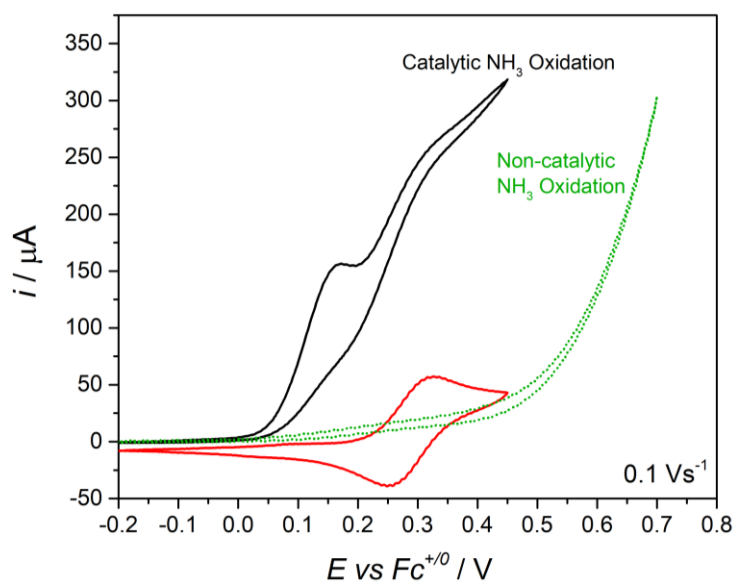


Figure 6.3.1 The CVs obtained in solutions: 4.05×10^{-3} M **5a** in NM (red), 4.05 mM **5a** in the presence of NH_3 in NM (black) and a solution of $\text{NH}_3(\text{sat'd})/\text{NM}$.

When the catalytic currents were normalized for the scan rate, the dependence appears different than what was previously observed for other catalysts in THF (Figure 6.3.2, bottom). It seems that while the onset of the catalytic current is moving to more favorable potentials with slower scan rates, the magnitude of the plateau current does not show a significant increase, which could be an indication of a different catalytic mechanism controlling the currents.

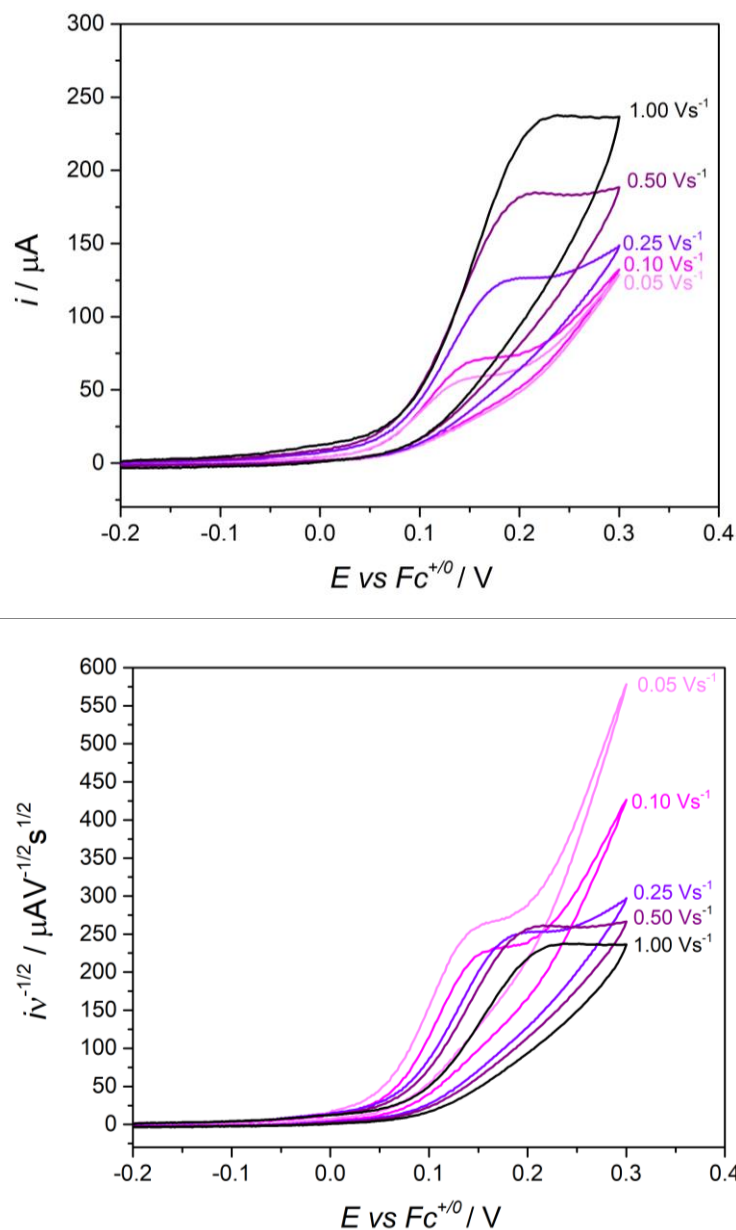


Figure 6.3.2 Top: The CVs of the catalytic ammonia oxidation in NM in the presence of 4.05×10^{-3} M **5a**, with different scan rates. **Bottom:** The normalized currents shown for the same set of data. The magnitudes of the normalized currents remain relatively constant at different scan rates.

The normalized currents obtained for the other complexes in NM, do not look similar to what were observed for **5a**. For instance, the shift in the onset of the catalytic currents obtained for **3a** in NM is also very negative compared to THF. However, the normalized catalytic currents behave similarly in both THF and NM (Figure 6.3.3), suggesting that the difference in Figure 6.3.2

(bottom) and Figure 6.3.3 (bottom, right) are related to the chemistry of the catalysis when **5a** is used as the catalyst.

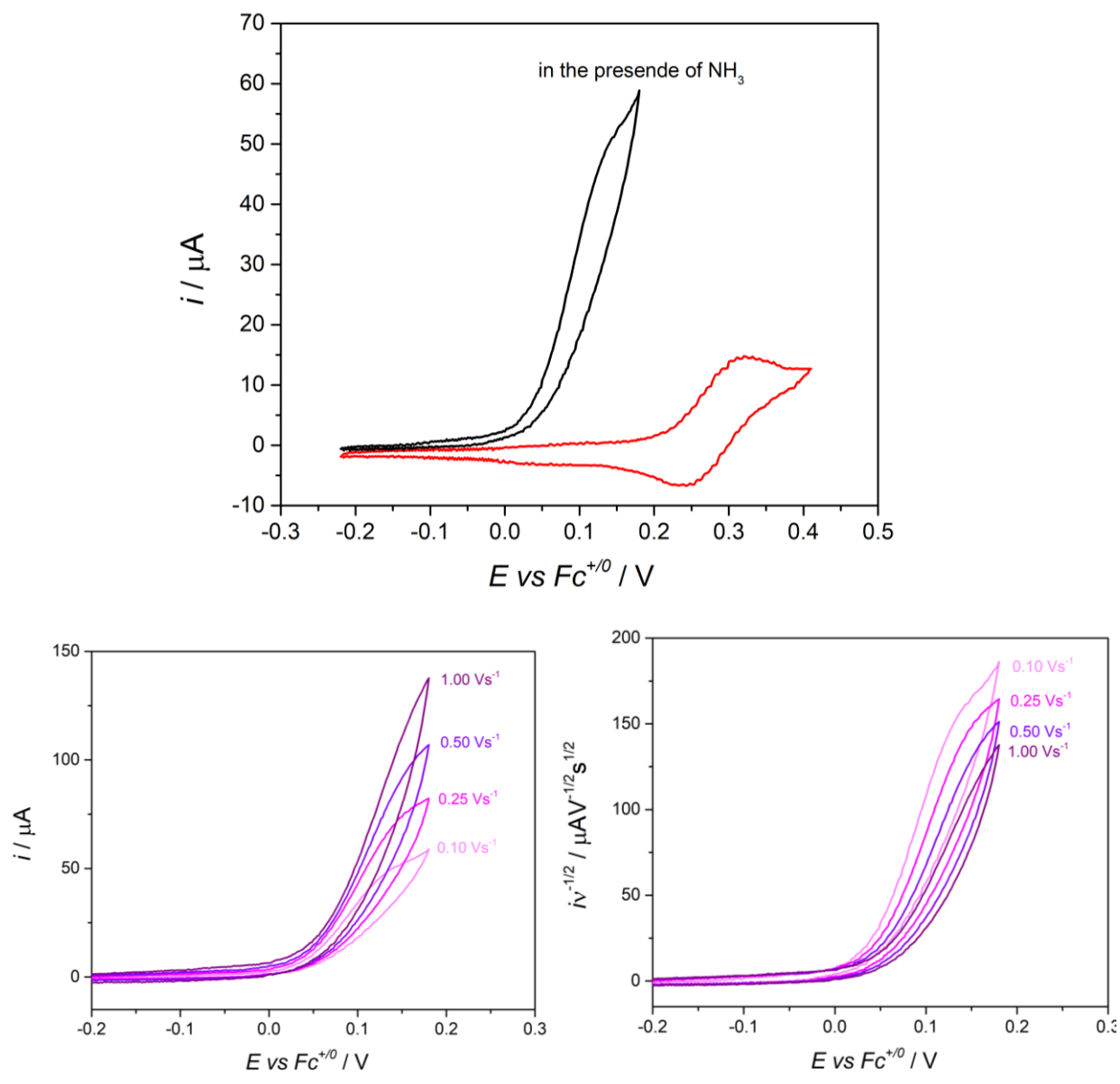


Figure 6.3.3 Top: CVs for 1.68×10^{-3} M **3a** in NM in the absence (red) and presence (black) of NH_3 . Scan rate 0.1 Vs^{-1} . Bottom: CVs of the catalytic ammonia oxidation in NM in the presence of 1.68×10^{-3} M **3a**, with different scan rates (left). The normalized currents shown for the same set of data (right).

6.4. Conclusions

The catalytic activity of three other ruthenium polypyridyl amine complexes was evaluated by cyclic voltammetry. Catalyst **4a** shows the lowest onset potential for the catalytic current.

Interestingly, the normalized catalytic currents for complex **5a** behave independently from the scan rate, suggesting that a different catalytic mechanism is in operation. Evolution of N₂ and H₂ for these complexes must be performed to further prove the catalytic activity as well as the efficiencies of the catalysts.

APPENDIX

A6.1 ^1H NMR Spectra

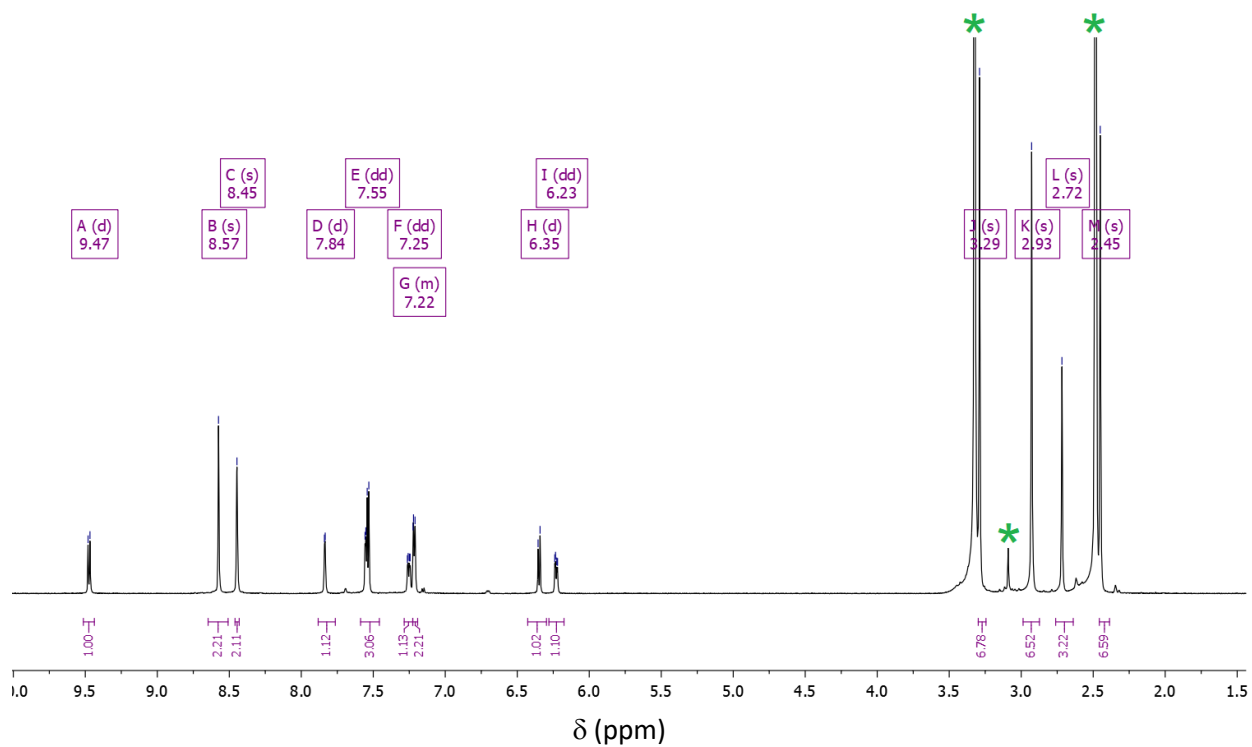


Figure A6.1.1 ^1H NMR spectrum of $[\text{Ru}(\text{Me}_3\text{trpy})(\text{dmabpy})\text{Cl}]\text{Cl}$ in $\text{DMSO}-d_6$. Top: full spectrum, Bottom: blow-up of the aromatic region. Starred peaks are solvent residuals or impurities.

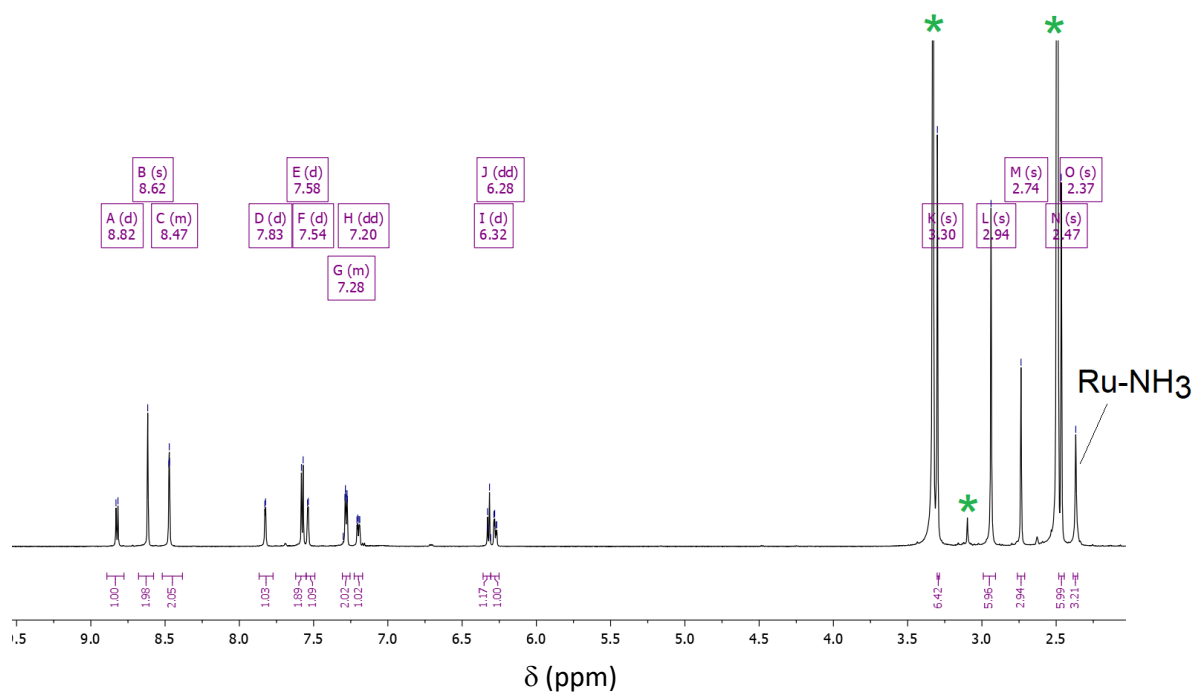


Figure A6.1.2 ^1H NMR spectrum of $[\text{Ru}(\text{Me}_3\text{trpy})(\text{dmabpy})\text{NH}_3](\text{PF}_6)_2$ in $\text{DMSO}-d_6$. Top: full spectrum, Bottom: blow-up of the aromatic region. Starred peaks are solvent/impurity related.

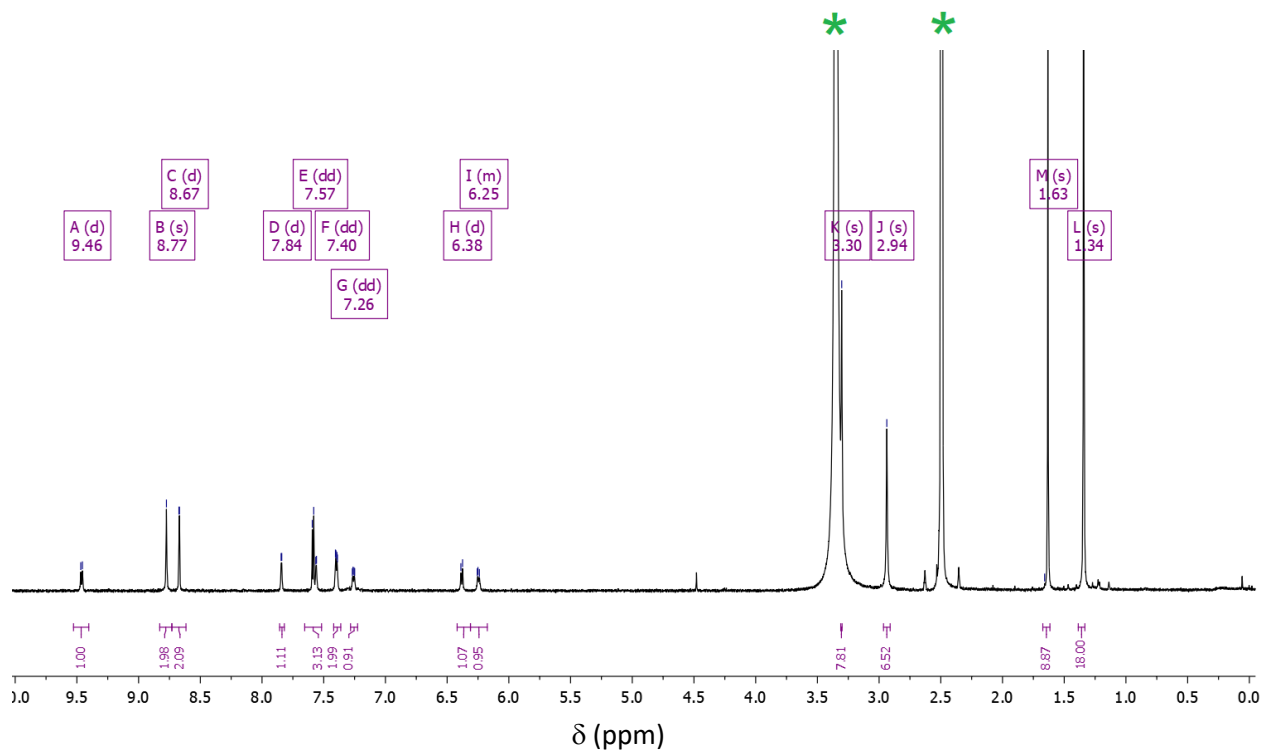


Figure A6.1.3 ^1H NMR spectrum of $[\text{Ru}(\text{tBu}_3\text{trpy})(\text{dmabpy})\text{Cl}]\text{Cl}$ in $\text{DMSO}-d_6$. Top: full spectrum, Bottom: blow-up of the aromatic region. Starred peaks are solvent residuals.

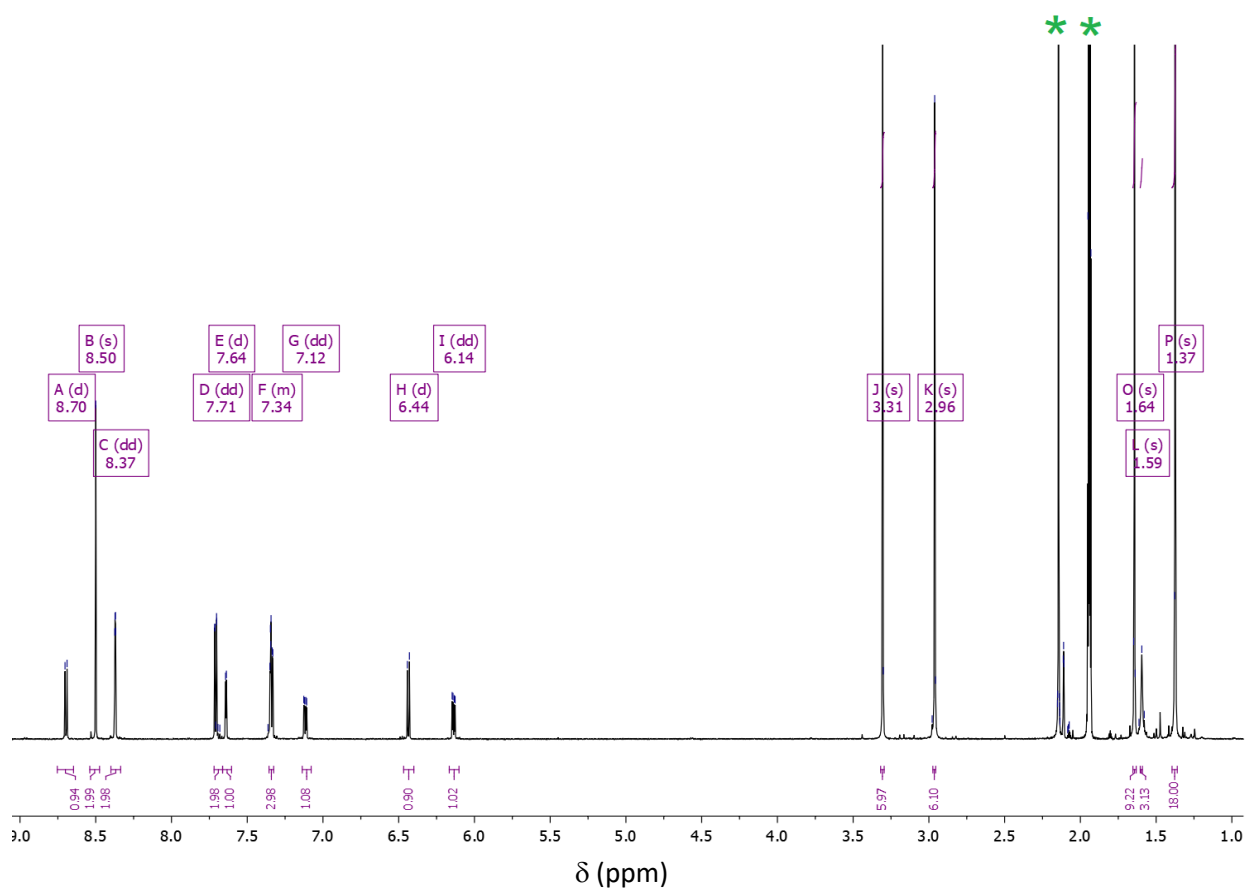


Figure A6.1.4 ^1H NMR spectrum of $[\text{Ru}(\text{'Bu}_3\text{trpy})(\text{dmabpy})\text{NH}_3](\text{PF}_6)_2$ in acetonitrile- d_3 . Top: full spectrum, Bottom: blow-up of the aromatic region. Starred peaks are solvent related.

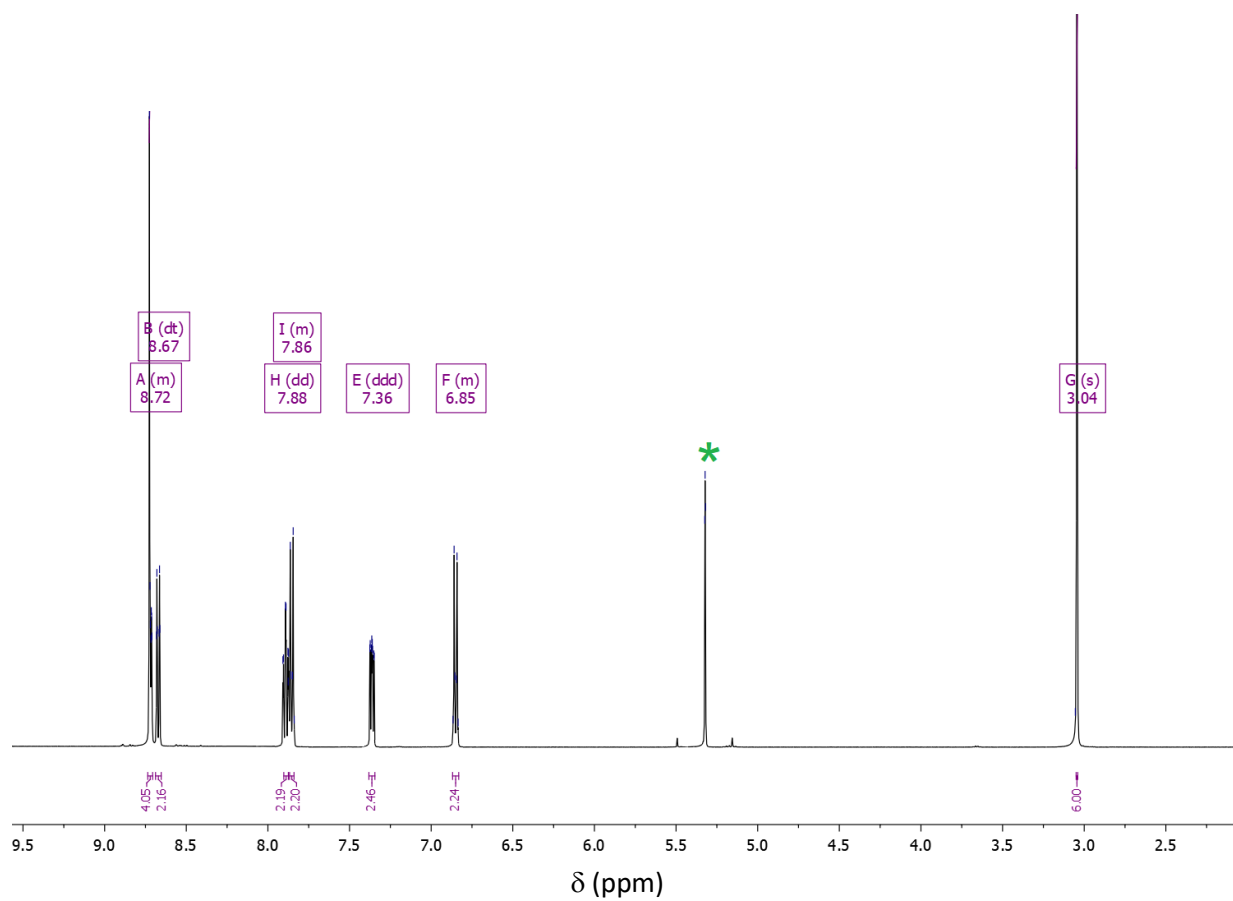


Figure A6.1.5 ^1H NMR spectrum of (4-N,N-dimethylaminophenyl)-2,2',6',2''-terpyridine in methylene chloride- d_2 . Starred peak is solvent residuals.

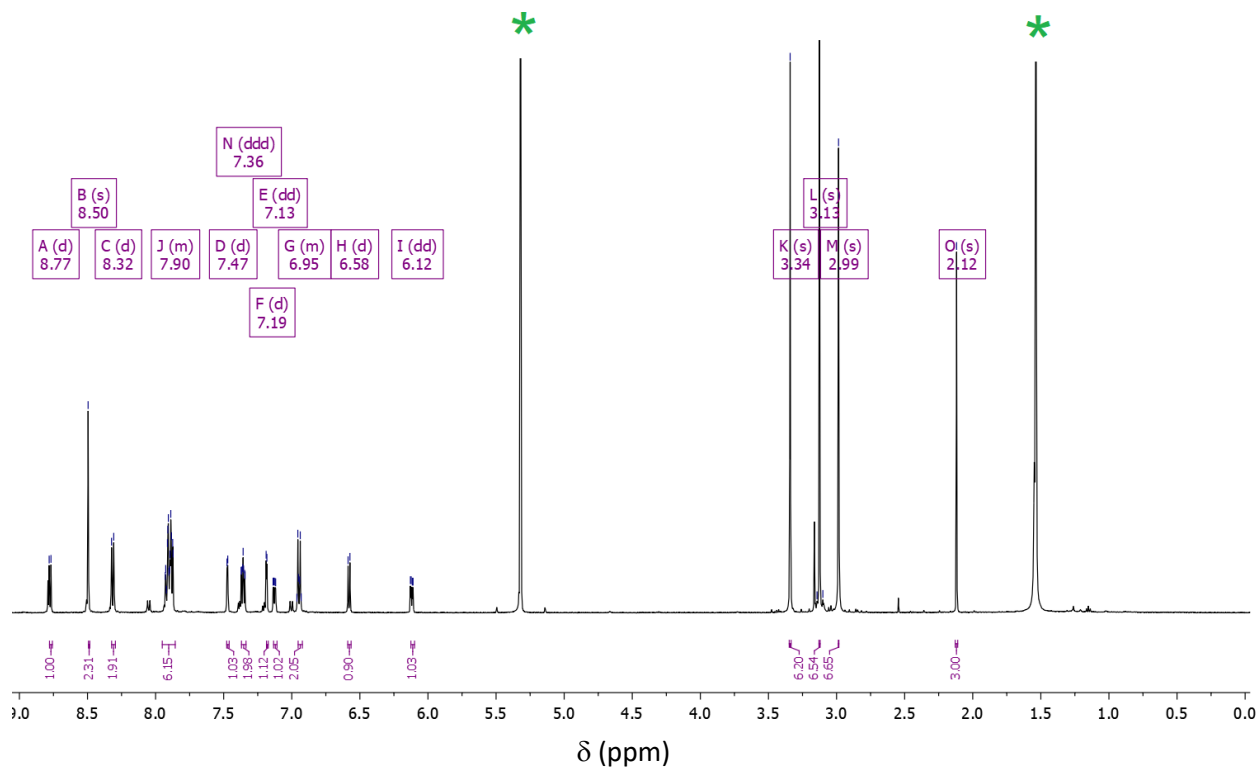


Figure A6.1.6 ^1H NMR spectrum of $[\text{Ru}(\text{dmaptrpy})(\text{dmabpy})\text{NH}_3](\text{PF}_6)_2$ in $\text{CD}_2\text{Cl}_2-d_2$. Starred peaks are solvent and impurity residuals. Some unknown impurities are not labeled.

REFERENCES

REFERENCES

- (1) Hanan, G. S.; Wang, J. *SYNLETT* **2005**, No. 8, 1251–1254.

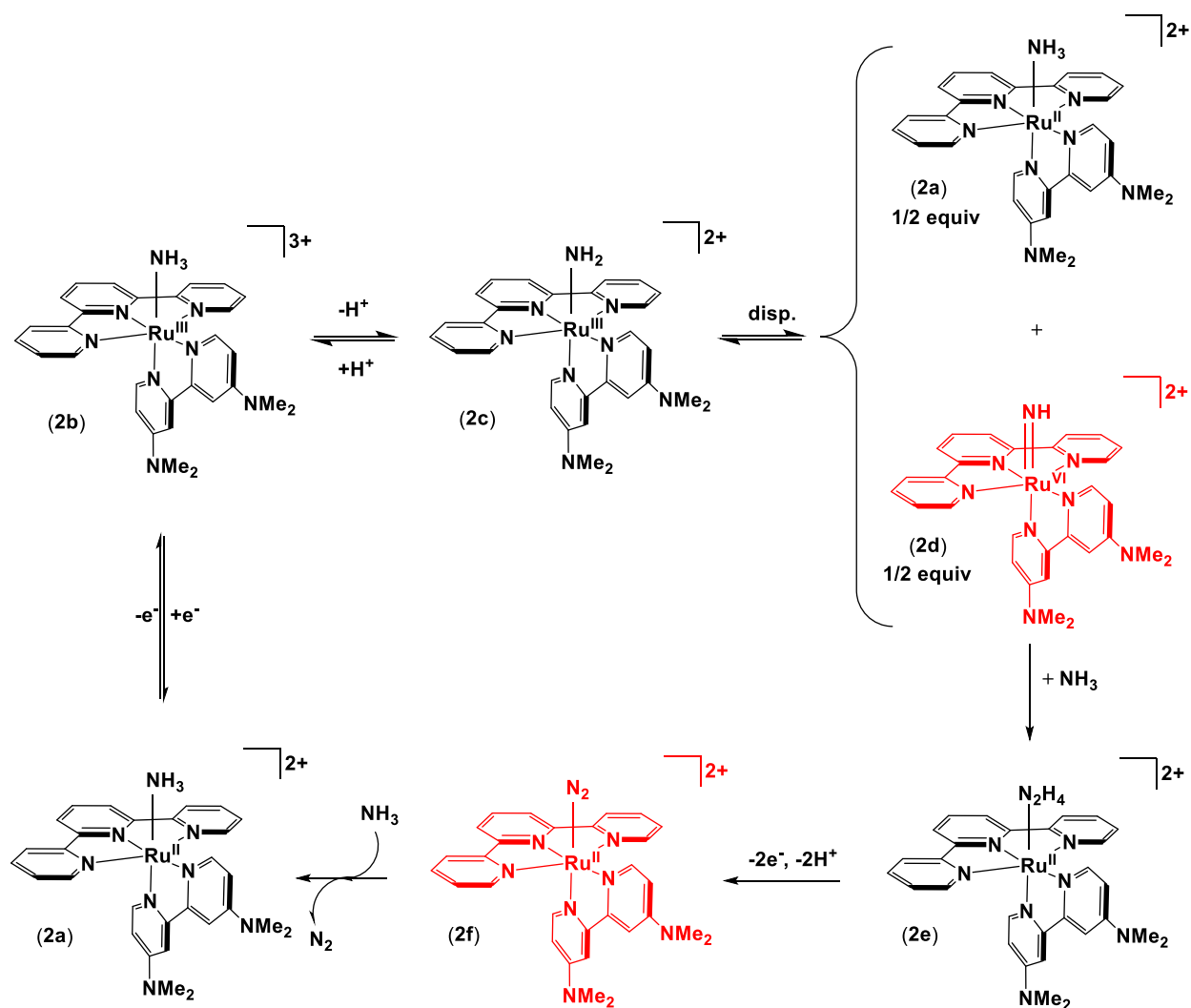
CHAPTER 7: CONCLUDING REMARKS AND FUTURE DIRECTIONS

In this work, molecular catalysts based on ruthenium polypyridyl amine complexes were synthesized and studied for their catalytic activity towards homogeneous oxidation of NH_3 to N_2 in non-aqueous media under mild conditions. The catalytic behavior was confirmed via electrochemical studies and the products of the ammonia splitting, N_2 and H_2 , were quantified in the headspace of a solution of NH_3 in THF in the presence of $[\text{Ru}(\text{trpy})(\text{bpy})\text{NH}_3](\text{PF}_6)_2$ after segments of controlled potential electrolysis. Those results confirmed that the onset of the oxidation of NH_3 in THF was reduced by approximately 300 mV upon addition of the catalyst and N_2 and H_2 were generated with ratios of approximately 1: 3, with faradaic efficiencies as high as 80%. Since the solution after the electrolysis, only contained the starting $[\text{Ru}(\text{trpy})(\text{bpy})\text{NH}_3](\text{PF}_6)_2$ catalyst after 180 min of electrolysis, it was concluded that the catalyst regeneration was fully achieved and a closed catalytic cycle was performing. Isotope labeling experiments suggested that the catalysis is ensued through a hydrazine pathway as no evidence was found to support the formation of N_2 bridged intermediates. The possibility of heterogeneous catalysis was ruled out after no N_2 and H_2 were detected in control rinse test experiments, as well as an examination of the surface of the electrode after the electrolysis did not show any depositions on the surface.

Next, understanding of the mechanism of the catalysis was pursued. The $[\text{Ru}(\text{trpy})(\text{bpy})\text{NH}_3](\text{PF}_6)_3$ intermediate was isolated and was further studied using a variety of techniques including ^1H NMR and electrochemical measurements. It was shown that the $[\text{Ru}(\text{trpy})(\text{bpy})\text{NH}_3](\text{PF}_6)_3$ was the first intermediate under catalytic conditions where the applied potential is positive to enable the one-electron oxidation of the $\text{Ru}(\text{II})$ center to $\text{Ru}(\text{III})$. Spectrophotocatalytic experiments revealed that this intermediate is unstable in the presence of a proton acceptor and undergoes deprotonation to give a $[\text{Ru}(\text{trpy})(\text{bpy})\text{NH}_2](\text{PF}_6)_2$ intermediate which was observed in mass spectrometry experiments. This second intermediate is very unstable and yielded half equivalent of

$[\text{Ru}(\text{trpy})(\text{bpy})\text{NH}_3](\text{PF}_6)_2$ as one product. Based on this observations and reported similar chemistry for analogous aqua complexes, a redox disproportionation pathway was considered to be occurring in which one equivalent of $[\text{Ru}(\text{trpy})(\text{bpy})\text{NH}_2](\text{PF}_6)_2$ disproportionated to 0.5 equivalent of $[\text{Ru}(\text{trpy})(\text{bpy})\text{NH}_3](\text{PF}_6)_2$ and 0.5 equivalent of $[\text{Ru}(\text{trpy})(\text{bpy})\text{NH}](\text{PF}_6)_2$, another intermediate that was not directly detected. However, since the hydrazine pathway for the catalytic cycle was previously established, the generation of the Ru(IV)NH intermediate was still envisioned to be a key step in the reaction mechanism. This was further studied in experiments which were conducted using an authentic $\text{Ru(II)N}_2\text{H}_4$ complex. The cyclic voltammograms of solutions of the hydrazine complex were closely comparable to the CVs of solutions of $[\text{Ru}(\text{trpy})(\text{bpy})\text{NH}_3](\text{PF}_6)_2$ and stoichiometric concentrations of NH_3 in THF. Cyclic voltammograms of the saturated solution of NH_3 in THF in the presence of $[\text{Ru}(\text{trpy})(\text{bpy})\text{N}_2\text{H}_4](\text{PF}_6)_2$ exhibited a catalytic current with an onset identical to that obtained when $[\text{Ru}(\text{trpy})(\text{bpy})\text{NH}_3](\text{PF}_6)_2$ was used as the catalyst.

Putting all the results together, we proposed a mechanistic cycle for the homogenous catalytic ammonia oxidation as shown in Scheme 0.1.



Scheme 0.1 The proposed catalytic cycle. The formation of the complexes highlighted in red has not yet been directly confirmed.

While direct evidence supports the roles of species **2a**, **2b**, **2c**, and **2e**, the Ru(IV)NH intermediate (**2d**) is still the missing puzzle piece. The very high reactivity of **2d** and its high expected acidity would be one reason that its detection in the presence of a base was not successful. While it not yet clear that what possible reactions **2d** might undergo in the presence of a non-coordinating base such as DBU, more experiments are necessary using solvents and based more innocent than the ones employed in this study (nitromethane and DBU).

Another approach that seems to be crucial to be taken is to move from hexafluorophosphate salts of the complexes to more soluble counter anions. For instance, swapping the counter ion from PF_6^- to a more lipophilic anion such as Tetrakis(3,5-bis(trifluoromethyl)phenyl)borate (BAr^{F}) would enable us to do more accurate NMR measurements in THF and more importantly, kinetic studies using stopped-flow techniques in DCM.

The steps of the catalytic cycle past the formation of the hydrazine intermediate are also still unknown. Independent synthesis of $[\text{Ru}(\text{trpy})(\text{bpy})\text{N}_2](\text{PF}_6)_2$ would provide useful approaches to final steps of the cycle. Another important consideration is the possibility of proton-coupled electron transfer steps. Cundari et al. at the University of North Texas are preparing a computational article which discusses the mechanism of the catalytic pathway for ammonia oxidation based on the catalysts **1a** and **2a** introduced in this study. Those results would be invaluable in terms of setting a guideline towards the electron and proton transfer kinetics and would be complementary to our efforts on establishing a proposed catalytic cycle. With the catalytic cycle being decoded, the work could be directed towards developing more effective catalysts and eventually achieve lower overpotentials as well as higher faradaic efficacies.